25 May 2012 | $10

Science

AAAS

Their research brightens the future of mankind.

Dr. Brian J. Druker
USA

Dr. Janet D. Rowley
USA

Dr. Nicholas B. Lydon
USA

Development of a new therapeutic drug targeting cancer-specific molecules

"Healthcare and Medical Technology" Field

Dr. Masato Sagawa
Japan

Development of the world's highest performance Nd-Fe-B type permanent magnet and contributing to energy conservation

"Environment, Energy and Infrastructure" Field

A drug that provides dramatic effectiveness as a treatment for chronic myelogenous leukemia and the molecular targeting approach that offers bright hopes for the future of cancer drug development. Also, the world's highest performance permanent magnet that achieves a massive improvement in the efficiency of motors, contributing to energy conservation on a global scale. These are people deserving of receiving the Japan Prize, which is awarded to those who are recognized as having achieved original and dramatic accomplishments that greatly enhance the progress of science and technology, thereby contributing to the peace and prosperity of mankind.

2012 (28th) Japan Prize Presentation Ceremony

▶ You can view the Presentation Ceremony and watch Commemorative Lectures by the Laureates.

www.japanprize.jp

JAPAN PRIZE

JAPAN PRIZE

LOCATION: Jackson Park Health Club
ARTICLE: *An Electronic Second Skin*
DATE: Sep 21, 7:43am

LOCATION: University Faculty Lounge
ARTICLE: *The Visual Impact of Gossip*
DATE: Sep 21, 4:22pm

LOCATION: Gyro King
ARTICLE: *Cavemen Craved Carbs, Too*
DATE: Sep 21, 1:13pm

LOCATION: Hemlock Bar
ARTICLE: *Quantum Simulation of Frustrated Classical Magnetism in Triangular Optical Lattices*
DATE: Sep 21, 9:21pm

LOCATION: Bed
ARTICLE: *Consciousness: What, How and Why*
DATE: Sep 21, 10:56pm

A new way to look at science

The new *Science* Reader app for iPad® from AAAS puts *Science* in your hands, wherever you go. Read abstracts, career advice, and highlights from our newest journals, *Science Signaling* and *Science Translational Medicine*. Plus, AAAS members can access full text articles from *Science*. Visit iTunes App Store℠ or content.aaas.org/ipad for details.

Available on the App Store

Science
AAAS

NEW ENGLAND BioLabs® Inc.
enabling technologies in the life sciences

Mix it up.

RE-Mix™ Restriction Enzyme Master Mixes

Restriction enzyme digests are now even easier! The same high quality restriction enzymes that you have come to trust from New England Biolabs are now available in master mix format, including enzyme, buffer and loading dye; simply add your DNA and digest.

With RE-Mix Master Mixes take advantage of:

- Simplified and shortened protocols
- Fast digestion in 15 minutes (Time-Saver qualified)
- High product quality with reproducible results

RE-Mix Master Mixes – just add your DNA and mix

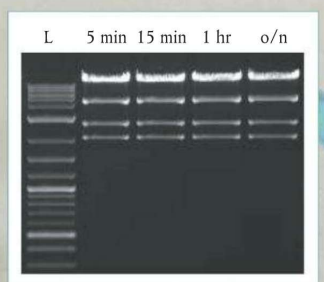

pXba DNA was digested with EcoRV-HF™ RE-Mix™ according to the recommended protocol. Lane L is the TriDye™ 2-Log DNA Ladder (NEB #N3270). The same results are obtained whether incubated for 5–15 minutes, 1 hour or overnight.

For more information, visit
www.NEBREMIX.com

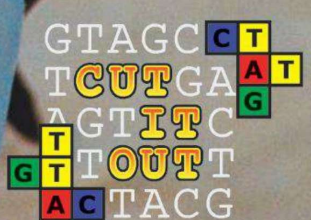

To experience the new restriction enzyme challenge from NEB, visit
www.NEBcutitout.com

Blue-footed Booby (Sula nebouxii)
© Tui De Roy

EDITORIAL

959 Cultivating Global Science
Subra Suresh

NEWS OF THE WEEK

964 A roundup of the week's top stories

NEWS & ANALYSIS

967 Dams Along Sudanese Nile Threaten Ancient Sites

968 Senate Bills Would Make Room for More STEM Graduates

969 NSF's 'Big Pitch' Tests Anonymized Grant Reviews

970 Homegrown Organic Matter Found on Mars, But No Life
>> Science *Express Report by A. Steele* et al.

971 Military's Plan to Buy Biofuels Hits Roadblock in U.S. House

972 NSF Gives Clinical Students a Shot at Winning Graduate Fellowships

NEWS FOCUS

973 An Evolutionary Theory of Dentistry
The Burdens of Being a Biped
>> Science *Podcast*

976 The Biology of Genomes Meeting
Single-Cell Sequencing Tackles Basic and Biomedical Questions
HDL Itself Does Not Prevent Heart Attacks

LETTERS

978 Support for Greece
H. Z. Hausen

"Two Heads Are Better" Stands to Reason
H. Mercier and D. Sperber

979 Life in Science: The Noblest Lesson
R. Sinclair

BOOKS *ET AL.*

980 The Power of Habit
C. Duhigg, reviewed by W. Wood

981 Measuring the Universe
M. Kukula and R. Higgitt, curators, reviewed by D. Dixon

POLICY FORUM

982 From "Science in Europe" to "European Science"
M. Nedeva and M. Stampfer

PERSPECTIVES

984 Pushing Your Back into Place
B. Bowerman and S. M. O'Rourke
>> *Research Article p. 999*

985 Guided Tour to the Heart of RISC
E. Kaya and J. A. Doudna
>> *Report p. 1036*

986 Resolving Some Old Problems in Protein Crystallography
P. Evans
>> *Reports pp. 1030 and 1032*

988 Kinship and Human Thought
S. C. Levinson
>> *Brevia p. 998; Report p. 1049*

989 Enter the Majorana Fermion
P. W. Brouwer
>> *Report p. 1003*

990 Systems Biology, Metabolomics, and Cancer Metabolism
M. Tomita and K. Kami
>> *Report p. 1040*

991 An Avian Magnetometer
M. Winklhofer
>> *Report p. 1054*

SCIENCE PRIZE ESSAY

993 Learning Biology by Recreating and Extending Mathematical Models
H. J. Chiel et al.

CONTENTS continued >>

page 973

page 980

COVER

Artist's rendering of an electronic device hosting Majorana fermions. The semiconducting nanowire (cylindrical structure) has a diameter of 100 nanometers and lies atop a gate structure consisting of many metallic stripes. The nanowire is contacted at the top with a gold electrode and at the bottom with a superconducting electrode (shown in blue). See page 1003.

Image: V. Mourik, K. Zuo, S. M. Frolov, S. R. Plissard, E. P. A. M. Bakkers, L. P. Kouwenhoven, with assistance from www.avalondesigns.nl

DEPARTMENTS

956 This Week in *Science*
961 Editors' Choice
963 *Science* Staff
997 AAAS News & Notes
1058 New Products
1059 *Science* Careers

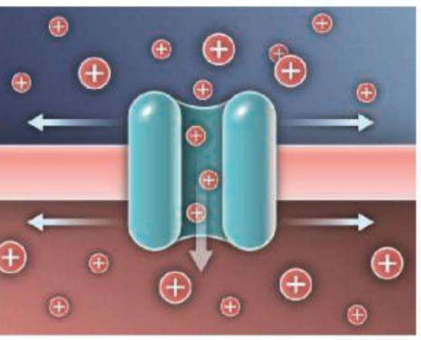

pages 991 & 1054

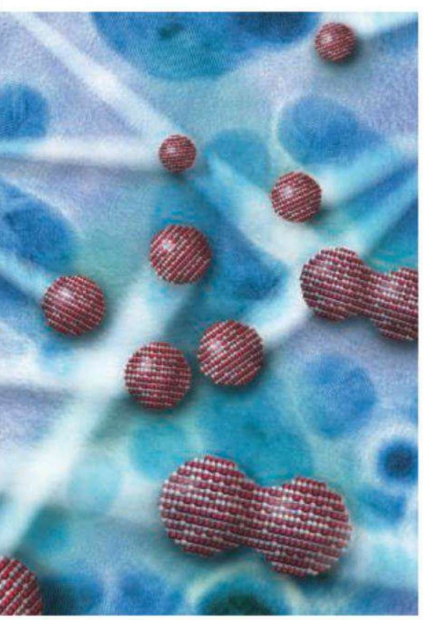

pages 1011 & 1014

BREVIA

998 Predicting Pragmatic Reasoning in Language Games
M. C. Frank and N. D. Goodman
A Bayesian inference model predicts how listeners decode communications.
>> *Perspective p. 988; Report p. 1049*

RESEARCH ARTICLE

999 Growing Microtubules Push the Oocyte Nucleus to Polarize the *Drosophila* Dorsal-Ventral Axis
T. Zhao et al.
The addition of tubulin monomers to microtubules provides the force to relocate the oocyte nucleus.
>> *Perspective p. 984*

REPORTS

1003 Signatures of Majorana Fermions in Hybrid Superconductor-Semiconductor Nanowire Devices
V. Mourik et al.
Theoretically predicted particles that double as their own antiparticles emerge in a superconductor-coupled indium antimonide nanowire.
>> *Perspective p. 989*

1007 Unidirectional Growth of Microbumps on (111)-Oriented and Nanotwinned Copper
H.-Y. Hsiao et al.
Oriented copper grains grown using direct-current electroplating serve as a template for intermetallic microbumps.

1011 Real-Time Imaging of Pt_3Fe Nanorod Growth in Solution
H.-G. Liao et al.
An in situ liquid stage is used to study the formation of nanowires from solution in a transmission electron microscope.

1014 Direction-Specific Interactions Control Crystal Growth by Oriented Attachment
D. Li et al.
Iron oxyhydroxide nanoparticles rotate until finding a perfect lattice match with a neighboring particle to grow.

1018 Large-Pore Apertures in a Series of Metal-Organic Frameworks
H. Deng et al.
Metal-organic frameworks with hexagonal channel pores up to almost 100 angstroms in diameter have been synthesized.

1023 Linking Petrology and Seismology at an Active Volcano
K. Saunders et al.
Volcanic minerals from a Mount St. Helens eruption reveal a causal relationship between magma processes and seismicity.

1028 Temperature-Dependent Alterations in Host Use Drive Rapid Range Expansion in a Butterfly
R. M. Pateman et al.
A warmer UK has enabled the brown argus butterfly to expand its range by feasting on the geranium.

1030 Linking Crystallographic Model and Data Quality
P. A. Karplus and K. Diederichs
A statistical method places model and data quality on the same scale and indicates how far one can model.

1032 Structures from Anomalous Diffraction of Native Biological Macromolecules
Q. Liu
Don't get MAD or be SAD; try lower energy.
>> *Perspective p. 986*

1036 The Crystal Structure of Human Argonaute2
N. T. Schirle and I. J. MacRae
The structure of the core protein of the human RNA interference machinery is determined at high resolution.
>> *Perspective p. 985*

1040 Metabolite Profiling Identifies a Key Role for Glycine in Rapid Cancer Cell Proliferation
M. Jain et al.
Rapidly growing cancer cells rely on the amino acid glycine to make nucleotides.
>> *Perspective p. 990*

1045 FKF1 Conveys Timing Information for CONSTANS Stabilization in Photoperiodic Flowering
Y. H. Song et al.
A plant protein sensitive to blue light links longer afternoons to more flowering.

1049 Kinship Categories Across Languages Reflect General Communicative Principles
C. Kemp and T. Regier
The systems of terms used in different languages to describe kin are optimized for simplicity and informativeness.
>> *Perspective p. 988; Brevia p. 998;* Science *Podcast*

1054 Neural Correlates of a Magnetic Sense
L.-Q. Wu and J. D. Dickman
Neurons in a pigeon's brain encode the direction and intensity of the geomagnetic field.
>> *Perspective p. 991*

CREDIT: (BOTTOM) ZINA DERETSKY

SCIENCEONLINE

SCIENCEXPRESS

www.sciencexpress.org

A Mitochondrial Pyruvate Carrier Required for Pyruvate Uptake in Yeast, *Drosophila*, and Humans
D. K. Bricker et al.
The genes encoding two components of the pyruvate transporter in mitochondria have been identified.
10.1126/science.1218099

Identification and Functional Expression of the Mitochondrial Pyruvate Carrier
S. Herzig et al.
Two components of the mitochondrial pyruvate transporter confer transport activity when expressed in bacteria.
10.1126/science.1218530

Recurrent Hemizygous Deletions in Cancers May Optimize Proliferative Potential
N. L. Solimini et al.
The genomes of cancer cells have preferentially lost genes that inhibit cell growth.
10.1126/science.1219580

The Structures of COPI-Coated Vesicles Reveal Alternate Coatomer Conformations and Interactions
M. Faini et al.
The flexible coatomer complex makes contact with a variable number of neighbors and coats vesicles of variable size.
10.1126/science.1221443

Structural Basis for Prereceptor Modulation of Plant Hormones by GH3 Proteins
C. S. Westfall et al.
Crystal structures of plant GH3 proteins reveal how these enzymes accommodate jasmonates, auxins, and benzoates.
10.1126/science.1221863

A Reduced Organic Carbon Component in Martian Basalts
A. Steele et al.
Analysis of 11 martian meteorites reveals complex hydrocarbons associated with magmatic minerals in 10 of them.
10.1126/science.1220715
>> News story p. 970

Hesperian Age for Western Medusae Fossae Formation, Mars
J. R. Zimbelman and S. P. Scheidt
Counts of impact craters provide age for a region on Mars close to the landing site of rover Curiosity.
10.1126/science.1221094

SCIENCENOW

www.sciencenow.org

Highlights From Our Daily News Coverage

Life at the Top Can Be Good for Your Health
A study suggests that high-ranking baboons have stronger immune systems.
http://scim.ag/Immune_Systems

Just a Spoonful of Castor Oil
A study reveals the molecular mechanism of castor oil.
http://scim.ag/Castor_Oil

Barely Breathing Microbes Still Living in 86-Million-Year-Old Clay
Organisms deep beneath the sea floor survive on minuscule amounts of oxygen.
http://scim.ag/Microbes-Oxygen

SCIENCESIGNALING

www.sciencesignaling.org

The Signal Transduction Knowledge Environment

22 May issue: http://scim.ag/ss052212

RESEARCH ARTICLE: Interferon-β Therapy Against EAE Is Effective Only When Development of the Disease Depends on the NLRP3 Inflammasome
M. Inoue et al.

PODCAST
M. L. Shinohara and A. M. VanHook
Characterization of an animal model may explain why not all patients with multiple sclerosis respond to interferon-β.

PERSPECTIVE: Structure of the First Sphingosine 1-Phosphate Receptor
A. L. Parrill et al.
The lipid sphingosine 1-phosphate may laterally diffuse through the membrane to bind a receptor.

PERSPECTIVE: Revisiting Channel Allostery—A Coherent Mechanism in IP_3 and Ryanodine Receptors
K. Hamada and K. Mikoshiba
Structural analyses suggest a similar gating mechanism in the IP_3 and ryanodine receptors.

SCIENCETRANSLATIONAL MEDICINE

www.sciencetranslationalmedicine.org

Integrating Medicine and Science

23 May issue: http://scim.ag/stm052312

FOCUS: Clinician-Investigators as Translational Bioscientists—Shaping a Seamless Identity
E. R. Edelman and K. LaMarco

COMMENTARY: Risk and Return for the Clinician-Investigator
S. Henrickson and D. Altshuler

PODCAST
E. R. Edelman and K. LaMarco
In this first of a series, senior scientists counsel early-career clinician-investigators on molding a successful research career.

RESEARCH ARTICLE: Effective Adjunctive Therapy by an Innate Defense Regulatory Peptide in a Preclinical Model of Severe Malaria
A. H. Achtman et al.
Anti-inflammatory drugs based on host defense peptides ameliorate malaria in mice.

RESEARCH ARTICLE: Adenosine A_{2A} Receptor Activation Prevents Wear Particle–Induced Osteolysis
A. Mediero et al.
Bone damage cause by particles from orthopedic implants is prevented by an adenosine receptor agonist in mice.

RESEARCH ARTICLE: PTH/PTHrP and Vitamin D Control Antimicrobial Peptide Expression and Susceptibility to Bacterial Skin Infection
B. Muehleisen et al.
Vitamin D and parathyroid hormone work together to maximize innate immune resistance to skin infections.

RESEARCH ARTICLE: Modeling the Dynamic Relationship Between HIV and the Risk of Drug-Resistant Tuberculosis
R. Sergeev et al.

FOCUS: TB and HIV—Deadly Liaison or Manageable Threat?
B. G. Williams
HIV-coinfected TB patients are less likely to be affected by drug-resistant TB.

LETTERS: Comments and Response on "The Predictive Capacity of Personal Genome Sequencing"
Comments: C. B. Begg and M. C. Pike; D. Golan and S. Rosset; E. J. Topol
Response: B. Vogelstein et al.

SCIENCECAREERS

www.sciencecareers.org/career_magazine

Free Career Resources for Scientists

Experimental Error: The Unwritten Rules of Journalism
A. Ruben
The key to understanding the way the media covers science is to know the rules to which science journalists adhere.
http://scim.ag/EE_SciWriters

Working for a Contract Research Organization
N. Lubick
Scientists interested in any phase of drug research and development can find opportunities within CROs.
http://scim.ag/CRO_Work

Content Collection: Lab Management
E. Pain
New group leaders need to learn how to manage people, projects, finances, and more.
http://scim.ag/CC_LabManagement

SCIENCEPODCAST

www.sciencemag.org/multimedia/podcast

Free Weekly Show

On the 25 May *Science* Podcast: classifying cousins, the evolution of bad teeth, where science and comedy meet, and more.

SCIENCE (ISSN 0036-8075) is published weekly on Friday, except the last week in December, by the American Association for the Advancement of Science, 1200 New York Avenue, NW, Washington, DC 20005. Periodicals Mail postage (publication No. 484460) paid at Washington, DC, and additional mailing offices. Copyright © 2012 by the American Association for the Advancement of Science. The title SCIENCE is a registered trademark of the AAAS. Domestic individual membership and subscription (51 issues): $149 ($74 allocated to subscription). Domestic institutional subscription (51 issues): $990; Foreign postage extra: Mexico, Caribbean (surface mail) $55; other countries (air assist delivery) $85. First class, airmail, student, and emeritus rates on request. Canadian rates with GST available upon request, GST #1254 88122. Publications Mail Agreement Number 1069624. **Printed in the U.S.A.**

Change of address: Allow 4 weeks, giving old and new addresses and 8-digit account number. **Postmaster:** Send change of address to AAAS, P.O. Box 96178, Washington, DC 20090–6178. **Single-copy sales:** $10.00 current issue, $15.00 back issue prepaid includes surface postage; bulk rates on request. **Authorization to photocopy** material for internal or personal use under circumstances not falling within the fair use provisions of the Copyright Act is granted by AAAS to libraries and other users registered with the Copyright Clearance Center (CCC) Transactional Reporting Service, provided that $30.00 per article is paid directly to CCC, 222 Rosewood Drive, Danvers, MA 01923. The identification code for *Science* is 0036-8075. *Science* is indexed in the *Reader's Guide to Periodical Literature* and in several specialized indexes.

AAAS
ADVANCING SCIENCE, SERVING SOCIETY

EDITED BY STELLA HURTLEY

Spring Into Flower >>

In spring, plants respond to increasing day length and shifts in the spectrum of solar irradiance by releasing the flowering induction pathway, which includes expression of the FLOWERING LOCUS T (FT) protein. **Song *et al.*** (p. 1045) have now identified a trio of controls brought to bear on FT gene expression by the FKF1 (FLAVIN-BINDING, KELCH REPEAT, F-BOX 1) protein. FKF1 removes a repressor and also stabilizes the activating CONSTANS (CO) protein in the afternoons through a binding interaction enhanced by blue light—an increasing component of solar irradiation during spring. Then FKF1 itself helps to activate transcription of the *CO* gene. Thus, by removing the repressor and shoring up the activator, FKF1 sets flowering on its way.

Pull Me–No!–Push You

The *Drosophila* dorsal-ventral (DV) axis is polarized by the movement of the nucleus from the posterior end of the oocyte to its anterior margin. It has long been assumed that the nucleus is pulled to the anterior end by the molecular motor dynein along the polarized microtubule cytoskeleton that defines the anterior-posterior (AP) axis. Using live imaging, **Zhao *et al.*** (p. 999, published online 12 April; see the Perspective by **Bowerman and O'Rourke**) now demonstrate that the nucleus is pushed toward the anterior by the force exerted by growing microtubules hitting its posterior side. DV polarity thus depends on the posterior positioning of the microtubule organizing center rather than on AP axis formation.

Subterranean Eruption Clues

Volcano monitoring relies upon detecting changing physical conditions around an active source, such as increased seismicity or ground deformation; however, relating these behaviors to magmatic processes below ground remains challenging. The geochemical signatures of erupted magmatic crystals, including chemically distinct zones formed during growth and cooling, provide clues as to the conditions of the magma chamber prior to the eruption. Through a combination of chemical analysis of orthopyroxene crystals and chronometry based on diffusion, **Saunders *et al.*** (p. 1023) were able to link the magmatic processes and seismic events leading up to and during the 1980–1986 series of eruptions at Mount St. Helens, USA. The seismic events corresponded to earthquakes caused by magma degassing and ground movement—events of which are routinely detected with geophysical instruments.

Tiny Tinny Bumps

One challenge in moving to three-dimensional integrated circuit architectures is the need for aligned interconnects to join neighboring layers. **Hsiao *et al.*** (p. 1007) applied rapid stirring to the direct current electroplating of copper to produce films with oriented copper grains that have a high density of nanotwin defects. The resulting material was an excellent platform for the growth of copper-tin intermetallic compounds in the form of arrays of microbumps potentially suitable for the soldering of electronic components.

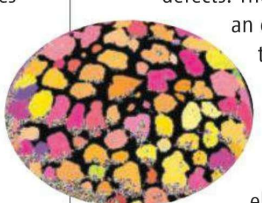

Majoranas Arrive

When a negatively charged electron meets a positron—its positively charged antiparticle—they annihilate each other in a flash of gamma rays. A Majorana fermion, on the other hand, is a neutral particle, which is its own antiparticle. No sightings of a Majorana have been reported in the elementary particle world, but recently they have been proposed to exist in solid-state systems and suggested to be of interest as a quantum computing platform. **Mourik *et al.*** (p. 1003, published online 12 April; see the cover; see the Perspective by **Brouwer**) set up a semiconductor nanowire contacted on each end by a normal and a superconducting electrode that revealed evidence of Majorana fermions.

Growing in Liquid

The ability to control the growth of materials at the nanometer scale is key to nanotechnology. Materials grown in liquids, however, are difficult to track on a particle-by-particle basis during growth. Two studies used an in situ liquid cell to follow the formation of larger nanoparticles or nanorods grown in solvents using high-resolution transmission electron microscopes. **Liao *et al.*** (p. 1011) watched platinum iron nanorods form from kinked chains of connected nanoparticles that gradually reoriented and straightened to form rigid rods. **Li *et al.*** (p. 1014) observed the coalescence of iron oxyhydroxide nanoparticles through an oriented attachment mechanism, whereby two similar particles rotated until their corresponding crystal lattices aligned.

Maximizing Molecular Pore Diameters

Amorphous materials, such as activated carbon, can have pore diameters of several nanometers, but the synthesis of ordered structures with very large pore diameters is often thwarted by the creation of interpenetrating networks or difficulties in removing guest molecules. **Deng *et al.*** (p. 1018) avoided these problems in the synthesis of metal-organic frameworks (MOFs) with very large diameters (some exceeding 3 nanometers) by using a combination of short and very long linking groups. The compounds formed channels almost 10 nanometers in diameter that could be visualized by electron microscopy and that were large enough to accommodate protein molecules.

CREDITS (TOP TO BOTTOM): TAKATO IMAIZUMI; HSIAO *ET AL.*

New Digs

Many studies predict range alterations among species in response to climate change. Species, however, cannot be thought of as truly independent entities, because they all exist as a part of an interacting community. Most discussions of such interactions have focused on the potential restrictions they might place on range expansion; however, **Pateman *et al.*** (p. 1028) show that climate change has the potential to increase the number of species that can interact and thus facilitate expansion. British data collected by the general public on sightings of the Brown Argus butterfly and its host plants revealed an increased affiliation between the butterflies and a previously little-used group of plants. As summers warmed, populations associated with the new host were more productive than those associated with the more "traditional" host, which facilitated expansion of the butterflies into novel regions.

Finessing Crystal Analysis

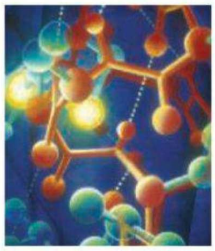

Protein crystallography has revolutionized our understanding of a whole variety of biological processes (see the Perspective by **Evans**). In crystallography, the measure of agreement between the data and the calculated model is not on the same scale as the measure of data quality, making it challenging to choose an optimal high resolution limit beyond which the data should be discarded. Now, **Karplus and Diederichs** (p. 1030) introduce a statistical model that assesses agreement of model and data accuracy on the same scale. Determining the structures of biological macromolecules by x-ray crystallography requires solving the phase problem. The two techniques that dominate phase evaluation (multi- and single-wavelength anomalous diffraction) rely on element-specific scattering from incorporated heavy atoms. **Liu *et al.*** (p. 1033) present procedures for routine structure determination of native proteins with no heavy atom incorporation. The technique, which relies on combining data from multiple crystals, was used to determine the structures of four native proteins, including a 1200-residue complex.

More Glycine, Please

To better characterize metabolic properties of cancer cells, **Jain *et al.*** (p. 1040; see the Perspective by **Tomita and Kami**) measured systematically the concentrations of hundreds of metabolites in cell culture medium in which 60 different cancer cell lines were growing. The fastest growing cancer cells tended to consume glycine, whereas more slowly growing cells excreted some glycine. The rapidly growing cancer cells appeared to need glycine for synthesis of purine nucleotides required for continued synthesis of DNA. Interfering with glycine metabolism slowed growth of the rapidly proliferating cancer cells. Thus, an increased dependence on glycine by rapidly growing cancer cells could potentially provide a target for therapeutic intervention.

Who's Who

Different languages rely on distinct sets of terminology to classify relatives, such as maternal grandfather in English, and precision in language usage is a key component for successful communication (see the Perspective by **Levinson**). **Kemp and Regier** (p. 1049) propose an organizing framework whereby kinship classification systems can all be seen to optimize or nearly optimize both simplicity and precision. The labels applied to kin are constructed from simple units and are precise enough to reduce confusion and ambiguity when used in communication. **Frank and Goodman** (p. 998) show that simplicity and precision also explain how listeners correctly infer the meaning of speech in the context of referential communication.

Magnetic Sense

Many species orient and navigate using aspects of Earth's magnetic field. Magnetic receptors have been found in the eyes, ears, and bills of birds, but there has been no clear evidence of the neural mechanism by which magnetic signals are translated into direction. Recording from the brainstem within conscious pigeons, **Wu and Dickman** (p. 1054, published online 26 April; see the Perspective by **Winklhofer**) reveal the presence of neurons in the pigeon's brain that encode the inclination angle and intensity of the geomagnetic field. Thus, pigeons—and perhaps other species—can develop an internal model of geopositional latitude to facilitate spatial orientation and navigation based on magnetoreception.

CREDIT: IRVING GEIS

What — You *Don't* Dip and Read™?!

Do less and get more from your ELISAs

- Quantitate 96 protein samples in 15 minutes, not hours
- Take advantage of a 4-log dynamic range and dilute less
- Run automated assays without wash steps or overnight incubations
- Analyze crude samples with less prep
- Get information-rich direct binding data, not end-point results
- Develop new assays in a few hours, not weeks

The Octet® Platform

Octet Systems with Dip and Read assays.
No hassle, label-free ELISAs.

fortéBIO
A Division of Pall Life Sciences

PALL Life Sciences

fortebio.com • 1-888-OCTET-75

Fast. Accurate. EASY.

Be the next winner!

2011 Winner
Dr. Tiago Branco
Postdoctoral Research Fellow
University College London

Get recognized!
US$ 25,000 Prize

Deadline for entries:
June 15, 2012

It´s easy to apply! Learn more at:
www.eppendorf.com/prize

eppendorf & Science PRIZE FOR NEUROBIOLOGY

Eppendorf & Science Prize for Neurobiology

Congratulations to Dr. Tiago Branco on winning the 2011 Eppendorf & *Science* Prize for his studies on how dendrites discriminate temporal input sequences and apply different integration rules depending on input location. The results of Dr. Branco's research provide insight on how the brain performs computations, and suggest that even single neurons can solve complex computational tasks.

You could be the 11th winner of this award.
The annual Eppendorf & *Science* Prize for Neurobiology honors young scientists for their outstanding contributions to neurobiological research based on methods of molecular and cell biology. The winner and finalists are selected by a committee of independent scientists, chaired by *Science's* Senior Editor, Dr. Peter Stern.

To be eligible, you must be 35 years of age or younger. If you're selected as this year's winner, you will receive US$ 25,000, have your work published in *Science* and be invited to visit Eppendorf in Hamburg, Germany. Past winners and finalists have come from as far a field as China, Chile, India and New Zealand.

Yes, it can happen to you. Enter your research now!

eppendorf
In touch with life

Science
AAAS

Kurstin Roe Photography

eppendorf® is a registered trademark of Eppendorf AG, Germany. Copyright © 2012 by Eppendorf AG.

Subra Suresh is director of the U.S. National Science Foundation, Arlington, Virginia. E-mail: ssuresh@nsf.gov.

Cultivating Global Science

IN OUR RAPIDLY EXPANDING GLOBAL SCIENTIFIC RESEARCH ENTERPRISE, GOOD SCIENCE ANYWHERE is good for science everywhere, provided that there exists an open flow of information with transparent processes to promote rigorous peer review and scientific integrity. Last year on this page, I emphasized that collaboration across national boundaries requires a global ecosystem that nurtures and accelerates the pace of scientific discoveries to address the many grand challenges facing humanity.* The heads of major science and engineering research funding agencies from nearly 50 countries—primarily representing the G-20 and the Organisation for Economic Co-operation and Development—took the first steps toward this goal by convening at the U.S. National Science Foundation (NSF) in Virginia, for the first Global Merit Review Summit. The outcomes and momentum from the meeting, held on 14 and 15 May 2012, reflect the serious commitment of nations to ensure that science functions in a coherent and well-coordinated manner among developed and developing nations, maintains the public trust, and addresses each nation's unique needs for economic growth, national security, and human capital development.

One major barrier to successful international scientific collaboration is variation in what constitutes appropriate peer review of research proposals. Over the past year, Summit participants and others held regional meetings coordinated by NSF in Brazil, South Africa, Saudi Arabia, Belgium, and India to discuss this issue. The results were synthesized into a coherent set of basic principles that were circulated for input from all participants. As a result, this inaugural summit released a *Statement of Principles of Scientific Merit Review*† and created a Global Research Council (GRC), a virtual organization of the heads of science and engineering funding agencies from around the world.

The principles identified in the statement include the most basic and essential ingredients of scientific merit review: expert assessment, transparency of the evaluation process, impartiality, appropriateness, confidentiality, and integrity and ethical consideration. The expectation is that the objectives are at such a universal level that countries will be strongly inclined to participate. As one example, across countries there is extreme variation in the selection process for those who review research proposals, presenting an obstacle for countries that wish to partner in specific research endeavors. To ensure fair evaluation across countries, principles are needed to guarantee that the appropriate scientific expertise is employed for peer review, with a clear awareness of potential conflicts of interest. Agreement on such issues would help to foster more effective international research cooperation.

The GRC represents a new model for discussing issues aimed at unifying and strengthening the global scientific enterprise. For countries with recently established funding agencies such as India's National Science and Engineering Research Board, as well as for countries, such as Nigeria and Vietnam, in the planning stages for such new agencies, participation in the GRC should accelerate their efforts in recognizing promising science, developing their science infrastructure, and collaborating with other nations.

Going forward, regional meetings over the next year will focus on identifying core principles of scientific integrity, seeking consensus on potential subjects such as authorship, accuracy of data, and human subjects protocols. Much work has been done on this topic, but the GRC hopes to identify principles on which there is widespread concurrence and explore compliance mechanisms. The objective will be to adopt basic principles at the 2013 Global Summit, which will be co-hosted by Germany and Brazil in Berlin. Regional meetings will also begin to address the very complex challenge of open and shared access to scientific information—both data and publications. By harmonizing the standards that underlie different national systems, we can create the smoothly operating system of global science essential to addressing the world's most pressing challenges.

– Subra Suresh

10.1126/science.1224580

*S. Suresh, *Science* **333**, 802 (2011). †www.nsf.gov/news/newsmedia/globalsummit/gs_principles.pdf

CREDITS: (TOP) SANDY SCHAEFFER; (RIGHT) ISTOCKPHOTO.COM

Eppendorf Consumables – It's Your Sample

eppendorf® and eppendorf Biopur® are registered trademarks of Eppendorf AG.
All rights reserved, including graphics and images.

Absolute Certainty!

Get peace of mind with Eppendorf

Experience peace of mind with Eppendorf guaranteed quality and order your free sample on www.eppendorf.com/consumables

Don't leave your results to chance – count on Eppendorf consumables

- Unique features to make every day routines faster and easier
- Minimized risk of chemical leaching from our consumables
- Purity grades tailored to even the highest requirements

eppendorf

In touch with life

Eppendorf South Pacific · Unit 4 · 112 Talavera Road · North Ryde, NSW 2113 · Australia
Phone +61-2-9889-5000 · Fax +61-2-9889-5111 · e-mail: info@eppendorf.com.au · Internet: www.eppendorf.com.au

CHEMISTRY

A Carbon Bond's Photo Finish

Photoinduced electron transfer is the initiating step in photosynthesis, so in a broad sense, it's been key to carbon-carbon bond formation since long before chemists (or humans more generally) arrived on the scene. Present-day synthetic organic chemistry rarely relies on that mechanism, though over the past several years its versatility has been coming into renewed focus. More specifically, catalysts such as tris(bipyridyl)ruthenium can easily lend out an electron after absorbing blue light, and substrates in the electron transfer chain often react differently than they would in a more conventional thermal context. DiRocco and Rovis apply this light-accelerated technique to one half of a dual catalytic cycle, oxidizing an amine to a more reactive iminium ion. A second catalyst—an asymmetrically substituted N-heterocyclic carbene—activates an aldehyde toward nucleophilicity in a dark portion of the cycle, ultimately linking the acyl carbon to the α carbon of the amine. The reaction couples a range of aldehydes to substituted tetrahydroisoquinolines, in many cases with enantiomeric excesses above 90%. — JSY

J. Am. Chem. Soc. **134**, 10.1021/ja3030164 (2012).

PLANT SCIENCES

Shared Symbiotic Signaling

Symbioses of plants with *Rhizobium* bacteria or mycorrhizal fungi find the microbes lodged in membrane-bound compartments within the host, called symbiosomes and arbuscules, respectively. Although functionally similar, they are morphologically distinct. Shared signaling components between these two symbioses suggest that the signaling pathway governing *Rhizobium*-legume interactions may have been co-opted from the more common mycorrhizal fungi symbiotic pathway. Ivanov *et al.* have now identified two members of the VAMP72 (vesicle-associated membrane protein) family, known for their involvement in exocytosis, as critical for the formation of the membrane interface that separates *Rhizobium* from its host. Medicago plants in which expression of the proteins was disrupted were deficient in the development of symbiosomes and arbuscules, but other aspects of the symbiotic system, such as the root nodule and infection threads, developed normally. VAMP72 proteins localized to exocytotic vesicles in developing symbiosomes. Thus, *Rhizobium* bacteria and mycorrhizal fungi establish their symbioses with similar subcellular mechanisms, although the fungal symbioses remain much more widespread than the symbioses involving bacteria. — PJH

Proc. Natl. Acad. Sci. U.S.A. **109**, 10.1073/pnas.1200407109 (2012).

GEOPHYSICS

Yellowstone's Deep Roots

Yellowstone National Park in the western United States, renowned for its geothermal features, including geysers and hot springs, rests on a ~4000-km^2 caldera attributed to a series of supervolcano eruptions over the past 2 million years. The volcanic and geothermal activity is caused by the presence of a hot spot currently resting below the park that migrated eastward over the course of millions of years. Conflicting geological evidence implies that the source of this hotspot volcanism is either a deep plume originating hundreds of km below Earth's surface in the lower mantle or more shallow upper mantle melting caused primarily by extension of the continental lithosphere—a process that occurs elsewhere in the western United States. Schmandt *et al.*, analyzing data collected by the dense USArray seismic network while it was deployed across the region, addressed this debate through seismic imaging of the mantle below Yellowstone. Comparing the temperature-sensitive depth variation of mantle discontinuities at 410 and 660 km to global averages indicates the presence of a high-temperature upwelling that is vertically heterogeneous. The shallowing of the 660-km discontinuity, which marks the boundary between the upper and lower mantle, suggests that this plume-like structure originates in the lower mantle, but just how deep down remains unclear. — NW

CREDITS (TOP TO BOTTOM): POWER AND SYRED/SCIENCE PHOTO LIBRARY; THINKSTOCK

Earth Planet. Sci. Lett. 10.1016/j.epsl.2012.03.025 (2012).

BIOCHEMISTRY

Locked and Loaded

Protein kinases that function in signaling pathways controlling cell growth and survival are potential drug targets for fighting cancer and other diseases. Predicting the actions of kinase inhibitors in cells, especially cancer cells, is difficult, however, without a detailed understanding of the normal regulation of the target enzymes. Lin *et al.* provide insight into how the kinase Akt

Continued on page 962

CHEMBRIDGE

High Quality Screening Libraries

800,000 Compounds to Support Your Research

DIVERSITY LIBRARIES

DIVERSet - 3D pharmacophore diversity in a highly cited library

PremiumSet - diverse compounds with high-scoring chemical features

NOVACore - in-house designed, scaffold-based, diverse chemistry with new compounds annually

PHARMACophore - diverse, in-house designed, scaffold-based chemistry

Pre-selected Diversity Sets - sets offering diversity or scaffold representation (MicroFormat, MW-Set, and CombiSet)

TARGETED LIBRARIES

CNS-Set - selected for increased probability of oral bioavailability and blood brain barrier penetration

ION Channel/IONCore - for ligand-gated and voltage-dependent ion channel targets

KINASet/KINACore - compounds scoring highly against pharmacophores derived from known kinase actives or ATP

GPCR - druglike compounds based on scaffolds representing ß-turn mimetics

NHRCore - scaffold-based, nuclear hormone receptor chemistry

Fragment - Rules of 3 biased compounds

All libraries undergo extensive QC. Rigorous druglike/leadlike filters are applied to yield premium compounds for your screening program.

ChemBridge

San Diego, CA 1-800-964-6143
sales@chembridge.com
www.chembridge.com

Continued from page 961

reacts to inhibitors that compete with adenosine triphosphate (ATP) for binding to the active site. ATP-competitive inhibitors actually increase the phosphorylation of Akt at its activating sites. This is because in the ATP-bound (but not ADP-bound) conformation, the activating phosphorylation sites are inaccessible to phosphatases that can dephopshorylate them. Thus, when activated and bound to ATP, the enzyme is resistant to inactivation until it has catalyzed one round of phosphorylation, at which point it becomes susceptible to inactivating phosphatases. Furthermore, the ATP-competitive inhibitor studied bound preferentially to the active form of Akt, leading the authors to propose that it might preferentially target tumor cells where Akt is highly activated, with fewer (potentially deleterious) effects on normal cells. — LBR

Sci. Signal. **5**, ra37 (2012).

CELL BIOLOGY

Cell-Cell Fusion

Osteoclasts are cells that promote bone remodeling, and their hyperactivity is linked to bone-destructive disorders, including osteoporosis. Activated osteoclast precursors develop columnar actin structures, known as podosomes, which are similar to the invadopodia observed in invasive cancer cells. During osteoclast differentiation, cells can fuse with one another to create multinucleate cells. Oikawa *et al.* found that in osteoclastic cell cultures, a protein known to be involved in Src-induced cancer cell invadopodia production, Tks5, was also induced during osteoclastogenesis. Tyrosine phosphorylation of Tks5 by Src was required for the generation of circumferential podosomes in osteoclasts and for their fusion. Knockdown of Tks5 in osteoclasts interfered with circumferential podosome formation and cell–cell fusion, whereas polarized membrane extensions seemed to be unaffected. Tks5-expressing osteoclasts were also able to fuse with melanoma cells. Similar osteoclast–cancer cell hybrid cells have been detected in bone lesions in myeloma patients. Thus, Src-Tks5 signaling may represent a potential therapeutic target for the treatment of bone-destructive diseases and malignancies. — SMH

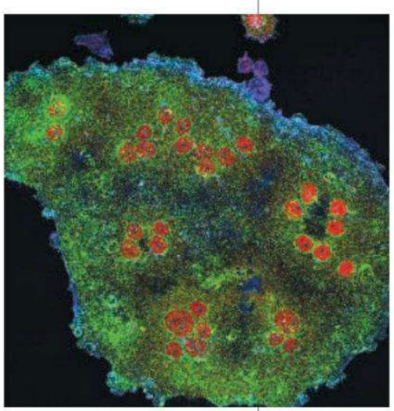

CREDIT: TSUKASA OIKAWA

J. Cell Biol. **197**, 553 (2012).

ECONOMICS

No Simple Links

Reported linkages of behavioral traits to particular genes indicate that political and economic attitudes might have a genetic component. To explore this possibility in more depth, Benjamin *et al.* analyzed genotype data from 9836 Swedish twins that had responded to a survey about their economical and political inclinations. Standard twin-based estimates of heritability indicated moderate (30 to 40%) heritability for these traits; however, another method of analysis that relied on dense single-nucleotide polymorphism (SNP) arrays found that the heritability for these traits was half of that. Overall, the authors' analyses indicated that political and economic preferences are highly polygenic, with individual SNPs contributing only small amounts to the heritability. According to the authors, future research endeavors should include larger samples, better methods of measuring economic and political phenotypes, and a focus on "behavioral phenotypes that are more biologically proximate." — BJ

Proc. Natl. Acad. Sci. U.S.A. **109,** 10.1073/pnas.1120666109 (2012).

CHEMISTRY

Switching Hands

Most stereoselective catalysts are designed to form just one stereoisomeric product, but there is increasing interest in catalysts that could switch the sense of the desired product through some external stimulus. Mortezaei *et al.* observed that the helical arrangement of two quinoline moieties in a particular polydentate ligand coordinated to copper varied depending on the metal's oxidation state. The ligand binds through the N atoms of the quinoline groups and either an O atom of a tethered methionine derivative for Cu(II) complexes or the S atom of the side chain for Cu(I) complexes. The authors went on to synthesize derivatives of these complexes in which the quinolines bear catalytic urea groups, so as to exploit the redox-driven conformational switching in control of product stereochemistry. They show that the Michael addition of diethyl malonate to *trans*-β-nitrostyrene occurs with ~70% enantiomeric excess for the *S* and *R* products with the Cu(II) and Cu(I) catalysts, respectively, in acetonitrile and in the presence of base. — PDS

J. Am. Chem. Soc. **134**, 10.1021/ja302283s (2012).

www.sciencemag.org

Science

1200 New York Avenue, NW
Washington, DC 20005
Editorial: 202-326-6550, FAX 202-289-7562
News: 202-326-6581, FAX 202-371-9227
Bateman House, 82-88 Hills Road
Cambridge, UK CB2 1LQ
+44 (0) 1223 326500, FAX +44 (0) 1223 326501

Subscription Services For change of address, missing issues, new orders and renewals, and payment questions: 866-434-AAAS (2227) or 202-326-6417, FAX 202-842-1065. Mailing addresses: AAAS, P.O. Box 96178, Washington, DC 20090-6178 or AAAS Member Services, 1200 New York Avenue, NW, Washington, DC 20005

Institutional Site Licenses please call 202-326-6755 for any questions or information

Reprints: Author Inquiries 800-635-7181
Commercial Inquiries 803-359-4578

Permissions 202-326-7074, FAX 202-682-0816

Member Benefits AAAS Travels: Betchart Expeditions 800-252-4910; Apple Store www.store.apple.com/us/go/eppstore/aaas; NASA Federal, 1-888-NASA-FCU (1-888-627-2328) or www.nasafcu.com; Cold Spring Harbor Laboratory Press Publications www.cshlpress.com/affiliates/aaas.htm; GEICO Auto Insurance www.geico.com/landingpage/go51.htm?logo=17624; Hertz 800-654-2200 CDP#343457; Office Depot https://bsd.officedepot.com/portalLogin.do; Seabury & Smith Life Insurance 800-424-9883; Subaru VIP Program 202-326-6417; VIP Moving Services www.vipmayflower.com/domestic/index.html; Other Benefits: AAAS Member Services 202-326-6417 or www.aaasmember.org.

science_editors@aaas.org	(for general editorial queries)
science_letters@aaas.org	(for queries about letters)
science_reviews@aaas.org	(for returning manuscript reviews)
science_bookrevs@aaas.org	(for book review queries)

Published by the American Association for the Advancement of Science (AAAS), *Science* serves its readers as a forum for the presentation and discussion of important issues related to the advancement of science, including the presentation of minority or conflicting points of view, rather than by publishing only material on which a consensus has been reached. Accordingly, all articles published in *Science*—including editorials, news and comment, and book reviews—are signed and reflect the individual views of the authors and not official points of view adopted by AAAS or the institutions with which the authors are affiliated.

AAAS was founded in 1848 and incorporated in 1874. Its mission is to advance science, engineering, and innovation throughout the world for the benefit of all people. The goals of the association are to: enhance communication among scientists, engineers, and the public; promote and defend the integrity of science and its use; strengthen support for the science and technology enterprise; provide a voice for science on societal issues; promote the responsible use of science in public policy; strengthen and diversify the science and technology workforce; foster education in science and technology for everyone; increase public engagement with science and technology; and advance international cooperation in science.

Information for Authors
See pages 752 and 753 of the 10 February 2012 issue or access www.sciencemag.org/about/authors

EDITOR-IN-CHIEF **Bruce Alberts**
EXECUTIVE EDITOR **Monica M. Bradford**
NEWS EDITOR **Colin Norman**
MANAGING EDITOR, RESEARCH JOURNALS **Katrina L. Kelner**
DEPUTY EDITORS **R. Brooks Hanson, Barbara R. Jasny, Andrew M. Sugden, Valda J. Vinson**

Editorial senior editors/commentary Lisa D. Chong, Brad Wible; **senior editors** Gilbert J. Chin, Pamela J. Hines, Paula A. Kiberstis (Boston), Marc S. Lavine (Toronto), Beverly A. Purnell, L. Bryan Ray, Guy Riddihough, H. Jesse Smith, Phillip D. Szuromi (Tennessee), Valda Vinson, Jake S. Yeston, Laura M. Zahn (San Diego); **associate editors** Kristen L. Mueller, Jelena Stajic, Sacha Vignieri, Nicholas S. Wigginton; **book review editor** Sherman J. Suter; **associate letters editor** Jennifer Sills; **editorial manager** Cara Tate; **senior copy editors** Jeffrey E. Cook, Cynthia Howe, Harry Jach, Lauren Kmec, Barbara P. Ordway, Trista Wagoner; **copy editor** Chris Filiatreau; **senior editorial coordinators** Carolyn Kyle, Beverly Shields; **editorial coordinators** Joi S. Granger, Anita Wynn; **publications assistants** Ramatoulaye Diop, Le-Toya Mayne Flood, Aneera Dobbins, Jeffrey Hearn, Lisa Johnson, Scott Miller, Jerry Richardson, Teresa R. Sakon, Brian White; **editorial assistant** Patricia M. Moore; **executive editorial assistant** Yolanda O'Bannon (San Francisco); **executive assistant** Alison Crawford; **administrative support** Maryrose Madrid; **editorial fellow** Melissa R. McCartney

Editorial director, web and new media Stewart Wills; **senior web editor** Sarah Crespi; **web editor** Kerry Klein; **web development manager** Martyn Green; **web developers** Corinna Cohn, Andrew Whitesell

News deputy news editors Robert Coontz, David Grimm (Online), Eliot Marshall, Jeffrey Mervis, Leslie Roberts, John Travis; **contributing editors** Elizabeth Culotta, Polly Shulman; **news writers** Yudhijit Bhattacharjee, Adrian Cho, Jennifer Couzin-Frankel, Carolyn Gramling, Jocelyn Kaiser, Richard A. Kerr, David Malakoff, Greg Miller, Elizabeth Pennisi, Robert F. Service (Pacific NW), Erik Stokstad; **web developer** Daniel Berger; **intern** Jane J. Lee; **contributing correspondents** John Bohannon, Jon Cohen (San Diego, CA), Daniel Ferber, Ann Gibbons, Sam Kean, Andrew Lawler, Mitch Leslie, Charles C. Mann, Virginia Morell, Gary Taubes; **copy editors** Melissa Raimondi, Linda B. Felaco; **administrative support** Scherraine Mack; **bureaus** San Diego, CA: 760-942-3252, FAX 760-942-4979; Pacific Northwest: 503-963-1940

Production director Wendy K. Shank; **assistant managers** Rebecca Doshi, Lori Murphy; **senior specialists** Steve Forrester, Chris Redwood, Anthony Rosen; **Preflight director** David M. Tompkins; **manager** Marcus Spiegler; **specialists** Jason Hillman, Tara Kelly

Art director Yael Fitzpatrick; **associate art director** Laura Creveling; **senior illustrators** Chris Bickel, Katharine Sutliff; **illustrators** Yana Hammond, Bricelyn Strauch; **senior art associates** Holly Bishop, Preston Huey, Nayomi Kevitiyagala; **art associate** Kay Engman; **photo editor** Leslie Blizard

***Science* International**

Europe (science@science-int.co.uk) **editorial: international managing editor** Andrew M. Sugden; **senior editor/commentary** Julia Fahrenkamp-Uppenbrink; **senior editors** Caroline Ash, Stella M. Hurtley, Ian S. Osborne, Peter Stern; **associate editor** Maria Cruz; **contributing editor** Helen Pickersgill; **editorial support** Samantha Hogg, Alice Whaley; **administrative support** Janet Clements, Nicola Morris, John Wood; **news: deputy news editor, u.k.** Daniel Clery; **contributing editor, europe** Martin Enserink; **contributing correspondents** Michael Balter (Paris), Kai Kupferschmidt (Berlin), Gretchen Vogel (Berlin)

Asia Japan Office: Asca Corporation, Tomoko Furusawa, Rustic Bldg. 7F, 77 Tenjin-cho, Shinjuku-ku, Tokyo 162-0808, Japan; +81 3 6802 4616, FAX +81 3 6802 4615, inquiry@sciencemag.jp; **asia news editor** Richard Stone (Beijing: rstone@aaas.org); **contributing correspondents** Dennis Normile [Japan: +81 (0) 3 3391 0630, FAX +81 (0) 3 5936 3531; dnormile@gol.com]; Hao Xin [China: cindyhao@gmail.com]; Mara Hvistendahl [China: mhvisten@aaas.org]; Pallava Bagla [South Asia: +91 (0) 11 2271 2896; pbagla@vsnl.com]

EXECUTIVE PUBLISHER **Alan I. Leshner**
PUBLISHER **Beth Rosner**

Fulfillment Systems and Operations (membership@aaas.org); **customer service supervisor** Pat Butler; **specialists** LaToya Casteel, Michelle Ofordire, April Marshall; **manager, data entry** Mickie Napoleoni; **data entry specialists** Tarrika Hill, JJ Regan, Eva Mae Campbell

Business Operations and Administration director Deborah Rivera-Wienhold; **business systems and financial analysis director** Randy Yi; **manager, fulfillment systems** Frits Buningh; **systems analyst** Nicole Mehmedovich; **manager, business analysis** Eric Knott; **manager, business operations** Jessica Tierney; **business analysts** Cory Lipman, Celeste Troxler; Christine Wehrli; **financial analyst** Julia Nguyen; **rights and permissions: administrator** Emilie David; **associate** Elizabeth Sandler; **marketing director** Ian King; **marketing managers** Allison Pritchard, Alison Chandler, Julianne Wielga, Samantha Smith; **marketing associates** Aimee Aponte, Mary Ellen Crowley, Elizabeth Sattler, Rebecca Riffin; **senior marketing executive** Jennifer Reeves; **director, site licensing** Tom Ryan; **director, corporate relations** Eileen Bernadette Moran; **senior publisher relations specialist** Kiki Forsythe; **publisher relations manager** Catherine Holland; **publisher relations, eastern region** Phillip Smith; **publisher relations, western region** Ryan Rexroth; **customer relations manager** Iquo Edim; **marketing manager** Christina Schlecht; **marketing associates** Paulina Curto, Mitchell Edmund; **electronic media: director** Lizabeth Harman; **assistant manager** Lisa Stanford; **production specialists** Antoinette Hodal, Thomas Jaensch, Nichele Johnston, Kimberly Oster; **project manager** Trista Snyder; **computer specialists** Walter Jones, Kai Zhang; **program director, aaas membercentral** Peggy Mihelich

director, global collaboration, custom publications, advertising Bill Moran
commercial editor Sean Sanders: 202-326-6430
assistant commercial editor Tianna Hicklin 202-326-6463

Product (science_advertising@aaas.org); **midwest** Rick Bongiovanni: 330-405-7080, FAX 330-405-7081; **east coast/e. canada** Laurie Faraday: 508-747-9395, FAX 617-507-8189; **west coast/w. canada** Lynne Stickrod: 415-931-9782, FAX 415-520-6940; **uk/europe/asia** Roger Goncalves: TEL/FAX +41 43 243 1358; **japan**, Makiko Hara: +81 (0) 3 6802 4616, FAX +81 (0) 3 6802 4615; ads@sciencemag.jp; **china/taiwan** Ruolei Wu: +86 1367 1015 294 rwu@aaas.org

worldwide associate director of *Science* Careers Tracy Holmes: +44 (0) 1223 326525, FAX +44 (0) 1223 326532

Classified (advertise@sciencecareers.org); **u.s.: midwest/west coast/south central/canada** Tina Burks: 202-326-6577; **east coast/industry** Elizabeth Early: 202-326-6578; **sales administrator** Marci Gallun; **europe/row sales** Simone Jux, Lucy Nelson; **sales assistant** Kelly Grace; **japan** Yuri Kobayashi +81 (6) 6627-9250; careerads@sciencemag.jp; **china/taiwan** Ruolei Wu: +86 1367 1015 294 rwu@aaas.org; **advertising support manager** Karen Foote: 202-326-6740; **advertising production operations manager** Deborah Tompkins; **senior production specialist/graphic designer** Amy Hardcastle; **production specialist** Yuse Lajiminmuhip; **senior traffic associate** Christine Hall; **sales coordinator** Shirley Young

AAAS Board of Directors retiring president, chair Nina V. Fedoroff; **president** William H. Press; **president-elect** Phillip A. Sharp; **treasurer** David E. Shaw; **chief executive officer** Alan I. Leshner; **board** May R. Berenbaum, Bonnie L. Bassler, Stephen L. Mayo, Raymond Orbach, Julia M. Phillips, Sue V. Rosser, David D. Sabatini, Inder M. Verma

AAAS
ADVANCING SCIENCE, SERVING SOCIETY

SENIOR EDITORIAL BOARD

A. Paul Alivisatos, *Lawrence Berkeley Nat'l. Laboratory*
Cori Bargmann, *The Rockefeller Univ.*
Ernst Fehr, *Univ. of Zurich*
Erin O'Shea, *Harvard Univ.*
Michael S. Turner, *University of Chicago*

BOARD OF REVIEWING EDITORS

Adriano Aguzzi, *Univ. Hospital Zürich*
Takuzo Aida, *Univ. of Tokyo*
Sonia Altizer, *Univ. of Georgia*
Sebastian Amigorena, *Institut Curie*
Angelika Amon, *MIT*
Kathryn Anderson, *Memorial Sloan-Kettering Cancer Center*
Siv G. E. Andersson, *Uppsala Univ.*
Peter Andolfatto, *Princeton Univ.*
Meinrat O. Andreae, *Max Planck Inst., Mainz*
Johan Auwerx, *EPFL*
David Awschalom, *Univ. of California Santa Barbara*
John A. Bargh, *Yale Univ.*
Ben Barres, *Stanford Medical School*
Jordi Bascompte, *Estación Biológica de Doñana, CSIC*
Facundo Batista, *London Research Inst.*
Ray H. Baughman, *Univ. of Texas, Dallas*
David Baum, *Univ. of Wisconsin*
Mark Bear, *Massachusetts Inst. of Technology*
Yasmine Belkaid, *NIAID, NIH*
Philip Benfey, *Duke Univ.*
Stephen J. Benkovic, *Penn State Univ.*
Gregory C. Beroza, *Stanford Univ.*
Gabriele Bergers, *Univ. of California, San Francisco*
Peer Bork, *EMBL*
Bernard Bourdon, *Ecole Normale Superieure de Lyon*
Ian Boyd, *Univ. of St. Andrews*
Christian Büchel, *Universitätsklinikum Hamburg-Eppendorf*
Joseph A. Burns, *Cornell Univ.*
William P. Butz, *Population Reference Bureau*
Gyorgy Buzsaki, *Rutgers Univ.*
Mats Carlsson, *Univ. of Oslo*
Mildred Cho, *Stanford Univ.*
David Clapham, *Children's Hospital, Boston*
David Clary, *Univ. of Oxford*
Jonathan D. Cohen, *Princeton Univ.*
Robert Cook-Deegan, *Duke Univ.*
James Collins, *Boston Univ.*
Alan Cowman, *Walter & Eliza Hall Inst.*
Robert H. Crabtree, *Yale Univ.*
Wolfgang Cramer, *Medit. Inst. for Ecology & Paleoecology*
F. Fleming Crim, *Univ. of Wisconsin*
Jeff L. Dangl, *Univ. of North Carolina*
Tom Daniel, *Univ. of Washington*
Frans de Waal, *Emory Univ.*
Stanislas Dehaene, *Collège de France*
Robert Desimone, *MIT*
Claude Desplan, *New York Univ.*
Ap Dijksterhuis, *Radboud Univ. of Nijmegen*
Dennis Discher, *Univ. of Pennsylvania*
Gerald W. Dorn II, *Washington Univ. School of Medicine*
Jennifer A. Doudna, *Univ. of California, Berkeley*
Julian Downward, *Cancer Research UK*
Bruce Dunn, *Univ. of California, Los Angeles*
Christopher Dye, *WHO*
David Ehrhardt, *Carnegie Inst. of Washington*
Tim Elston, *Univ. of North Carolina at Chapel Hill*
Gerhard Ertl, *Fritz-Haber-Institut, Berlin*
Barry Everitt, *Univ. of Cambridge*
Paul G. Falkowski, *Rutgers Univ.*
Ernst Fehr, *Univ. of Zurich*
Tom Fenchel, *Univ. of Copenhagen*
Michael Feuer, *The George Washington Univ.*
Alain Fischer, *INSERM*
Susan Fiske, *Princeton Univ.*
Anne C. Ferguson-Smith, *Univ. of Cambridge*
Wulfram Gerstner, *EPFL Lausanne*
Karl-Heinz Glassmeier, *TU Braunschweig*
Elizabeth Grove, *Univ. of Chicago*
Kip Guy, *St. Jude's Children's Research Hospital*
Taekjip Ha, *Univ. of Illinois at Urbana-Champaign*
Christian Haass, *Ludwig Maximilians Univ.*
Steven Hahn, *Fred Hutchinson Cancer Research Center*
Gregory J. Hannon, *Cold Spring Harbor Lab.*
Martin Heimann, *Max Planck Inst., Jena*
Isaac Held, *NOAA*
James A. Hendler, *Rensselaer Polytechnic Inst.*
Janet G. Hering, *Swiss Fed. Inst. of Aquatic Science & Technology*
Ray Hilborn, *Univ. of Washington*
Michael E. Himmel, *National Renewable Energy Lab.*
Kai-Uwe Hinrichs, *Univ. of Bremen*
Kei Hirose, *Tokyo Inst. of Technology*
David Hodell, *Univ. of Cambridge*
David Holden, *Imperial College*
Lora Hooper, *UT Southwestern Medical Ctr at Dallas*
Jeffrey A. Hubbell, *EPFL Lausanne*
Steven Jacobsen, *Univ. of California, Los Angeles*
Kai Johnsson, *EPFL Lausanne*
Peter Jonas, *Universität Freiburg*
William Kaelin Jr., *Dana-Farber Cancer Inst.*
Daniel Kahne, *Harvard Univ.*
Joel Kingsolver, *Univ. of North Carolina at Chapel Hill*
Robert Kingston, *Harvard Medical School*
Roberto Kolter, *Harvard Medical School*
Alberto R. Kornblihtt, *Univ. of Buenos Aires*
Leonid Kruglyak, *Princeton Univ.*
Thomas Langer, *Univ. of Cologne*
Mitchell A. Lazar, *Univ. of Pennsylvania*
David Lazer, *Harvard Univ.*
Virginia Lee, *Univ. of Pennsylvania*
Ottoline Leyser, *Cambridge Univ.*
Olle Lindvall, *Univ. Hospital, Lund*
Marcia C. Linn, *Univ. of California, Berkeley*
John Lis, *Cornell Univ.*
Jianguo Liu, *Michigan State Univ.*
Jonathan Losos, *Harvard Univ.*
Ke Lu, *Chinese Acad. of Sciences*
Laura Machesky, *CRUK Beatson Inst. for Cancer Research*
Anne Magurran, *Univ. of St Andrews*
Oscar Marin, *CSIC & Univ. Miguel Hernández*
Charles Marshall, *Univ. of California, Berkeley*
Martin M. Matzuk, *Baylor College of Medicine*
Graham Medley, *Univ. of Warwick*
Yasushi Miyashita, *Univ. of Tokyo*
Richard Morris, *Univ. of Edinburgh*
Edvard Moser, *Norwegian Univ. of Science and Technology*
Sean Munro, *MRC Lab. of Molecular Biology*
Thomas Murray, *The Hastings Center*
Naoto Nagaosa, *Univ. of Tokyo*
James Nelson, *Stanford Univ. School of Med.*
Timothy W. Nilsen, *Case Western Reserve Univ.*
Pär Nordlund, *Karolinska Inst.*
Helga Nowotny, *European Research Advisory Board*
Luke O'Neill, *Trinity College, Dublin*
Stuart Newman, *New York Medical College*
N. Phuan Ong, *Princeton Univ.*
Joe Orenstein, *Univ. of California, Berkeley & Lawrence Berkeley National Lab*
Stuart H. Orkin, *Dana-Farber Cancer Inst.*
Harry Orr, *Univ. of Minnesota*
Christine Ortiz, *MIT*
Andrew Oswald, *Univ. of Warwick*
Steve Palumbi, *Stanford Univ.*
Jane Parker, *Max-Planck Inst. of Plant Breeding Research*
Donald R. Paul, *Univ. of Texas at Austin*
P. David Pearson, *Univ. of California, Berkeley*
Reginald M. Penner, *Univ. of California, Irvine*
John H. J. Petrini, *Memorial Sloan-Kettering Cancer Center*
Simon Phillpot, *Univ. of Florida*
Joshua Plotkin, *Univ. of Pennsylvania*
Philippe Poulin, *CNRS*
Colin Renfrew, *Univ. of Cambridge*
Trevor Robbins, *Univ. of Cambridge*
Barbara A. Romanowicz, *Univ. of California, Berkeley*
Jens Rostrup-Nielsen, *Haldor Topsoe*
Mike Ryan, *Univ. of Texas, Austin*
Shimon Sakaguchi, *Kyoto Univ.*
Miquel Salmeron, *Lawrence Berkeley National Lab*
Jürgen Sandkühler, *Medical Univ. of Vienna*
Randy Seeley, *Univ. of Cincinnati*
Vladimir Shalaev, *Purdue Univ.*
Joseph Silk, *Institut d'Astrophysique de Paris*
Denis Simon, *Univ. of Oregon*
Alison Smith, *John Innes Centre*
Davor Solter, *Inst. of Medical Biology, Singapore*
Peter Sorger, *Harvard Medical School*
John Speakman, *Univ. of Aberdeen*
Allan C. Spradling, *Carnegie Institution of Washington*
Jonathan Sprent, *Garvan Inst. of Medical Research*
Paula Stephan, *Georgia State Univ. and National Bureau of Economic Research*
Elsbeth Stern, *ETH Zürich*
Ira Tabas, *Columbia Univ.*
Yoshiko Takahashi, *Kyoto Univ.*
Sarah Teichmann, *Cambridge Univ.*
John Thomas, *Duke Univ.*
Herbert Virgin, *Washington Univ.*
Bert Vogelstein, *Johns Hopkins Univ.*
Cynthia Volkert, *Univ. of Gottingen*
Bruce D. Walker, *Harvard Medical School*
Douglas Wallace, *Dalhousie Univ.*
Ian Walmsley, *Univ. of Oxford*
David A. Wardle, *Swedish Univ. of Agric Sciences*
David Waxman, *Fudan Univ.*
Detlef Weigel, *Max-Planck Inst., Tübingen*
Jonathan Weissman, *Univ. of California, San Francisco*
Sue Wessler, *Univ. of California, Riverside*
Kathy Willis, *Oxford Univ.*
Ian A. Wilson, *The Scripps Res. Inst.*
Timothy D. Wilson, *Univ. of Virginia*
Jan Zaanen, *Leiden Univ.*
Kenneth Zaret, *Univ. of Penn. School of Medicine*
Mayana Zatz, *University of Sao Paolo*
Jonathan Zehr, *Univ. of California, Santa Cruz*
Maria Zuber, *MIT*

BOOK REVIEW BOARD

John Aldrich, *Duke Univ.*
David Bloom, *Harvard Univ.*
Angela Creager, *Princeton Univ.*
Richard Shweder, *Univ. of Chicago*
Ed Wasserman, *DuPont*
Lewis Wolpert, *Univ. College London*

AROUND THE WORLD

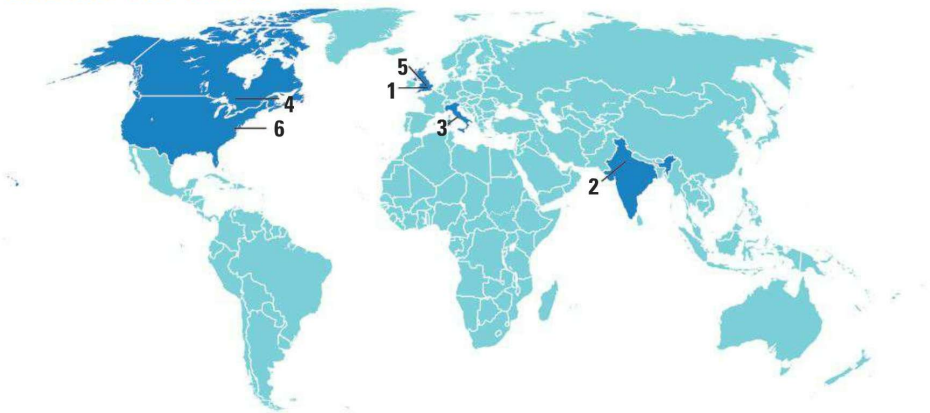

London **1**

British Team Cancels Geoengineering Experiment

A U.K. project examining the feasibility of geoengineering Earth's climate to reduce global warming will no longer involve the Stratospheric Particle Injection for Climate Engineering (SPICE) project. The project was to investigate whether aerosols, such as sulfate particles, could be injected into Earth's stratosphere to scatter sunlight back into space, thereby stalling global warming. But following concerns that researchers on the SPICE project could have a commercial interest in its success, planners canceled the project on 16 May.

SPICE scientists were hoping to test an aerosol delivery system later this year: A balloon that would carry aloft a kilometer-long pipe that would release 150 liters of water (a substitute for sulfates).

Project leader Matthew Watson of the University of Bristol said in a 16 May statement that the cancellation of the test was partly due to concerns that the pipe-delivery technology was the subject of a U.K. patent application before the project began. Efforts are now underway to make sure the intention of the patent application is to protect intellectual property and not to pave the way for commercial gain, he added.

http://scim.ag/noSPICE

New Delhi **2**

Hope for Reversal of Tiger Reserves Research Ban

Field biologists seeking research permits to work in the tiger reserves of Karnataka in southern India may be getting a reprieve. Over the last 2 years, then–chief wildlife warden Brij Kishore Singh has denied permits to about 40 researchers, suggesting that the habitats were to be left "inviolate" (*Science*, 23 March, p. 1429). But new warden Dipak Sarmah, who took charge on 2 May, says he plans to issue some permits—although, he warns, "there will have to be some rationing." Ecologist Raman Sukumar of the Indian Institute of Science in Bangalore says he is hopeful after resubmitting his papers 17 May to study human-elephant conflict in the Nagarahole National Park tiger reserve because Sarmah, he says, gave him "a patient hearing."

Last week, at an international meeting of the Global Tiger Forum in New Delhi, India's environment minister, Jayanthi Natarajan,

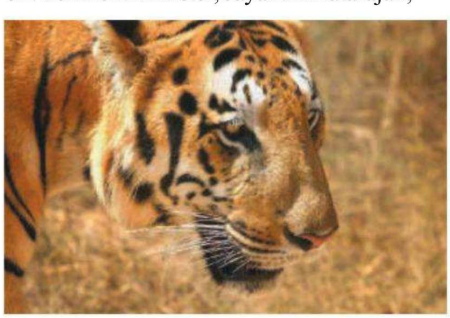

reiterated that researchers were welcome and that the federal government had "not imposed any ban on wildlife research." India is home to about half of the world's 3200 wild tigers, which remain endangered due to poaching and habitat loss.

Rome **3**

Supervolcano Drilling Plan Gets Green Light

A project to drill 500 meters into the heart of a "supervolcano" in southern Italy got the go-ahead on 17 May, despite claims that the drilling would put the population of Naples at risk for small earthquakes or an explosion.

Part of Campi Flegrei caldera

The Campi Flegrei Deep Drilling Project was set up by an international collaboration of scientists to assess the risks posed by the Campi Flegrei caldera, a geological formation just a few kilometers west of Naples. Researchers will place sensors inside the wells to study the region's "bradyseisms," the rising and falling of Earth's surface resulting from the movement of magma inside a caldera, and determine whether they are connected to volcanic eruptions.

Originally scheduled for 2009, the plan was put on hold by then-mayor Rosa Russo Iervolino after scientists expressed concerns that the drilling might cause earthquakes or an explosion if it releases high-pressure supercritical fluids that then come into contact with magma.

Collaboration member Ulrich Harms of the German Research Centre for Geosciences in Potsdam said at the time that if the drilling is done in a controlled way, "there is no risk to the public." **http://scim.ag/volcdrill**

Ontario, Canada **4**

Experimental Lakes on the Cutting Block

A wave of budget cuts to Canada's Department of Fisheries and Oceans, in which 330 DFO scientists and professionals have been warned their positions might disappear or change, is now engulfing a unique research area in Ontario. The Canadian government's announcement on 17 May that it would close the Experimental Lakes Area (ELA), composed of 58 small lakes and their drainage basins, has set off alarms in the environmental science community.

Canadian researchers have experimented with the whole-lake laboratories in Ontario since the 1960s, exploring impacts of phosphorus, acid rain, and metal contaminants to natural ecosystems. Recent projects there include the Mercury Experiment to Assess Atmospheric Loadings in Canada and the United States (METAALICUS), a partnership with researchers from the U.S. Geological Survey to explore mercury methylation and uptake in fish in real-world settings (*Science*, 28 November 2008, p. 1316).

ELA is "a one-of-a-kind place" to perform whole-ecosystem experiments, says one researcher who has worked on the

CREDITS (TOP TO BOTTOM): WIKIMEDIA COMMONS; STEVE EVANS/WIKIMEDIA COMMONS

METAALICUS project, and closing it would be "devastating to Canadian scientists and those around the world." Scientists and others are mustering to protest. In a 17 May press release, a scientists' union, the Professional Institute of the Public Service of Canada, labels the proposed ELA closure and other cuts to DFO as hits to science-based decision-making by the federal government.

Harpenden, U.K. **5**

Intruder Arrested at GM Field Trial

A protester was arrested the morning of 20 May after attempting to break into a field trial of genetically modified wheat (below) at Rothamsted Research, an agricultural research station in Harpenden, U.K. The attack damaged fences and some of the "buffer zone" crops surrounding the experimental wheat, but damaged "less than 0.1%" of the test crop, says Darren Hughes, head of communications at Rothamsted.

Take the Flour Back, a group of activists that has invited the public to a day of protest at the site on 27 May, has said it has no connection to yesterday's incident. According to an e-mailed statement, the group's Eleanor Baylis says: "We have no information about this incident, but are relieved if the quantity of GM pollen released from the trial has been reduced." The group said it plans to go ahead with its protest plans for next weekend, which include destroying the experimental plot. Scientists involved in the trial have issued a public plea to the protesters to allow the trial to proceed. Both sides debated the issue last week on a leading BBC news program. **http://scim.ag/GMintruder**

Washington, D.C. **6**

Prostate Cancer Test a Failure

The U.S. Preventive Services Task Force, an independent group that advises the U.S. government, trashed a popular blood test for prostate cancer risk on 21 May, saying its use is doing more harm than good.

Measuring levels of prostate-specific antigen (PSA) in circulation is unnecessary for healthy men, regardless of age, the panel concludes. The test has prevented few deaths—at best 1 in 1000 men screened—but for every 1000 men screened, the subsequent medical treatment leaves one with a blood clot, two with treatment-related heart attacks, and up to 40 with impotence or urinary incontinence.

Sushil S. Lacy, a professor of urology at the University of Nebraska Medical Center in Omaha and president of the American Urological Association, called the announcement a "disservice to American men."

Similar concerns about the government oversight of medical practice arose in 2009 when the same task force (but with different members) downgraded the value of mammography as a way of preventing death from breast cancer. Like those guidelines, the prostate cancer recommendations may be debated in Congress. **http://scim.ag/prostatefail**

CREDITS (TOP TO BOTTOM): COURTESY OF HERITAGE AUCTIONS; © ROTHAMSTED RESEARCH LTD; DOMINICK REUTER/MIT

Dueling Over a Mongolian Dinosaur

An Asian relative of the titanic *Tyrannosaurus* sparked a tussle this weekend. Questions surrounding the origin of a nearly complete *Tarbosaurus* skeleton, auctioned off on 20 May in New York City, touched off a protest by the Mongolian government. *Tarbosaurus* specimens are found in only Mongolia, which prohibits removal of vertebrate fossils from the country. Officials with Heritage Auctions, the Texas-based company responsible for the sale, said the 2.5-meter-tall, 7-meter-long specimen came from a seller in the United Kingdom who stated in writing that he had legal ownership. On 19 May, lawyers for the Mongolian government obtained a temporary restraining order from a district court judge in Dallas, Texas, to halt the sale pending confirmation of the fossil's origin. But Heritage Auctions President Greg Rohan says the restraining order was directed at the wrong corporation and thus was not enforceable. So the company went ahead with the auction. However, Heritage Auctions won't accept payment or release the fossil to the buyer until the legal issues are resolved. For now, *Tarbosaurus* still resides in New York City.

NEWSMAKERS

Three Q's

Electrical engineer **L. Rafael Reif** was voted president of the Massachusetts Institute of Technology (MIT) in Cambridge on 16 May. A faculty member for 32 years, the Venezuelan native assumes his post on 2 July. Reif replaces neuroscientist Susan Hockfield, who has been MIT's president since 2004.

Q: Why do you want this job?

I view MIT as my home, my extended family. So the opportunity to be sort of head of the household is something that I really want to do. >>

>>NEWSMAKERS

Q: Despite gains by MIT's female science and engineering faculty, there are perceptions that some hold their positions due to gender rather than expertise. How do you combat those perceptions?

I think people here respect each other for what they have achieved. But I don't doubt that that perception exists at other places. The way to address that is just to do what we do: hire the best people we can find regardless of sex. If we keep hiring the best people we find, they will succeed in society, and that's all we expect them to do.

Q: MIT and Harvard University recently announced that they would offer free online courses. Why open up your classrooms like this?

The driving force for doing this is to improve the way we educate on campus. In the future, [a] particular course will be a combination of something you learn online, plus something you do in the classroom. It doesn't cost us anything to share [our online material] with the world.

FINDINGS

Indelible Ink

The fossilized ink sac of a cephalopod—the group of tentacled invertebrates that includes today's octopi and squid—that lived 162 million years ago may still contain some ink pigment, according to a study online this week in the *Proceedings of the National Academy of Sciences*.

Images of the 30-millimeter-long fossil taken with a scanning electron microscope reveal tiny spherical structures similar to structures in the ink of the modern-day cuttlefish (*Sepia officinalis*). But minerals could have replaced the original pigment particles, so the researchers tested samples of the fossil in a solution that breaks down melanin pigments.

The reaction generated two substances found only in eumelanin, a brownish-black form of the pigment also found in the ink of today's cephalopods. The new findings may help scientists identify eumelanin or its remnants in other fossils, such as feathers or skin—which may, in turn, shed light on the role of pigments in ancient organisms.

BY THE NUMBERS

86% Percentage of 258 major fish stocks reviewed by the National Oceanic and Atmospheric Administration that are not being overfished, according to a 14 May report.

15% Percentage of U.S. teenagers who have prediabetes or diabetes, according to a study published online 21 May by *Pediatrics* and based on data spanning from 1999 to 2008.

Solid Advance for Solar Cells

Solar prices continue to drop slowly. But that trend could get a needed shove from an improvement to a 20-year-old solar technology that's never managed to catch on.

Eighty percent of the market for solar cells is taken up by crystalline silicon cells, which convert about 20% of the energy in incoming sunlight into electricity. Most of the rest of the market comes from "thin film" cells made from metal alloys that are less efficient but also less expensive.

Dye-sensitized solar cells (DSSCs), produced by a third technology, are the cheapest to make and are up to 12% efficient. But they rely on a liquid electrolyte to help move the electrical charges through the material—and liquid electrolytes can leak and lead to corrosion in other parts of the cell. Researchers have also tried solid electrolytes, which have so far been about only 6% efficient.

But this week, researchers led by Mercouri Kanatzidis, a chemist at Northwestern University in Evanston, Illinois, report in *Nature* that they've developed a new solid electrolyte that gives DSSCs greater than 10% efficiency. That could be just what DSSCs need to make a splash in the market.

Science LIVE

Join us Thursday, 31 May, at 3 p.m. EDT for a live chat on geoengineering. http://scim.ag/science-live

Random Sample

Something Old and Something New

The storage rooms of the University of Cambridge's Museum of Archaeology and Anthropology contain thousands of methodically labeled artifacts of human history in the British Isles and around the world. With funding from Arts Council England, the museum closed temporarily to delve into its collections and find new ways to describe complex migration and trading routes through Cambridgeshire, as well as human history back to the Paleolithic.

The museum's light, airy displays, which reopen today, paint rich portraits: Several iron Viking spears confirm that people's reputation as fierce warriors, but they are juxtaposed with a whalebone ironing board (*left*) in the same showcase, creating an image of the Vikings' softer domestic side. A 1700-year-old coffin made from rock quarried 40 miles north of Cambridge, with a lead inner case, demonstrates the Roman commitment to preserving their dead. From the oldest, a 1.8-million-year-old stone tool from Tanzania, to the newest, a carving completed last week by George Nuku in traditional Maori style but applied to Perspex rather than wood, the museum's collection "make[s] it possible for the audience to imagine stories" about daily life across the ages, says museum Director Nicholas Thomas. "Archaeology," Thomas says, "is not just about science, it's also about imagination."

Curator Mark Elliott says he also wanted to remind viewers of the archaeological research process by displaying a few of the museum's hundreds of drawers of samples, filled with treasures and discoveries such as cutlery and personal adornments.

CREDITS TOP TO BOTTOM): PHOTOGRAPH COURTESY OF THE BRITISH GEOLOGICAL SOCIETY; MUSEUM OF ARCHAEOLOGY AND ANTHROPOLOGY, CAMBRIDGE (2)

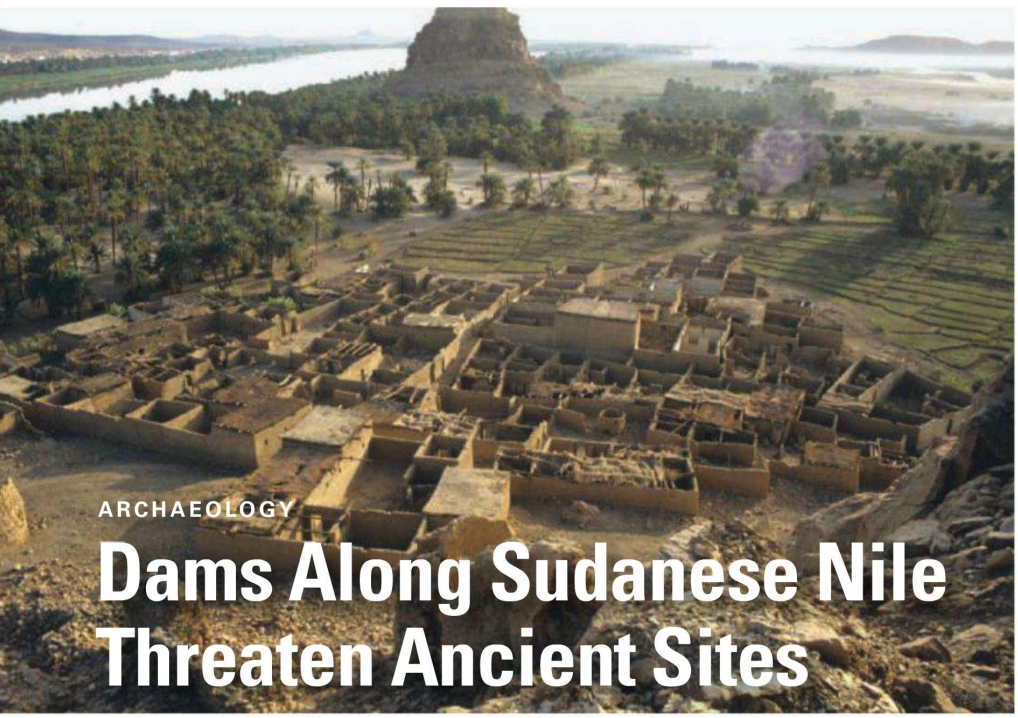

ARCHAEOLOGY

Dams Along Sudanese Nile Threaten Ancient Sites

Damned village. The proposed Kajbar dam would flood the medieval settlement of Nauri on the Nile.

CREDITS (TOP TO BOTTOM): MAHAS SURVEY PROJECT; © D. A. WELSBY

LONDON—Sudanese officials said last week that their government intends to move ahead with three massive dams along the Nile River and its tributaries, threatening hundreds of largely unexplored ancient sites. Archaeologists are gearing up to record and save what they can, but they fear being drawn into a political dispute over the controversial multibillion-dollar projects, which aim to generate electricity and expand agriculture in struggling Sudan.

Engineers and archaeologists gathered at the British Museum here for a sometimes-stormy emergency meeting designed to alert scientists to the impending cultural-heritage crisis.* "We're appealing to the scientific community to come to Sudan" to help document sites that face inundation, said Abdel Rahman Ali, director general of Sudan's National Corporation for Antiquities and Museums (NCAM). "We need to work together to minimize the loss." Countless Neolithic villages, ancient Egyptian temples, early Christian churches, elaborate rock carvings, and medieval forts may be affected. "There is much wonderful and fantastic stuff there," said David Edwards, an archaeologist at the University of Leicester in the United Kingdom, who has long experience in Sudan.

The Upper Nile in northern Sudan served as the major transportation corridor between sub-Saharan Africa and Egypt for thousands of years and includes part of the region known as Nubia, which has a rich prehistory. Africa's first civilization and writing south of Egypt also emerged there. In 2009, the $2 billion Merowe Dam on the Nile's fourth cataract in Sudan flooded a vast area after limited archaeological investigations. "The lesson from that is we need to get into these areas as soon as possible," said Neal Spencer, an archaeologist with the British Museum.

Work is already under way on the first of the three dams, on the Upper Atbara tributary of the Nile, about 400 kilometers southeast of the Sudanese capital of Khartoum. The 500,000 hectares that will be flooded by 2015 include hundreds of Neolithic settlements and cemeteries, says NCAM's El-Hassan Ahmed Mohammed, who surveyed the area in 2010.

Two other dams are in the works. Contracts have been signed to build the Kajbar and Shereiq dams on the Nile itself; these will take 6 years to complete once the government gives a final green light, said Muawia Mohamed Salih of Sudan's dam-implementation unit. Both dams threaten an enormous spread of sites from the Neolithic to more recent times. The Kajbar region, south of the Egyptian border, was at the frontier of Egypt's New Kingdom around 1600 B.C.E. and at the southern fringe of the 16th century C.E. Ottoman Empire. In preliminary surveys, Edwards counted more than 700 sites spanning 5000 years, including a rare settlement predating the Kerma civilization, the first Nubian kingdom, which flourished starting about 2500 B.C.E. Because so little is known about the origins of Kerma, excavating that settlement is "an absolute priority," Edwards says. He also cataloged a "massive and classic Kerma site" as well as New Kingdom Egyptian sites. Medieval churches and forts dot the area, as do later traditional Nubian fortified tower houses and rock carvings. Farther south, the Shereiq Dam would inundate forts from several periods, added Mariusz Drzewieki of Adam Mickiewicz University in Poznań, Poland.

NCAM's Ali pledged logistical support for foreign archaeology teams to conduct salvage excavations before the waters rise and said teams would be allowed to take home a portion of the artifacts. Some monuments threatened by the Kajbar dam—from rock art to Christian frescoes—may be important enough to require moving them to higher ground. This would require new roads, heavy trucks, and an enormous amount of expertise and money—"vast amounts of work," said British Museum archaeologist Derek Welsby, who has studied the monuments most likely to be affected.

Ships underwater? These rare, 4000-year-old boat drawings on rock would be difficult to rescue from rising waters.

These Nile sites are important in under-

*Sudan Dams Appeal, The British Museum, London, 15 May 2012; see http://preservethemiddlenile.files.wordpress.com/2012/02/ncam-dams-appeal2.jpg.

standing interactions between Egypt and Nubia, tracing the impact of climate change, and preserving the region's complex religious and cultural heritage, the archaeologists agreed. But a few recalled that protests by villagers against the Merowe Dam led to violent clashes with the government, sometimes putting archaeologists in difficult and dangerous situations. Some worry that salvage work for the new dams might imply support for the projects. "Can we conduct a research program without being part of building dams?" asked Bruce Williams, an archaeologist at the University of Chicago in Illinois, to scattered applause. But Spencer countered that "we can't be debating ethics while dams are built."

Despite the signed contracts, exactly when—or whether—the Kajbar and Shereiq dams will be built remains unclear. Rising inflation, a continued embargo imposed by the United States, and the loss of oil revenues with the creation last year of South Sudan threaten Khartoum's plans. "The pace of construction may be affected," admits Khalid al-Mubarak, media counselor at Sudan's embassy in London. And locals most affected by the projects are organizing to stop them. "There will be no compromise; we Nubians will fight to the end," promised Halim Sabba, a member of an organization that distributed leaflets at the meeting decrying the dams as a threat to their cultural survival.

Sabba and archaeologists are heartened by the Sudanese government's informal decision to put on hold plans for the Dal Dam between Kajbar and Egypt's High Aswan Dam to the north. That structure would drown important Egyptian and Nubian temples and settlements, requiring a huge multibillion-dollar rescue effort, and Sudanese officials said privately that the plans for that dam have quietly been shelved. **–ANDREW LAWLER**

IMMIGRATION REFORM

Senate Bills Would Make Room for More STEM Graduates

The U.S. Senate has waded into the debate over whether to permit more foreign-born scientists trained at U.S. universities to stay in the country. Although prospects are uncertain for two bills introduced last week, one of which is bipartisan, the legislation is seen as a sign that Congress is finally thinking seriously about how to tweak immigration laws to retain technical talent without triggering a political free-for-all on the more contentious issue of illegal immigration.

"Short of comprehensive immigration reform, which we'd love for Congress to tackle, we're happy to see these bills," says Barry Toiv of the Association of American Universities, a group of 61 prominent research universities. "These immigrants are job creators," notes Kasey Pipes, a spokesman for a coalition called Compete America that has marshaled high-tech companies, professional societies, and other higher-education organizations in urging Congress to act. "And while we're not taking sides, both bills are asking the right question: How do we keep more skilled foreign students in the country after they graduate?"

Both bills—one from Senator John Cornyn (R–TX), and the second from senators Chris Coons (D–DE) and Lamar Alexander (R–TN)—argue that the U.S. economy is weakened by current barriers facing foreign students who receive graduate degrees in science, technology, engineering, and math (STEM) fields and want to put down roots in the United States. Cornyn's plan, called the STAR Act, would allow STEM graduates from institutions receiving at least $5 million in federal research grants to lay claim to permanent residency without increasing the overall number of so-called green cards issued each year. It would do so by ending a program that awards 55,000 green cards to all manner of applicants via a lottery; those slots would go to STEM graduates. "This is about better targeting the visas we currently have," says one Cornyn aide.

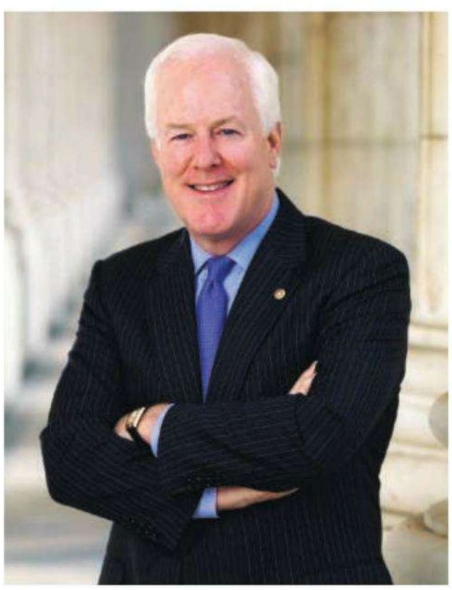

STEM-winder. John Cornyn says his plan would create more jobs.

The second bill, dubbed the SMART Jobs Act, would create a new visa category for students pursuing graduate STEM degrees and provide them with a direct route to a green card once they have found a job. They would not count against the current immigration ceiling.

Both bills would, in effect, remove the need for foreign graduates to temporarily extend their right to remain in the country by having employers certify that they are uniquely qualified for the job. That certification earns them an H-1B visa. (Cornyn's bill excludes postdocs, while Coons and Alexander would consider them to be eligible.) But holders of H-1B visas often fail to obtain permanent residency because caps on the number of green cards can mean long waits for immigrants from particular countries.

"American universities are educating the world's leading STEM graduate students—only to export this talent to our competitors overseas," Cornyn declared in a statement accompanying the release of his bill. The next day, Coons offered a historical perspective on why changes to the current law are needed. "Fifty years ago, if you came here from another country and got a doctorate, … your chances of applying your skills and strengths to create jobs in your home country were dramatically less than here. But times have changed, … and it's time for us to modernize."

Last year, representatives Zoe Lofgren (D–CA) and Raúl Labrador (R–ID) introduced bills in the U.S. House of Representatives that, using very similar language, would give foreign STEM graduates a clear path to permanent residency as well as strengthening STEM education programs for U.S. citizens. But neither bill has made it out of committee. Supporters of STEM immigration reform think a bill being readied by Representative Tim Griffin (R–AR) may stand a better chance. Representative Lamar Smith (R–TX), chair of the House Judiciary Committee, is believed to be the pivotal player in any decision to move a reform bill before the current Congress adjourns in December. And he's holding his cards close to the vest.

That uncertainty doesn't bother reform advocates, however. "What's important right now is less the details than that Congress may finally be trying to address the issue," Toiv says. **–JEFFREY MERVIS**

CREDIT: U.S. CONGRESS

SCIENCE FUNDING

NSF's 'Big Pitch' Tests Anonymized Grant Reviews

Is the U.S. National Science Foundation (NSF) turning down deserving research proposals because of potential biases in the grant-review process? The answer may be yes, if preliminary findings of an experiment being conducted by NSF officials hold up. But the officials caution against drawing any firm conclusions from what they acknowledge is limited data.

Known as The Big Pitch and launched 2 years ago by officials in the agency's Molecular and Cellular Biosciences (MCB) Division, the effort aims to find out if making proposals anonymous—and shorter—has an impact on how they fare in the review process. "We wanted to find ways to identify transformative ideas that are getting lost in the regular peer-review process," says Parag Chitnis, head of the MCB division. "So we asked: What would happen if we strip off the name of the PI [principal investigator] and institution and distill proposals down to just the big question or the core idea?"

What's in a name? Taylor (*left*) and Mydlarz (*right*) are among a handful of researchers who won NSF grants based on anonymous, two-page proposals describing the big idea behind their projects.

What happens is a lot, according to the first two rounds of the Big Pitch. NSF's grant reviewers who evaluated short, anonymized proposals picked a largely different set of projects to fund compared with those chosen by reviewers presented with standard, full-length versions of the same proposals.

In the first round, Chitnis and his colleagues identified 55 proposals relating to a single topic—biological effects of climate change—that MCB had received. They invited the applicants to supplement their standard, 15-page project descriptions and itemized cost estimates with two-page synopses that left out the details of each proposal but underscored the central idea. All of the applicants agreed to participate.

The division assembled two peer-review panels. One rated the traditional full proposals, while the other evaluated the two-page versions, which omitted the names and affiliations of applicants. The panel that reviewed the full proposals rated 14 proposals as "high priority." The other panel came up with its own list of 11 proposals that it judged as "high priority."

The two lists were almost entirely different, with only three proposals in common. According to a comparative analysis prepared by NSF, there was only "a weak correlation" between the two panels' ratings. In other words, the panels' assessments strongly diverged.

In the fall of 2011, the division repeated the experiment with 50-odd proposals for research concerning evolution. NSF has not released details of the results, but officials there say that once again, there was little overlap between the two panels' choices.

In the climate change round, the division ended up funding three out of five projects chosen exclusively through the two-page reviews, five out of eight projects chosen through the full proposal reviews, and two out of the three projects that were rated "high priority" by both review panels. Likewise, in the evolution round, NSF program managers divvied up the 18 awards between the sets of "high priority" projects identified through the two review mechanisms.

The experiment was not designed to separate out the effect of anonymity, but it may have been a factor. In both Big Pitch rounds, reviewers evaluating the anonymous two-pagers were later told the identity of the applicants. In some cases, Chitnis says, panelists were surprised to learn that a highly rated two-pager had come from a researcher they had never heard of. In others, he notes, reviewers "thought they knew who this person is going to be" only to find that the application came from a former student of the presumed bigwig, working at a small institution.

Noting that their grant-review process is anonymous and confidential, NSF declined to make any of the panelists available to explain their choices and would not identify any of the losing proposals. But *Science* spoke to some of the awardees about the process.

Shirley Taylor, an awardee during the evolution round of the Big Pitch, says a comparison of the reviews she got on the two versions of her proposal convinced her that anonymity had worked in her favor. An associate professor of microbiology at Virginia Commonwealth University in Richmond, Taylor had failed twice to win funding from the National Institutes of Health to study the role of an enzyme in modifying mitochondrial DNA.

Sea change. Mydlarz's grant will help study coral immunity

Both times, she says, reviewers questioned the validity of her preliminary results because she had few publications to her credit. Some reviews of her full proposal to NSF expressed the same concern. Without a biographical sketch, Taylor says, reviewers of the anonymous proposal could "focus on the novelty of the science, and this is what allowed my proposal to be funded."

The Big Pitch format could "remove bias and allow better support of smaller, innovative research groups that otherwise might be overlooked," Taylor adds. "The current sys-

CREDITS (TOP TO BOTTOM): COURTESY OF LAURA MYDLARZ; RICHARD MORAN; LAURA MYDLARZ

tem is definitely a 'buddy system' where it's not what you know but who you know, where you work, and where you publish. And the rich get richer."

Making proposals anonymous could help researchers from institutions that are not known for research, says J. Gary Tallman, a biologist at Willamette University in Salem, Oregon, whose proposal to study how global warming could hurt thermotolerant plants was funded through the Big Pitch. Tallman notes that he has seen prejudice against small universities like his own while serving on grant-review panels.

Not everybody who was funded through the Big Pitch's two-page proposal review believes anonymity is desirable for grant-making decisions. Laura Mydlarz, a cell biologist at the University of Texas, Arlington, whose two-pager won her a grant to study how global warming is affecting a Caribbean coral species, says review panels need to look at applicants' track records to judge whether they "can really do the work." In her case, she adds, true anonymity was impossible anyway: "If anybody on the panel knew anything about corals, they would have figured out who the PI was."

Chitnis says the division is planning to conduct a third round of the Big Pitch, possibly redesigned to get cleaner insights on the impact of anonymity versus summarizing. For example, a third review panel might review the short versions along with the biographical sketches of the applicants.

Two divisions within NSF's Directorate for Biological Sciences are already applying one insight gained from the Big Pitch: Shorter might be better. In January, the divisions of Integrative Organismal Systems and Environmental Biology began inviting four-page preproposals that reviewers evaluate before soliciting full proposals from a subset of applicants. (The Big Pitch grant reviewers told NSF officials that four pages of information would be better than two.) Chitnis says his own division, MCB, plans to institute the same system soon. But names of proposers and their institutions won't be whited out from applications—at least for now.

Whether the Big Pitch format truly helps identify good ideas that would otherwise get rejected may take years to find out. To do that, Chitnis says, the agency intends to track the success of the different proposals deemed high priority and funded by the pairs of review panels. "We can't immediately change wholesale how we do grant reviews," he says. "But we definitely want to do some more analysis." **–YUDHIJIT BHATTACHARJEE**

PLANETARY SCIENCE

Homegrown Organic Matter Found on Mars, But No Life

When Curiosity, NASA's next Mars rover, arrives at the Red Planet on 6 August, it will be searching for the ancient remains of environments that could have supported microscopic life eons ago. The rover (a.k.a. Mars Science Laboratory) will also be checking for a particular kind of fossil: molecular traces of long-dead life.

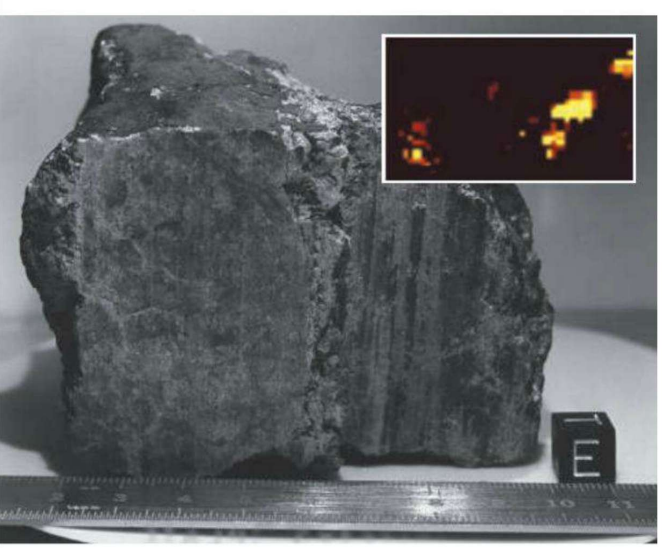

Bearer of martian crud. In meteorites from Mars like ALH84001 (*above*), analysts have found concentrations of carbon compounds (inset, 17 μm across) that formed without life.

But a discovery announced online this week in *Science* will add another layer of complexity to the interpretation of any geochemical markers of past life that Curiosity may find (http://scim.ag/ASteele). Researchers have discovered organic matter encased in once-molten martian rocks, demonstrating that the planet has been producing its own organic matter for eons with no help from life.

Organic compounds, carbon-containing chemicals such as those that make up the stuff of life on Earth, had been found in rocks that were blasted off Mars millions of years ago by large asteroid impacts and fell to Earth as meteorites. But no one could be sure the organics in martian meteorites weren't just earthly contamination. So microbiologist Andrew Steele of the Carnegie Institution for Science's Geophysical Laboratory in Washington, D.C., and his colleagues looked in the most protected parts of martian meteorites: microscopic mineral grains that had been securely locked in larger crystals for up to 4 billion years. Using a half-dozen kinds of analytical techniques, they probed for organic matter through the encasing minerals. Then, for more detail, they broke the minerals open and looked again.

The researchers found organic chemicals in 10 of 11 once-molten meteorites they examined at an abundance of about 20 parts per million. Raman spectroscopy showed that they include large, complex carbon compounds rich in benzene-like rings of carbon atoms. Organic-rich meteorites from the (lifeless) asteroid belt also have such "macromolecular carbon." Mass spectroscopy showed that in the one martian meteorite examined using this technique, the macromolecular carbon included polycyclic aromatic hydrocarbons. These multi-ring compounds are found in the soot from burning almost anything that is organic, as well as in meteorites.

Given the way the organic matter was sealed in the rock, "it is carbon from Mars," not terrestrial contamination, Steele says. Monica Grady, a meteoriticist at The Open University in Milton Keynes, U.K., agrees. "The huge trouble they've gone to to demonstrate [that the organic matter] is indigenous to the specimen," she says, means that the organic material Steele and colleagues found formed on Mars, without life, as magma cooled and solidified into rock.

Eons of weathering on Mars likely released the organic products of this nonbiological chemistry into the environment. For Curiosity, this weathered organic matter might masquerade as a product of life, Steele notes. On the plus side, the organic compounds in martian rock could also have served as food for life (if any) that did exist on Mars, says Jennifer Eigenbrode of NASA's Goddard Space Flight Center in Greenbelt, Maryland, and the Curiosity team. Rock organic matter "doesn't complicate things," she says. "It puts an interesting spin to the story that will come out." **–RICHARD A. KERR**

CREDITS: NASA IMAGES; (INSET) ANDREW STEELE

Grounded? A move by Congress to end the military's use of advanced biofuels could threaten the field.

ALTERNATIVE ENERGY

Military's Plan to Buy Biofuels Hits Roadblock in U.S. House

The U.S. House of Representatives last week blocked the Department of Defense (DOD) from buying more costly substitutes for petroleum-based fuels. The ban, if enacted, would not only throw a monkey wrench into the military's plans to go green but also stunt commercial development of a homegrown source of transportation fuel.

The House acted as part of several votes on the department's proposed $637 billion 2013 budget. One amendment would prevent the military from buying any fuel that costs more than the market price of petroleum. The $26-a-gallon price of the advanced biofuels that the U.S. Navy planned to buy for its fighter planes and ships is more than eight times the going rate for jet fuel. A second amendment would open the door to fuels that emit more carbon dioxide than conventional fossil fuels.

The two provisions were introduced by Representative Mike Conaway (R–TX). "The Department of Defense should not be in the business of driving fuel markets and fuel innovations," said Conaway at a hearing of the House Armed Services Committee on 9 May, a week before the bill went to the House floor. "The Department of Defense is [supposed to] defend the country and get the best bang it can for the money it is spending, and this is an area where we don't need to spend the money to prove anything."

Conaway doesn't have anything against biofuels per se, says his press secretary, Sam Ray. But with the federal government tightening its belt, Ray says, DOD needs to focus its resources on its primary mission.

That view represents a "fundamental misunderstanding of what we are up to," Navy Secretary Ray Mabus told Bloomberg Television on 20 March after a hearing in which Conaway and other Republicans criticized the Navy's plan to buy 450,000 gallons of advanced biofuel for $12 million. A vibrant, advanced biofuels industry, Mabus told the media company, would help reduce U.S. vulnerability to oil shortages and lessen the intermittent price spikes that last year cost DOD $3.6 billion. "We are doing this for national security and energy security. We are doing this to be better fighters," Mabus said.

Companies that are trying to develop advanced biofuels say the House's amendments, if adopted by the Senate and signed into law, would deprive them of their biggest customer. "The U.S. military, and more specifically the U.S. Navy, is the single most important group on the planet for making renewable fuels," says Stephen Mayfield, an algal biofuels expert at the University of California, San Diego. He's also a scientific founder of Sapphire Energy, an algal biofuels company in San Diego.

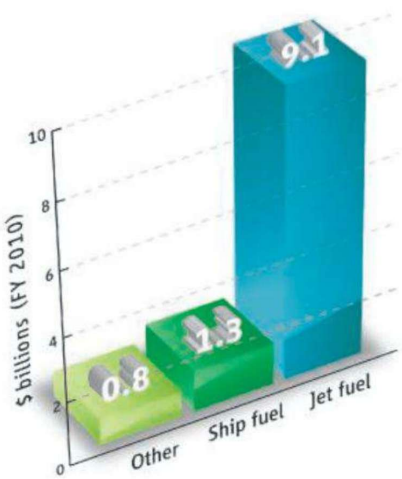

Steep price. DOD is trying to drive down its energy costs, which are dominated by fuel for jet planes.

DOD accounts for 2% of total U.S. fuel use, and Mayfield and others say its commitment to sustained purchases sends an important signal to investors. Without that pull from the market, "you're just not going to see much investment in advanced biofuels," says Wallace Tyner, an agricultural economist and biofuels expert at Purdue University in Lafayette, Indiana.

Biofuel use is already widespread. But almost all commercial biofuel is ethanol derived from corn or sugar cane. Because it has a lower energy content, ethanol cannot be used in jet fighters and naval ships. But other "advanced" biofuels technologies derived, for example, from algae and Camelina can be blended with conventional petroleum fuels and burned in standard ship and airplane engines.

The Navy has set a goal of using advanced biofuels for 50% of its needs by 2020, and the Air Force wants to reach the same target even sooner, by 2016. As part of this effort, last year the Navy, Department of Energy, and U.S. Department of Agriculture agreed to spend $510 million over 3 years to produce marine and aviation biofuels to power military and commercial ships and planes.

Fuels aren't the only front in the energy wars. According to a report last year by the Pew Charitable Trusts, DOD expects to spend $2.25 billion annually on clean energy technologies, including those aimed at more efficient buildings, by 2015, and $10 billion a year by 2030.

Congressional Republicans have so far confined their objections to the fuel provisions. But the price tag isn't the only issue. Conaway's second successful amendment would exempt DOD from a 2007 law prohibiting use of any alternative fuels that produce more greenhouse gas emissions than conventional petroleum fuels. The repeal opens the door to alternative fuels from coal and other high-carbon energy sources, an opportunity that legislators from coal-producing states would like to take advantage of.

This week, the Senate took up its version of the defense authorization bill behind closed doors, and at presstime there were reports that Senator James Inhofe (R–OK) would propose amendments similar to Conaway's. But with Democrats in control of the Senate, that provision faces an uphill battle. Last year, a similar ban voted on by the House was stripped from the final defense authorization bill during negotiations between the two bodies. A final spending bill could be delayed until after the November election.

In the meantime, the U.S. Navy is going ahead with its plans. In July, a military exercise called the Great Green Fleet, in which a carrier group powered by biofuels, nuclear power, and other alternatives, will conduct exercises in the Pacific Rim. So the future of green fighting machines could depend on a ground war within Congress.

–ROBERT F. SERVICE

CREDITS (TOP TO BOTTOM): U.S. NAVY PHOTO BY KELLY SCHINDLER/RELEASED; G. GRULLÓN/*SCIENCE*

In training. Katherine MacDuffie (*left*) examines brain images with University of Auckland neuropsychologist Donna Rose Addis.

PSYCHOLOGY

NSF Gives Clinical Students a Shot At Winning Graduate Fellowships

This spring, Katherine MacDuffie received one of the most prestigious U.S. awards for budding scientists: a Graduate Research Fellowship (GRF) from the National Science Foundation. A doctoral student in psychology at Duke University, MacDuffie is spending this year at the University of Auckland in New Zealand on a Fulbright award studying neuroimaging techniques. She may seem like an ideal candidate for a GRF award, but if she had applied a year earlier, she would have been turned down flat.

What gives?

In MacDuffie's case, it would have been the fact that she was enrolled in Duke's clinical psychology program. Never mind that her research, on how a person's view of the future depends on how well they measure up to their expectations for themselves, is basic to the core. In 2010, after years of tolerating an ambiguous policy on whether students like MacDuffie fit into NSF's mission to fund basic science, agency officials announced that they would reject any application—without even reviewing it—from students in clinical or counseling psychology graduate programs.

Fortunately for MacDuffie, the psychological science community protested the decision. And within a year, NSF had restored eligibility for scores of graduate psychology students.

The reversal has had a significant impact. "In our little microcosm, there was a 180-degree turnaround" from last year, says Robert Levenson, who directs the clinical psychology program at the University of California, Berkeley. Last year, about half a dozen students in his program who applied for a GRF had their applications tossed before review. This year, a new cohort of six students applied—and every proposal was reviewed. Even better, four were funded. Although NSF doesn't keep statistics by subfield, the directors of 10 other clinical psych doctoral programs report that their students were also given a fair shot at the prestigious fellowships.

NSF's rapid change of heart comes as basic and clinical research in psychology are converging, says Alan Kraut, executive director of the Association for Psychological Science. "To be an effective clinical psychology researcher these days, you need to know about cognitive science, social development, psychophysiology, genetics, epigenetics, [and] neuroscience," he argues. Kraut applauds NSF for recognizing that trend.

Locked out

The GRF program, begun soon after NSF was created in 1950, plays a critical role in the training of U.S. basic scientists. The 3-year fellowships provide students with a $30,000-a-year stipend, and their institutions receive a $12,000 tuition allowance. "One of these fellowships is the cat's meow," says Steven Breckler, executive director of the American Psychological Association's science directorate and a former NSF program director.

Research proposals in clinical psychology have long been ineligible for NSF support. But in 1995, NSF officials informally agreed that students from clinical psychology programs proposing basic research projects would not automatically be barred from the GRF competition. That understanding eroded over time, however.

Breckler thinks that NSF gradually hardened its stance as a way to separate itself from the government's health research behemoth, the National Institutes of Health (NIH). "Over the last decade, NSF has been working really hard to draw a bright line between what they fund and what NIH funds, and I think students who are in these clinical programs create a fuzzy boundary," Breckler says. Drawing that imaginary line has been a persistent challenge, agrees Susan Duby, who retired as director of NSF's graduate education division in 2001. "One of the hardest things I had to do as program director was to decide, on a case-by-case basis, who was eligible to apply," she says.

NSF's announcement in 2010 that all students from clinical programs would be ineligible caught the community by surprise. Kraut complained to Cora Marrett, then acting NSF deputy director (she has since been confirmed to the post), saying the new policy reflected "an outdated view of clinical psychology programs." Kraut's letter sparked a series of meetings with NSF officials, as well as with clinical scientists and training-program directors. Community leaders bolstered their argument by pointing to a new system of accrediting research-focused clinical psychology programs and a new journal on clinical research that will debut next year.

James Lightbourne, director of NSF's graduate education division, acknowledges the role played by the Association for Psychological Science and other professional societies in changing the agency's mind. "We decided that the prohibition on students in those programs was a little too severe," he says. The GRF program solicitation issued last summer removes the blanket prohibition and replaces it with more nuanced language. That opened the door for MacDuffie and her peers.

Lightbourne says NSF will monitor the situation closely to see how well it is working. For example, the agency plans to make sure that all psychology review panels include researchers with expertise in clinical science. "There's a lot at stake for the individual students, so it's not something we take lightly," Lightbourne says. **–SIRI CARPENTER**

Siri Carpenter is a science writer in Madison, Wisconsin.

CREDIT: GODFREY BOEHNKE

Healthy bite. This ancient Egyptian had healthier teeth and jaws than most living humans.

An Evolutionary Theory of Dentistry

Why are our teeth so rotten? Biologists point to a mismatch between our diets and lifestyles and those of our ancestors

DURHAM, NORTH CAROLINA—Remember the Coca-Cola jingle that went, "I'd like to buy the world a Coke and keep it company"? Well, it worked. And here's what happens when everyone can buy a soda every day in a small town on the northern tip of Mexico's Yucatán Peninsula: Young adults in the town of Dzilam González had three times as many cavities as those who live in a poorer, more isolated village nearby where people can't afford soft drinks every day, according to a new study. In the poorer village, people eat a traditional diet of maize tortillas at every meal. The richer village has a pizzeria in its central square, shops with ads for soft drinks, dentists' offices—and significantly more tooth decay in people aged 20 to 30, according to a new study by Elma Vega Lizama and Andrea Cucina of the Autonomous University of Yucatán in Mérida, Mexico.

Cucina presented the study of these two Maya villages at a recent meeting* here. The work offers an elegant demonstration of the message that emerged at the meeting: Human teeth, jaws, and mouths are not adapted in a healthy way to the diet of modern industrial society. We evolved to thrive on coarse seeds, nuts, tubers, fruit, and meat. In our skeletons, too, our evolutionary history leaves us prone to medical problems (see sidebar, p. 974). But when it comes to our mouths, the mismatch between our adaptations and our environment causes the dental cavities, overcrowding of teeth, overbite, and gum disease that run rampant today.

Not-so-sweet tooth. This German jaw from the 16th to 18th century shows the perils of a poor diet in tooth loss, cavities, and gum disease.

CREDITS: AMARNA PROJECT; LESLIE WILLIAMS

*"Evolution of Human Teeth and Jaws: Implications for Dentistry and Orthodontics," National Evolutionary Synthesis Center, 28–30 March, Durham, North Carolina.

The Maya of the two villages are before-and-after images of a population undergoing the so-called nutrition transition in which people switch from a traditional subsistence diet to an Industrial Age diet of refined sugars and processed foods. At the meeting, an unusual mix of paleoanthropologists, archaeologists, dental researchers, and food scientists explored what is known about the diets and dental health of ancient humans, and how that information might be useful to dentists today. "How does our oral environment today differ from those in which our teeth evolved?" asked co-organizer Peter Ungar of the University of Arkansas (UA), Fayetteville. "Can an understanding of this discordance inform clinical research and ultimately dental and orthodontic practice?"

Online
sciencemag.org
Podcast interview with author Ann Gibbons (http://scim.ag/pod_6084).

When the ancients smiled

The meeting began with grim slides of primates with terrible teeth and swollen gums, demonstrating that humans aren't the only ones with toothache. "Trauma, dysplasia, hypoplasia, arthritis, cysts—it's all there in animals," says anatomist Christopher Dean of University College London (UCL). "These are usual in wild animals in the last decades of their life, as part of the aging process." But tooth decay and gum disease get worse with a soft, sugar-rich diet in captivity.

Cavities and periodontal disease used to be diseases of aging in humans, too. In fossils of ancient humans, "you can count the number of cases of dental caries [cavities] on one hand," says UCL bioarchaeologist Simon Hillson. Researchers, such as Ungar, who have examined thousands of fossilized human ancestors estimate that cavities appear in fewer than 2% of teeth from earlier than 20,000 years ago. Traditional foragers, such as Australian aboriginals in the 1940s, still had beautiful teeth, with cavities in only the very old. (Other foragers with diets rich in plant carbohydrates, which are sugars, are an exception.) Gum disease and malocclusion—problems in the way the upper and lower teeth fit together,

such as overbite—are also surprisingly rare in prehistoric teeth, says Robert Corruccini of Southern Illinois University in Carbondale, who reviewed 20 years of research on cross-cultural differences in occlusion.

This clean bill of dental health began to deteriorate, however, as farming started to take root as early as 13,000 years ago in the Middle East and later in other parts of the world. Roughly 9% of Neolithic people—the first farmers—had cavities, as they began to consume cereal grains rich in carbohydrates, Ungar says. Even so, many millennia elapsed before dietary changes resulted in serious oral damage. For example, the skeletons of 93 commoners excavated at Amarna, Egypt, who apparently died between about 1330 B.C.E. and 1350 B.C.E., had surprisingly good teeth, says UA anthropologist Jerome Rose. These Egyptians ate more carbohydrates than hunter-gatherers did, in the form of coarse bread, but they also ate so much grit and fiber that the surfaces of their teeth—including any cavities—wore down rapidly. "The wear was fast enough to erase decay until late in life when decay showed up between teeth," Rose says.

The Burdens of Being a Biped

Just as many dental problems are rooted in our evolutionary history (see main text, p. 973), a number of musculoskeletal issues are also traceable to our past, in particular to the switch to walking upright more than 7 million years ago. "We've taken a body that was adapted to being horizontal to the ground and made it erect," says Bruce Latimer, a comparative anatomist at Case Western Reserve University in Cleveland, Ohio. "We've had to change nearly every bone in the body, and as a consequence, there are many things that humans suffer from that no other animal does."

Shifting from a four-legged support system to a two-legged one put extra stress on the legs and vertebrae. Adaptations in the feet, knees, hips, pelvis, and spine accommodate these forces, but at a cost. Imperfect evolution and constraints on how our bodies could change have left us with vertebrae that break more easily, weaker bones, and feet prone to heel spurs and sprained ankles. Our relatively inactive lifestyles and longer life span only exacerbate our orthopedic imperfections. A brief tour of the body reveals a number of design flaws, the legacy of our past.

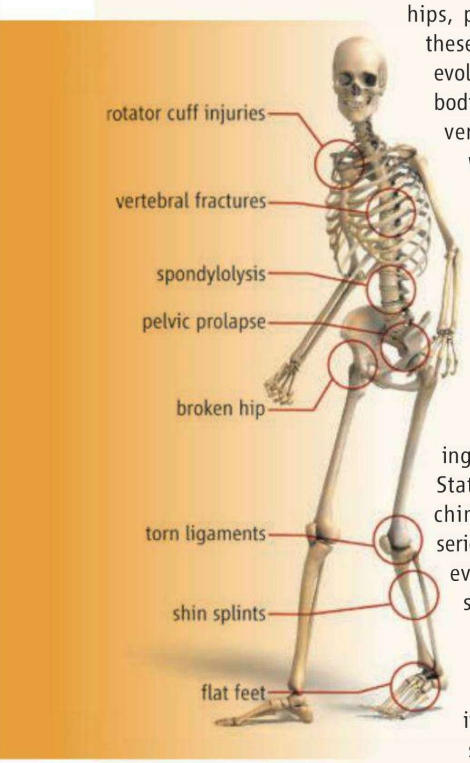

Walking can be a pain. Bipedalism leaves the human body vulnerable to a range of problems, just a few of which are pinpointed here.

Spine. Back pain is the leading health complaint in the United States. In dogs, horses, and even chimpanzees, the backbone is a series of vertebrae neatly stacked and evenly spaced to form a relatively stiff, gently curving beam. Not so with the human spine, which is highly flexible and can even bend backward. Yet this flexibility creates wear and tear on joint surfaces and predisposes us to osteoarthritis.

Furthermore, evolution has left our spines with an S-shaped curve, which is necessary to keep the upper body centered over the hips. Thus the lower spine curves toward the belly button, causing a hollow in the back and bringing the torso upright. To keep the head centered, the thoracic vertebrae in the chest curve in the other direction. "Spinal curvatures cause a lot of problems in humans that other animals don't have," particularly slipped disks and broken vertebrae, says Carol Ward, an anatomist at the University of Missouri, Columbia.

One type of break, called spondylolysis, affects about 6% of the U.S. population and is a leading cause of lower-back pain in teenage athletes. In this condition, the neural arch—a triangle of bone that surrounds the spinal cord—detaches from the rest of its vertebra, allowing the spine to slip forward relative to the back of the pelvis, pinching nerves and causing pain.

Ward, Latimer, and their colleagues surveyed thousands of human skeletons in the 1990s and determined that the problem lies in inadequate spacing between the joints connecting the vertebrae. If the lower vertebrae are too crowded, the bone is chronically pinched, eventually causing it to dissolve and the neural arch to separate. "When people don't have that correct spacing, they tend to get spondylolysis," Ward says. X-rays can reveal vulnerability to this condition, Latimer notes, and children with narrow vertebral spacing should avoid gymnastics, swimming butterfly stroke, and other sports that involve excessive back arching.

Feet. To cope with the added load on just two feet, the foot evolved a shock-absorbing arch by bringing what was a grasping big toe into line with the other toes. When that arch fails to form fully, as in people with flat feet, fatigue fractures can result. And when the big toe's tendon gets misaligned from improper shoes, bunions develop. Latimer blames heel spurs, plantar fasciitis, hammer toes, shin splints, chronically sprained ankles, and even varicose veins on our erect posture.

Fragile bones. The added load on two feet also caused knee and hip joints to expand, creating more surface area to absorb foot-fall forces. But the joints—and vertebrae as well—evolved to be bigger by enlarging the spongy, inner bone and thinning the hard, outer bone. As a result, human bones are less dense than those of other primates, a team led by mechanical engineer Christopher Hernandez of Cornell University, who studies osteoporosis, reported on 19 October 2011 in *PLoS ONE*.

Bone builds mass during childhood—more so if stressed with exercise—then loses mass during adulthood. With humans having ever longer life spans, bones, particularly vertebrae, may become fragile and break spontaneously. Apes lose bone mass as they age as well, but they don't suffer fractures because their bones are so much denser to begin with. Humans could have more apelike bones if they got more exercise as youths, as early humans did, Ward says. "If we treated our skeletons the way they were designed to be treated, they would serve us better later in life."

Bipedality leaves its mark in other parts of our bodies, too, for example in the difficulty of childbirth and in our vulnerability to rotator cuff injuries of the shoulder. Understanding these connections can suggest preventive measures, as in the case of spondylolysis, notes Latimer, who urges such understanding even if there's no immediate biomedical application. He helped organize a series of workshops through the National Evolutionary Synthesis Center to come up with evolutionary medicine curricula about musculoskeletal disorders. "If you don't understand the evolutionary background," he says, "you are treating the symptoms without understanding the underlying cause."

–ELIZABETH PENNISI

CREDIT: 123RF.COM

The Egyptians' coarse diet also had a positive impact on jaw development. Chewing stresses stimulate growth of alveolar bone, the thin layer of bone surrounding the roots of teeth, which causes children's lower jaws to grow more robust and longer, with little overbite or malocclusion. As a result, when the ancient Egyptians closed their jaws, their upper and lower incisors (the four front teeth) met in an edge-to-edge bite, with good spacing between the teeth in their robust faces. People today, who eat softer foods, have a "scissors configuration" bite, in which the upper incisors protrude over the lower incisors, because the lower jaw is smaller than the upper one.

Following the old ways. Maya in the Yucatán of Mexico who still eat a traditional diet have fewer cavities.

CREDIT: ELMA MARIA VEGA LIZAMA

Perils of a sweet tooth

In Europe, less than 10% of individuals had cavities until Alexander the Great brought sugar to Greece in the 4th century B.C.E., according to earlier studies, says pediatric dentist Kevin Boyd of Children's Memorial Hospital in Chicago, Illinois. Cavities increased first in Greece, then Rome; their incidence also rose throughout Europe in the Middle Ages. But the biggest spike was from 1800 to 1850, when Britain took control of the West Indies and imported far more sugar than previously. Sugar helped fuel the Industrial Revolution, which was a transition from an agriculture-based economy to a machine-based economy. In 1874, the British reduced the tax on sugar, and it became available to all social classes. "In London, mostly 1800 onwards, they have absolutely dreadful teeth," Hillson says.

The damage caused by refined sugar is well known: It alters the optimum pH of 5.4 in the mouth, making saliva more acidic. That saliva, as well as acid produced by bacteria in plaque, dissolves minerals in the enamel, causing cavities. By the middle of the 20th century, between 50% and 90% of the population in Europe and the United States had cavities. This improved in the 1970s when water was fluoridated. But for the first time in 40 years, the U.S. Centers for Disease Control and Prevention recently noted an increase in cavities in children aged 2 to 5 years. Dentists blame snacking and sugars in juice and sodas.

In the latter half of the 20th century, overcrowding of teeth and malocclusion became rampant. Today, nine in 10 adolescents in the United States have some malocclusion, and half could benefit from orthodontic treatment, Corruccini says. Impaction of the third molars, or wisdom teeth, occurs 10 times more frequently in people eating an Industrial Age diet than in hunter-gatherers. "Our jaws are underdeveloped because softened, highly processed foods do not provide the chewing stresses needed to stimulate normal growth of the jaw during childhood," Corruccini says.

As researchers at the workshop reviewed the data, it became clear that the biggest challenge for our teeth wasn't the initial transition to agriculture, as many researchers had once thought. It was the Industrial Revolution and then, in the 1980s, another marked increase in refined sugars in processed foods, such as high fructose corn syrup in sodas. "Caries and malocclusion is not a Neolithic problem, but an industrial problem," Boyd says.

After establishing the complexity of the problem, the researchers began to consider solutions. "If we remove carbohydrates from the diet, do we have less disease? Is this something I should be recommending to my patients?" asked dentist John Sorrentino of Hopewell Junction, New York.

The answer, it appears, is not simple, other than the obvious advice to cut back on refined sugars. The role of starch in causing cavities is not well known and needs study, Hillson says. Boyd suggested that consuming sugars with more fiber, such as fructose in fruit, lessens the damage because the sugars are absorbed more slowly in the gut, rather than rapidly in the mouth. But our ancestors consumed a variety of diets, so the solution may not be as simple as trying to recreate a hunter-gatherer's diet. "There was not a single oral environment to which our teeth and jaws evolved—there is no single caveman diet," Ungar says. "Still, we need to acknowledge that our ancestors did not have their teeth bathed in milkshake."

Further research is needed on how sugar affects the balance of species of bacteria in the mouth, such as *Streptococcus* strains, which are linked to cavities in humans. These complex communities of bacteria mix with minerals from saliva and immune cells to form plaque on the teeth. Our immune systems react to the bacteria, causing gum disease. "Normally, young kids are more resistant to the effects of plaque than adults," Dean says. But with more sugars in the diet, plaque-forming bacteria may flourish, which may trigger a bigger immune response and inflammatory reaction. That, in turn, can lead to a higher risk of systemic diseases such as cardiovascular disease and diabetes. But the response to plaque varies: "Everyone's mouth is its own ecological field," Dean says.

As for malocclusion and jaw disorders, Corruccini noted that a "fringe" branch of evolutionary dentistry has emerged in which children do mouth exercises and wear devices that put stronger force on their growing jaws. Ungar admitted feeding beef jerky to his own children to boost chewing stresses on their developing jaws, but he says the jury is still out on those methods to reduce overbite. "An understanding of this discordance [between traditional and modern diets and lifestyles] can inform clinical research and, ultimately, dental and orthodontic practice," Ungar says.

For now, one thing is perfectly clear: Our teeth have not evolved a defense against sodas. "People should understand that evolution is not as fast as the cultural changes we're seeing," Cucina says. **–ANN GIBBONS**

One at a time. By sequencing single sperm cells, researchers are pinning down recombination rates.

Single-Cell Sequencing Tackles Basic and Biomedical Questions

Over the past couple of decades, researchers have sequenced thousands of genomes from numerous species. In virtually every case, the deciphered DNA was extracted from millions of cells and pooled. The result has been a wealth of data, but, says Joel Hirschhorn, a geneticist at the Broad Institute in Cambridge, Massachusetts, "there are a lot of phenomena where there's a lot of cell-to-cell variability that won't be apparent when you look across populations of cells." That may be about to change.

At the meeting, four groups described new insights into how genomes generate diversity and what makes specific tumors resistant to treatment—all derived from sequencing DNA from individual human cells. Their reports sparked a lot of excitement about the potential of single-cell sequencing. "We're just starting to scratch the surface," Hirschhorn says.

Because the cell is the basic unit of biology, researchers are increasingly trying to isolate, study, and compare them individually (*Science*, 7 January 2011, p. 24). The DNA work has mostly involved sequencing the relatively simple genomes of single-cell microbes; the much larger and more complex genomes of human cells have been a bigger challenge. But the cost of sequencing has plummeted to the point at which it is becoming practical to decipher the 3-billion-base genome from single cells and compare sequences from cell to cell.

For Adam Auton, a statistical geneticist at Albert Einstein College of Medicine in New York City, single-cell sequencing provides a window on recombination, the process by which matching chromosomes exchange pieces of their DNA during cell division. Recombination helps generate genetic diversity by putting various versions of genes together in new combinations. It is also a cell's method of weeding out DNA gone bad.

Researchers have long sought a way to determine the amount of recombination that occurs in humans, and they have come up with several indirect ways to measure it in families or in populations. Sequencing and comparing the genomes of individual sperm cells allows for a direct and much more systematic investigation of the phenomenon, Auton says.

So when China's sequencing powerhouse, the Beijing Genomics Institute, told Auton it had sequenced 167 individual sperm from a healthy 50-year-old Asian male, he was eager to see the data. His initial analysis highlighted how difficult it is to isolate a single cell and reliably copy its DNA for sequencing. The researchers found that several of the sequences represented DNA from multiple cells; only 40 passed muster. By comparing each sperm's DNA with that obtained from a blood sample, Auton and his colleagues detected nearly 1000 recombination events, or about 24.5 per sperm cell, a number that agrees with estimates from indirect methods. Recombination occurs unevenly across the chromosomes, with "hot spots" representing places with elevated recombination rates. For the most part, the hot spots Auton's team identified coincided with where researchers had seen them in other studies. However, there was also a spike of recombination on chromosome 15, Auton reported at the meeting.

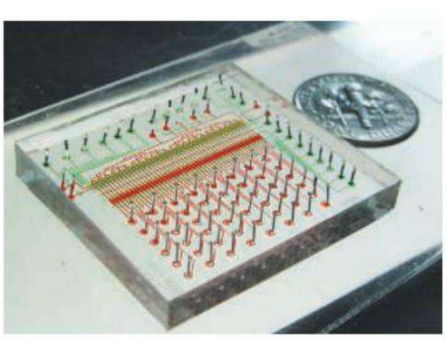

Lab on a chip. This microfluidics device isolates single cells and copies their DNA.

Stephen Quake of Stanford University in Palo Alto, California, has been developing single-cell techniques using a so-called lab on a chip. Samples pass through a series of tiny channels and valves to isolate single cells from which DNA is extracted and copied thousands of times to get enough for sequencing. Quake reported that he had solved many of the technical issues. He sequenced his first human single cells last year, and now he is using the technology to study recombination and assess mutation rates in sperm cells.

He determined the recombination rate from a study of 100 sperm, finding many new recombination hot spots and a rate that was on par with what indirect methods have found. Then he sequenced eight sperm to a greater degree, enough to determine the mutation rate. He found that rate to be 30 mutations per billion bases, a bit higher than what others have found, he reported at the meeting.

Timour Baslan, a graduate student at Cold Spring Harbor Laboratory in New York, has been using single-cell technology to study cancer cells. With Nicholas Navin, a molecular geneticist now at MD Anderson Cancer Center in Houston, Texas, his laboratory developed what it calls single-nucleus sequencing to profile tumors. They have used it to follow the evolution of cancers, tracking different subpopulations of cells as they become more common over time and spread. Baslan and his colleagues now add genetic barcodes to individual cells before sequencing, which allows them to pool samples for sequencing and still be able to identify sequences from individual cells in the mix, a cost-saving measure.

To date, Baslan reported, they have applied the approach to a dozen breast cancer

CREDIT (TOP TO BOTTOM): © DENNIS KUNKEL MICROSCOPY INC./VISUALS UNLIMITED/CORBIS; JIANBIN WANG

patients, sampling their tumor cells before and after treatment. Each patient reacted differently. In one tumor, the proportion of one type of cancer cell increased after therapy, indicating that the drug used was effective against part, but not all, of the tumor. In another patient, they saw a major rearrangement on the X chromosome and extra copies of a gene for a protein that would enable the tumor to counteract the effects of the drug. The chromosomes of a third patient's tumor cells were shattered by the therapy. The method "is routine for us now," and he can readily profile hundreds of single cells, Baslan said. He plans to incorporate microfluidics devices to streamline the approach even further. The goal is to understand tumor evolution and get a sense of which cancer cells will respond to the various treatments.

Meanwhile, Navin has continued to refine single-nucleus sequencing. By picking out cells that have just doubled their chromosomes in preparation for cell division and cutting down on the number of copying and processing steps, he needs only a few nanograms of DNA instead of a few micrograms. At the meeting, he reported that he had found variation in a breast cancer cell line that profiling showed to be homogeneous. "As you bring the magnifying glass closer, you detect more variation at the level of the base pair," he pointed out.

Navin found a similar trend when he sequenced four tumor cells from a more complex tumor, an invasive breast cancer. The sequence of a million-cell sample of the tumor uncovered six mutations, all in known cancer genes. The single-cell sequencing revealed an additional 30 mutations in each cell that were not detected in the larger sample, he reported. When he looked at 100 other cells from the same tumor, he found many of these mutations at very low frequencies. "This diversity is probably driving the cancer," he said. He also found the same mutations when he sequenced just the exons.

Geneticist Elaine Ostrander of the National Human Genome Research Institute in Bethesda, Maryland, calls the prospect of analyzing individual cancer cells "unbelievably exciting" as a "promising and elegant" way to pin down what's happening in a tumor. But others are more circumspect. "It will be hard to get these kinds of data, because [you] will have to sequence a lot of cells," says Elaine Mardis, co-director of the Genome Institute at Washington University in St. Louis in Missouri.

While researchers agree that single-cell sequencing may not yet have a high enough throughput to be practical for cancer assessments, "it can't be overemphasized how fast the technology is advancing," Auton says. "As the technology matures, we'll see some quite revolutionary things coming out."

HDL Itself Does Not Prevent Heart Attacks

If you are hoping to lower your risk of a heart attack simply by raising your levels of "good" cholesterol—high-density lipoproteins (HDLs)—you may be disappointed. Although epidemiological studies point to HDLs as protective against heart disease, a new genetic analysis shows that while high HDL might correlate with a healthier heart, it's not itself responsible for lowering heart attack risks.

To establish the role of HDL in protecting against heart attacks, Benjamin Voight, a human geneticist at the University of Pennsylvania, and his colleagues at the Broad Institute in Cambridge, Massachusetts, performed what's called a Mendelian randomization study, using records of 170,000 people who participated in existing studies. For this trial—done on a computer—he examined whether people who have a version of a gene that confers high HDL levels had fewer heart attacks than those who have versions of the gene that don't raise HDL.

For one study, he and his colleagues focused on a mutation in the endothelial lipase gene, whose protein is involved in cholesterol metabolism. The mutation increases HDL by about 5.4 milligrams per deciliter, about 10%. About 2.6% of people have this mutation. Working with data from 51,000 people, 4200 of whom had had heart attacks, he determined whether those with the mutation had fewer heart attacks than those with other versions of the gene. Based on the epidemiological evidence, the risk of heart attack should have decreased by 13% in those carrying the mutation, but "carriers versus noncarriers had absolutely no difference in risk," he reported at the meeting. "Epidemiological correlation doesn't tell you causality."

In a related study, Voight looked at 14 mutations in several genes associated with higher HDL levels. For a group of about 54,000 people, 12,000 of whom had had heart attacks, he summed the number of HDL-raising mutations and checked to see if those with higher mutation scores had lower heart disease risk. They did not, he reported at the meeting and in the 16 May issue of *The Lancet*.

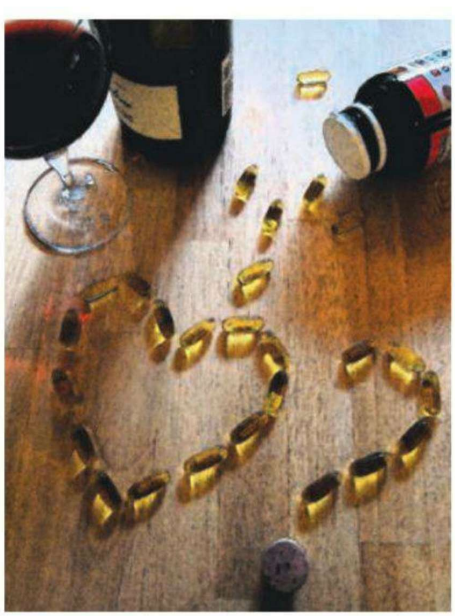

CREDIT: STACIE BUMGARNER

Helpful how? The heart-health benefits of red wine and fish oil may not come from raising HDLs.

In contrast, when he looked at people with mutations predisposing them to high levels of LDLs—"bad cholesterol"—those people did have more heart attacks. "With LDL it's very clear: LDL really does look like it's causal," says Andrew Clark, a geneticist at Cornell University.

Drug companies have been trying to develop drugs that raise HDL. But, Voight says, "we should think very carefully about how we plan an intervention around HDL. It might not work as advertised."

Ewan Birney, a bioinformaticist at the European Bioinformatics Institute in Hinxton, U.K., is very impressed with the approach Voight took in determining whether high HDL protects against heart attacks. "It's an incredibly powerful tool," he says. Mendelian randomization is a technique that's been around for about 10 years, but it is only now starting to be used because the approach requires data on thousands of people. Now that researchers have genotyped large cohorts of people with various diseases, the approach could be useful for studying ties to other conditions. "It's a way of teasing apart a hypothesis that's not true," Birney says. **–ELIZABETH PENNISI**

LETTERS

edited by Jennifer Sills

Support for Greece

THE GREEK SOCIETY AND ITS INSTITUTIONS ARE GOING THROUGH VERY DIFFICULT TIMES, emanating from several years of severe economic crisis. The gross national product of Greece decreased by almost 7% last year alone, and the unemployment rate exceeded 20%. Meanwhile, fiscal cutbacks threaten the survival of Greece's best centers of creative potential. A recent commentary in *Physics Today* (*1*) points out that funds are potentially available and can be used to remedy some of the above problems. Such funds, named structural funds, derive from "value-added" (sales) taxes throughout the European Union (EU) and are to be used to support the development of the poorer member-areas of the Union. Greece is entitled, annually, to a fraction of these European structural funds. For several years, Greece has used a sizable fraction of these funds to cover its research and technology budget. The disbursement of these funds requires actions from both sides, the EU and Greece. In the past 2 years, for various reasons, these actions did not come to fruition, resulting in the current crisis of Greek initiatives in education, research, and technology. This is halting the prospects of weathering the current crisis.

Now is the time for European leaders to secure the survival and future development of Greece's most competitive scientific and technological institutions by reinitiating these measures. To succeed, the following items need to be implemented. (i) For short-term benefits, release a substantial part of the EU structural funds that are available to Greece, to be used by innovative Greek programs in science and technology. (ii) For long-term benefits, also use these funds to initiate a broad program promoting the close cooperation of major European research and technology centers with Greek clusters of excellence. (iii) Ensure the continued support of Greek participation in major European institutions, such as the European Molecular Biology Laboratory. (iv) Initiate a program to establish new joint EU-Greek institutions of excellence, focusing on scientific areas where Greece already has a strong presence in the European landscape and which could be crucial to Greece's further technological development.

With these points in mind, 22 internationally renowned leaders in various fields of science and technology (*2*) have drafted and signed a petition addressed to Martin Schulz, President of the European Parliament; Herman Van Rompuy, President of the European Council; and José Manuel Durão Barroso, President of the EU Commission. The signatories of this petition sincerely hope that scientists and science policy leaders will take these issues seriously and will take whatever steps are in their power to address them. The petition follows:

Greece is in the midst of a prolonged and deep economic recession that has already changed dramatically the lives of its citizens and threatens the very existence of its structures necessary for future recovery. To regain its forward momentum, keep alive its competitive institutions, and implement its huge reform agenda, Greece needs our help. We are confident that Greece, which has contributed enormously to European culture, can do what is called for to create a brighter future. To succeed in this difficult task, special emphasis should be given among other things to science and technology, areas in which Greece possesses particularly strong institutions and human potential. By utilizing existing structural funds, and by promoting close cooperation between major European science and technology centers and existing Greek clusters of excellence, Greece can be enabled to sustain its scientific structures, build up its own technological future, and secure a competitive economy in the long run.

HARALD ZUR HAUSEN

Deutsches Krebsforschungszentrum, Im Neuenheimer Feld 280, 69120, Heidelberg, Germany. E-mail: zurhausen@dkfz-heidelberg.de

Letters to the Editor

Letters (~300 words) discuss material published in *Science* in the past 3 months or matters of general interest. Letters are not acknowledged upon receipt. Whether published in full or in part, Letters are subject to editing for clarity and space. Letters submitted, published, or posted elsewhere, in print or online, will be disqualified. To submit a Letter, go to www.submit2science.org.

References and Notes

1. T. Feder, "Science endures as conditions in Greece worsen," *Physics Today*, April 2012, p. 24 (www.physicstoday.org/resource/1/phtoad/v65/i4/p24_s1?view=print).
2. The signatories of the "Support Greece" petition are Peter C. Agre, Nobel Prize in Chemistry 2003; Elizabeth H. Blackburn, Nobel Prize in Physiology or Medicine 2009; Günter Blobel, Nobel Prize in Physiology or Medicine 1999; Edmond H. Fischer, Nobel Prize in Physiology or Medicine 1992; Carol W. Greider, Nobel Prize in Physiology or Medicine 2009; Jules A. Hoffmann, Nobel Prize in Physiology or Medicine 2011; H. Robert Horvitz, Nobel Prize in Physiology or Medicine 2002; Sir Richard Timothy (Tim) Hunt, Nobel Prize in Physiology or Medicine 2001; Eric R. Kandel, Nobel Prize in Physiology or Medicine 2000; Wolfgang Ketterle, Nobel Prize in Physics 2001; Roger D. Kornberg, Nobel Prize in Chemistry 2006; Yuan T. Lee, Nobel Prize in Chemistry 1986; Robert, Lord May of Oxford, Royal Swedish Academy's Crafoord Prize 1996; John C. Mather, Nobel Prize in Physics 2006; Prof. Iain Mattaj, Director General, European Molecular Biology Laboratory; Sir Paul M. Nurse, Nobel Prize in Physiology or Medicine 2001; Sir Venkatraman Ramakrishnan, Nobel Prize in Chemistry 2009; Sir Richard J. Roberts, Nobel Prize in Physiology or Medicine

CREDIT: ALEX SLOBODKIN/ISTOCKPHOTO.COM

Sensing magnetism
991

IBI Prize Essay
993

[1]Faculté des Lettres et Sciences Humaines, Cognitive Science Center, University of Neuchâtel, Neuchâtel 2000, Switzerland. [2]Department of Cognitive Science and Department of Philosophy, Central European University, 1051 Budapest, Hungary. [3]Institut Jean Nicod, Département d'Etudes Cognitives, Ecole Normale Supérieure, 75005 Paris, France.

*To whom correspondence should be addressed. E-mail: hugo.mercier@gmail.com

References

1. B. Bahrami *et al.*, *Science* **329**, 1081 (2010).
2. H. Mercier, D. Sperber, *Behav. Brain Sci.* **34**, 57 (2011).
3. J. A. Minson, V. Liberman, L. Ross, *Pers. Soc. Psychol. Bull.* **37**, 1325 (2011).
4. D. Moshman, M. Geil, *Thinking Reasoning* **4**, 231 (1998).
5. P. R. Laughlin, B. L. Bonner, A. G. Miner, *Org. Behav. Hum. Decision Processes* **88**, 605 (2002).
6. W. Doise, G. Mugny, *The Social Development of the Intellect* (Pergamon Press, Oxford, 1984).
7. M. K. Smith *et al.*, *Science* **323**, 122 (2009).
8. K. Dunbar, in *The Nature of Insight*, R. J. Sternberg, J. E. Davidson, Eds. (1995), pp. 365–395.
9. H. Mercier, *Cognit. Dev.* **26**, 177 (2011).
10. D. J. Devine, L. D. Clayton, B. B. Dunford, R. Seying, J. Pryce, *Psychol. Public Pol. Law* **7**, 622 (2001).
11. H. Mercier, H. Landemore, *Politi. Psychol.* **33**, 243 (2012).

1993; Hamilton O. Smith, Nobel Prize in Physiology or Medicine 1978; Thomas A. Steitz, Nobel Prize in Chemistry 2009; Kurt Wüthrich, Nobel Prize in Chemistry 2002; and Harald zur Hausen, Nobel Prize in Physiology or Medicine 2008.

"Two Heads Are Better" Stands to Reason

IN 2010, BARHAMI *ET AL*. (*1*) SHOWED THAT, in perceptual decision-making tasks, "two heads are better than one," provided they communicate with each other: Multiple decision-makers jointly adopt the more confident judgment, which, in ordinary circumstances, tends to be the more accurate. In his Report "When are two heads better than one and why?" (20 April, p. 360), A. Koriat shows that communication among the two heads is not even necessary: Asking for the degree of confidence of the participants and directly adopting the most confident judgment is an even better way of aggregating information. This suggests that the "wisdom of the crowd" could boil down to the ability to identify the crowd's most confident members and abide by their judgment.

These studies focus on group decisions based on perception or memory. When group decisions are based on reasoning, communication is focused not on individual confidence but on shareable arguments (*2*). Experimental evidence reveals a number of differences between the two scenarios. In various judgment tasks, the exchange of arguments outperforms bargaining, even though bargaining should enable participants to form estimates of one another's confidence (*3*). The exchange of arguments often allows the group to converge on the best answer, even if defended by a minority (*4*)—something that would not be possible in Koriat's model, which links confidence and consensus. The group can also reach a collective decision outside—and superior to—the range of individual answers available before the discussion (*5*, *6*). Through group discussion, participants can reach a deep understanding of the task, transferable to new problems (*7*).

Two heads are better than one not only in the kind of perceptual or memory tasks analyzed in Barhami *et al*. and Koriat's studies, but also in solving mathematical or logical problems (*4*) and in meeting a variety of challenges in science (*8*), education (*9*), law (*10*), and politics (*11*). In all these cases, the authority of the more confident individuals can be superseded by the quality of the more convincing arguments.

HUGO MERCIER[1]* AND DAN SPERBER[2,3]

CREDIT: PETER AND MARIA HOEY/WWW.PETERHOEY.COM

LIFE IN SCIENCE

The Noblest Lesson

One morning this past October, I woke up to find an email from my father. Reading the subject line, I immediately burst into tears. My father, Robert Kirshner, is an astronomy professor at Harvard University. The subject of his e-mail was, "My Students won the Nobel Prize!" A News Focus story about that prize—awarded for the discovery of the acceleration of the expanding universe (*1*)—later described me as being angry. I wasn't angry. I was freaked out.

I was worried because I knew my father to be incredibly competitive. (His cutthroat Monopoly playing style famously made my grandmother, his mother-in-law, cry.) But more important, I knew that he had dedicated the majority of his life's work to this project. I grew up watching my father's passion for science, his determination to understand things, the thrill he felt when he was able to synthesize ideas and understand the bigger picture. He has inspired me and taught me. And I was worried that by not getting the Nobel Prize for his contribution to this discovery, he would feel as though he had somehow failed.

But as it turns out, his response to not winning is the lesson I really value. When I spoke to him that morning, he amazed me: He was proud of the people he has worked with and taught; he was generous-spirited; he was funny; and he had perspective. What a relief! It turns out that a guy who spent his life trying to understand the immensity of the universe could put into perspective the relative importance of which particular earthling took home the ribbons and the medals and got to bow to the King of Sweden. It turns out that what was really important to him was the work itself, the wonder of this extraordinary universe, the honor and the fun of trying to figure things out, and maybe, just a little bit, the thrill of the chase. I admire all the terrific scientists who contributed to this greater understanding of the universe we live in, but in particular I admire my father, whose expansive understanding of what really matters taught me something of astronomical importance.

REBECCA SINCLAIR

Los Angeles, CA 90068, USA. E-mail: rrks@mac.com

EDITOR'S NOTE

This is an occasional feature highlighting some of the day-to-day humorous realities that face our readers. Can you top this? Submit your best stories at www.submit2science.org.

Reference

1. Y. Bhattacharjee, *Science* **336**, 26 (2012).

PSYCHOLOGY

On Ruts and Getting Out of Them

Wendy Wood

If you are looking for inspiration to get off the couch and exercise or to extinguish that cigarette and become a former smoker, *The Power of Habit* is for you. Charles Duhigg, an investigative reporter for the *New York Times*, offers engaging stories that should convince even the most ingrained procrastinator that one can change one's behavior.

The Power of Habit
Why We Do What We Do in Life and Business
by Charles Duhigg
Random House, New York, 2012. 395 pp. $28.
ISBN 9781400069286.

The book is a brilliant read, and Duhigg bases his analysis on extensive research into the neuroscience and psychology of habit formation and change. Yet his account sidesteps important distinctions between habits, addictions, and other types of mindless responding. In so doing, it betrays the central message that successful behavior change requires understanding of the psychological mechanisms that maintain the unwanted behavior.

Duhigg's approach reflects the spirit of a new wave of theories of behavioral change that recognize the key role of the environment. In the past, change prescriptions tended to be largely informational, explaining what habits people should adopt in order to reach their goals. For example, to be healthy, people should eat "five-a-day" fruits and vegetables and follow the food pyramid. But to make changes in behavior stick requires more than just information. In 2000, an entire issue of *Health Psychology* was devoted to the problem of people's failures to maintain behavioral changes (*1*). In line with the newer approach, Duhigg focuses on the context cues that automatically trigger unwanted behaviors. Because we outsource control of everyday habits to such cues, tackling cuing is a promising approach to long-term change.

Building on this basic insight, the book provides a simple, scientifically sound model of habits. These develop as people learn to associate cues, routines, and rewards—when people repeatedly respond (e.g., drinking alcohol) to a cue (e.g., anxiety) with some reward (e.g., escape). Once such cue-response associations are learned, perception of the cue automatically brings the response to mind. And it's usually easier to carry out the response in mind rather than to make a decision to do something else. The early chapters invoke enough neuroscience data to convince readers that the brain inevitably forms habit associations. If habits happen, then we may as well make them work for us instead of against us.

Cue-response associations are basic to habit performance. By these cognitive associations, habits can be performed automatically, with little thought or effort. But these associations also promote unwanted habits, thus confounding attempts to change behavior. For example, people continue to eat habitually even when you'd expect them to quit—when they have already overindulged or when food is stale and they explicitly report not liking it (*2*, *3*). Cuing explains why people stick with habits even when the "reward" following the response is not rewarding.

Instead of building on this insight, Duhigg explains habit persistence in terms of addiction and appetitive reward, and he argues that a craving for the reward powers habit performance. However, habits are not addictions (a distinction that the book acknowledges and then disregards). Overlooking this difference contorts the logic of habits. Players on Tony Dungy's football team are said to have craved executing habitual game plays, and Alcoa managers supposedly followed corporate routines because they craved promotions. (I wish that promotions in my job were sufficiently frequent to be addictive.)

To get habits working for us, Duhigg offers a "golden rule" of habit change, which involves consciously inserting a new routine between the cue and reward (i.e., counterconditioning in behavioral therapy). With repetition, this new routine becomes the reigning habit. Although this strategy might work for some people or habits, alternatives may be more effective for others. Most promising is disrupting habit cues so that the old response is not brought to mind and new habits can be learned. For example, one can displace cues to eating by manipulating the size of plates and the accessibility of food (*4*). In addition, by moving house, people can disrupt the cues that activate many old habits and free themselves up to act on their current intentions (*5*, *6*). This is one reason why new residents are deluged with ads—merchants know that this is a sensitive period for forming new purchasing habits. So, there are perhaps many golden rules, including "disrupt cues, enable new habits."

By equating habit and addiction, the book overlooks distinctions that are important for behavior change. We know that strategies successful at changing habits are not effective with other kinds of automaticity (*7*). For example, being highly vigilant to the cues that trigger an unwanted response can control habits but not responses to temptations. Being mindful of that tempting piece of chocolate cake in the refrigerator will probably make you more, not less, likely to eat it.

These critical distinctions between habit, addiction, and other types of mindless behavior are further muddied in the book's second and third sections, which address organizations and societies. There, Duhigg places habits under the same concep-

CREDIT: © BETTMANN/CORBIS

The reviewer is at the Department of Psychology and the Marshall School of Business, University of Southern California, Los Angeles, CA 90089–1061, USA. E-mail: wendy.wood@usc.edu

tual umbrella as willpower, motivation, social norms, leadership, diffusion of responsibility, and intergroup relations. Despite the compelling stories he recounts, even casual readers should be sensitive to these kinds of scientific details. Without clearer delineation of the psychology behind these highly diverse kinds of mindless behavior, readers may be left, once again, with behavior changes that they cannot maintain.

References

1. *Health Psychol.* **19** (1, suppl.) (2000).
2. E. Tricomi, B. W. Balleine, J. P. O'Doherty, *Eur. J. Neurosci.* **29**, 2225 (2009).
3. D. T. Neal, W. Wood, M. Wu, D. Kurlander, *Pers. Soc. Psychol. Bull.* **37**, 1428 (2011).
4. B. Wansink, *Mindless Eating: Why We Eat More Than We Think* (Bantam-Dell, New York, 2006).
5. W. Wood, M. G. Witt, L. Tam, *J. Pers. Soc. Psychol.* **88**, 918 (2005).
6. B. Verplanken, I. Walker, A. Davis, M. Jurasek, *J. Environ.* **28**, 121 (2007).
7. J. M. Quinn, A. M. Pascoe, W. Wood, D. T. Neal, *Pers. Soc. Psychol. Bull.* **36**, 499 (2010).

10.1126/science.1222294

EXHIBITIONS: ASTRONOMY

Transit Reflections

Deborah Dixon

The Royal Observatory is a rich palimpsest of scientific practice and discovery. Located on a promontory in Greenwich Park, London, the site comprises several buildings. Flamsteed House, the earliest and the original observatory, was built in 1675 on the orders of King Charles II. Later additions—the Meridian Building, the Altazimuth Pavilion, the Astronomy Centre, and the Peter Harrison Planetarium—stretch back from the Meridian Courtyard and Gardens. Their standing collections, displays, and demonstrations make clear the crucial role played by Greenwich astronomers and their diverse instruments in charting the immense spaces of the cosmos. They also evidence how the observatory operated as one of many nodes in a vast cultural, as well as scientific, network enamored with discerning the nature of the universe.

This simultaneously site-specific and globe-spanning history forms the basis of Measuring the Universe, an exhibition developed to mark the 5–6 June transit of Venus.

The reviewer is at the Institute of Geography and Earth Sciences, Aberystwyth University, Aberystwyth, Ceredigion SY23 3DB, Wales, UK. E-mail: dxd@aber.ac.uk

CREDIT: © WOLFGANG TILLMANS/COURTESY MAUREEN PALEY, LONDON

Wolfgang Tillmans's *Venus transit* (2004).

Over a 243-year cycle, Venus passes between Earth's orbital plane and the Sun four times—twice in pairs 8 years apart, with the pairs separated by gaps of 121.5 and 105.5 years—appearing as a small, dark spot crawling slowly across the Sun's disc. After June, the rare event will not recur until 2117.

The exhibition uses text and images to provide a capsule history of how, over the past 400 years, astronomers have sought to use transits to gauge the distance between Earth and Sun. The principle of parallax was crucial to such efforts, and designer Richard Hogg's animated video provides a useful primer on this. In 1716, Edmund Halley (soon to become Royal Astronomer) exhorted governments to organize geographically disparate expeditions as a means of achieving the greatest parallax possible for the transit of 1761. Over a hundred observers subsequently took part. In 1769, James Cook took measurements in Tahiti from a point subsequently labeled "Point Venus," while French astronomer Guillaume Le Gentil tragically missed observing both events due to rough waters off of Mauritius in 1761 and overcast skies in Pondicherry eight years later.

Yet, as the story unfolds around the room, it becomes clear that such techniques became overshadowed by new means of measuring astronomical distances—not only between Earth and Sun but also between stars, between galaxies, and beyond. With the introduction of radar pulses and spectroscopic observations, for example, cosmic horizons were pushed ever further away. In consequence, the scientific importance of the transit of Venus became a largely historical curiosity, while the exhibit itself risks becoming a somewhat moribund account of ever-reaching scientific progress.

That fate is avoided, however, and the exhibition given uncommon animation by the careful effort to incorporate recent art. Photographer Wolfgang Tillmans's *Venus transit* occupies a prominent position. In it, the tiny spectacle of Venus passing in front of the Sun becomes a sublime wonder that places the observer in the midst of an overwhelmingly vast, lonely space, while evoking pleasure that such a spectacle can kindle the imagination. This evocation of the sublime underscores Lynette Wallworth's immersive video installation *ReKindling Venus* (*1*), which will be playing next door at the planetarium in June (*2*). This piece is based on the artist's continuing preoccupation with the complexity and fragility of the Great Barrier Reef as well as an attentiveness to the ways in which gaze-enhancing technologies play with light and shadow. The collaborative spirit that characterized scientific efforts to track the transit of Venus resonates with Wallworth's working relationship with marine biologists and, importantly, with the urgent need for a transdisciplinary, transborder response to climate change.

These artworks are re-presented at the Royal Observatory not as a means of explaining scientific principles or illustrating key events but rather as creative responses to the worlds around us, made visible via scientific modes of inquiry. Their emphasis on the sublimity of these worlds, and the sheer sensuousness of seeing, lends a Romantic glow to what may otherwise appear to be somewhat naturalistic, empirical accounts and provides a useful reminder of the wonder and excitement that underscore so much of what scientists do. More tellingly for exhibitions such as *Measuring the Universe*, they possess a powerful, visceral appeal that serves scientists well by reaching and engaging the general public.

Measuring the Universe
From the Transit of Venus to the Edge of the Cosmos
Marek Kukula and Rebekah Higgitt, curators
Royal Observatory
Greenwich, London.
1 March to 2 September 2012.
www.rmg.co.uk/visit/events/measuring-the-universe

References and Notes

1. http://rekindlingvenus.com.
2. *ReKindling Venus* will play at the planetarium Thursdays through Sundays, 7 June to 6 July 2012.

10.1126/science.1222944

SCIENCE POLICY

From "Science in Europe" to "European Science"

Early impacts of the European Research Council suggest shifts toward competition and excellence in EU-wide basic science.

Maria Nedeva,[1,2]* and Michael Stampfer[3]

According to proposals of the European Commission (EC) for Horizon 2020 (*1*), the next Framework Programme (FP) for Research and Innovation will direct resources to three priorities: (i) excellence in Europe's science base; (ii) industrial leadership; and (iii) societal challenges. We examine the agenda for improving Europe's science base and discuss changes in the policy system, with a focus on the European Research Council (ERC). Describing the European-level policy system through its statement of added value and rationale, target of intervention, and science support organizations, we argue that it is transitioning from a period we term "science in Europe," to a period we refer to as "European science." Although we argue this transition in terms of clear differences, we acknowledge that, in reality, the process is gradual, nuanced, and far from complete.

From Science in Europe . . .

From the 1950s to the early 2000s, European science policy was "focused largely on supporting technology (application), whereas support for basic science rests firmly with member states" (*2*). This was shaped by the "principle of subsidiarity," which states that the European Union (EU) could act only when action by individual countries was insufficient and by a focus on industrial competitiveness stated by the European Treaty. It influenced two assumptions regarding the added value of, and rationale for, European-level policy. First, "European added value" was interpreted through different forms of subsidiarity and the coordination of national-level science and research (*3*); it was redefined often to accommodate changing and multiple goals of the EU FPs and became increasingly inoperable (*4*). Second, there was the assumption that Europe was a world leader in science, but was lagging in industrial and economic exploitation of scientific ideas (*5*, *6*). Thus, support was targeted at technology and application, lessening the perceived importance of publicly funded fundamental research for the industrial and economic future of Europe.

Hence, European-level science and research policy focused on applied research and development or on broad social conditions for research, such as collaboration and networking, while leaving development of the science to the national level. In parallel, multinational agreements pursued large-scale scientific endeavors and infrastructures [e.g., the European Organization for Nuclear Research (CERN) in particle physics].

This shaped the organization of science support at the European level, characterized by three types of organizations: field specific, intergovernmental large research facilities like CERN and the European Molecular Biology Laboratory (EMBL); umbrella organizations like the European Science Foundation (ESF) coordinating national activities (*7*); and the FPs with large budgets but no explicit focus on scientific research. Despite great ambitions and sometimes success (*8*–*10*), these organizations were (and are) focused on specific fields; lacked focus, funding, and authority; or did not place real emphasis on scientific excellence. Hence, overall science policy at the European level had no crystallizing organizational actor.

Correspondingly, European scientists competed for global recognition and mainly national resources. Both the availability of research funds and the conditions and criteria of funding varied greatly between countries. This contributed to the perceived underperformance of science in Europe as a whole, with blame attributed to its segmentation and fragmentation (*11*).

In addition, the FPs had an increasing variety of goals, including emphasis on cross-national networks, small and medium enterprises, and technology transfer. It became more difficult to identify strong, attributable, and intended effects of FP efforts (*12*), even for the core goal of industrial competitiveness. Although the FPs have had some positive effects in certain sectors, like the European telecommunications industry (*13*, *14*), their impact on industry at large remains much more opaque. Impact on scientific performance is also unclear. It has been suggested that, for universities, FP resources are just convenient sources of funding that do not generate structural effects (*15*).

. . . toward "European science"

Toward the end of the 20th century, assumptions about the added value of and rationale for science policy at the European level, as reflected in official documents, started to shift. First, the understanding of European added value changed to incorporate competition. In 2003, an expert group called for competition in the context of excellence in research to become "an essential part of a new, forward-looking definition of European added value" (*16*). A year later, this call was answered in official EC documents as "the added value which comes from competition at EU level" (*17*). This coincided with a change of focus marked by the notion of the European Research Area (ERA) (*18*) and included stated intentions for "integration" (*19*). Policy attention shifted from mainly coordinating national efforts to developing a pan-European science base. It also precipitated implementation, alongside tried and tested policy initiatives, of new instruments aiming to increase the level of integration in different aspects of the European science system (*20*).

Second, Europe had to recognize that its problems in science went beyond applications. By the late 1990s, it was recognized that European countries were lagging behind the United States and Japan both in science and its applications (*6*, *21*). European policy for science and research could no longer focus on technology and applications. Reframing science by introducing the notion of "frontier" research (*22*) by-passed the basic-applied divide and made it possible (i) to recast the EC as a funder of research, innovation, and science and (ii) to set up organizations that disrupted the established way of supporting research at the European level.

These two changes of policy assumptions and rationales made possible the establish-

[1]Manchester Institute of Innovation Research, University of Manchester, Manchester M139PL, UK. [2]Research Policy Institute, Lund University, SE-221 00 Lund, Sweden. [3]Vienna Science and Technology Fund, A-1090 Vienna, Austria.

*Author for correspondence. E-mail: maria.nedeva@mbs.ac.uk

ment of the ERC in 2007, the first dedicated research-funding agency at the European level to support investigator-driven research, with a focus on excellence. The ERC aims to support risky, adventurous research and to create leverage toward structural improvements in the research system of Europe (*23*) and a "truly European research base" (*24*).

The ERC is different from the organizational arrangements discussed above in five substantive ways: It (i) explicitly focuses on supporting research at or beyond the frontiers of knowledge; (ii) supports investigator-driven, rather than programmatic, research; (iii) has a budget and allocates funding (unlike the ESF and European Cooperation in Science and Technology); (iv) has few clear and targeted goals (unlike the FPs); and (v) uses peer-reviewed scientific excellence as the sole criterion for selection rather than as a discourse for achieving other political goals.

These objectives are pursued through two main funding instruments (*25*): Starting Independent Researcher Grants targeting researchers at relatively early career stages and Advanced Investigator Grants meant for researchers at the forefront of their fields. Legally, the ERC is an EC executive agency tasked with administering the IDEAS Programme (*26*). However, the Scientific Council has guaranteed autonomy to decide its scientific direction and to implement its work program. Although the ERC is still comparatively small (*27*), it embodies distinguishing characteristics of the new stage in European-level science and research. It is the organization congruent with the transformed policy rationales and targets and marks the emergence of European science.

Where We Stand and Early Effects

European-level science policy is still a mixture of cooperation and competition, scientific excellence and political goals, and established and novel organizations. The transformation discussed in this article is at an early stage; its future and long-term prospects unclear. On one hand, EC proposals for Horizon 2020 suggest a 77% funding increase for the ERC. On the other hand, the legal position of the ERC as an executive agency generates tensions mainly associated with the relation with the EC and the appropriateness of its financial rules and regulations in light of its objectives. There is also strain between the inherently long-term agenda of the ERC and political pressures for short-term effects.

European science as a new policy platform, and the ERC as one of its key distinguishing features, could have far-reaching effects on the science base; indeed, early impact already can be glimpsed. EURECIA (*28*) studied the effects of the ERC and its funding schemes on (i) researchers, research, and careers; (ii) universities and research institutes; (iii) national funding; and (iv) European funding.

Many of the projects the ERC supports are innovative and work on or exploit recent scientific innovations (*29*, *30*). The ERC has had some effects on universities and research organizations in Europe (*31*). These are most pronounced in organizations ranking just below the top research performers, which use ERC grants to develop and implement structures and practices conducive to research excellence, like support for grant preparation and administration; ERC as a marker for research excellence also enables them to perform, compete, and align their activities in a European, rather than national, context.

At the national level, establishment of the ERC provided impetus for an overhaul of systems that did not include dedicated research funding agencies (*32*), such as in France and Poland, where the ERC was the model for a research funding agency. At the European level of the funding landscape, the ERC has coshaped a number of changes, e.g., strengthening the importance of excellence for the ERA agenda, changes in traditional principles in EU support to research by supporting individuals rather than organizations, and no "just retour" (*33*).

European science policy and organization are undergoing a transformation, and early evidence suggests wide-ranging effects on the science system; but only time, and more research, will tell whether these intended effects will bloom or wither away.

References and Notes

1. EC, Communication from the Commission to the European Parliament, the Council, the European Economic and Social Committee and the Committee on the Regions: Horizon 2020—The Framework Programme for Research and Innovation, COM(2011) 808 Final (EC, Brussels, 2011).
2. M. Sharp, in *Science in Tomorrow's Europe*, R. Barre, M. Gibbons, J. Maddox, B. Martin, P. Papon, Eds. (Economica International, Paris, 1997), pp. 201–217.
3. L. Georghiou, *Res. Policy* **27**, 611 (1998).
4. M. Stampfer, *European Added Value of Community Research Activities: Expert Analysis in Support of Ex Post Evaluation of FP6* [Official Report, Vienna Science and Technology Fund (WWTF) Vienna, 2008].
5. G. Dosi, P. Llerena, M. S. Labini, *Res. Policy* **35**, 1450 (2006).
6. K. Pavitt, *Sci. Public Policy* **27**, 455 (2000).
7. D. J. V. H. Gronbaek, *Sci. Public Policy* **30**, 391 (2003).
8. CERN, Convention for the Establishment of a European Organization for Nuclear Research, Paris, 1 July 1953; http://council.web.cern.ch/council/en/Governance/Convention.html.
9. ESF, Call for proposals: 2012 research conference, www.esf.org/.
10. T. Luukkonen, *Res. Policy* **31**, 437 (2002).
11. EC, Communication from the Commission to the Council, the European Parliament, the Economic and Social Committee and the Committee of the Regions: Towards a European research area; COM(2000) 6 (EC, Brussels, 2000).
12. K. Guy, W. Polt, G. Streicher, N. Vonortas, E. Amanatidou, FP5 impact assessment: Survey conducted as a part of the 5-year assessment of EU research activities (1999–2003) (Atlantis Research, Athens, 2005).
13. W. Polt, N. Vonortas (coordinators), *IST Evaluation and Monitoring* (Joanneum Research, Vienna, 2006); http://ec.europa.eu/dgs/information_society/evaluation/data/pdf/studies/s2005_04/d02_blueprint.pdf.
14. EC, DG Information Society and Media: Self Assessment of the Effectiveness of IST-RTD in the 6th FP, Ex-post Evaluation of the IST Research in FP6 (EC, Brussels, 2007).
15. E. Arnold *et al.*, *Impacts of the Framework Programme in Sweden* [Swedish Governmental Agency for Innovation Systems (VINNOVA), Stockholm, 2008].
16. ERC Expert Group, *The European Research Council: A Cornerstone in the European Research Area: Report from an Expert Group* (Danish Ministry of Science, Technology, and Innovation, Copenhagen, 2003).
17. EC, COM(2004) 9 Final, Europe and Basic Research, (EC, Brussels, 2004).
18. The notion of ERA, adopted in 2000, can be regarded as a means to achieve the ambitious targets of the Lisbon Strategy of the EU. Initially, ERA focused on creating an "internal market" in European-level research by aligning national effort and integrating research capacity. During the last decade, it has broadened its remit to incorporate, among others, the promotion of excellence in European-level research.
19. T. Luukkonen, M. Nedeva, *Res. Policy* **39**, 674 (2010).
20. One clear implication of the notion of ERA was overcoming the "harmful" fragmentation of science in Europe and achieving a "better organisation of the European research effort" being conditional upon the development of a European research space (system) that went "beyond the current static structure of '15+1' towards a more dynamic configuration" [p. 7 in (*21*)].
21. N. Rosenberg, in *Knowledge for Inclusive Development*, P. Conceição, D. V. Gibson, M. V. Heitor, G. Sirrilli, F. Veloso, Eds. (Quorum Books, Westport, CT, 2002), chap. 1.
22. High-Level Expert Group, *Frontier Research: the European Challenge* (Directorate General for Research, EC, Brussels, 2005).
23. ERC, http://erc.europa.eu/.
24. W. Krull, H. Nowotny, *Science* **306**, 941 (2004).
25. More recently, the ERC introduced two more schemes: the Synergy Grant and the Proof-of-Concept grant.
26. IDEAS is one of four main program lines of FP7: "The objective … is to reinforce excellence, dynamism and creativity in European research and improve the attractiveness of Europe for the best researchers from both European and third countries … by providing a Europe-wide competitive funding structure, in addition to and not replacing national funding, for 'frontier research' executed by individual teams"; http://cordis.europa.eu/fp7/ideas/home_en.html.
27. During the 7th FP, ERC's budget was €7.51 billion (U.S. $9.76 billion); http://erc.europa.eu/facts-and-figures.
28. EURECIA is an international research project funded by the ERC, grant no 229286; www.eurecia-erc.net.
29. G. Laudel, J. Gläser, The ERC's impact on the grantees' research and their careers (Work package 4 (WP4) report, EURECIA, 2012); www.eurecia-erc.net/wp-content/upLoads/EURECIA-ImpactOnResearchContentAndCareers-SummaryReport.pdf.
30. D. Thomas, M. Nedeva, Survey of starting independent researchers (EURECIA, WP3 Summary Report, 2011); www.eurecia-erc.net/wp-content/upLoads/EURECIA-SurveyOfStartingIndependentResearchers.pdf.
31. J. Edler *et al.*, *Impact of the ERC on Universities and Public Research Organisations* (EURECIA, 2012); www.eurecia-erc.net/wp-content/upLoads/EURECIA-ImpactOnResearch-Organisations.pdf.
32. T. Luukkonen, *The Impact of the ERC on National Funding Bodies* (EURECIA, 2012); www.eurecia-erc.net/wp-content/upLoads/EURECIA-ImpactOnNationalFunders-Final.pdf.
33. T. Luukkonen, *The ERC and the European Research Funding Landscape* (EURECIA, 2012); www.eurecia-erc.net/wp-content/upLoads/EURECIA-ImpactOnEuropeanFunding-Landscape-Final.pdf.

10.1126/science.1216878

DEVELOPMENT

Pushing Your Back into Place

Establishment of the dorsal-ventral body axis during fly oogenesis depends on pushing forces provided by polymerizing microtubules.

Bruce Bowerman and Sean M. O'Rourke

In multicellular animals, the localization of specific molecules to some but not other cells during development defines three body axes: anterior-posterior (AP; head to tail), dorsal-ventral (DV; back to belly), and left-right. On page 999 of this issue, Zhao *et al.* (*1*) describe an elegant application of live-cell imaging to investigate molecular polarity and body axis establishment in the fruit fly *Drosophila melanogaster*. Their insights debunk a long-standing linkage between the mechanisms that establish the AP and DV body axes, and illuminate a new role for microtubule polymerization pushing forces.

The fruit fly AP and DV body axes are established during oogenesis, through polarization of an oocyte (*2*, *3*). The effector molecules and mechanisms that specify these axes are well understood, but how the molecules are initially localized in the oocyte has not been clear. Oogenesis occurs within ovarioles, with ~18 of these egg production tubes forming each of the two ovaries (*2*, *3*). Ovarian and follicular stem cells at the anterior end of each ovariole produce oocyte and somatic follicle cell precursors. An oocyte precursor undergoes four cellular divisions, generating an egg chamber with 16 cells connected by ring canals: one cell becomes the oocyte while the others become nurse cells. Nurse cell contents are transported through the ring canals into the oocyte, which enlarges during maturation (see the figure). Proliferating follicle cells produced by the follicular stem cells surround each egg chamber.

The origins of the AP and DV body axes during *Drosophila* oogenesis require a relay of signals. One early signal from the oocyte instructs adjacent follicle cells to adopt a posterior fate. Subsequently, these posterior follicle cells signal back to the oocyte to reorganize the microtubule cytoskeleton (*2*, *3*). Microtubules are polarized polymers in which one end (minus end) is stable and does not grow, while the other (plus end) is dynamic and grows or shortens through the addition or subtraction of tubulin subunits. Before generation of the posterior follicle cell signal, oocyte microtubules are organized with their minus ends abutting the posterior surface (cortex) of the oocyte, and their growing plus ends extend through ring canals into the nurse cells. This early network of polarized microtubules facilitates the transport of macromolecules from the nurse cells into the oocytes, with force and cargo delivery provided by the microtubule motor protein dynein. In response to the posterior follicle cell signal, microtubule minus ends disappear from the posterior cortex and eventually reappear at the anterior and lateral oocyte cortex, while new plus ends become enriched at the posterior oocyte cortex. Plus end– and minus end–directed motor proteins then transport two key messenger RNAs (mRNAs), one to each pole of the oocyte. After fertilization, the proteins encoded by these two mRNAs establish anterior and posterior cell fates and hence the AP axis (*4*).

Reorganization of microtubules triggers another key event in axis formation: migration of the oocyte nucleus to the peripheral anterior cortex. Subsequently, the nucleus generates a signal that specifies dorsal follicle cell fate (*5*, *6*). Because inactivation of dynein results in mispositioning of the oocyte nucleus, the dogma has been that dynein motors, through their association with the nuclear envelope, pull the oocyte nucleus to an anterodorsal site as they move along polarized microtubules (*7*, *8*). In this view, establishing the AP and DV axes depends on the same polarized microtubules that are oriented by the posterior follicle cell signal. However, mislocalization of the oocyte nucleus in dynein mutants was observed in late-stage oocytes, and nuclear position at the time of migration had not previously been reported.

Zhao *et al.* conducted live-cell examination of oocyte nuclear migration and microtubule dynamics using spinning-disk confocal microscopy and transgenic fly strains that express fluorescent protein fusions. They observed that in an oocyte, a microtubule organizing center (MTOC), which nucleates microtubule polymerization, is positioned posterior to the oocyte nucleus before its migration. Microtubule plus ends grow out from the MTOC and push on the nucleus. These pushing forces produce substantial "dents" in the oocyte nucleus that cannot be explained by microtubule minus end–directed dynein pulling forces acting from the oocyte nuclear envelope. Indeed, the dent positions correlate precisely with the MTOC's position

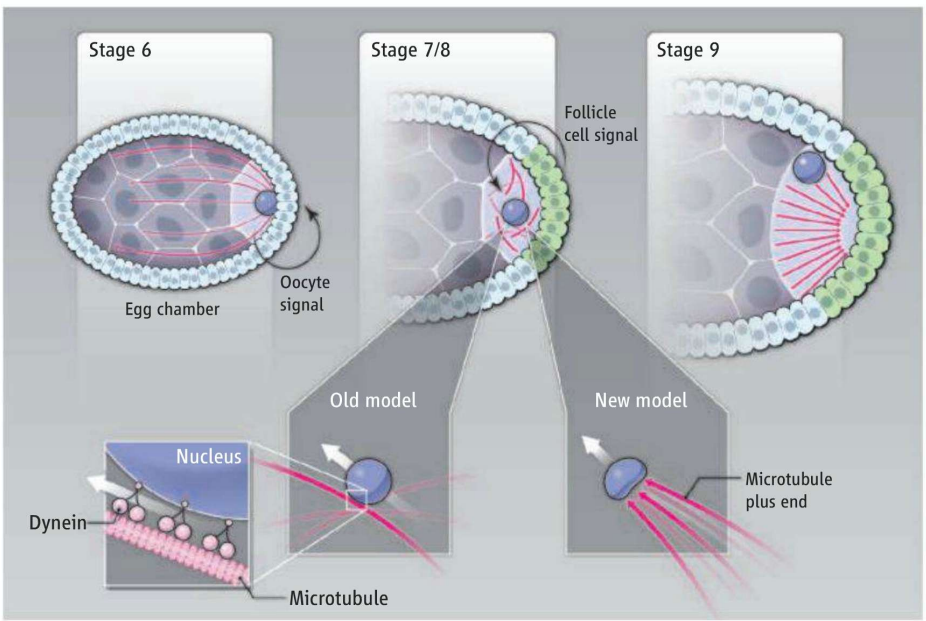

Pushing forces. (**Top**) At stage 6 of *Drosophila* oogenesis, a signal from the oocyte specifies the follicle cells to adopt a posterior fate (green). A signal from the posterior follicle cells to the oocyte (stages 7 and 8) induces reorganization of the oocyte microtubule cytoskeleton such that microtubule polarity is reversed by stage 9. (**Bottom**) One model shows oocyte nuclear migration mediated by the microtubule motor protein dynein. In the model of Zhao *et al.*, forces are provided by microtubule polymerization posterior to the oocyte nucleus.

CREDIT: Y. HAMMOND/SCIENCE

Institute of Molecular Biology, University of Oregon, Eugene, OR 97403, USA. E-mail: bbowerman@molbio.uoregon.edu

and the direction of nuclear movement, and laser ablation of the MTOC eliminates both the dents and movement.

Presumably, MTOC-nucleated microtubules that reach the posterior cortex contribute to the pushing forces and maintain MTOC proximity to the moving nucleus. The precise path taken by the nucleus in an oocyte is somewhat random, but the geometry of the oocyte ensures that these pushing forces ultimately move the nucleus to a peripheral site at the anterior oocyte cortex. Zhao *et al*. also found that nuclear migration is normal in mutant oocytes lacking dynein function. Mislocalization of the oocyte nucleus in these mutants later in oogenesis indicates that dynein anchors the nucleus after it arrives, but does not do the moving.

These results of Zhao *et al*. show that establishment of the DV and AP axes is not linked through a common dependence on the same polarized microtubules. Indeed, as first suggested by an earlier study (*9*), the MTOC that organizes the pushing forces may mediate the reversal of microtubule polarity that occurs in response to the posterior follicle cell signal and is required for proper localization of the anterior and posterior determinant mRNAs. Thus, DV may even precede AP axis formation. These results also provide an intriguing example of how microtubule polymerization can generate functionally important pushing forces within a cell.

The identity of the follicle cell signal that induces oocyte nuclear movement and microtubule reorganization remains unknown. Also not clear is the dynamic organization of microtubules within the developing oocyte. The further application of live-cell imaging—in particular, the tracking of microtubule plus end growth—may provide clarity. Seeing is believing, especially when done over time in a living tissue.

References

1. T. Zhao *et al*., *Science* **336**, 999 (2012); 10.1126/science.1219147.
2. S. Roth, J. A. Lynch, *Cold Spring Harb. Perspect. Biol.* **1**, a001891 (2009).
3. J. Steinhauer, D. Kalderon, *Dev. Dyn.* **235**, 1455 (2006).
4. D. St Johnston, C. Nüsslein-Volhard, *Cell* **68**, 201 (1992).
5. A. González-Reyes *et al*., *Nature* **375**, 654 (1995).
6. S. Roth *et al*., *Cell* **81**, 967 (1995).
7. J. E. Duncan, R. Warrior, *Curr. Biol.* **12**, 1982 (2002).
8. J. Januschke *et al*., *Curr. Biol.* **12**, 1971 (2002).
9. J. Januschke *et al*., *Development* **133**, 129 (2006).

10.1126/science.1223141

BIOCHEMISTRY

Guided Tour to the Heart of RISC

The crystal structures of human and yeast Argonaute proteins reveal the intricacies of the multidomain enzyme at the hub of the RNA interference machinery.

Emine Kaya[1] and Jennifer A. Doudna[1,2,3,4]

How do eukaryotic cells use small RNAs to control the expression levels of proteins? The answer is of interest both to basic researchers and to those harnessing RNA interference (RNAi) pathways for therapeutic applications. As laboratories around the world have steadily uncovered the complex network of RNAi components, Argonaute (Ago) proteins emerged early on as key players within a complex machinery that exists in all RNAi-competent cells. On page 1037 of this issue, Schirle and MacRae report the crystal structure of human Argonaute2 (Ago2), the flagship member of this class of multidomain enzymes (*1*). Together with a recently reported structure of an Argonaute protein from the budding yeast *Kluyveromyces polysporus* (*Kp*Ago) (*2*), this work provides an exciting glimpse into the core of the molecular pathway for small RNA-mediated gene regulation and fundamental insights into structural evolution of RNAi in eukaryotes.

The function of Ago2 is straightforward: Upon binding to a small RNA molecule (21 to 23 nucleotides in length), Ago2 uses this RNA to target a messenger RNA (mRNA) bearing a complementary target sequence, triggering mRNA degradation. But determining just how Ago proteins achieve this feat has proven much more challenging, and the story gains more complexity with every chapter. Multiple kinds of Ago proteins are present in cells, many different small RNA guide molecules can bind to them, and (depending on the type of guide RNA used) the degradation of the targeted mRNA may or may not involve translational repression.

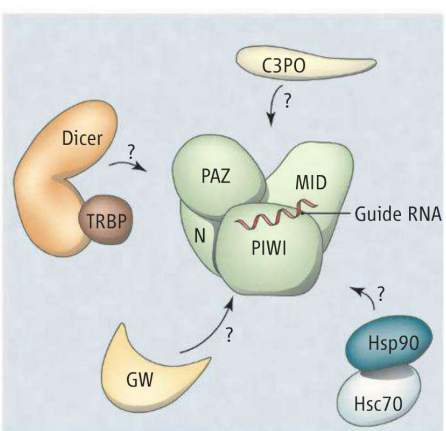

Ago2 and its binding partners. The Ago2 protein is the key player during RNAi pathways. Its multidomain architecture, comprising the N-terminal (N), PAZ, MID, and PIWI domains, enables the protein to recruit a large number of protein partners. The Ago2 crystal structure presented by Schirle and MacRae will help to shed light on this hitherto depictive picture of RNAi network and unravel the interaction with Dicer/TRBP, the Hsc70-Hsp90 chaperon complex, C3PO, GW proteins, and many other binding partners. (Protein sizes are not to scale).

Human cells produce eight Ago proteins with different expression profiles and substrate specificities. These protein variants can be divided into two subfamilies: the Ago subfamily and the Piwi subfamily. Expression of Piwi proteins is mostly restricted to male germ cells and is important for germline stability and repression of mobile DNA elements (called transposons). In contrast, the Ago subfamily is ubiquitously expressed. Each Ago protein can bind to a distinct type of small regulatory RNA, resulting in the formation of different RNA-induced silencing complexes (RISCs). In some organisms, such as fruit flies, Ago2 typically binds to guide sequences called short interfering RNAs (siRNAs) and catalyzes mRNA target destruction by direct endonucleolytic cleavage (slicing). Human proteins Ago1 to Ago4 typically associate with micro RNAs (miRNAs) and mediate translational repression of target mRNAs in the absence of endonucleolytic cleavage. However, human Ago2 also binds siRNAs and can directly cleave target RNAs that are perfectly complementary to the siRNA guide.

In all of its guises, RNAi is a complex network in which Ago2 serves as a platform for recruiting and interacting with numerous other proteins. For example, loading of Ago2 with an RNA guide requires formation of a RISC-loading complex (RLC) that includes,

[1]Department of Molecular and Cell Biology. [2]Howard Hughes Medical Institute, University of California, Berkeley, CA 94720, USA. [3]Department of Chemistry, University of California, Berkeley, CA 94720, USA. [4]Physical Biosciences Division, Lawrence Berkeley National Laboratory, Berkeley, CA 94720, USA. E-mail: doudna@berkeley.edu

at a minimum, Ago2, the enzyme Dicer, and a double-stranded RNA binding protein such as TRBP (see the figure). Other proteins, such as the chaperone complex Hsc70-Hsp90 (*3*) or C3PO (*4*), are also recruited by Ago2 and accelerate RISC-loading or increase turnover rates, respectively. Most notably, Ago2 recruits glycine-tryptophan (GW) proteins, the key players of miRNA-mediated translational repression and mRNA degradation, to the mRNA transcript.

How are Ago proteins able to recruit such an impressive number of binding partners? How does the cell regulate these events? These key questions can now be addressed more directly based on the crystal structures of human Ago2 and *Kp*Ago as well as previous work on Ago homologs. Past crystal structures of archaeal and bacterial Argonaute proteins (*5*–*7*), together with crystal structures of eukaryotic Ago2 domains (*8*, *9*), revealed two lobes in the protein's architecture and a multidomain conformation (see the figure). Similar to these earlier structures, human Ago2 has four domains in which the N-terminal and PAZ domains form one lobe and the MID and PIWI domains form the second lobe. The PAZ domain binds the 3′ end of the guide RNA, while the MID domain provides a binding pocket for the 5′-terminal phosphate group of the guide. Furthermore, both biochemical and structural studies have revealed a crucial role for the PIWI domain in slicing. The crystal structure of *Kp*Ago shows that the slicing activity is regulated by conformational changes of Ago upon guide loading. This rearrangement leads to formation of a catalytic tetrad in the enzyme's active site and allows endonucleolytic activity. Interestingly, a similar and presumably induced rearrangement of the active site can be seen in the structure of human Ago2, suggesting this as a regulatory mechanism for RISC specificity.

Although their overall architectures are similar to those of their archaeal and bacterial counterparts, the human Ago2 and *Kp*Ago crystal structures are a key step toward a complete structural and mechanistic understanding of RNAi pathways. These crystal structures open the way for designing synthetic RNAs or potent small molecules as new drugs for efficient RNAi-based therapies. It will now be possible to map mutations and interaction surfaces onto protein structures with established biochemical functions. The first hints of the insights that will be forthcoming are from experiments by Schirle and MacRae to elucidate the nature of human Ago2 binding to tryptophan, in an effort to mimic binding to tryptophan-rich GW proteins. The interaction between Ago2 and GW proteins, which is essential for efficient and robust mRNA silencing (*10*, *11*), is an attractive target for potential manipulation of gene silencing efficiency. For example, it might be possible to design therapeutic peptides or small molecules to compete with GW protein binding and thereby inhibit downstream processes. Future research can now build upon a solid structural foundation to define the molecular mechanisms that enable cells to use RNA for the control of protein expression levels.

References

1. N. T. Schirle, I. J. MacRae, *Science* **336**, 1037 (2012).
2. K. Nakanishi, D. E. Weinberg, D. P. Bartel, D. J. Patel, *Nature* (2012); 10.1038.nature11211.
3. S. Iwasaki *et al.*, *Mol. Cell* **39**, 292 (2010).
4. X. Ye *et al.*, *Nat. Struct. Mol. Biol.* **18**, 650 (2011).
5. J. J. Song *et al.*, *Science* **305**, 1434 (2004).
6. Y. Wang *et al.*, *Nature* **456**, 921 (2008).
7. Y. R. Yuan *et al.*, *Mol. Cell* **19**, 405 (2005).
8. A. Boland *et al.*, *Proc. Natl. Acad. Sci. U.S.A.* **108**, 10466 (2011).
9. F. Frank *et al.*, *Nature* **465**, 818 (2010).
10. J. E. Braun *et al.*, *Mol. Cell* **44**, 120 (2011).
11. M. R. Fabian *et al.*, *Nat. Struct. Mol. Biol.* **18**, 1211 (2011).

10.1126/science.1223549

BIOCHEMISTRY

Resolving Some Old Problems in Protein Crystallography

Two methods improve the quality and ease of structural modeling by showing how to include diffraction data that are often thrown away.

Phil Evans

Scientific conclusions should be supported by the observed data. However, in x-ray crystallography, the raw diffraction data are rather remotely connected to the final coordinates of the molecule because the experimental data undergo a Fourier transform during the analysis. Thus, any individual feature of the structural model—where a particular atom is located—depends on all of the measured diffraction intensities. Also, the phase information essential for this reconstruction is lost in the experiment (the "phase problem"). Although the coordinate model is repeatedly tested against the data in the course of structure solution, it is common practice to choose what data to use early in the process. Two papers in this issue suggest in different ways that crystallographers have often been excluding useful data from structure determination. On page1030, Karplus and Diederichs (*1*) show that the "resolution" of data sets is frequently underestimated, so that the final model is not as good as it could be. On page 1033, Liu *et al.* (*2*) show that averaging data from multiple crystals can give helpful information for solving the phase problem by using intrinsic sulfur atoms in the protein, circumventing the need to introduce heavier atoms.

The high-resolution diffraction data are found at high scattering angles and give the precise atomic positions in a structure, but in these outer regions of the pattern, the intensity I of diffraction fades away into the background noise because of various disorder effects. A high-resolution cutoff is typically applied to the data, and ideally should be at the point where adding more observations would not add significant information. Unfortunately, this point is hard to estimate.

An obvious criterion is the average signal-to-noise $\langle I/\sigma(I)\rangle$ as a function of resolution. Estimates of the noise term $\sigma(I)$ are generally rather unreliable, but even so, this guide for applying a cutoff is often used. However, another commonly used criterion based on a measure of internal consistency, R_{merge}, is particularly ill-suited to this purpose, despite its widespread use. Diederichs and Karplus point out that R_{merge} cannot be compared with the crystallographic R-factor used to compare observed and calculated data (R_{cryst} or R_{free}), because as the relative error increases with higher resolution, R_{merge} tends to infinity, whereas R_{cryst} tends to a constant value. R_{merge}, or its improved multiplicity-weighted cousin R_{meas} [which the same authors and others introduced some time ago (*3*, *4*)], can be useful as a general guide and for comparison between different data sets, but are not suit-

MRC Laboratory of Molecular Biology, Hills Road, Cambridge CB2 0QH, UK. E-mail: pre@mrc-lmb.cam.ac.uk

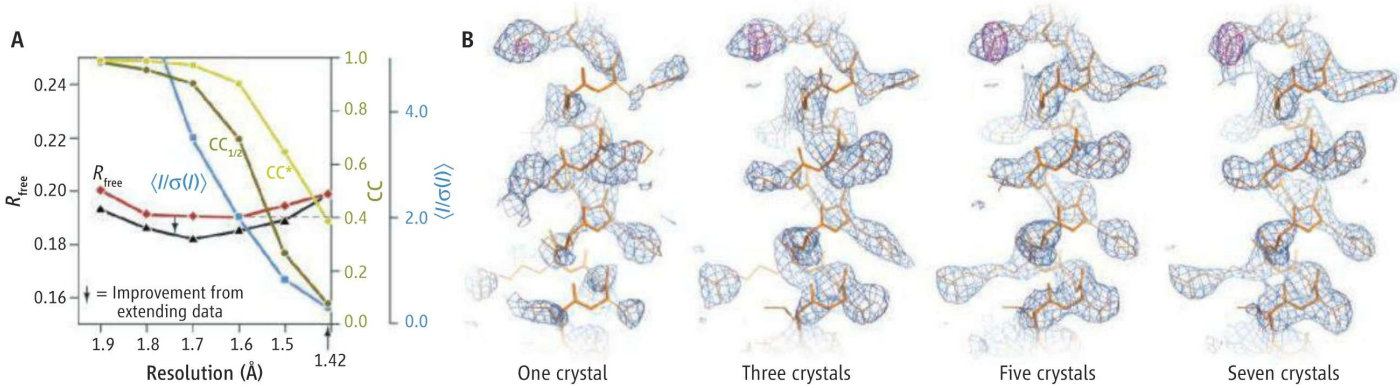

Waste not, want not. Two types of crystallographic data normally thrown away can be put to use. (**A**) Karplus and Diederichs showed that as the resolution of the data is extended, the overall fit between model and observations improved, as measured by R_{free} from paired refinements extending the resolution in steps of 0.1 Å . The red line is R_{free} before extension, and the black line is after extension. The improvement extends to the maximum resolution of 1.42 Å, even though the measures of signal/noise (blue line; dashed line indicates $\langle I/\sigma(I)\rangle = 2.0$) and of internal consistency ($CC_{1/2}$ and CC*, green lines) are getting worse (scale bars on the right). (**B**) Liu *et al*. demonstrate improvement in electron density using phases from S anomalous scattering from increasing numbers of crystals of the protein TorS. Purple contours show Bijvoet-difference (anomalous) density for a methionine S. Thirteen crystals were used, and at least seven were needed to locate the S atoms, so the maps shown for one, three, and five crystals used information only available by using seven or more crystals.

able metrics for deciding the "real resolution."

A better and more reliable measure of internal consistency is the correlation coefficient between two data sets generated by randomly splitting the data into halves, $CC_{1/2}$. Diederichs and Karplus make a strong case that $CC_{1/2}$ provides a good criterion for deciding where to apply a resolution cutoff. Most importantly, they show that the improvement in the fit of the model to the data by adding another shell of data correlates well with $CC_{1/2}$ remaining significantly above zero, based on a series of paired refinements that extend the resolution in steps (see the figure, panel A).

The use of half–data set correlation measures is not particularly new: The idea of splitting observations in half is a very old one in statistics; a similar measure (Fourier shell correlation) has been used in single-particle electron microscopy since the early 1980s [see, for example, (*5*, *6*)]; and its use in x-ray crystallography has been suggested both for assessing anomalous differences [within or between data sets (*7*)] and for the present purpose (*8*, *9*). However, it is encouraging to see here a direct link between data quality and model quality, and CC*, the estimate of the "true" CC derived from $CC_{1/2}$, can be compared directly to a correlation coefficient with data calculated from the model.

The lesson for the crystallographic community is that we should not prematurely exclude too much high-resolution data. Anecdotal evidence suggests that including higher-resolution data can make automated model-building methods work better. There is also a lesson for referees not to complain on the basis of R_{merge}, about authors "overstating the resolution." For the wider community of structure users, we need to wean ourselves from interpreting the nominal resolution of a crystallographic data set as a single number representing the quality and reliability of a structure. Resolution tells us how many observations were used. Although higher resolution will in general be better, the answers we want from a structure are about local conformations, and their correctness cannot be indicated by global scores—neither measures of internal consistency of the data nor of the overall fit of the model to the data.

Hendrickson's group [Liu *et al*. (*2*)] describe an improved approach to the phase problem that uses data from multiple crystals to solve structures, where the phase information comes from the anomalous diffraction from intrinsic sulfur (S) atoms. In the absence of a related model to use for "molecular replacement," the crystallographic phase problem for macromolecules is generally solved by using a few marker atoms heavier than carbon, nitrogen, or oxygen, and measuring their effect on the diffraction pattern, often from their so-called anomalous diffraction. The most common method used at present relies on replacing the native amino acid methionine with engineered selenomethionine, a method introduced earlier by Hendrickson and co-workers (*10*).

In most unmodified proteins, the heaviest atoms are S, but rather few structures have been solved by S anomalous scattering because the very small signal is easily swamped by noise. Although the accuracy of measuring this signal can be improved by measuring several crystals and averaging the results, crystallographers have often shied away from combining data from many crystals because of worries that they may not be the same (nonisomorphous). Liu *et al*. now show that with careful data collection (longish wavelength and avoidance of radiation damage) and cluster analysis to eliminate nonconforming crystals, even quite large proteins with poorly diffracting crystals can be solved just by using the S anomalous signal (see the figure, panel B). This result is of practical importance because introducing traditional heavy atoms, including selenomethionine, can be difficult, whereas almost all proteins contain a reasonable number of S atoms (nucleic acids contain phosphorus, which is equally good). It is commonplace to collect many data sets from equivalent crystals, so combining all of the data together to help the structure solution is worth trying.

Referees and authors alike will need to assess carefully the quality of a structure determination when these two methods are used because the inclusion of weaker, noisier data can give better structures only when used in a statistically robust way. For this reason, it is desirable that referees should be given access to the unmerged diffraction intensities (and preferably the diffraction images) and that these data should be deposited in public databases.

References

1. P. A. Karplus, K. Diederichs, *Science* **336**, 1030 (2012).
2. Q. Liu *et al*., *Science* **336**, 1033 (2012).
3. K. Diederichs, P. A. Karplus, *Nat. Struct. Biol.* **4**, 269 (1997).
4. M. S. Weiss, *J. Appl. Cryst.* **34**, 130 (2001).
5. P. B. Rosenthal, R. Henderson, *J. Mol. Biol.* **333**, 721 (2003).
6. R. Henderson *et al*., *Structure* **20**, 205 (2012).
7. T. R. Schneider, G. M. Sheldrick, *Acta Crystallogr.* **D58**, 1772 (2002).
8. P. R. Evans, *Acta Crystallogr.* **D62**, 72 (2006).
9. P. R. Evans, *Acta Crystallogr.* **D67**, 282 (2011).
10. W. A. Hendrickson, J. R. Horton, D. M. LeMaster, *EMBO J.* **9**, 1665 (1990).

10.1126/science.1222162

PSYCHOLOGY

Kinship and Human Thought

Language and communication are central to shaping concepts such as kinship categories.

Stephen C. Levinson

In 1860, Lewis Henry Morgan heard an Iowa man on a Nebraska reservation describe a small boy as "uncle." Fascinated, he embarked on lifelong research into the kinship systems of the world's cultures, which culminated in a typology of kin categories (see the figure, panel A) (*1*, *2*). Work on kinship categories flourished for a hundred years, but then became unfashionable. Yet, kinship is crucial to the transmission of human genes, culture, mores, and assets. Recent studies have begun to reinvigorate the study of kinship categories (*3*, *4*). On page 1049 of this issue, Kemp and Regier (*5*) explore the relation between observed kinship systems and all possible such systems (the potential "design space"). They suggest that actual kinship systems optimize both ease of conception and communicative import. On page 998 in this issue, Frank and Goodman (*6*) provide an experimentally grounded characterization of communicative optimization.

Kinship is a fertile domain in which to ask a question at the heart of the cognitive sciences: Why do humans have the conceptual categories they do? On the one hand, kinship offers a forest of systems. There are more than 6000 languages, each with a different system of kin classification, at least in detail. On the other hand, kinship has a biological basis, namely the set of primary kin relations: father, mother, spouse or partner, brother, sister, son, and daughter. Each such person has the same set of links, resulting in an indefinitely large network of kin. Languages and cultures reduce these to a much smaller set of categories. In English, a father's brother, mother's brother, mother's sister's husband and father sister's husband are all called "uncles." In other languages, "uncle" may denote kinsmen on only the mother's or only the father's side and can spread over two or more generations, the source of Morgan's fascination (see the figure).

What constrains this exuberant diversity of systems? Murdock collated data from about 500 systems worldwide (*7*), identified half a dozen major types, and showed strong correlations with social organization (see the figure) (*8*). Recently, Jones (*4*) showed systematic principles of merger. For example, more distant relatives tend to get lumped together, as in our category "cousins."

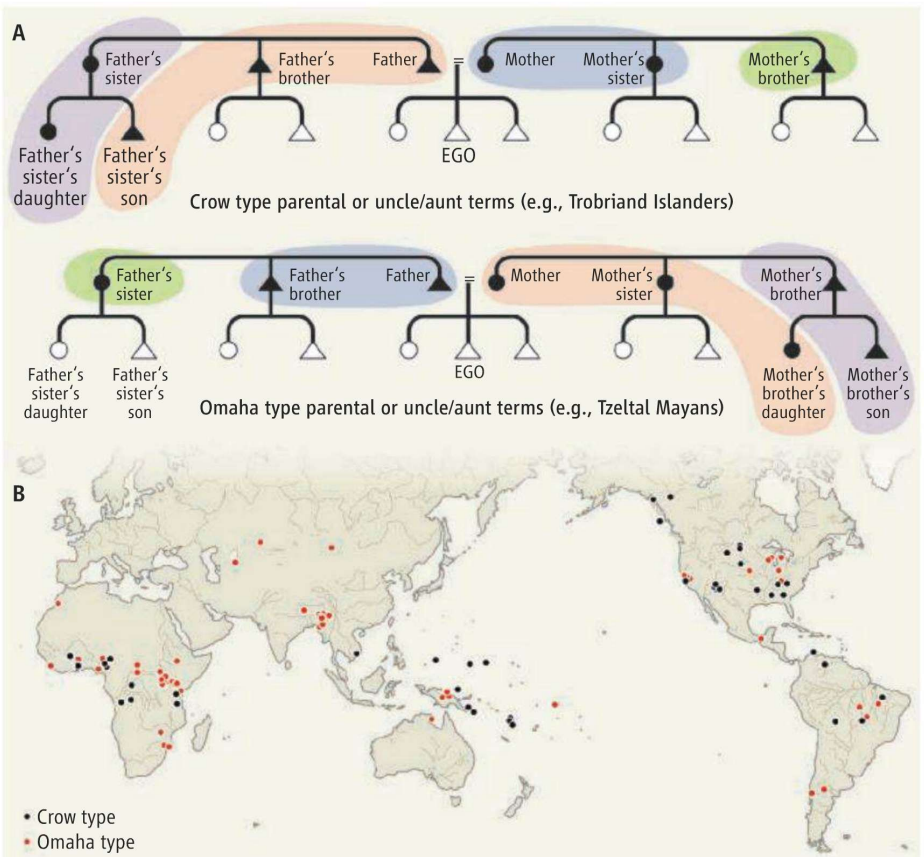

Two inverse types of kin category systems and their worldwide distribution. The world's kinship systems fall into half a dozen major types. For example, the Crow system correlates with matrilineal clans, and the inverse Omaha system with patrilineal ones; the two systems have mirror-image "parental" and "uncle"/"aunt" categories, as color-coded in (**A**). Both systems are found across the world (**B**) (data from 7, *8*). Kemp and Regier argue that intrinsic constraints based on ease of conceptualization and communication determine the observed kinship category systems. However, they are also shaped by social functions and by common descent from earlier cultures.

Using Murdock's data (*7*), Kemp and Regier now show that actual existing kinship systems occur in only a tiny corner of the possible design space. Although 85% of their 487 sample systems have some distinct categories, they all conform to a tendency to balance maximal informativeness (discriminating kin types) while avoiding cognitive complexity. Calculating that there are 10^{55} theoretically possible systems over the 56 relatives they focus on, they show that attested kinship systems cluster in the corner of design space that minimizes both complexity and communicative cost. That is, cultures do not construct kin categories that are hard to define and hard to communicate.

Cognitive psychologists have suggested that categories, for example color concepts (*9*), are formed to maximize within-category similarity and between-category dissimilarity (*10*). However, these studies have downplayed the role of language and communication. Kemp and Regier elucidate the crucial role of communication in shaping our categories.

Frank and Goodman explore the nature of inference in communication. Because the reference of words will often be context-dependent, listeners must combine assumptions of speakers' informativeness with what is salient in the context in order to resolve a

Max Planck Institute for Psycholinguistics, PB 310 Nijmegen 6500AH, and Donders Institute, PB 9104 Nijmegen 6500 HE, Netherlands. E-mail: stephen.levinson@mpi.nl

CREDIT: L. CILISSEN/MAX PLANCK INSTITUTE FOR PSYCHOLINGUISTICS, NIJMEGEN

message. The authors show that listeners follow a precise model of Bayesian inference in making these inferences. Kemp and Regier's model uses corpus frequencies as an analog of saliency. The two approaches are closely connected, sharing an information-theoretic approach to informativeness.

Neither model tells us where our categories come from; they merely place constraints on what is good to think and good to communicate. Here, they could be usefully complemented by another recent line of work in the evolutionary modeling of culture. One approach is experimental and shows how categories get honed through iterated learning across simulated generations (cohorts of participants) (*11*). A second approach uses the computational techniques of biological phylogenetics to extract the historical development of patterning in cultural categories (*12*). This work puts into question the importance of Kemp and Regier's finding that attested kin term systems cluster in a small corner of the potential space. Existing systems may be largely descended from one another in deep historical time (*13*) and reflect patterns of irreversible evolution (*14*). But the study of kinship categories seems set for a revival, for they epitomize the nature of human concepts as biocultural in nature.

References

1. L. H. Morgan, *Systems of Consanguinity and Affinity of the Human Family* (Smithsonian Contributions to Knowledge, Washington, DC, 1871).
2. T. R. Trautmann, *Lewis Henry Morgan and the Invention of Kinship* (Univ. of Nebraska Press, Lincoln, 2008).
3. D. Jones, *Behav. Brain Sci.* **33**, 367 (2010).
4. D. Read, *Ethnology* **46**, 329 (2007).
5. C. Kemp, T. Regier, *Science* **336**, 1049 (2012).
6. M. C. Frank, N. D. Goodman, *Science* **336**, 998 (2012).
7. G. P. Murdock, *Ethnology* **9**, 165 (1970).
8. G. P. Murdock, *Social Structure* (MacMillan, New York, 1949).
9. T. Regier, P. Kay, N. Khetarpal, *Proc. Natl. Acad. Sci. U.S.A.* **104**, 1436 (2007).
10. C. B. Mervis, E. Rosch, *Annu. Rev. Psychol.* **32**, 89 (1981).
11. T. C. Scott-Phillips, S. Kirby, *Trends Cogn. Sci.* **14**, 411 (2010).
12. S. C. Levinson, R. D. Gray, *Trends Cogn. Sci.* **16**, 167 (2012).
13. D. Jones, *Am. Anthropol.* **105**, 501 (2003).
14. F. M. Jordan, *Hum. Biol.* **83**, 297 (2011).

10.1126/science.1222691

PHYSICS

Enter the Majorana Fermion

Electrical measurements on a semiconductor–superconductor hybrid structure reveal the signature of this long-predicted exotic particle.

Piet W. Brouwer

All known fundamental particles are either bosons or fermions. Fermions are subject to the Pauli principle, which forbids two particles being in the same quantum state; bosons, by contrast, tend to bunch together in the same state. The same rule applies to the excitations of most solid-state systems, such as metals and semiconductors, which can be classified as fermionic or bosonic. However, sometimes excitations—quasiparticles—of a fundamentally different type emerge that resemble particles that hitherto have been considered only as a mathematical possibility. On page 1003 of this issue, Mourik *et al.* (*1*) report on a superconducting nanostructure that harbors such an exotic quasiparticle, a "Majorana bound state," an excitation that can best be described as half a fermion. The Majorana bound state is named after the Italian physicist Ettore Majorana, who proposed an equation describing a fermionic particle with a real-valued wave function (*2*). In contrast to the standard (Dirac) fermion, which has a complex wave function, a particle with a real-valued wave function is equal to its own antiparticle. No fundamental particles are known to be Majorana fermions, although there are speculations that the neutrino is one (*3*). The reported bound state is a localized version of Majorana's fermion.

Dahlem Center for Complex Quantum Systems and Institut für Theoretische Physik, Freie Universität Berlin, Arnimallee 14, 14195 Berlin, Germany. E-mail: brouwer@zedat.fu-berlin.de

Mathematically, two Majorana fermions combine into one Dirac fermion, just as two real numbers form a complex number. This is why a Majorana bound state can be considered as a half-fermion. Because the Majorana fermion is its own antiparticle, the Majorana bound state always has zero energy (a particle and its antiparticle have opposite energy ε, so $\varepsilon = 0$ is the only possibility if they are one and the same). Majorana fermions are also intriguing because they are examples of what are called non-Abelian anyons (*4*). These are a particular class of particles whose quantum state can change simply by exchanging particles, unlike standard bosons and fermions, whose exchange does not have measurable consequences. Once they can be controlled and manipulated, non-Abelian anyons are expected to find application in topological quantum computing (*5*, *6*), a radically different computer design that uses the exchange of non-Abelian anyons to perform certain computational tasks.

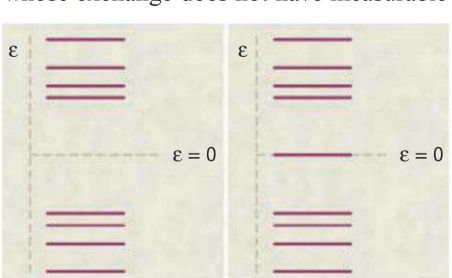

Now you see it. Schematic of the two possibilities of the excitation spectrum of a superconductor. The two spectra are said to be topologically different, because no continuous rearrangement of energy levels can transform one spectrum into the other, while preserving the symmetry of the spectrum. Mourik *et al.* report the creation of a topological superconductor with a spectrum like that of the right panel. The state at zero energy is the Majorana bound state.

Mourik *et al.* build on a series of theoretical proposals, which showed that Majorana bound states can be engineered in nanostructures that combine a superconductor and other materials (*7*–*10*). In this context, an antiparticle is in fact a hole, an excitation that consists of removing an electron from the device. In superconductors the electrons form bosonic Cooper pairs, which then condense into a single quantum state. Superconductors are a natural environment for particles that are their own antiparticle because the Cooper pair condensate blurs the difference between electron-like and hole-like excitations.

Indeed, the theory of superconductivity treats electron-like and hole-like excitations on an equal footing and has all excitations appear as a pair at opposite energies, $\pm\varepsilon$. Particle-hole symmetric (i.e., Majorana) states can occur at $\varepsilon = 0$ only. Once there is a single excitation with energy $\varepsilon = 0$, its existence is said to be topologically protected, because no continuous perturbation can drive it away from its position at $\varepsilon = 0$ (see the figure).

In the experiment of Mourik *et al.*, an InSb wire, a semiconductor with strong spin-orbit coupling, is coated with the superconductor

NbTiN and placed in a large magnetic field parallel to its axis. The number of electrons in the wire is tuned via capacitive coupling to metal gates. At certain electron densities, the combination of the superconducting coating, the strong spin-orbit coupling in the InSb wire, and the magnetic field drive the InSb wire into an unconventional superconducting state that theorists predict has Majorana bound states at its ends (*11*–*13*). Measurement of the density of states at the wire's end reveal a peak at zero energy that persists over a range of electron densities and magnetic fields, consistent with the idea of topological protection. No peak was present if the experiment was repeated without any one of the two crucial ingredients in the theoretical proposals (superconductivity, magnetic field perpendicular to spin-orbit field). Ruling out other known causes for zero-energy states, they interpret their observation as a signature of a Majorana bound state.

The experiment of Mourik *et al*. opens a new direction in a field that so far has been dominated by theory (*4*). Follow-up experiments will strengthen the evidence that the observed zero-bias peak is indeed that of a single Majorana bound state [such as the observation of a quantized tunneling conductance (*14*), which is presently obscured by finite-temperature effects]. Once applied to a network of semiconductor wires, the experimental setup allows for the exchange of Majorana bound states (*15*) and, hence, ultimately for the direct observation of their non-Abelian anyonic nature.

References

1. V. Mourik *et al*., *Science* **336**, 1003 (2012); 10.1126/science.1222360.
2. E. Majorana, *Soryushiron Kenkyu* (Engl. transl.) **63**, 149 (1981) [transl. from *Nuovo Cimento* **14**, 171 (1937)].
3. F. Wilczek, *Nat. Phys.* **5**, 614 (2009).
4. C. Nayak *et al*., *Rev. Mod. Phys.* **80**, 1083 (2008).
5. A. Yu. Kitaev, *Ann. Phys.* **303**, 2 (2003).
6. M. H. Freedman, *Proc. Natl. Acad. Sci. U.S.A.* **95**, 98 (1998).
7. L. Fu, C. L. Kane, *Phys. Rev. Lett.* **100**, 096407 (2008).
8. J. D. Sau *et al*., *Phys. Rev. Lett.* **104**, 040502 (2010).
9. R. M. Lutchyn *et al*., *Phys. Rev. Lett.* **105**, 077001 (2010).
10. Y. Oreg *et al*., *Phys. Rev. Lett.* **105**, 177002 (2010).
11. R. Jackiw, C. Rebbi, *Phys. Rev. D Part. Fields* **13**, 3398 (1976).
12. N. Read, D. Green, *Phys. Rev. B* **61**, 10267 (2000).
13. A. Yu. Kitaev, *Phys. Usp.* **44**, 131 (2001).
14. K. T. Law *et al*., *Phys. Rev. Lett.* **103**, 237001 (2009).
15. J. Alicea *et al*., *Nat. Phys.* **7**, 412 (2011).

10.1126/science.1223302

CANCER

Systems Biology, Metabolomics, and Cancer Metabolism

Constructing metabolic profiles of 60 cancer cell lines by integrating metabolomics and systems biology revealed increased glycine consumption in highly proliferative cancer cells.

Masaru Tomita and Kenjiro Kami

Recent breakthroughs in cancer metabolism include the identification of an alternative glycolytic pathway in proliferative cells (*1*) and an essential role for the serine synthesis pathway in breast cancer (*2*). With a data-driven approach, as opposed to the conventional hypothesis-driven approach, in this issue, on page 1040, Jain *et al*. (*3*) determined that rapidly proliferating cancer cells require large amounts of the nonessential amino acid glycine, which has clear and direct implications for cancer therapy.

Since its emergence, systems biology has primarily been driven by in silico studies rather than experimental data, particularly for the elucidation of metabolic networks (*4*, *5*) with the use of a limited amount of experimental data. Then data-driven systems biology advanced dramatically (*6*), facilitated by the emergence of metabolomics technologies (*7*, *8*). Applied increasingly to elucidate cancer metabolism (*9*), this recent "omics" technology was used by Jain *et al*. in a sophisticated way that combined its advantages with those of a systems biology approach. The authors first used liquid chromatography–tandem mass spectrometry (LC-MS/MS) to measure 219 metabolites in the culture media of 60 human cancer cell lines from the NCI-60 panel. This set of cell lines was derived from nine tissues and has been subjected to a variety of large-scale experiments, including pharmacological characterization in response to more than 100,000 chemical compounds, chromosome karyotyping, and gene expression analysis (*10*). The authors then determined the consumption and release (CORE) profile of each metabolite in the medium to generate an atlas of cancer metabolism. This atlas is a rich community resource for identifying links between a specific metabolic profile and a genotypic or phenotypic context, which could for example be used to uncover cancer-specific weaknesses for exploitation by drugs.

The idea of profiling the metabolic properties of cells by analyzing the metabolome of the culture medium is not new; however, the scale of the study is unprecedented and the metabolomics approach is novel and straightforward. Essentially, the authors treated the intracellular metabolome profile as a black box, and solely analyzed alterations in the extracellular metabolome by means of a simple equation to evaluate the influx/outflux rate of each metabolite in the culture medium.

The authors went on to demonstrate the value of their metabolite CORE analysis by complementing it with doubling time and metabolite gene expression profiles available for the NCI-60 cell line panel and found a strong association between growth rate and glycine demand.

Glycine is produced from serine by serine hydroxymethyltransferase (SHMT); this reaction is mediated by the cofactor tetrahydrofolate (THF), which is generated by methylenetetrahydrofolate dehydrogenase (MTHFD) (see the figure). The authors found that high expression levels specifically of the mitochondrial forms of the enzymes, SHMT2, MTHFD2, and MTHFD1L, but not their cytosolic forms, SHMT1 and MTHFD1, were significantly correlated with the growth rates of the cell lines. They also found that breast cancer patients with above-median expression levels of the mitochondrial forms of these enzymes, but not their cytosolic paralogs, had higher mortality. This fits with the view that changes in mitochondria are a key factor in cancer cell proliferation (*11*, *12*). Intriguingly, the mitochondrial forms of the aforementioned enzymes are known to be highly

Institute for Advanced Biosciences, Keio University, Tsuruoka, Yamagata 997-0035, Japan; Systems Biology Program, Graduate School of Media and Governance, Keio University, Fujisawa, Kanagawa 252-8520, Japan; and Human Metabolome Technologies Inc., Tsuruoka, Yamagata 997–0052, Japan. E-mail: mt@sfc.keio.ac.jp

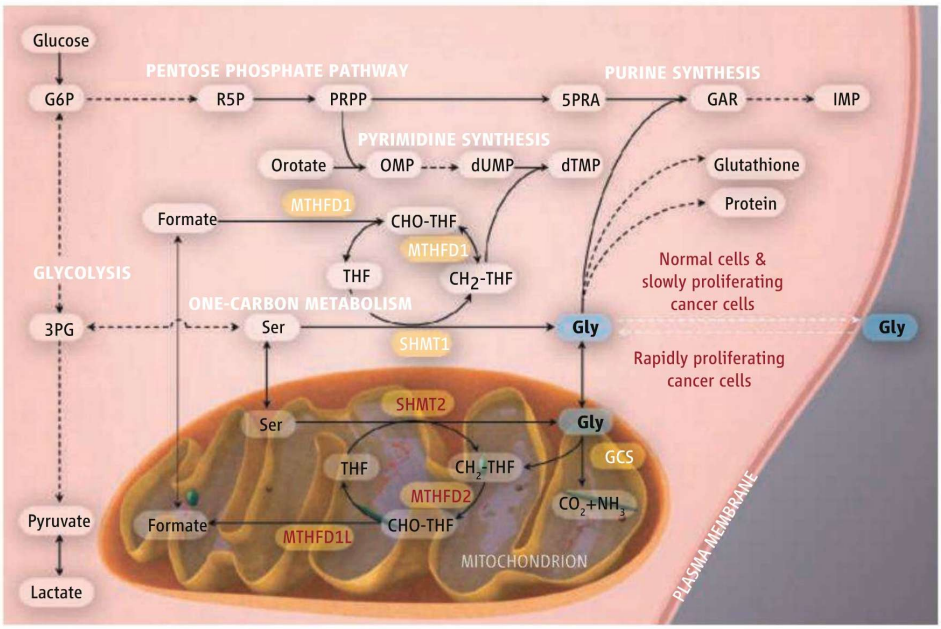

Cytosolic and mitochondrial glycine metabolism. Differences in metabolism in these cellular compartments may aid in targeting cancer therapeutics. 3PG, 3-phosphoglycerate; 5PRA, 5-phosphoribosylamine; CH_2-THF, 5,10-methylenetetrahydrofolate; CHO-THF, 10-formyltetrahydrofolate; G6P, glucose 6-phosphate; GAR, glycinamide ribonucleotide; GCS, glycine cleavage system; IMP, inosine monophosphate; MTHFD, methylenetetrahydrofolate dehydrogenase; PRPP, 5-phosphoribosyl pyrophosphate; R5P, ribose 5-phosphate; SHMT, serine hydroxymethyltransferase; THF, tetrahydrofolate.

expressed not only in transformed cells but also in embryonic cells (*13*).

In contrast to the cancer cell lines, the authors found that rapidly proliferating nontransformed cells, including human bronchial epithelial cells and lymphocytes, release rather than consume glycine. This finding is particularly crucial for cancer therapeutics because it may be possible to target aggressive cancer cells specifically by inhibiting glycine influx, synthesis, or consumption. For example, antifolates such as methotrexate and pemetrexed, which limit one-carbon metabolism involving glycine, have been used for the treatment of lung, breast, and other cancers. The results of Jain *et al*. indicate that analysis of mitochondrial enzyme expression in individual patients can be used to predict drug efficacy and thus improve the quality of personalized therapy. The finding of a tissue-independent yet cancer-specific target makes this especially promising as a drug target.

The authors showed in fast-growing melanoma (LOX IMVI) cells that glycine was consumed in part for de novo synthesis of purines, which are constituents of nucleic acids as well as energy carriers such as adenosine triphosphate and guanosine triphosphate. However, a high influx of glycine may confer additional advantages to proliferative cancer cells. For example, glycine is not only a neurotransmitter but also exhibits cytoprotective effects against hypoxic stress, which is a common condition in solid tumors (*14*). Moreover, activity of the glycine decarboxylase complex, or glycine cleavage system (GCS), plays an important role in promoting tumorigenesis in non–small cell lung cancer (*15*). GCS combines glycine and THF to produce 5,10-methylene-THF (CH_2-THF), which is then used as a building block for pyrimidines (see the figure). Further studies will be required to fully elucidate the effect of increased glycine influx on tumorigenesis.

The results of Jain *et al*. provide insight into the metabolic transformations associated with cancer. In addition, they may aid in the development of targeted cancer therapeutics based on the inhibition of glycine influx, which may be effective against the highly proliferative cancers that are often associated with poor prognosis.

References

1. M. G. Vander Heiden *et al*., *Science* **329**, 1492 (2010).
2. R. Possemato *et al*., *Nature* **476**, 346 (2011).
3. M. Jain *et al*., *Science* **336**, 1040 (2012).
4. M. Tomita *et al*., *Bioinformatics* **15**, 72 (1999).
5. M. W. Covert *et al*., *Nature* **429**, 92 (2004).
6. N. Ishii *et al*., *Science* **316**, 593 (2007).
7. T. Soga *et al*., *J. Proteome Res.* **2**, 488 (2003).
8. L. Coulier *et al*., *Anal. Chem.* **78**, 6573 (2006).
9. A. Hirayama *et al*., *Cancer Res.* **69**, 4918 (2009).
10. J. N. Weinstein, Y. Pommier, *C. R. Biol.* **326**, 909 (2003).
11. T. N. Seyfried, L. M. Shelton, *Nutr. Metab.* **7**, 7 (2010).
12. C. Sakai *et al*., *Biochim. Biophys. Acta* **1820**, 643 (2012).
13. K. E. Christensen, R. E. MacKenzie, *Bioessays* **28**, 595 (2006).
14. J. M. Weinberg, J. A. Davis, M. Abarzua, T. Rajan, *J. Clin. Invest.* **80**, 1446 (1987).
15. W. C. Zhang *et al*., *Cell* **148**, 259 (2012).

10.1126/science.1223066

PHYSIOLOGY

An Avian Magnetometer

Michael Winklhofer

Neurons in the pigeon brain encode information on Earth's magnetic field for orientation and navigation.

Homing pigeons have remarkable navigational skills that allow them to find their way back to the loft when released from an unfamiliar location hundreds of miles away. To perform such a feat, they rely on various cues, such as odors and Earth's magnetic field (*1*, *2*). Yet, how birds and other animals obtain magnetic-field information has been a mystery. On page 1054 of this issue, Wu and Dickman (*3*) report how this information is neurally encoded and suggest a candidate magnetic sensory organ in the inner ear of the pigeon (*4*).

The prevailing model of avian magnetoreception postulates two magnetic sensory structures: one in the eye that delivers a magnetic reference direction (*5*), and the other in the upper beak to measure magnetic-field intensity as input for the navigational map (*6*). Strong evidence for this dualism from electrophysiology is missing, however. Early attempts to measure the electrical activity of candidate magnetic sensory neurons from the beak (*7*) were limited by the equipment and could not be conducted systematically enough to obtain internally consistent results.

Wu and Dickman recorded electrical activity from more than 300 neurons in a region of the pigeon brain stem that receives sensory input from the inner ear (lagena) (*4*). Of these neurons, 16% showed systematic variations in their firing rates as a function

Department of Earth and Environmental Sciences, Ludwig-Maximilians University, Munich, Germany. E-mail: michael@geophysik.uni-muenchen.de

CREDIT: (MITOCHONDRIA) THINKSTOCK

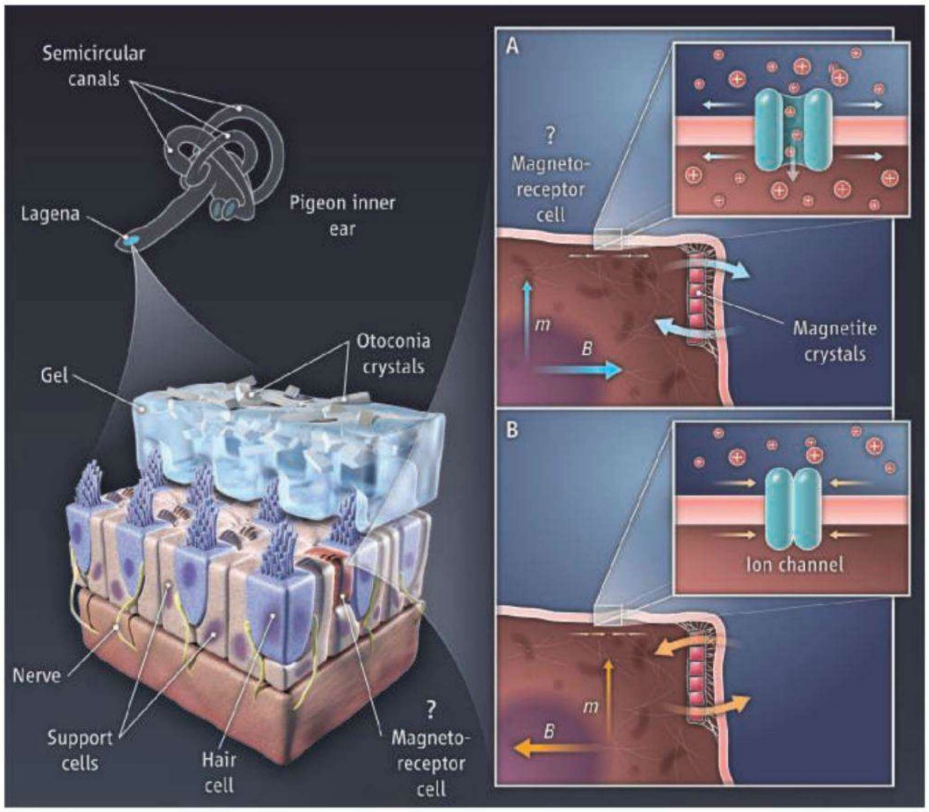

Magnetoreception. The lagena in the inner ear is a candidate site of the magnetic sensory organ in the pigeon. (Left) Schematic view of the lagena otolith composed of a gelatinous membrane loaded with otoconia crystals; vestibular hair cells, with attached nerve fibers; supporting cells; and a hypothetical magnetoreceptor cell. (Right) A chain of magnetite crystals acting as a permanent magnet (with dipole moment *m* indicated by arrow) is the key component in a transduction model in which ion channels gate the inflow of extracellular ions in response to the local membrane tension and thereby modulate the electric potential across the membrane. (**A**) External magnetic field *B* parallel to the direction of maximum stimulation produces a clockwise force couple (pair of arrows) that twists the top of the magnet in one direction, thereby stretching the membrane to open ion channels, which enhances the firing rate. (**B**) Field of opposite polarity produces counterclockwise force couple, which closes the channels and reduces the firing rate.

of both vector orientation and intensity of an applied Earth-strength magnetic field. The authors found that the firing rate of individual neurons encodes the direction and intensity of Earth's magnetic field through the scalar projection of the applied magnetic-field vector onto the preferential direction of stimulation. Such a projection is also measured by most kinds of technical magnetic-field sensors, and it requires three orthogonally mounted sensors to obtain an instantaneous measurement of the full vector.

Could a pigeon similarly orient by the magnetic field on the basis of just three sensors, each tuned along a different direction? Perhaps, but the accuracy of each sensor reading would be limited by intrinsic noise. Yet, the data of Wu and Dickman strongly suggest that the vestibular brain stem receives a large number of simultaneous readings of different projections of the field vector, so that the brain with its parallel processing capacity can obtain a precise representation of the instantaneous field vector. This task is similar to, yet mathematically simpler than, reconstructing the three-dimensional geometry of an object from slightly blurred images taken from a number of different angles.

Why would pigeons need magnetic sensors with two complementary functions in the eye and beak, when the sensors in the inner ear apparently can do both jobs simultaneously? Experimental support for the magnetic eye-beak dualism exists for songbirds (*5*, *8*), but not for pigeons. After all, the ancestors of songbirds and pigeons split at least 55 million years ago (*9*), allowing plenty of time for independent evolution. A putative magnetoreceptor structure in the upper beak skin of pigeons was considered a highly conserved feature also among songbirds and the phylogenetically even more distant domestic chicken (*10*). However, the very structures in the pigeon beak skin are not neuronal, but simply macrophages loaded with iron minerals (*11*).

Wu and Dickman also provide important hints about the location and properties of candidate magnetoreceptor cells. The neurons that they studied encode magnetic polarity, which implies that permanently magnetized material such as single-domain magnetite (Fe_3O_4) is involved in the primary detection process. This should spur efforts to search for magnetic cells in the lagena, an otolith organ of the inner ear (see the figure) that is common to all vertebrates except live-bearing mammals.

Although otoliths normally detect acceleration in the vestibular system, the role of the lagena in birds is not yet clear. Iron, among other trace elements in lagena otholiths, has been implicated in magnetic sense (*12*). However, the iron appears to be simply incorporated as a paramagnetic impurity in the otoconia crystals made of calcite ($CaCO_3$). Magnetite crystals would be suitable for magnetic-field detection if connected to mechanosensitive ion channels in the membrane of a receptor cell, but not when embedded in the otoconia layer (*13*). It may be that the magnetoreceptor cells are dispersed in the hair cell layer of the otolith, similar to the candidate magnetoreceptor cells in the olfactory epithelium of fish (*14*). These fish cells have distinct crystalline inclusions in the form of permanent magnets, most likely single-domain magnetite (*15*).

There are more challenges ahead, such as physiological characterization of candidate magnetoreceptor cells and identification of the neuronal levels at which magnetic and motional information are integrated and tied to the mental representation of the geomagnetic landscape. The findings of Wu and Dickman pave the way for revealing more magnetic secrets from the avian brain.

References

1. R. Wiltschko, W. Wiltschko, *Magnetic Orientation in Animals* (Springer, Berlin, 1995).
2. A. Gagliardo, P. Ioalè, M. Savini, M. Wild, *J. Exp. Biol.* **212**, 3119 (2009).
3. L.-Q. Wu, J. D. Dickman, *Science* **336**, 1054 (2012); 10.1126/science.1216567.
4. L.-Q. Wu, J. D. Dickman, *Curr. Biol.* **21**, 418 (2011).
5. M. Zapka *et al.*, *Nature* **461**, 1274 (2009).
6. C. V. Mora, M. Davison, J. M. Wild, M. M. Walker, *Nature* **432**, 508 (2004).
7. P. Semm, R. C. Beason, *Brain Res. Bull.* **25**, 735 (1990).
8. D. Heyers, M. Zapka, M. Hoffmeister, J. M. Wild, H. Mouritsen, *Proc. Natl. Acad. Sci. U.S.A.* **107**, 9394 (2010).
9. A. Feduccia, *Science* **267**, 637 (1995).
10. G. Falkenberg *et al.*, *PLoS ONE* **5**, e9231 (2010).
11. C. D. Treiber *et al.*, *Nature* **484**, 367 (2012).
12. Y. Harada, *Acta Otolaryngol.* **128**, 432 (2008).
13. M. Winklhofer, J. L. Kirschvink, *J. R. Soc. Interface* **7**, (suppl. 2), S273 (2010).
14. M. M. Walker *et al.*, *Nature* **390**, 371 (1997).
15. C. E. Diebel, R. Proksch, C. R. Green, P. Neilson, M. M. Walker, *Nature* **406**, 299 (2000).

10.1126/science.1223786

CREDIT: C. BICKEL/SCIENCE

IBI* SERIES WINNER

Learning Biology by Recreating and Extending Mathematical Models

Dynamics of Biological Systems, the IBI Prize–winning module, brings mathematics into the biology laboratory.

Hillel J. Chiel,[1,2,3]† Jeffrey P. Gill,[1] Jeffrey M. McManus,[1] Kendrick M. Shaw[1]

Biological systems are dynamic. Proteins fold into three-dimensional shapes to serve as catalysts, motors, or regulators. A fertilized egg divides exponentially, and gradients and internal cell states choreograph fetus formation. Neurons become active or are inhibited in shifting spatial and temporal patterns as an animal moves through its environment. Flocks of birds migrate together, and schools of fish form and disperse to avoid predators and forage for food. The only constant in biological systems is change.

Although biological systems generate beautiful patterns that unfold in space and time, most students are taught biology as static lists of names. Names of species, anatomical structures, cellular structures, and molecules dominate, and sometimes overwhelm, the curriculum and the student. Cookbook labs may demonstrate advanced techniques but have a foregone conclusion. Not surprisingly, students often conclude that biology is boring.

In contrast, students who participate in research discover that biological systems can be understood by developing a "feeling for the organism," a qualitative sense of the system (*1*). Successful students learn the skill of asking the right question with the right technique to find the key elements that make biological systems work.

Can biology be taught by focusing on unfolding patterns in space and time? Can one also reach students who are repelled by details; are more comfortable with abstractions and clear principles; and who often become mathematicians, physicists, or engineers? The divide between the cultures of biology and the more quantitative sciences is unfortunate because interdisciplinary opportunities are expanding. Engineers are fascinated by self-assembling, self-repairing, and self-replicating nanomachines (*2*), exemplified by proteins. How can these nanomachines be combined into cell-like modular reorganizing components? What is the basis for multifunctional designs that allow biological organisms to use the same neural control and periphery to flexibly switch among multiple behaviors (*3*)? How do many agents use distributed computing and cooperation to solve common goals (*4*)? Can we further enhance evolutionary algorithms (*5*) to solve otherwise intractable problems? Life is an alien technology whose mastery would create novel approaches to hard problems.

CREDIT: JEFFREY P. GILL

Classroom setup. Each of the six hexagonal tables in the classroom has power outlets and connections to the CWRU fiber optic network for students' laptops.

These considerations are the basis for the inquiry-based module Dynamics of Biological Systems, developed at Case Western Reserve University (CWRU) (*6*, *7*). The module's learning goals are as follows: construct and extend mathematical models of biological phenomena, analyze these models using the concepts and tools of nonlinear dynamical systems theory, and write clearly about the modeling process and the results obtained from the model.

During the module's first half, students work in teams (see the photo) to solve increasingly complex problems by creating mathematical models using a programming language (*Mathematica*) and to analyze these models using nonlinear dynamical systems theory. After being shown how to find modeling papers, each team selects a peer-reviewed paper that describes a mathematical model of a biological system. They spend the second half of the module using the skills gained in the first half to reconstruct, analyze, and then modify and extend the published model. At the module's end, each student submits a final term paper (*7*).

Biology students develop an intuition for mathematical descriptions of biological phenomena and how to program them as they work on concrete biological problems and systems. Engineers see how the details of a biological system can be fit together into a quantitative model that can be analyzed mathematically, which helps them master biological complexity. The course provides students experience in teamwork, in solving difficult problems that allow them to pursue independent inquiry, and in writing clearly about their results (*7*).

[1]Department of Biology, Case Western Reserve University, Cleveland, OH 44106, USA. [2]Department of Neurosciences, Case Western Reserve University, Cleveland, OH 44106, USA. [3]Department of Biomedical Engineering, Case Western Reserve University, Cleveland, OH 44106, USA.
*IBI, Science Prize for Inquiry-Based Instruction; www.sciencemag.org/site/feature/data/prizes/inquiry/.
†Author for correspondence. E-mail: hjc@case.edu

Students test their hypotheses by manipulating their models and comparing the results with published data or by doing additional mathematical analysis of the model that suggests further biological experiments. Model extensions fall into four general categories: exploring the effects of novel patterns of input to the model; exploring different, biologically based parameter values on the model predictions; changing the form of a model; and identifying and exploring qualitative changes in the dynamics of the model that can be triggered by a small change in parameters (i.e., performing a bifurcation analysis).

The interactive textbook for the course is provided free of charge (http://biol300.case.edu/). All students need a licensed copy of *Mathematica* to use this textbook. If their home institution does not have a *Mathematica* site license, students can purchase a 6-month license for $44.95. Thus, if one assumes that a student has a laptop that can run *Mathematica*, the cost in supplies and other expendables per student is less than $50.

Student assessment, like student progress, is continuous. The instructors talk with team members during class to see the progress they are making on the problems, to provide helpful hints, to evaluate how teammates are interacting with one another, and to ask them questions to determine their level of understanding. After class, the instructors meet to review student progress, providing continuously updated information on how well the students are grasping the material, potential problems in comprehension, and/or friction between teammates.

During the module, students are given attitude and concept assessments (see the charts). At the outset, biology majors have a significantly better attitude toward and sense of competence in biology relative to engineering majors ($P < 0.0001$). At the end of the semester, engineers show a significantly higher view of their competence in computer programming and in biology ($P < 0.006$), and biology majors show a strong trend to feel more competent in computer programming. The entire class shows a highly significant increase in the number of correct answers to the conceptual exam ($P < 0.0001$).

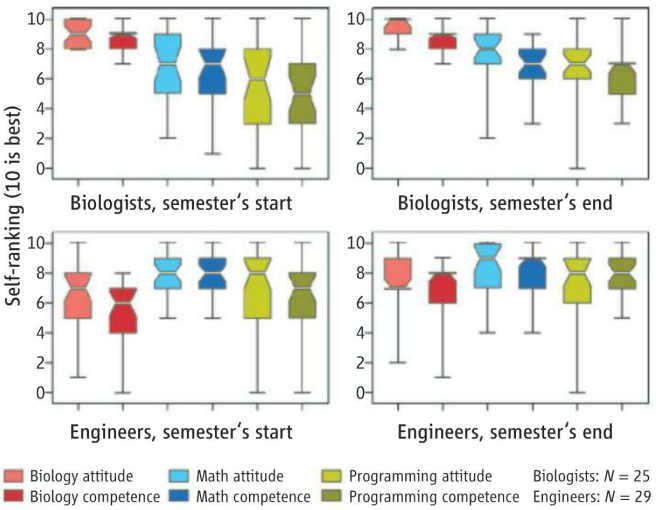

Improved attitudes. Data shown are pooled from the attitudes questionnaire. Results are divided by major and are shown for the beginning and end of the semester. Students rate how much they like and how competent they feel they are in biology, mathematics, or computer programming on a scale from 0 to 10 (best). Box and whisker charts showing (in order): maximum value (top whisker), 75th percentile (top of box), median (white line, location of notch), 25th percentile (bottom of box), and minimum value (bottom whisker).

The module has taught us important lessons about education and students. First, switching from lectures to a continuous progress approach has improved students' comprehension and skill levels. Second, reinforcing material through application is important. Material from the first half of the module provides students the key tools to reproduce, analyze, and extend models. Third, having students rebuild models provides them with the depth of understanding needed to further extend and analyze their models. Indeed, students often find that the original papers have errors, ranging from minor to serious, which are only revealed as they reconstruct the model. This teaches them the importance, and the limitations, of peer review. Fourth, relating assessment directly to the educational goals ensures that students understand the purpose of everything they do. In particular, specific rubrics guide them as they write each component of their term paper. Fifth, assessing and providing feedback on a continuous basis helps students track their current mastery of the material and learn how to master it better. Finally, when instructors and students are allowed to continuously interact as students build a working model, the process creates solidarity and enthusiasm that makes teaching a pleasure.

About the authors

Authors are pictured from left to right. **Hillel J. Chiel** received an English B.A. from Yale University and a Ph.D. from M.I.T. in Neural and Endocrine Regulation and did postdoctoral fellowships in Columbia University's Center for Neurobiology and Behavior and in AT&T Bell Labs Molecular Biophysics Department. He is currently Professor of Biology, Neurosciences, and Biomedical Engineering at CWRU. His research focuses on the neuromechanical basis of adaptive behavior in the marine mollusk *Aplysia californica*. **Kendrick M. Shaw** received his B.S. and M.S. from CWRU in Computer Science, worked for Microsoft, and is currently in the Medical Scientist Training Program at CWRU. He focuses on the mathematical and experimental analysis of pattern generation. **Jeffrey M. McManus** received his B.S. in Biology from CWRU and focuses on the experimental analysis of the neuromechanics of multifunctionality in *Aplysia*. **Jeffrey P. Gill** received his B.S. from CWRU in Systems Biology and studies modeling of biological systems. All three are working on their Ph.D. degrees with Dr. Chiel.

References and Notes

1. E. F. Keller, *A Feeling for the Organism: The Life and Work of Barbara McClintock* (W. H. Freeman, San Francisco, 1983).
2. L. M. Smith, *Nature* **465**, 167 (2010).
3. H. J. Chiel, L. H. Ting, O. Ekeberg, M. J. Z. Hartmann, *J. Neurosci.* **29**, 12807 (2009).
4. M. Dorigo, M. Birattari, *Scholarpedia* **2**, 1462 (2007).
5. K. Deb, *Multi-Objective Optimization Using Evolutionary Algorithms* (Wiley, Chichester, UK, 2001).
6. The latest version of the course Web site is at http://biol300.case.edu/. The course policies, syllabus, and the textbook chapters (as *Mathematica* notebooks) are freely available at this site. Notebooks can be read using the *Mathematica* reader, available at http://www.wolfram.com/products/player/. Student surveys and grades require an official student login and password, and thus are only available to students taking the course.
7. H. J. Chiel, J. M. McManus, K. M. Shaw, *CBE Life Sci. Educ.* **9**, 248 (2010); www.lifescied.org/content/9/3/248.full.

Acknowledgments: H.J.C. is supported by NSF grants DMS-10100434 and IIS-1065489 and J.P.G. by the Graduate Assistance in Areas of National Need program (P200A090191-11). K.M.S.'s training is partially supported by NIH grant T32-GM007250. We gratefully acknowledge the encouragement of the previous Chairs of the Department of Biology at CWRU (N. Rushforth and J. Koonce), the current Chair (C. Cullis), the previous Chair of the Department of Biomedical Engineering, P. Crago, and the helpful feedback and suggestions from the students in the module, who have helped us steadily improve both the module and our teaching.

Supplementary Materials

www.sciencemag.org/cgi/content/full/336/6084/993/DC1

10.1126/science.1214192

PHOTO CREDIT: JEFFREY P. GILL

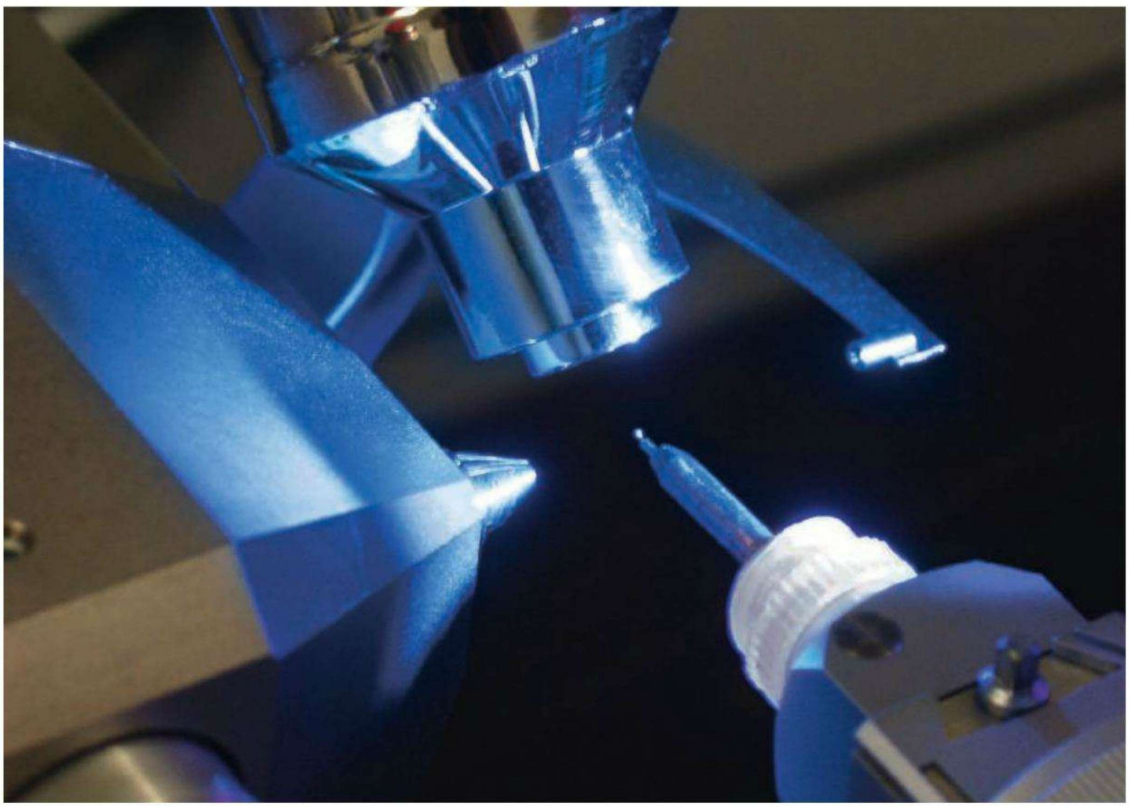

"X-ray diffraction" developed by the industrial company Crelux, partner in the Oncotyrol competence center which carries out intensive cancer research.

Photo: Crelux

Back to the future

Austria is a good place for science – and has been for a long time. Today international companies such as Boehringer Ingelheim or Novartis are working on future solutions in the field of life sciences where the genetics genius Gregor Mendel once conducted research

It all began with a pea plant. In the gardens of the Augustinian monastery Alt-Brünn, Gregor Mendel laid the foundation for modern genetics in 1856 with his crossing experiments. "Mendel's laws" have been a well-known concept until this very day. In the early 20th century Austria already ranked among the leading scientific nations. Today the focus is also on research and development. In 2011 R&D expenditures comprised some 2.8 percent of the gross domestic product, considerably higher than the EU average. In particular, companies in the field of life sciences encompassing pharmaceuticals, biotechnology, medical engineering and cancer research value Austria as a business location. Whoever carries out research pays lower taxes. Moreover, research companies based in Austria are entitled to a research premium of ten percent paid in cash.

EFFICIENT NETWORKS. Institutions such as the Austrian Research Promotion Agency offer numerous funding programs for the benefit of foreign companies. A strong network linking the scientific and business communities leads to synergies enabling the optimal exploitation of potential. Thus the German pharmaceutical group Boehringer Ingelheim coordinates its entire cancer research from Vienna. Another life science hot spot is the Oncotyrol competence center in Innsbruck, Tyrol. About 80 scientists conduct intensive cancer research there – together with partners such as Roche, Merck or Novartis. Within the context of the EU project "Optatio", new strategies are currently being developed against a still incurable bone marrow tumor. "Oncotyrol successfully bridges the gap between research and the commercial development of cancer therapies", says René Siegl, Managing Director of ABA-Invest in Austria, which advises international companies free of charge and provides consulting in setting up business operations in Austria.
www.investinaustria.at

Investments in research

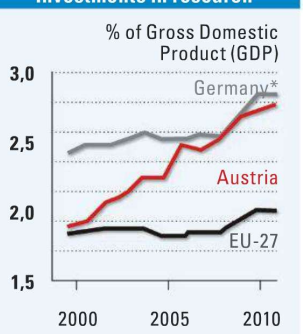

Development of R&D expenditures in Austria, Germany* and the EU-27

*2010 estimated

Source: Eurostat

SCIENCE & DIPLOMACY

A quarterly publication from the AAAS Center for Science Diplomacy

Launched in March 2012, **SCIENCE & DIPLOMACY** provides an open access forum for rigorous thought, analysis, and insight to serve stakeholders who develop, implement, and teach all aspects of science and diplomacy. **SCIENCE & DIPLOMACY** features a mix of original perspectives and research articles by leading science and diplomacy practitioners and thinkers. Learn more about the latest ideas in science diplomacy and receive regular updates by registering for free at **www.sciencediplomacy.org/user/register**.

WWW.SCIENCEDIPLOMACY.ORG

Senior Advisory Board

Norman P. Neureiter (Chair), *AAAS*
Peter C. Agre, *Johns Hopkins*
Nicholas Burns, *Harvard*
David C. Clary, *Oxford and UK FCO*
Paula J. Dobriansky, *Harvard*
Nina V. Fedoroff, *Penn State and KAUST*
Richard N. Foster, *Yale*
David A. Hamburg, *AAAS*
Mohamed Hassan, *IAP*
Neal F. Lane, *Rice*

Science & Diplomacy is published by the Center for Science Diplomacy of the American Association for the Advancement of Science (AAAS), the world's largest general scientific society.

AAAS
ADVANCING SCIENCE. SERVING SOCIETY

SCIENCE POLICY

As U.S. Nears a "Fiscal Cliff," Concerns Rise for Future R&D

Fiscal and political pressure on U.S. research and development spending is likely to grow more intense in coming years, with some scenarios suggesting that sweeping cuts may occur as early as 2013. Unless lawmakers find compromise budget agreements, the cuts could dramatically impair innovation and the long-term strength of the nation's economy, experts said at the AAAS Forum on Science and Technology Policy.

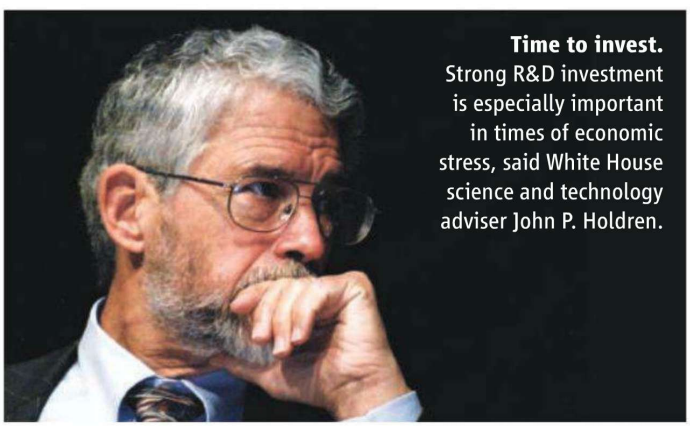

Time to invest. Strong R&D investment is especially important in times of economic stress, said White House science and technology adviser John P. Holdren.

The pressures are coming from multiple sources, including the 2013 budget negotiations and the need to cover the escalating costs of entitlement programs such as Social Security and Medicare in the decades ahead. But the most immediate threat is that discretionary portions of the U.S. budget early next year will be subject to "sequestration"—across-the-board spending cuts of 8 to 10%—unless bitterly divided lawmakers agree on some mix of spending cuts and new revenue to close a gap of up to $1.2 trillion over the next 10 years.

In talks that were often blunt and unusually pessimistic, policy leaders at the Forum described how the fiscal pressures threaten to undermine U.S. research preeminence and global leadership in areas ranging from food production and public health to energy development, space exploration, and science education.

"It just seems like an incredibly tense moment, where the whole world is watching what we choose to do," said Maya MacGuineas, a high-level budget adviser who served on the bipartisan Debt Reduction Task Force in 2010. Failure to find a compromise, MacGuineas added, will result in "nothing but a self-inflicted wound."

The 37th annual AAAS Forum convened in Washington, D.C., on 26 to 27 April, with more than 400 government and business leaders, researchers, educators, and journalists attending. But in a diverse program that explored prospects for startup tech firms, voter psychology, and science diplomacy, the intertwined budget and political crises were front and center.

John P. Holdren, the White House science and technology adviser, outlined President Barack Obama's plans for research to drive innovation and economic productivity. Especially in a time of fiscal stress, Holdren said, it is crucial to invest in areas such as advanced manufacturing, "big data" computing, and science education.

U.S. Representative Lamar Smith, the Texas Republican who coauthored a landmark patent system reform signed by Obama last year, assured the audience of bipartisan support for R&D in Congress. But, he said, recent levels of federal borrowing are not sustainable, and science advocates must "be prepared to negotiate and compromise."

R&D is already suffering from years of budget stress, aggravated by the historic 2008 recession. Matt Hourihan, director of the AAAS R&D Budget and Policy Program, told the Forum audience that federal research investment, adjusted for inflation, has been essentially flat since 2003. Seen through a longer lens, public-sector R&D has fallen from 1.27% of gross domestic product in 1976 to 0.87% now.

At the National Institutes of Health (NIH), 40% or more of applicants won grants in the 1980s; today, just under 20% succeed. At the state level, declining government support for higher education has led to higher tuition and deep spending cuts. Texas has closed over 500 programs—some in the basic sciences—in a push for efficiency and productivity. The University of Oklahoma (OU) also is evaluating whether programs and facilities are relevant and able to support themselves.

"We can't just wait this out and come out the other end and it is like it was before," said Kelvin K. Droegemeier, OU's vice president for research. "It is not going to be like it was before."

In fact, things may get worse. Under terms of a 2011 agreement to raise the federal debt ceiling, lawmakers must narrow the gap by up to $1.2 trillion; failing that, sequestration will impose automatic cuts of 8 to 10%, split between defense and nondefense discretionary spending.

For the NIH research community, "that's a really big cut" with "scary" ramifications, said Carrie Wolinetz, associate vice president for federal relations with the Association of American Universities.

But the budget approved by the Republican-controlled House of Representatives earlier this year would shift the onus of sequestration cuts mostly onto nonmilitary programs, creating an even worse worst-case scenario for science. Health and agriculture research could be cut by 22% compared with the proposed White House plan through 2021, Hourihan said. Transportation and natural resources could be cut by about a third. Energy R&D could be slashed 67%.

The Senate is not likely to approve such a draconian spending plan, he said, but it sets a troubling baseline for negotiations in the months ahead.

–Earl Lane, Bob Roehr, and Edward W. Lempinen

COMMUNICATION

Screeners Needed for Journalism Awards

Volunteer scientists are needed to review entries in the prestigious AAAS Kavli Science Journalism Awards competition. If interested, please contact Angela Bradley (202-326-6408; abradley@aaas.org) in the AAAS Office of Public Programs.

Predicting Pragmatic Reasoning in Language Games

Michael C. Frank* and Noah D. Goodman

One of the most astonishing features of human language is its ability to convey information efficiently in context. Each utterance need not carry every detail; instead, listeners can infer speakers' intended meanings by assuming utterances convey only relevant information. These communicative inferences rely on the shared assumption that speakers are informative, but not more so than is necessary given the communicators' common knowledge and the task at hand. Many theories provide high-level accounts of these kinds of inferences (*1*–*3*), yet, perhaps because of the difficulty of formalizing notions like "informativeness" or "common knowledge," there have been few successes in making quantitative predictions about pragmatic inference in context.

We addressed this issue by studying simple referential communication games, like those described by Wittgenstein (*4*). Participants see a set of objects and are asked to bet which one is being referred to by a particular word. We modeled human behavior by assuming that a listener can use Bayesian inference to recover a speaker's intended referent r_S in context C, given that the speaker uttered word w:

$$P(r_s|w,C) = \frac{P(w|r_s,C)P(r_s)}{\sum_{r' \in C} P(w|r',C)P(r')} \quad (1)$$

This expression is the product of three terms: the prior probability $P(r_S)$ that an object would be referred to; the likelihood $P(w|r_S,C)$ that the speaker would utter a particular word to refer to the object; and the normalizing constant, a sum of these terms computed for all referents in the context.

We defined the prior probability of referring to an object as its contextual salience. This term picks out not just perceptually but also socially and conversationally salient objects, capturing the common knowledge that speaker and listener share, as it affects the communication game. Because there is no a priori method for computing this sort of salience, we instead measured it empirically (*5*).

The likelihood term in our model is defined by the assumption that speakers choose words to be informative in context. We quantified the informativeness of a word by its surprisal, an information-theoretic measure of how much it reduces uncertainty about the referent. By assuming a rational actor model of the speaker, with utility defined in terms of surprisal, we can derive the regularity that speakers should choose words proportional to their specificity (*6*, *7*):

$$P(w|r_s,C) = \frac{|w|^{-1}}{\sum_{w' \in W} |w'|^{-1}} \quad (2)$$

where $|w|$ indicates the number of objects to which word w could apply and W indicates the set of words that apply to the speaker's intended referent.

In our experiment, three groups of participants each saw communicative contexts consisting of sets of objects varying on two dimensions (Fig. 1A). We systematically varied the distribution of features on these dimensions. To minimize the effects of particular configurations or features, we randomized all other aspects of the objects for each participant. The first group (speaker condition) bet on which word a speaker would use to describe a particular object, testing the likelihood portion of our model. The second group (salience condition) was told that a speaker had used an unknown word to refer to one of the objects and was asked to bet which object was being talked about, providing an empirical measure of the prior in our model. The third group (listener condition) was told that a speaker had used a single word (e.g., "blue") and again asked to bet on objects, testing the posterior predictions of our model.

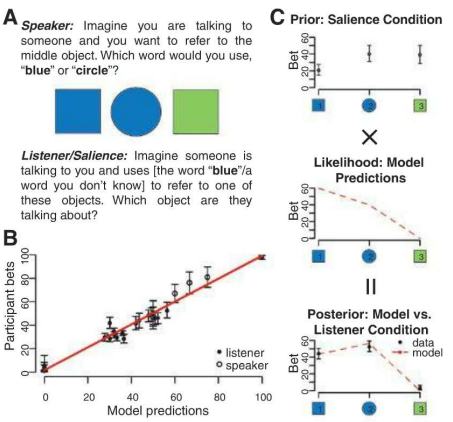

Fig. 1. (**A**) An example stimulus from our experiment, with instructions for speaker, listener, and salience conditions. (**B**) Human bets on the probability of a choosing a term (speaker condition, $N = 206$) or referring to an object (listener condition, $N = 263$), plotted by model predictions. Points represent mean bets for particular terms and objects for each context type. The red line shows the best linear fit to all data. (**C**) An example calculation in our model for the context type shown in (A). Empirical data from the salience condition constitute the prior term, $N = 20$ (top); this is multiplied by the model-derived likelihood term (middle). The resulting posterior model predictions (normalization step not shown) are plotted alongside human data from the listener condition, $N = 24$ (bottom). All error bars show 95% confidence intervals.

Mean bets in the speaker condition were highly correlated with our model's predictions for informative speakers ($r = 0.98$, $P < 0.001$; Fig. 1B, open circles). Judgments in the salience and listener conditions were not themselves correlated with one another ($r = 0.19$, $P = 0.40$), but when salience and informativeness terms were combined via our model, the result was highly correlated with listener judgments ($r = 0.99$, $P < 0.0001$, Fig. 1B, solid circles). This correlation remained highly significant when predictions of 0 and 100 were removed ($r = 0.87$, $P < 0.0001$). Figure 1C shows model calculations for one arrangement of objects.

Our simple model synthesizes and extends work on human communication from a number of different traditions, including early disambiguation models (*8*), game-theoretic signaling models (*9*), and systems for generating referring expressions (*10*). The combination of an information-theoretic definition of "informativeness" along with empirical measurements of common knowledge enables us to capture some of the richness of human pragmatic inference in context.

Department of Psychology, Stanford University, Stanford, CA 94305, USA.

*To whom correspondence should be addressed. E-mail: mcfrank@stanford.edu

References and Notes

1. H. Grice, in *Syntax and Semantics*, P. Cole, J. Morgan, Eds. (Academic Press, New York, 1975), vol. 3, pp. 41–58.
2. D. Sperber, D. Wilson, *Relevance: Communication and Cognition* (Harvard Univ. Press, Cambridge, MA, 1986).
3. H. Clark, *Using Language* (Cambridge Univ. Press, Cambridge, 1996).
4. L. Wittgenstein, *Philosophical Investigations* (Blackwell, Oxford, 1953).
5. H. Clark, R. Schreuder, S. Buttrick, *J. Verbal Learn. Verbal Behav.* **22**, 245 (1983).
6. Materials and methods are available as supplementary materials on *Science* Online.
7. F. Xu, J. B. Tenenbaum, *Psychol. Rev.* **114**, 245 (2007).
8. S. Rosenberg, B. D. Cohen, *Science* **145**, 1201 (1964).
9. A. Benz, G. Jäger, R. Van Rooij, Eds., *Game Theory and Pragmatics* (Palgrave Macmillan, Hampshire, UK, 2005).
10. R. Dale, E. Reiter, *Cogn. Sci.* **19**, 233 (1995).

Supplementary Materials

www.sciencemag.org/cgi/content/full/336/6084/998/DC1
Materials and Methods
Supplementary Text

3 January 2012; accepted 10 April 2012
10.1126/science.1218633

Growing Microtubules Push the Oocyte Nucleus to Polarize the *Drosophila* Dorsal-Ventral Axis

Tongtong Zhao,[1] Owen S. Graham,[2] Alexandre Raposo,[1]* Daniel St Johnston[1]†

The *Drosophila* dorsal-ventral (DV) axis is polarized when the oocyte nucleus migrates from the posterior to the anterior margin of the oocyte. Prior work suggested that dynein pulls the nucleus to the anterior side along a polarized microtubule cytoskeleton, but this mechanism has not been tested. By imaging live oocytes, we find that the nucleus migrates with a posterior indentation that correlates with its direction of movement. Furthermore, both nuclear movement and the indentation depend on microtubule polymerization from centrosomes behind the nucleus. Thus, the nucleus is not pulled to the anterior but is pushed by the force exerted by growing microtubules. Nuclear migration and DV axis formation therefore depend on centrosome positioning early in oogenesis and are independent of anterior-posterior axis formation.

The correct positioning of the nucleus is important for several developmental processes, such as cell migration, formation of the neuromuscular junction, and asymmetric cell divisions, whereas nuclear mislocalization is a feature of neurological disorders, such as lissencephaly (*1*). Positioning of the nucleus plays an essential role in *Drosophila* axis formation, because the movement of the nucleus from the posterior of the oocyte to a point at its anterior circumference breaks radial symmetry to polarize the dorsal-ventral (DV) axis (*2*, *3*). At stage 7 of oogenesis, an unknown signal from the posterior follicle cells induces a major reorganization of the oocyte microtubule cytoskeleton. The posterior microtubule organizing center (MTOC) is disassembled, and microtubules are nucleated from the anterior-lateral cortex, resulting in an anterior-posterior (AP) gradient of microtubules that defines the AP axis (*4*). It is believed that dynein subsequently uses this polarized microtubule cytoskeleton to pull the nucleus to the oocyte anterior, making polarization of the DV axis dependent on the prior polarization of the AP axis (*5*–*9*).

The nucleus is pushed to the anterior by growing microtubules. To investigate the mechanism

[1]The Gurdon Institute and the Department of Genetics, University of Cambridge, Tennis Court Road, Cambridge CB2 1QN, UK. [2]The Department of Engineering, University of Cambridge, Trumpington Street, Cambridge CB2 1PZ, UK.

*Present address: Instituto Gulbenkian de Ciência, Rua da Quinta Grande, 6, P-2780-156 Oeiras, Portugal.
†To whom correspondence should be addressed. E-mail: d.stjohnston@gurdon.cam.ac.uk

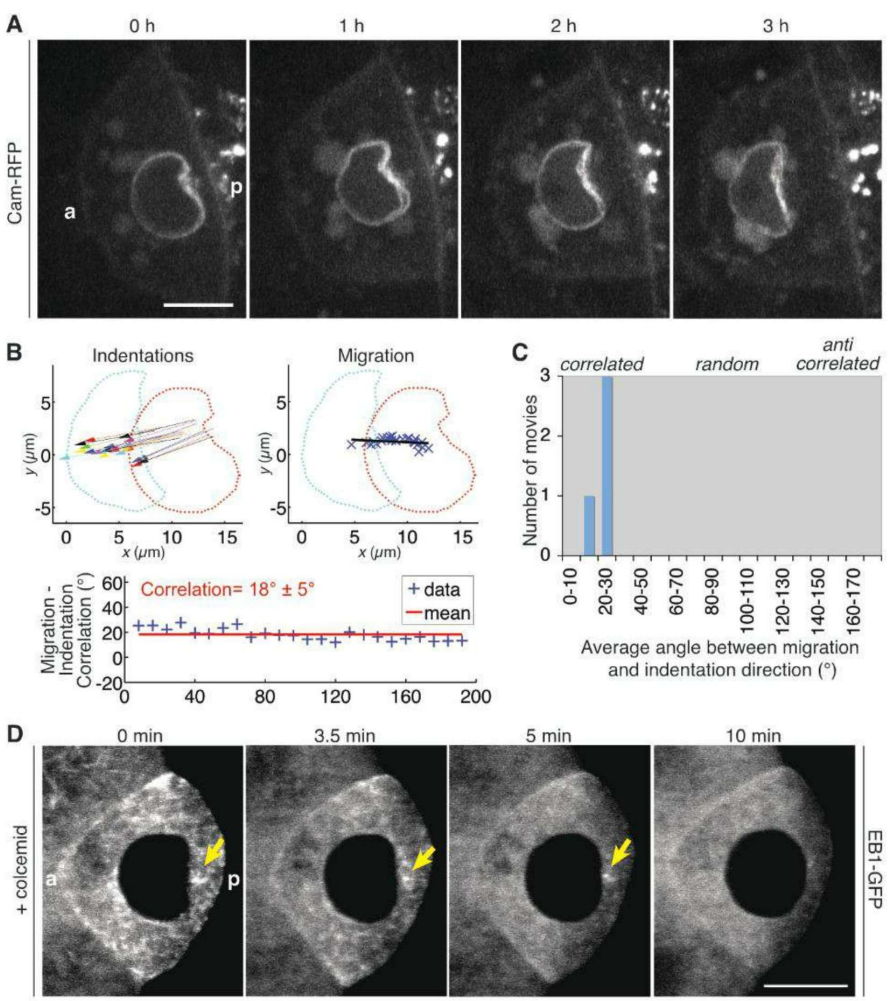

Fig. 1. Nuclear migration is driven by a posterior microtubule pushing force. (**A**) Time course of a migrating nucleus. RFP indicates red fluorescent protein. (**B**) Analysis of directions of nuclear indentations during migration (left), direction of overall migration (right), and the correlation between them, expressed as the angle between the directional vectors (bottom) (mean ± SD). Red and cyan dots show the outline of the nucleus at the start and end of migration, respectively; blue ×s show the centroid of the nucleus during migration. (**C**) Mean angle between migration and indentation directions from four migrating nuclei. (**D**) Temporal merges of an EB1-GFP movie of a colcemid-treated egg chamber. Each image is a maximum projection of five time frames (equal to 10 s). Arrow, MTOC. In (A) and (D), a, anterior; p, posterior; scale bars, 10 μm.

of nuclear positioning directly, we imaged the movement of the nucleus in living oocytes. The nucleus migrates at a speed of 4.0 ± 0.7 μm/hour (n = 6) and takes 2 to 3 hours to move across the oocyte (Fig. 1). The trajectory of the nucleus is variable: Sometimes it moves around the cortex of the oocyte directly to an anterior corner, but it often migrates up the center of the oocyte and then turns to move along the anterior cortex (fig. S1 and movie S1), confirming the random nature of this symmetry-breaking event. We observed that all migrating nuclei have large posterior indentations, suggesting that they are being pushed rather than pulled toward the anterior (Fig. 1A and movie S2). This could reflect an intrinsic reorganization of the nuclear architecture or a deformation induced by an external force to the nucleus. In support of the latter view, the direction of the indentation correlates with the direction of migration, suggesting that the same force creates the indentation and moves the nucleus (Fig. 1, B and C). This indentation is not an artifact of long-term imaging in oil, because egg chambers dissected directly into strong fixative have identical indentations (fig. S2).

This idea that the nucleus is pulled to the anterior by dynein has its basis in the finding that mutations in the dynein accessory factors, *Lis1* and *Bic-D*, as well as disruption of the dynactin complex result in mislocalized nuclei at stage 10 (*5*–*9*). This is not compatible with the pushing model of nuclear movement, because motor proteins can only pull their cargoes. We therefore reexamined the role of the dynein complex by imaging the nucleus in *Lis1* mutant egg chambers. *Lis1* mutant oocytes are much smaller than normal because dynein is required for transport from the nurse cells into the oocyte (*6*). Nevertheless, the oocyte nucleus migrates normally with a prominent posterior indentation (movie S3). Thus, dynein is presumably required for the anchoring of the nucleus once it has reached the anterior, rather than for its migration. Consistent with this, the nuclei are only rarely mispositioned in *Lis1* and *Bic-D* mutant oocytes at stage 9 but are mislocalized much more frequently at later stages (fig. S3).

Both actin and microtubule polymerization can generate pushing forces that lead to cellular or organelle deformations (*10*). Two lines of evidence suggest that microtubules are responsible for the nuclear indentation: First, depolymerization of actin with latrunculin A or B does not affect nuclear positioning, whereas the microtubule-depolymerizing drug colcemid induces mislocalized nuclei (*11*). Secondly, several microtubule-associated proteins become enriched on the posterior nuclear envelope during migration, including the dynein light intermediate chain (Dlic), calmodulin (Cam), and the *Drosophila* NuMA homolog mushroom body defect, Mud (fig. S4) (*12*–*14*).

To test the role of microtubules in the formation of the indentation, we added colcemid to living egg chambers expressing the +TIP protein, EB1-GFP (end binding-1–green fluorescent protein), which forms a "comet" on the growing plus ends of microtubules (*15*). Colcemid takes 3.5 min to diffuse into the oocyte, as monitored by a decrease in the number of EB1 comets on growing microtubule plus ends. As soon as microtubule growth starts to decrease, the indentation diminishes in size (Fig. 1D and movie S4). A focus of EB1-GFP persists posterior to the nucleus for several minutes, and, as this dis-

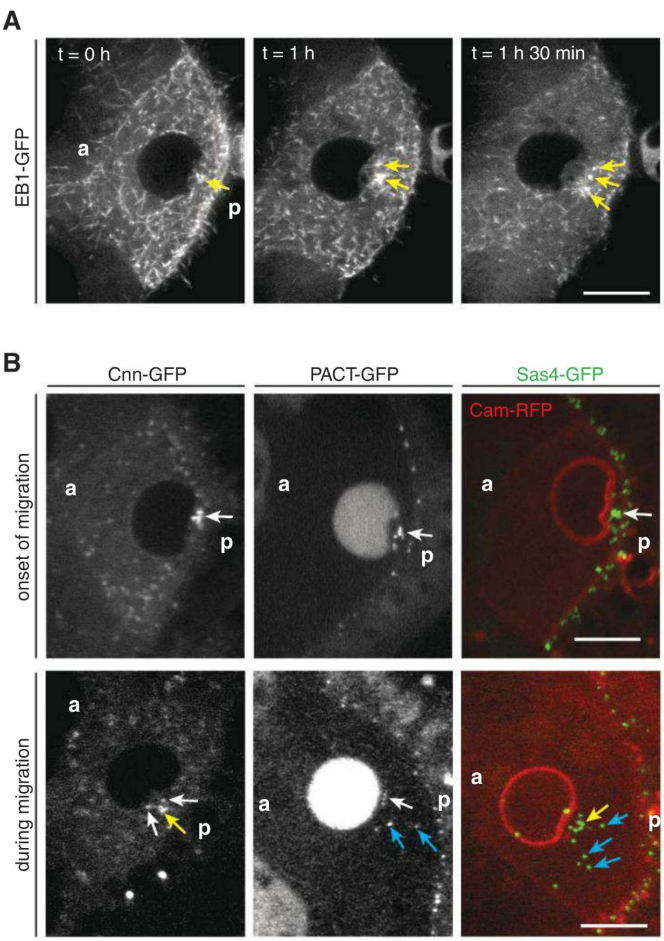

Fig. 2. Active centrosomes are localized behind the nuclear indentation. (**A**) Temporal merges (20 time frames, equal to 10 s) of an EB1-GFP movie reveal active MTOCs (arrows) between the nuclear indentation and the posterior oocyte cortex. (**B**) The centriolar markers PACT-GFP and Sas-4-GFP and the PCM marker Cnn-GFP are localized behind the nucleus at the onset of migration (top). During migration, MTOCs can be clustered together (yellow arrows), associated with the nucleus (white arrows), or dispersed in the cytoplasm (blue arrows) (bottom). Scale bars, 10 μm.

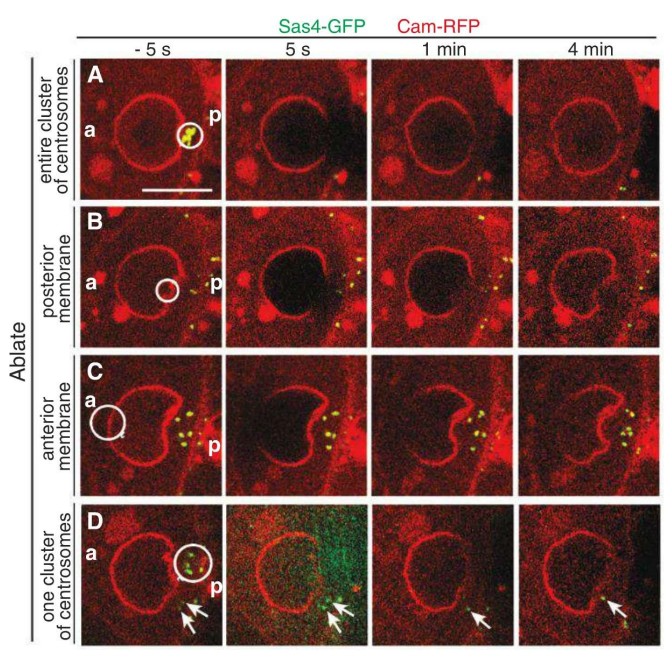

Fig. 3. Laser ablation of the centrosomes abolishes the nuclear indentation. (**A** and **D**) Clusters of centrosomes were bleached for 5 s. One to 4 min after ablation, the nuclear indentation facing the ablated centrosomes disappeared. (**B** and **C**) When the nuclear membrane or the anterior of the nucleus was bleached, the indentation was maintained. Circles, area of bleaching; arrows, nonablated, active centrosomes; scale bar, 10 μm.

appears, the nucleus relaxes completely and becomes spherical. Thus, the nuclear indentation depends on microtubule polymerization, and its size is proportional to the number of growing microtubules.

The nuclear indentation depends on active posterior centrosomes. Using EB1-GFP to track the growing microtubule plus ends in time-lapse movies of nuclear migration revealed several strong foci of EB1-GFP behind the indentation, with growing microtubules emanating from them in all directions (Fig. 2A and movie S5). This indicates that microtubules are nucleated from MTOCs behind the nucleus. These MTOCs resemble the centrosomes, which migrate from the nurse cells into the oocyte during early oogenesis in a dynein-dependent manner, and localize to the posterior cortex as a result of the initial oocyte polarity (*16*–*20*). Indeed, the centriolar markers Sas4 and PACT, as well as a marker for pericentriolar material (PCM), centrosomin (Cnn) (*21*), localize to the foci behind the nuclear indentation at the onset of migration (Fig. 2B). The centrosomes behave rather dynamically during migration and change reversibly from a dense cluster to a more dispersed distribution (Fig. 2B). Upon completion of nuclear migration, the centrosomes are recruited to the anterior-dorsal cortex of the oocyte, presumably as a consequence of the activation of the dynein-dependent anchoring mechanism that retains the nucleus in this position (fig. S5 and movies S6 and S7). Active centrosomes are therefore positioned behind the nucleus before and during migration.

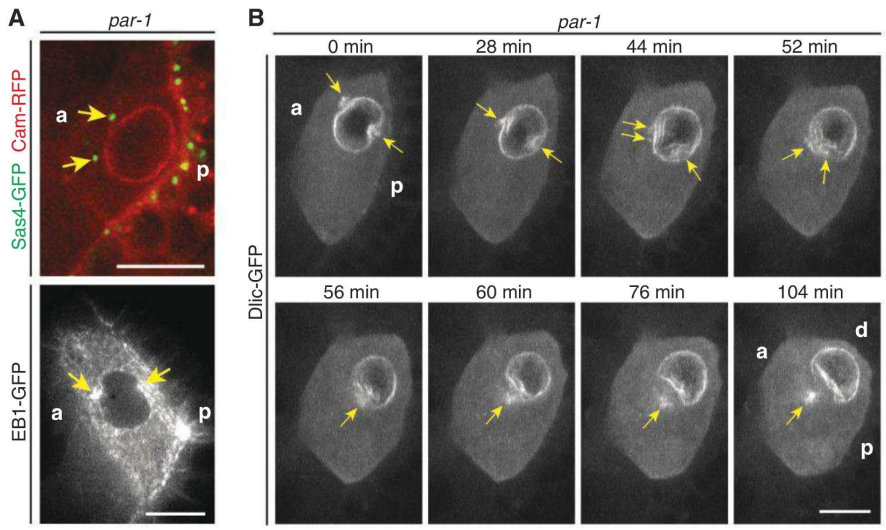

Fig. 4. Mispositioned centrosomes induce ectopic nuclear indentations. (**A**) Sas4-GFP (top) and a temporal merge of EB1-GFP (20 frames, equals 10 s) (bottom) reveal active, anterior centrosomes in *par-1*^{6323}/*par-1*^{W3} mutants, which induce an anterior indentation in the nucleus. (**B**) Nuclear migration in *par-1*^{6323}/*par-1*^{W3} mutants. At the onset of migration, the anterior centrosomes induce an ectopic anterior nuclear indentation. The anterior centrosomes eventually move around the nuclear membrane to cluster with the posterior centrosomes, inducing a broad nuclear indentation and rapid nuclear movement. d, dorsal; arrows, centrosomes; scale bars, 10 μm.

To test the role of the centrosomes in creating the nuclear indentation, we inactivated them by laser ablation. Upon ablation of the entire cluster of centrosomes, the indentation disappears, and the nucleus becomes spherical within 1 min (Fig. 3A and movie S8). This nuclear relaxation may occur more rapidly, because centrosome ablation causes local bleaching of the nuclear envelope, making it impossible to monitor nuclear shape during the first minute. However, local laser ablation of the nuclear envelope at the site of the indentation has no effect, excluding the possibility that the disappearance of the indentation is a consequence of bleaching of the nuclear membrane (Fig. 3B and movie S9). Furthermore, ablation of the anterior of the nucleus does not affect the indentation, arguing against any pulling force from the anterior (Fig. 3C and movie S10). As described above, centrosomes are sometimes scattered behind the nucleus, causing multiple indentations. Ablating one cluster of centrosomes abolishes only the indentation facing them. The nonablated centrosomes remain active and induce an indentation on the adjacent side of the nucleus (Fig. 3D and movie S11). Thus, the nucleus is not a rigid structure, and the growing microtubules from the centrosomes exert force on the nuclear envelope to induce its deformation.

The centrosomes are dispensable for oogenesis (*22*). We therefore examined nuclear migration in *DSas-4* mutant ovaries that lack centrosomes. Consistent with the previous study, all nuclei migrate to the anterior-dorsal corner ($n = 117$) and show a posterior indentation during migration (fig. S6 and movie S12). GFP-Cnn is still localized in foci behind the nucleus, and EB1-GFP tracks reveal active posterior MTOCs (fig. S6). Thus, acentrosomal MTOCs form in the absence of centrosomes and can provide the pushing force for nuclear migration.

Nuclear migration is independent of AP axis formation. As a further test of the idea that the centrosomal microtubules push the nucleus to the anterior, we examined *par-1* hypomorphs, in which some centrosomes fail to migrate to the posterior of the oocyte (*19*). These anterior

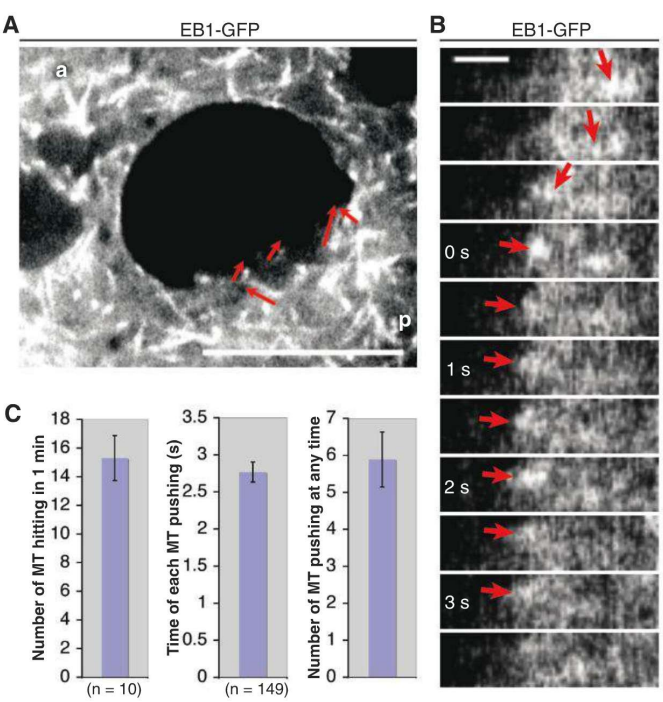

Fig. 5. The force of microtubule polymerization is sufficient to move the nucleus. Quantification of the number of microtubules hitting the posterior of the nucleus. (**A**) Temporal merge of 20 frames (equal to 10 s) of an EB1-GFP movie. Red arrows indicate tracked microtubules that hit the nuclear indentation. Scale bar, 10 μm. (**B**) Kymograph of a microtubule that pushes against the nuclear indentation for 3 s; arrows indicate the position of the EB1-GFP comet (plus end of a microtubule). Scale bar, 1 μm. (**C**) Quantification of the number of microtubules hitting the nuclear indentation, the time that each microtubule pushes, and the resulting average number of microtubules that are pushing against the indentation at any given time (error bars, ±SEM).

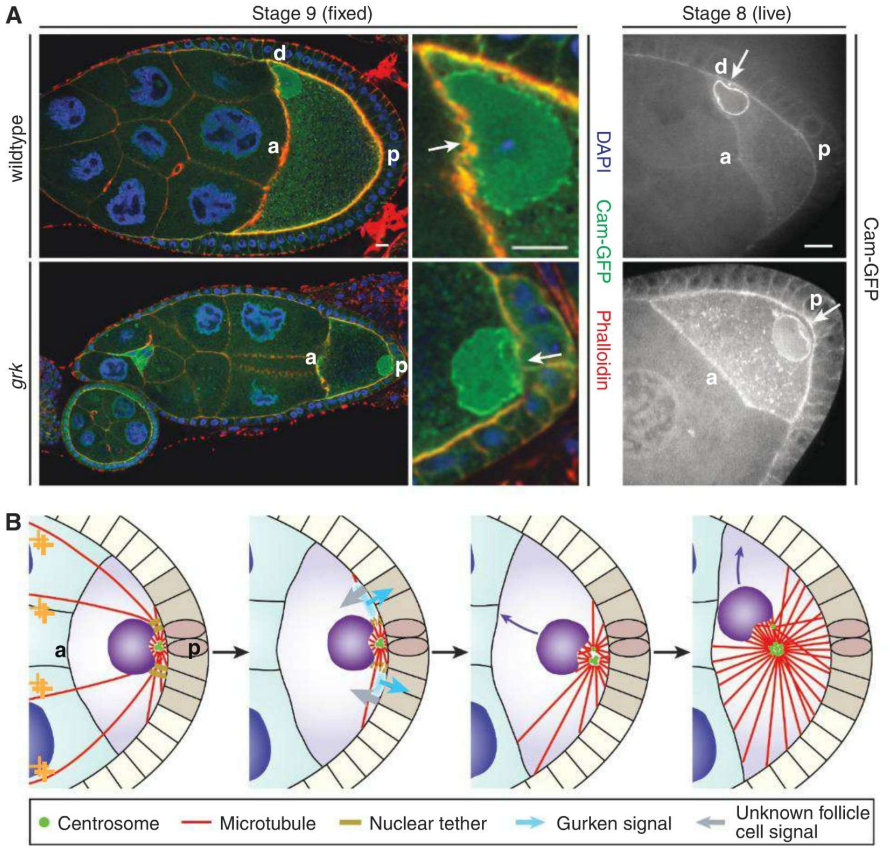

Fig. 6. The nucleus is anchored to the posterior before migration. (**A**) The nuclei often fail to migrate in grk^{2B6}/$grk2^{E12}$ mutants but still have prominent posterior indentations (arrows), indicating that they are tethered at the posterior. DAPI, 4′,6-diamidino-2-phenylindole; scale bars, 10 μm. (**B**) A microtubule pushing model for nuclear migration. Before migration, the nucleus is tethered at the posterior with active centrosomes behind it (left). The posterior follicle cell signal induces the release of the nucleus from the tether, and growing microtubules then push the nucleus anteriorly (middle). This movement is essentially random and continues until the oocyte becomes wedged in an anterior corner (right).

centrosomes induce anterior nuclear indentations, leading to dumbbell-shaped nuclei, confirming the role of centrosomal microtubules in pushing the nucleus (Fig. 4A). These ectopic centrosomes eventually fuse with the posterior centrosomes to move the nucleus to the anterior-dorsal corner (Fig. 4B and movie S13). This explains why the nucleus migrates normally in *par-1* mutants even though the AP axis is not polarized (*23*). Consistent with this, the nucleus in wild-type oocytes can migrate to the anterior before the anterior-to-posterior microtubule gradient is established (Fig. 2A and fig. S7).

Microtubule growth provides sufficient force to move the nucleus. Another documented example of nuclear positioning by microtubule pushing comes from *Schizosaccharomyces pombe*, where microtubule bundles push against the cell ends to maintain the nucleus in the cell center (*24*). The oocyte nucleus moves a much greater distance, however, and appears to be pushed by the force exerted by single growing microtubules. To test the feasibility of this mechanism, we used Stoke's law ($F = 6\pi\eta r v$) to estimate the drag force (F) exerted on the nucleus. Assuming a cytoplasmic viscosity (η) ≈ 100 Pas (*25*, *26*) and the measured values of the nuclear radius (r) ≈ 5 μm and the velocity of migration (v) ≈ 4 μm/hour yields a drag force ≈ 10 pN. We expect the actual drag force to be lower, because nuclear migration is so slow (1 nm/s) that the cytoplasmic actin mesh will turn over ahead of the nucleus, decreasing the effective viscosity (*27*, *28*). The longest microtubules can reach ~10 μm between the posterior of the nucleus and the posterior oocyte cortex, resulting in a critical buckling force $F_c \approx 5$ pN (*29*). This value is probably an underestimate, because microtubules embedded within an elastic cytoplasm in vivo have been reported to bear compressive loads 100 times higher than those in vitro (*30*). Each microtubule can therefore generate a pushing force of at least 5 pN. Thus, the force of only two microtubules pushing at any time should be sufficient to move the nucleus to the oocyte anterior.

We measured the number of microtubules pushing the nucleus by using EB1-GFP. In one z plane, 15.3 ± 1.6 (SEM) microtubules hit the nuclear indentation per minute (n = 10, 2 oocytes), and they continued growing and presumably exerting force on the nucleus for 2.77 ± 0.14 s (n = 149) (Fig. 5, A to C, and movie S14). Given the thickness of a confocal section (0.8 μm) and the radius of the indentation [4.3 ± 0.2 μm (n = 10)], an average of 5.9 ± 0.7 microtubules were pushing the nucleus at any given time. Microtubule polymerization can therefore provide sufficient pushing force to drive nuclear migration.

Nuclear migration is triggered by release from a posterior anchor. The migration of the nucleus is triggered by an unknown signal from the posterior follicle cells, which could act either by activating the centrosomes or by releasing the nucleus from a posterior tether. To address this question, we examined when the indentation appears during oogenesis. Active centrosomes are already localized behind the nucleus at stage 5 of oogenesis and induce a posterior indentation (fig. S8A). This suggests that the centrosomes continually exert a pushing force on the nucleus, which is tethered to the posterior until it receives a signal for migration. The nucleus remains at the posterior in *gurken* (*grk*) mutants, which block follicle cell signaling to the oocyte (39% penetrance, n = 70) (*2*, *3*). These posterior nuclei still maintain a posterior indentation later in oogenesis (Fig. 6A), suggesting that they fail to migrate because they are not released from the posterior tether (fig. S8B and movie S15). Indeed, microtubules growing from active centrosomes probably always exert a pushing force on the nucleus that must be countered by an opposing pulling force or anchor to keep the nucleus in place. For example, a nuclear indentation is still visible adjacent to the centrosomes after the nucleus is anchored at the anterior (fig. S5A).

Our results lead to a revised model for how the oocyte nucleus moves to break radial symmetry and polarize the *Drosophila* DV axis (Fig. 6B). This model explains the failure to recover mutants that specifically disrupt nuclear migration, because the driving force is provided solely by microtubule polymerization. Furthermore, our results imply that migration is triggered by the release of the nucleus from a posterior anchor,

rather than by microtubule reorganization. Thus, polarization of the DV axis is independent of the formation of the microtubule array that defines the AP axis, as previously proposed.

References and Notes

1. I. Dupin, S. Etienne-Manneville, *Int. J. Biochem. Cell Biol.* **43**, 1698 (2011).
2. A. González-Reyes, H. Elliott, D. St Johnston, *Nature* **375**, 654 (1995).
3. S. Roth, F. S. Neuman-Silberberg, G. Barcelo, T. Schüpbach, *Cell* **81**, 967 (1995).
4. R. Bastock, D. St Johnston, *Curr. Biol.* **18**, R1082 (2008).
5. A. Swan, B. Suter, *Development* **122**, 3577 (1996).
6. A. Swan, T. Nguyen, B. Suter, *Nat. Cell Biol.* **1**, 444 (1999).
7. Y. Lei, R. Warrior, *Dev. Biol.* **226**, 57 (2000).
8. J. E. Duncan, R. Warrior, *Curr. Biol.* **12**, 1982 (2002).
9. J. Januschke *et al.*, *Curr. Biol.* **12**, 1971 (2002).
10. A. Mogilner, G. Oster, *Curr. Biol.* **13**, R721 (2003).
11. E. A. Koch, R. H. Spitzer, *Cell Tissue Res.* **228**, 21 (1983).
12. Y. C. Lee, J. Wolff, *J. Biol. Chem.* **257**, 6306 (1982).
13. J. R. Kardon, R. D. Vale, *Nat. Rev. Mol. Cell Biol.* **10**, 854 (2009).
14. A. E. Radulescu, D. W. Cleveland, *Trends Cell Biol.* **20**, 214 (2010).
15. Y. Mimori-Kiyosue, N. Shiina, S. Tsukita, *Curr. Biol.* **10**, 865 (2000).
16. A. P. Mahowald, J. M. Strassheim, *J. Cell Biol.* **45**, 306 (1970).
17. N. C. Grieder, M. de Cuevas, A. C. Spradling, *Development* **127**, 4253 (2000).
18. J. Bolívar *et al.*, *Development* **128**, 1889 (2001).
19. J. R. Huynh, J. M. Shulman, R. Benton, D. St Johnston, *Development* **128**, 1201 (2001).
20. P. Fichelson, M. Jagut, S. Lepanse, J. A. Lepesant, J. R. Huynh, *Development* **137**, 815 (2010).
21. N. M. Rusan, G. C. Rogers, *Traffic* **10**, 472 (2009).
22. N. R. Stevens, A. A. Raposo, R. Basto, D. St Johnston, J. W. Raff, *Curr. Biol.* **17**, 1498 (2007).
23. J. M. Shulman, R. Benton, D. St Johnston, *Cell* **101**, 377 (2000).
24. P. T. Tran, L. Marsh, V. Doye, S. Inoué, F. Chang, *J. Cell Biol.* **153**, 397 (2001).
25. A. R. Bausch, W. Möller, E. Sackmann, *Biophys. J.* **76**, 573 (1999).
26. R. M. Hochmuth, *J. Biomech.* **33**, 15 (2000).
27. K. Dahlgaard, A. A. Raposo, T. Niccoli, D. St Johnston, *Dev. Cell* **13**, 539 (2007).
28. N. Watanabe, *Proc. Jpn. Acad. Ser. B* **86**, 62 (2010).
29. M. Dogterom, J. W. Kerssemakers, G. Romet-Lemonne, M. E. Janson, *Curr. Opin. Cell Biol.* **17**, 67 (2005).
30. C. P. Brangwynne *et al.*, *J. Cell Biol.* **173**, 733 (2006).

Acknowledgments: We would like to thank J. Raff for providing the Dlic-GFP fly stock and centrosomal markers; H. Nash for providing the Mud antibody; S. Young for help with image analysis; and J. Guck, Y.-C. Oei, and P. K. Trong for help with the force calculations. This work was supported by a Wellcome Trust Principal Research Fellowship to D.St., Ph.D. scholarships from the FAZIT Stiftung, the Boehringer Ingelheim Fonds and the Cambridge European Trust to T.Z., the Gulbenkian Ph.D. scholarship of the Fundação para a Ciência e Tecnologia to A.R., and core support from the Wellcome Trust and Cancer Research UK.

Supplementary Materials

www.sciencemag.org/cgi/content/full/science.1219147/DC1
Materials and Methods
Figs. S1 to S8
References (*31*–*43*)
Movies S1 to S15

16 January 2012; accepted 27 March 2012
Published online 12 April 2012;
10.1126/science.1219147

REPORTS

Signatures of Majorana Fermions in Hybrid Superconductor-Semiconductor Nanowire Devices

V. Mourik,[1]* K. Zuo,[1]* S. M. Frolov,[1] S. R. Plissard,[2] E. P. A. M. Bakkers,[1,2] L. P. Kouwenhoven[1]†

Majorana fermions are particles identical to their own antiparticles. They have been theoretically predicted to exist in topological superconductors. Here, we report electrical measurements on indium antimonide nanowires contacted with one normal (gold) and one superconducting (niobium titanium nitride) electrode. Gate voltages vary electron density and define a tunnel barrier between normal and superconducting contacts. In the presence of magnetic fields on the order of 100 millitesla, we observe bound, midgap states at zero bias voltage. These bound states remain fixed to zero bias, even when magnetic fields and gate voltages are changed over considerable ranges. Our observations support the hypothesis of Majorana fermions in nanowires coupled to superconductors.

All elementary particles have an antiparticle of opposite charge (for example, an electron and a positron); the meeting of a particle with its antiparticle results in the annihilation of both. A special class of particles, called Majorana fermions, are predicted to exist that are identical to their own antiparticle (*1*). They may appear naturally as elementary particles or emerge as charge-neutral and zero-energy quasi-particles in a superconductor (*2*, *3*). Particularly interesting for the realization of qubits in quantum computing are pairs of localized Majoranas separated from each other by a superconducting region in a topological phase (*4*–*11*).

On the basis of earlier and later semiconductor-based proposals (*6*, *7*), Lutchyn *et al.* (*8*) and Oreg *et al.* (*9*) have outlined the necessary ingredients for engineering a nanowire device that should accommodate pairs of Majoranas. The starting point is a one-dimensional (1D) nanowire made of semiconducting material with strong spin-orbit interaction (Fig. 1A). In the presence of a magnetic field B along the axis of the nanowire (i.e., a Zeeman field), a gap is opened at the crossing between the two spin-orbit bands. If the Fermi energy μ is inside this gap, the degeneracy is twofold, whereas outside the gap it is fourfold. The next ingredient is to connect the semiconducting nanowire to an ordinary s-wave superconductor (Fig. 1A). The proximity of the superconductor induces pairing in the nanowire between electron states of opposite momentum and opposite spins and induces a gap, Δ. Combining this twofold degeneracy with an induced gap creates a topological superconductor (*4*–*11*). The condition for a topological phase is $E_Z > (\Delta^2 + \mu^2)^{1/2}$, with the Zeeman energy $E_Z = g\mu_B B/2$ (g is the Landé g factor, μ_B is the Bohr magneton). Near the ends of the wire, the electron density is reduced to zero, and subsequently, μ will drop below the subband energies such that μ^2 becomes large. At the points in space where $E_Z = (\Delta^2 + \mu^2)^{1/2}$, Majoranas arise as zero-energy (i.e., midgap) bound states—one at each end of the wire (*4*, *8*–*11*).

Despite their zero charge and energy, Majoranas can be detected in electrical measurements. Tunneling spectroscopy from a normal conductor into the end of the wire should reveal a state at zero energy (*12*–*14*). Here, we report the observation of such zero-energy peaks and show that they rigidly stick to zero energy while changing B and gate voltages over large ranges. Furthermore, we show that this zero-bias peak (ZBP) is absent if we take out any of the necessary ingredients of the Majorana proposals; that is, the rigid ZBP disappears for zero magnetic field, for a magnetic field parallel to the spin-orbit field, or when we take out the superconductivity.

[1]Kavli Institute of Nanoscience, Delft University of Technology, 2600 GA Delft, Netherlands. [2]Department of Applied Physics, Eindhoven University of Technology, 5600 MB Eindhoven, Netherlands.

*These authors contributed equally to this work.
†To whom correspondence should be addressed. E-mail: l.p.kouwenhoven@tudelft.nl

We use InSb nanowires (*15*), which are known to have strong spin-orbit interaction and a large *g* factor (*16*). From our earlier quantum-dot experiments, we extract a spin-orbit length $l_{so} \approx 200$ nm corresponding to a Rashba parameter $\alpha \approx 0.2$ eV·Å (*17*). This translates to a spin-orbit energy scale $\alpha^2 m^*/(2\hbar^2) \approx 50$ μeV ($m^* = 0.015 m_e$ is the effective electron mass in InSb, m_e is the bare electron mass, and $\hbar$ is Planck's constant h divided by 2π). Importantly, the *g* factor in bulk InSb is very large ($g \approx 50$), yielding $E_Z/B \approx 1.5$ meV/T. As shown below, we find an induced superconducting gap $\Delta \approx 250$ μeV. Thus, for $\mu = 0$, we expect to enter the topological phase for $B \sim 0.15$ T where E_Z starts to exceed Δ. The energy gap of the topological superconductor is estimated to be a few kelvin (*17*), if we assume a ballistic nanowire. The topological gap is substantially reduced in a disordered wire (*18*, *19*). We have measured mean free paths of ~300 nm in our wires (*15*), implying a quasi-ballistic regime in micrometer-long wires. With these numbers, we expect Majorana zero-energy states to become observable below 1 K and around 0.15 T.

A typical sample is shown in Fig. 1B. We first fabricate a pattern of narrow (50-nm) and wider (300-nm) gates on a silicon substrate (*20*). The gates are covered by a thin Si_3N_4 dielectric before we randomly deposit InSb nanowires. Next, we electrically contact those nanowires that have landed properly relative to the gates. The lower contact in Fig. 1B fully covers the bottom part of the nanowire. We have designed the upper contact to only cover half of the top part of the nanowire, avoiding complete screening of the underlying gates. This allows us to change the Fermi energy in the section of the nanowire (NW) with induced superconductivity. We have used either a normal (N) or superconducting (S) material for the lower and upper contacts, resulting in three sample variations: (i) N-NW-S, (ii) N-NW-N, and (iii) S-NW-S. Here, we discuss our main results on the N-NW-S devices, whereas the other two types, serving as control devices, are described in (*20*).

To perform spectroscopy on the induced superconductor, we created a tunnel barrier in the nanowire by applying a negative voltage to a narrow gate (dark green area in Fig. 1, B and C). A bias voltage applied externally between the N and S contacts drops almost completely across the tunnel barrier. In this setup, the differential conductance dI/dV at voltage V and current I is proportional to the density of states at energy $E = eV$ (where e is the charge on the electron) relative to the zero-energy dashed line in Fig. 1C. Figure 1D shows an example taken at $B = 0$. The two peaks at ±250 μeV correspond to the peaks in the quasi-particle density of states of the induced superconductor, providing a value for the induced gap, $\Delta \approx 250$ μeV. We generally find a finite dI/dV in between these gap edges. We observe pairs of resonances with energies symmetric around zero bias superimposed on nonresonant

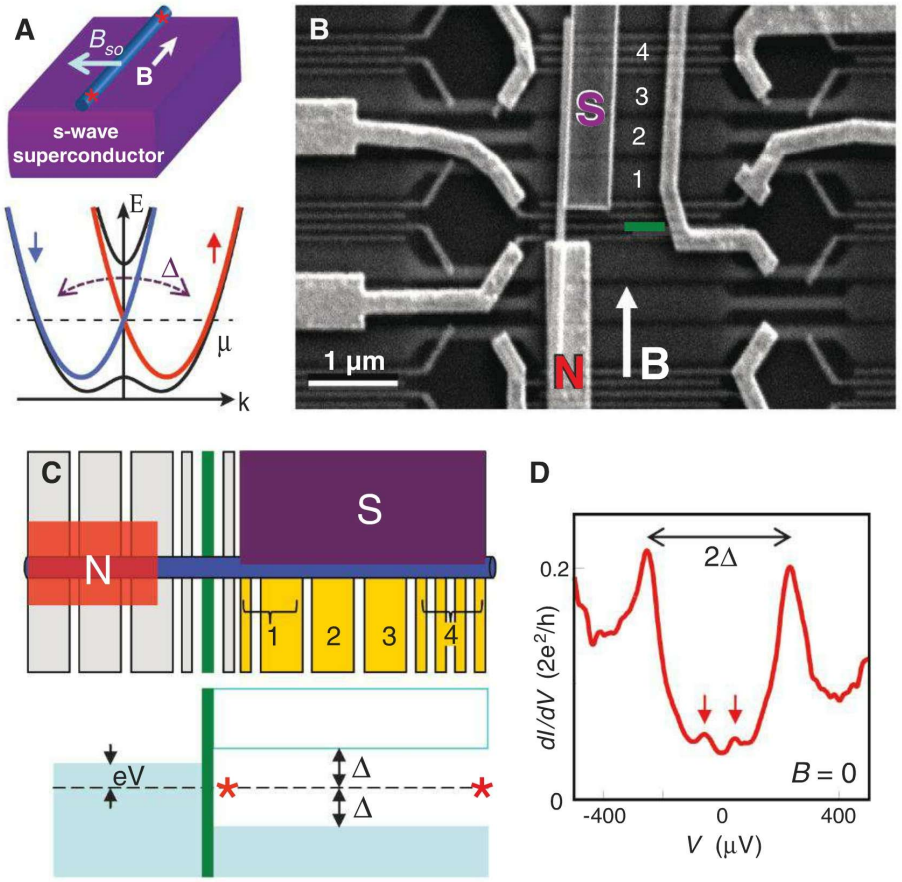

Fig. 1. (**A**) Outline of theoretical proposals. (Top) Conceptual device layout with a semiconducting nanowire in proximity to an s-wave superconductor. An external *B* field is aligned parallel to the wire. The Rashba spin-orbit interaction is indicated as an effective magnetic field, B_{so}, pointing perpendicular to the nanowire. The red stars indicate the expected locations of a Majorana pair. (Bottom) Energy, *E*, versus momentum, *k*, for a 1D wire with Rashba spin-orbit interaction, which shifts the spin-down band (blue) to the left and the spin-up band (red) to the right. Blue and red parabolas are for $B = 0$; black curves are for $B \neq 0$, illustrating the formation of a gap near $k = 0$ of size E_z (μ is the Fermi energy with $\mu = 0$ defined at the crossing of parabolas at $k = 0$). The superconductor induces pairing between states of opposite momentum and opposite spin, creating a gap of size Δ. (**B**) Implemented version of theoretical proposals. Scanning electron microscope image of the device with normal (N) and superconducting (S) contacts. The S contact only covers the right part of the nanowire. The underlying gates, numbered 1 to 4, are covered with a dielectric. [Note that gate 1 connects two gates, and gate 4 connects four narrow gates; see (C).] (**C**) (Top) Schematic of our device. (Bottom) illustration of energy states. The green rectangle indicates the tunnel barrier separating the normal part of the nanowire on the left from the wire section with induced superconducting gap, Δ. [In (B), the barrier gate is also shown in green.] An external voltage, *V*, applied between N and S drops across the tunnel barrier. Red stars again indicate the idealized locations of the Majorana pair. Only the left Majorana is probed in this experiment. (**D**) Example of differential conductance, dI/dV, versus *V* at $B = 0$ and 65 mK, serving as a spectroscopic measurement on the density of states in the nanowire region below the superconductor. Data are from device 1. The two large peaks, separated by 2Δ, correspond to the quasi-particle singularities above the induced gap. Two smaller subgap peaks, indicated by arrows, likely correspond to Andreev bound states located symmetrically around zero energy. Measurements are performed in dilution refrigerators with the use of the standard low-frequency lock-in technique (frequency = 77 Hz, excitation = 3 μV) in the four-terminal (devices 1 and 3) or two-terminal (device 2) current-voltage geometry.

currents throughout the gap region. Symmetric resonances likely originate from Andreev bound states (*21*, *22*), whereas nonresonant current indicates that the proximity gap has not fully developed (*23*).

Figure 2 summarizes our main result. Figure 2A shows a set of dI/dV-versus-V traces taken at increasing *B* fields in 10-mT steps from 0 (bottom trace) to 490 mT (top trace), offset for clarity. We again observe the gap edges at ±250 μeV. When we apply a *B* field between ~100 and ~400 mT along the nanowire axis, we observe a peak at $V = 0$. The peak has an amplitude up to $\sim 0.05 \cdot 2e^2/h$ and is clearly discernible from the background

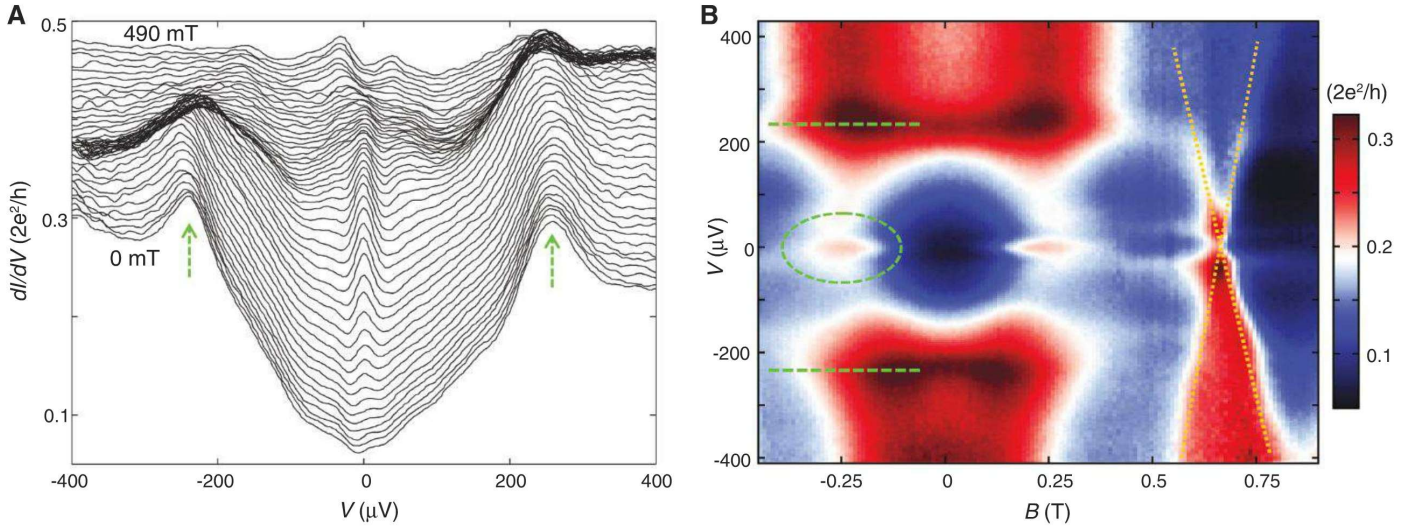

Fig. 2. Magnetic field–dependent spectroscopy. (**A**) *dI/dV* versus *V* at 70 mK taken at different *B* fields (from 0 to 490 mT in 10-mT steps; traces are offset for clarity, except for the lowest trace at $B = 0$). Data are from device 1. Arrows indicate the induced gap peaks. (**B**) Color-scale plot of *dI/dV* versus *V* and *B*. The ZBP is highlighted by a dashed oval; green dashed lines indicate the gap edges. At ~0.6 T, a non-Majorana state is crossing zero bias with a slope equal to ~3 meV/T (indicated by sloped yellow dotted lines). Traces in (A) are extracted from (B).

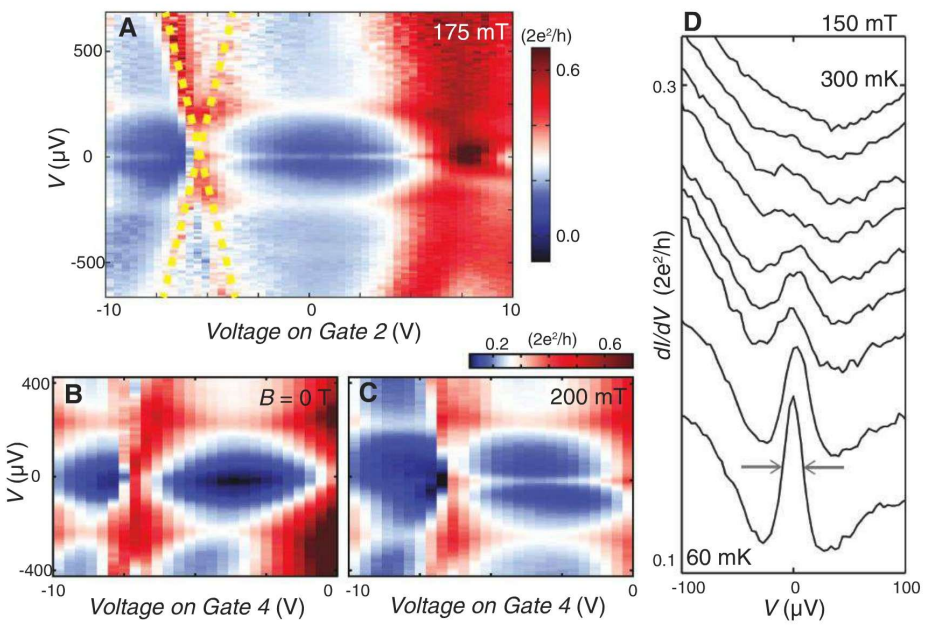

Fig. 3. Gate-voltage dependence. (**A**) A 2D color plot of *dI/dV* versus *V* and voltage on gate 2 at 175 mT and 60 mK. Andreev bound states cross through zero bias, for example, near –5 V (yellow dotted lines). The ZBP is visible from –10 to ~5 V (although in this color setting, it is not equally visible everywhere). Split peaks are observed in the range of 7.5 to 10 V (*20*). In (**B**) and (**C**), we compare voltage sweeps on gate 4 for 0 and 200 mT with the ZBP absent and present, respectively. Temperature is 50 mK. [Note that in (C) the peak extends all the way to –10 V (*19*).] (**D**) Temperature dependence. *dI/dV* versus *V* at 150 mT. Traces have an offset for clarity (except for the lowest trace) and are taken at different temperatures (from bottom to top: 60, 100, 125, 150, 175, 200, 225, 250, and 300 mK). *dI/dV* outside the ZBP at $V = 100$ μeV is $0.12 \pm 0.01 \cdot 2e^2/h$ for all temperatures. A FWHM of 20 μeV is measured between the arrows. All data in this figure are from device 1.

conductance. Above ~400 mT, we observe a pair of peaks. The color panel in Fig. 2B provides an overview of states and gaps in the plane of energy and *B* field from –0.5 to 1 T. The observed symmetry around $B = 0$ is typical for all of our data sets, demonstrating reproducibility and the absence of hysteresis. We indicate the gap edges with horizontal green dashed lines (highlighted only for $B < 0$). A pair of resonances crosses zero energy at ~0.65 T with a slope on the order of E_Z (highlighted by orange dotted lines). We have followed these resonances up to high bias voltages in (*20*) and identified them as Andreev states bound within the gap of the bulk NbTiN superconducting electrodes (~2 meV). In contrast, the ZBP sticks to zero energy over a range of $\Delta B \sim 300$ mT centered around ~250 mT. Again at ~400 mT, we observe two peaks located at symmetric, finite biases.

To identify the origin of these ZBPs, we need to consider various options including the Kondo effect, Andreev bound states, weak antilocalization, and reflectionless tunneling versus a conjecture of Majorana bound states. ZBPs due to the Kondo effect (*24*) or Andreev states bound to s-wave superconductors (*25*) can occur at finite *B*; however, with changing *B*, these peaks then split and move to finite energy. A Kondo resonance moves with $2E_Z$ (*24*), which is easy to dismiss as the origin for our ZBP because of the large *g* factor in InSb. (Note that even a Kondo effect from an impurity with $g = 2$ would be discernible.) Reflectionless tunneling is an enhancement of Andreev reflection by time-reversed paths in a diffusive normal region (*26*). As in the case of weak antilocalization, the resulting ZBP is maximal at $B = 0$ and disappears when *B* is increased; see also (*20*). We thus conclude that the above options for a ZBP do not provide natural explanations for our observations. We are not aware of any mechanism that could explain our observations, besides the conjecture of a Majorana.

To further investigate the zero-biasness of our peak, we measured gate voltage dependences. Figure 3A shows a color panel with voltage sweeps on gate 2. The main observation is the occurrence of two opposite types of behavior. First, we observe peaks in the density of

states that change with energy when changing gate voltage (highlighted with yellow dotted lines); these are the same resonances as shown in Fig. 2B and analyzed in (*20*). The second observation is that the ZBP from Fig. 2, which we take at 175 mT, remains stuck to zero bias while changing the gate voltage over a range of several volts. Clearly, our gates work because they change the Andreev bound states by ~0.2 meV per volt on the gate. Panels (B) and (C) in Fig. 3 underscore this observation with voltage sweeps on a different gate, number 4. Fig. 3B shows that, at zero magnetic field, no ZBP is observed. At 200 mT, the ZBP becomes again visible in Fig. 3C. Comparing the effect of gates 2 and 4, we observe that neither moves the ZBP away from zero.

Initially, Majorana fermions were predicted in single-subband, 1D wires (*8*, *9*), but further work extended these predictions to multisubband wires (*27*–*30*). In the nanowire section that is uncovered, we can gate tune the number of occupied subbands from 0 to ~4 with subband separations of several millielectron volts. Gate tuning in the nanowire section covered with superconductor is much less effective due to efficient screening. The number of occupied subbands in this part is unknown, but it is most likely multiple subbands. As shown in figs. S9 and S11 of (*20*), we do have to tune gate 1 and the tunnel barrier to the right regime to observe the ZBP.

We have measured in total several hundred panels sweeping various gates on different devices. Our main observations are (i) a ZBP exists over a substantial voltage range for every gate starting from the barrier gate until gate 4, (ii) we can occasionally split the ZBP in two peaks located symmetrically around zero, and (iii) we can never move the peak away from zero to finite bias (*20*). Data sets such as those in Figs. 2 and 3 demonstrate that the ZBP remains stuck to zero energy over considerable changes in B and gate voltage V_g.

Figure 3D shows the temperature dependence of the ZBP. We find that the peak disappears at ~300 mK, providing a thermal-energy scale of $k_BT \sim 30$ μeV (where k_B is Boltzmann constant and T is temperature). The full width at half maximum (FWHM) at the lowest temperature is ~20 μeV, which we believe is a consequence of thermal broadening as $3.5 \cdot k_BT(60\ \text{mK}) = 18$ μeV.

Next, we verify explicitly that all the required ingredients in the theoretical Majorana proposals (Fig. 1A) are indeed essential for observing the ZBP. We have already verified that a nonzero B field is needed. We then test to see whether spin-orbit interaction is crucial for the absence or presence of the ZBP. Theory requires that the external B has a component perpendicular to B_{so} (the spin-orbit magnetic field). We have measured a second device in a different setup containing a 3D vector magnet such that we can sweep the B field in arbitrary directions. In Fig. 4, we show dI/dV versus V while varying the angle for a constant field magnitude. In Fig. 4A, the plane of rotation is approximately equal to the plane of the substrate. We clearly observe that the ZBP comes and goes, depending on the angle. The ZBP is completely absent around π/2, which we thus deduce as the direction of B_{so}. In Fig. 4B, the plane of rotation is perpendicular to B_{so}. Indeed, we observe that the ZBP is now present for all angles, because B is now always perpendicular to B_{so}. These observations are in full agreement with expectations for the spin-orbit direction in our samples (*17*, *31*). We have further verified that this angle dependence is not a result of the specific magnitude of B or a variation in g factor (*20*).

As a last check, we have fabricated and measured a device of identical design but with the superconductor replaced by a normal Au contact (that is, a N-NW-N geometry). In this sample, we have not found any signature of a peak that sticks to zero bias while changing both B and V_g (*20*). This test experiment shows that superconductivity is also an essential ingredient for our ZBP.

To summarize, we have reproduced our observation of a rigid ZBP in three different devices and in two different setups. Our general observations are: (i) a ZBP appears at finite B and sticks to zero bias over a range from 0.07 to 1 T; (ii) the ZBP remains at zero bias while changing the voltage on any of our gates over large ranges; (iii) the ZBP comes and goes with the angle of the B field with respect to the wire axis, which is in agreement with the expected spin-orbit interaction; and (iv) the rigid ZBP is

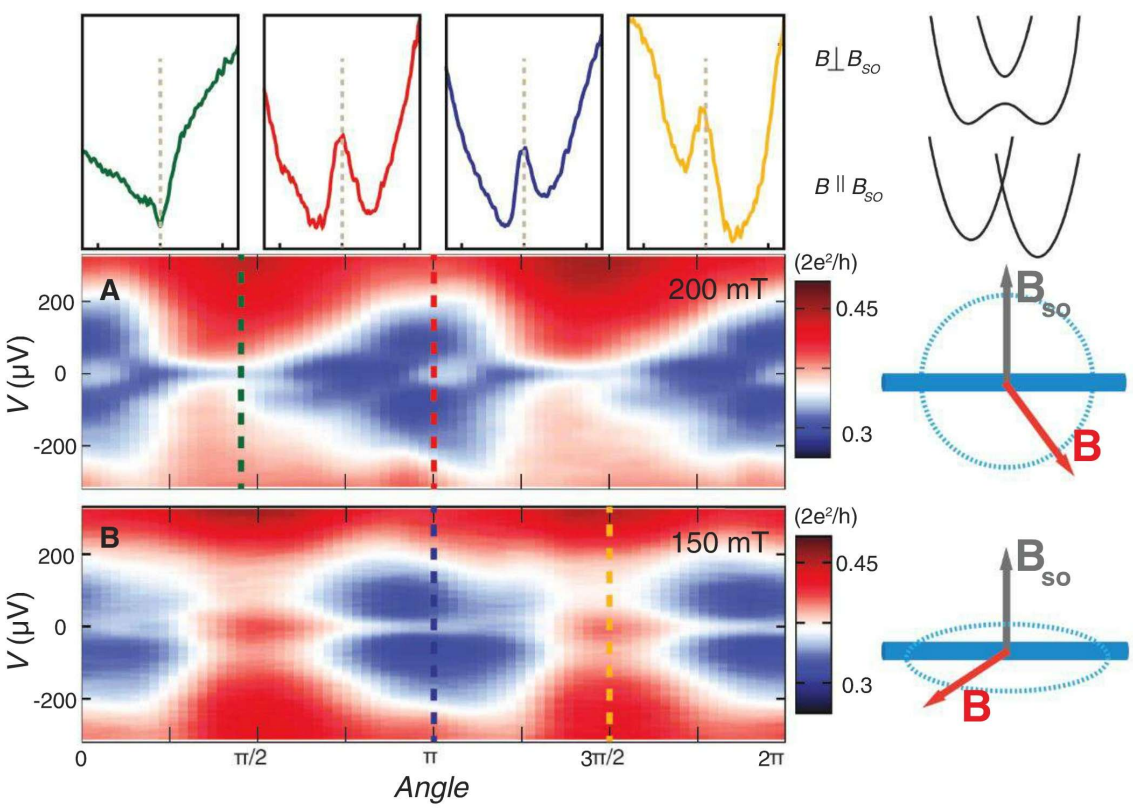

Fig. 4. Magnetic-field orientation dependence. dI/dV versus V and varying the angle of B at fixed magnitude. Data from device 2 are measured in a different setup at ~150 mK; zero angle is along the nanowire for both panels. (**A**) Rotation of $|B| = 200$ mT in the plane of the substrate. The ZBP is at a maximum when B is parallel and is absent when B is perpendicular to the wire. (**B**) Rotation of $|B| = 150$ mT in the plane perpendicular to B_{so}. The ZBP is now present for all angles. The panels on top show linecuts at angles with corresponding colors in (A) and (B). Panels on the right side illustrate, from top to bottom: (i) For B perpendicular to B_{so} a gap opens lifting fermion doubling, as is required for Majoranas. (ii) For B parallel to B_{so}, the two spin bands from Fig. 1A shift vertically by $2E_Z$. In this configuration, a zero-energy Majorana is not expected. (iii) Panel of rotation of B for data in (A) is shown. (iv) Panel of rotation of B for data in (B) is shown.

absent when the superconductor is replaced by a normal conductor. Based on these observations, we conclude that our spectroscopy experiment provides evidence for the existence of Majorana fermions.

Improving the electron mobility and optimizing the gate coupling will enable us to map out the phase diagram of the topological superconductor in the plane of E_Z and μ (*27*–*30*). It will be interesting to control the subband occupation underneath the superconductor down to a single subband to make direct comparisons to theoretical models. Currently, we probe induced gaps and states from all occupied subbands, each with a different coupling to the tunnel barrier. The topological state in the topmost subband likely has the weakest coupling to the tunnel barrier. Single-subband models (*8*, *9*) predict that one should observe a closing of the topological gap; however, in multisubband systems, this gap closing may not be visible. The constant gap in Fig. 2 may come from lower subbands. The presence of multiple subbands together with our finite temperature may also be the reason that our ZBP is currently only ~5% of the theoretical zero-temperature limit of $2e^2/h$ (*12*, *14*).

Finally, we note that this work does not address the topological properties of Majorana fermions. The first step toward demonstrating topological protection would be the observation of conductance quantization (*12*, *32*). Second, in a Josephson tunnel junction with phase difference φ and a pair of Majoranas on either side, the current-phase relation becomes proportional to $\sin(\varphi/2)$. The factor 2 is another distinct Majorana signature, which should be observable as an h/e flux periodicity in a superconducting quantum interference device measurement (*8*, *9*). The last type of experiment involves the exchange of Majoranas around each other. Such braiding experiments can reveal their non-Abelian statistics, which are the ultimate proof of topologically protected Majorana fermions (*33*–*35*).

References and Notes

1. E. Majorana, *Soryushiron Kenkyu* (Engl. transl.) **63**, 149 (1981) [translation from *Nuovo Cimento* **14**, 171 (1937)].
2. F. Wilczek, *Nat. Phys.* **5**, 614 (2009).
3. M. Franz, *Physics* **3**, 24 (2010).
4. A. Yu. Kitaev, *Phys. Usp.* **44**, 131 (2001).
5. L. Fu, C. L. Kane, *Phys. Rev. Lett.* **100**, 096407 (2008).
6. J. D. Sau, R. M. Lutchyn, S. Tewari, S. Das Sarma, *Phys. Rev. Lett.* **104**, 040502 (2010).
7. J. Alicea, *Phys. Rev. B* **81**, 125318 (2010).
8. R. M. Lutchyn, J. D. Sau, S. Das Sarma, *Phys. Rev. Lett.* **105**, 077001 (2010).
9. Y. Oreg, G. Refael, F. von Oppen, *Phys. Rev. Lett.* **105**, 177002 (2010).
10. C. W. J. Beenakker, http://arxiv.org/abs/1112.1950 (2011).
11. J. Alicea, http://arxiv.org/abs/1202.1293 (2012).
12. K. T. Law, P. A. Lee, T. K. Ng, *Phys. Rev. Lett.* **103**, 237001 (2009).
13. K. Flensberg, *Phys. Rev. B* **82**, 180516 (2010).
14. J. D. Sau, S. Tewari, R. Lutchyn, T. Stanescu, S. Das Sarma, *Phys. Rev. B* **82**, 214509 (2010).
15. S. R. Plissard *et al.*, *Nano Lett.* **12**, 1794 (2012).
16. H. A. Nilsson *et al.*, *Nano Lett.* **9**, 3151 (2009).
17. S. Nadj-Perge *et al.*, *Phys. Rev. Lett.* **108**, 166801 (2012).
18. P. W. Brouwer, M. Duckheim, A. Romito, F. von Oppen, *Phys. Rev. Lett.* **107**, 196804 (2011).
19. J. D. Sau, S. Tewari, S. Das Sarma, *Phys. Rev. B* **85**, 064512 (2012).
20. See supplementary materials on *Science* Online.
21. J. D. Pillet *et al.*, *Nat. Phys.* **6**, 965 (2010).
22. T. Dirks *et al.*, *Nat. Phys.* **7**, 386 (2011).
23. H. le Sueur, P. Joyez, H. Pothier, C. Urbina, D. Esteve, *Phys. Rev. Lett.* **100**, 197002 (2008).
24. S. Sasaki *et al.*, *Nature* **405**, 764 (2000).
25. M. Zareyan, W. Belzig, Yu. V. Nazarov, *Phys. Rev. B* **65**, 184505 (2002).
26. B. J. van Wees, P. de Vries, P. Magnée, T. M. Klapwijk, *Phys. Rev. Lett.* **69**, 510 (1992).
27. M. Wimmer, A. R. Akhmerov, M. V. Medvedyeva, J. Tworzydło, C. W. Beenakker, *Phys. Rev. Lett.* **105**, 046803 (2010).
28. A. C. Potter, P. A. Lee, *Phys. Rev. Lett.* **105**, 227003 (2010).
29. R. M. Lutchyn, T. D. Stanescu, S. Das Sarma, *Phys. Rev. Lett.* **106**, 127001 (2011).
30. T. D. Stanescu, R. M. Lutchyn, S. Das Sarma, *Phys. Rev. B* **84**, 144522 (2011).
31. P. Středa, P. Šeba, *Phys. Rev. Lett.* **90**, 256601 (2003).
32. M. Wimmer, A. R. Akhmerov, J. P. Dahlhaus, C. W. J. Beenakker, *N. J. Phys.* **13**, 053016 (2011).
33. N. Read, D. Green, *Phys. Rev. B* **61**, 10267 (2000).
34. D. A. Ivanov, *Phys. Rev. Lett.* **86**, 268 (2001).
35. C. Nayak, S. H. Simon, A. Stern, M. Freedman, S. Das Sarma, *Rev. Mod. Phys.* **80**, 1083 (2008).

Acknowledgments: We thank D. Thoen and T. Klapwijk for sharing their NbTiN technology and A. Akhmerov, J. Alicea, C. Beenakker, M. Freedman, F. Hassler, G. Immink, H. Keijzers, C. Marcus, S. Nadj-Perge, Y. Nazarov, I. van Weperen, M. Wimmer, and D. van Woerkom for discussions and assistance. This work has been supported by European Research Council, Netherlands Organization for Scientific Research (NWO), Foundation for Fundamental Research on Matter (FOM), and Microsoft Corporation Station Q.

Supplementary Materials

www.sciencemag.org/cgi/content/full/science.1222360/DC1
Supplementary Text
Figs. S1 to S14
References (*36*, *37*)
Data Files

23 March 2012; accepted 5 April 2012
Published online 12 April 2012;
10.1126/science.1222360

Unidirectional Growth of Microbumps on (111)-Oriented and Nanotwinned Copper

Hsiang-Yao Hsiao,[1] Chien-Min Liu,[1] Han-wen Lin,[1] Tao-Chi Liu,[1] Chia-Ling Lu,[1] Yi-Sa Huang,[1] Chih Chen,[1]* K. N. Tu[2]*

Highly oriented [111] Cu grains with densely packed nanotwins have been fabricated by direct-current electroplating with a high stirring rate. The [111]-oriented and nanotwinned Cu (nt-Cu) allow for the unidirectional growth of Cu_6Sn_5 intermetallics in the microbumps of three-dimensional integrated-circuit packaging; a uniform microstructure in a large number of microbumps of controlled orientation can be obtained. The high-density twin boundaries in the nt-Cu serve as vacancy sinks during the solid-state reaction between Pb-free solder and Cu and greatly reduce the formation of Kirkendall (or Frenkel) voids.

A change from two-dimensional to three-dimensional integrated circuits (3D IC) is under way in the microelectronics industry as the limits of very-large-scale integration in silicon chip technology are approached (*1*). In essence, 3D IC is intended to bring packaging technology and chip technology together. With respect to scaling the density of solder bumps on a chip surface, the diameter of a flip-chip solder bump is about 100 μm today, and it should be possible to reduce this to 1 μm. This improvement will increase the density of bumps per unit area by 4 orders of magnitude, yet the solder volume will be reduced by 6 orders of magnitude. However, the melting point of the solder remains unchanged, meaning that each microbump may contain only a few grains after processing. Variation in the grain orientation may lead to a wide distribution of the orientation-dependent properties of microbumps, which may in turn lead to early failure and low reliability. This is because certain grain orientations allow fast diffusion and electromigration (*2*, *3*). Because there are a large number of microbumps on a stack of chips in a 3D IC, achieving a uniform microstructure in several thousand of these microbumps on each chip is a critical issue.

Maintaining control over the microstructure of the microbumps is nontrivial because of

[1]Department of Materials Science and Engineering, National Chiao Tung University, Hsinchu, Taiwan 30010, Republic of China. [2]Department of Materials Science and Engineering, University of California at Los Angeles, Los Angeles, CA 90095, USA.

*To whom correspondence should be addressed. E-mail: chih@mail.nctu.edu.tw (C.C.); kntu@ucla.edu (K.N.T.)

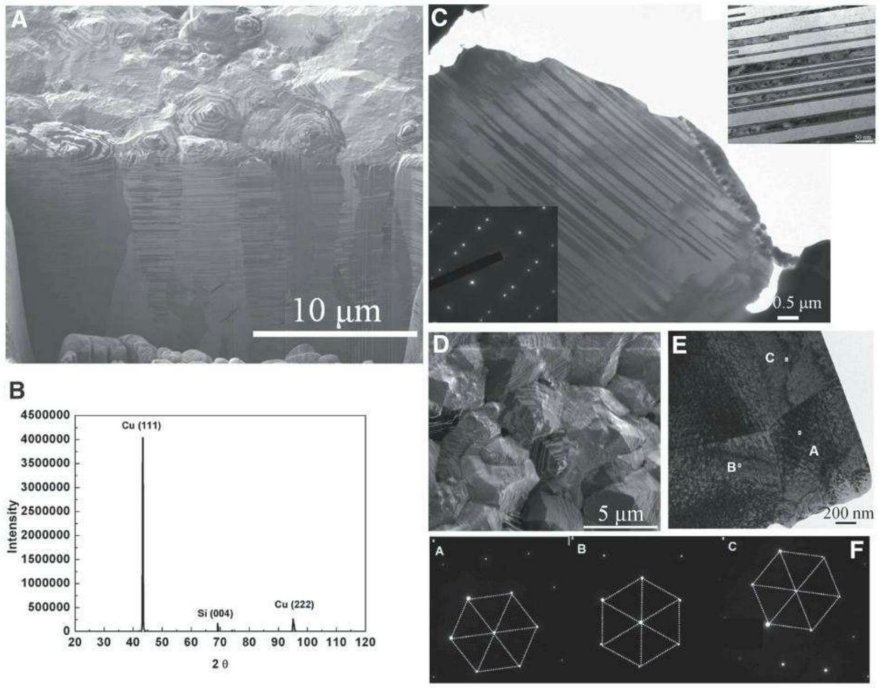

Fig. 1. The microstructural characterization of the electroplated Cu at a current density of 80 mA/cm^2 for 30 min at a stirring speed of 1200 rpm. (**A**) Cross-sectional FIB micrograph. (**B**) X-ray diffraction. (**C**) Cross-sectional image showing the Cu nanotwins near the cone. (**D**) Plan-view FIB micrograph. (**E**) Plan-view TEM image. (**F**) Diffraction patterns of the three grains in (E).

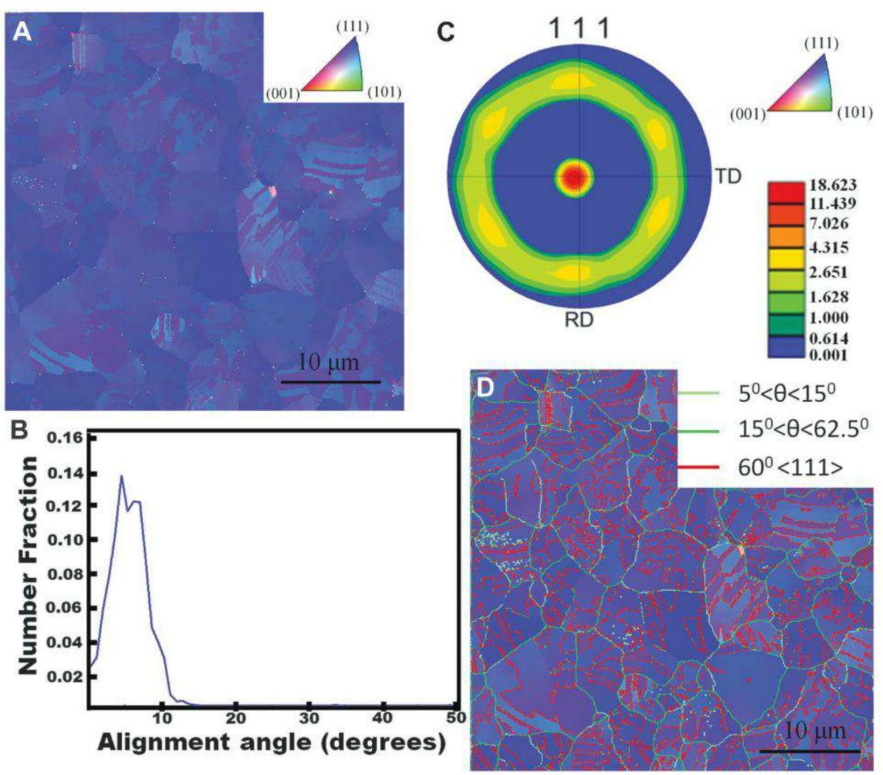

Fig. 2. EBSD analysis of the nt-Cu. (**A**) Plan-view inverse pole figure maps of the Cu surface. Color coding displays the out-of-plan direction in terms of the inverse pole figure. (**B**) Number fraction of the Cu grains deviated from [111] as a function of angle. (**C**) {111} pole figures of the fabricated Cu. TD and RD represent transverse direction and rolling direction, respectively. (**D**) Grain boundary characteristics.

reflow. Reflow means that the solder bump is melted to achieve chip-to-chip or chip-to-substrate joints. It is very difficult to control the solid-state microstructure as a molten solder bump solidifies; typically, the grains are randomly oriented. Furthermore, during the solid-state aging of the microbumps, the solder will transform into intermetallic compounds. These compounds will dominate the properties of the microbumps because the solder thickness decreases to about 10 μm or less in microbumps to connect the through-Si-vias (TSVs).

We report that using [111]-oriented nanotwinned Cu (nt-Cu) as the under-bump metallization promotes the unidirectional growth of intermetallic compounds in a large number of microbumps, leading to a uniform microstructure of all the microbumps. Unidirectional growth recalls the single-crystal turbine blades of a superalloy, requiring a crystal seed and a temperature gradient (*4*). To seed thousands of individual microbumps on a chip is impractical. Instead, we report a method of unidirectional growth that uses reactive epitaxial growth of

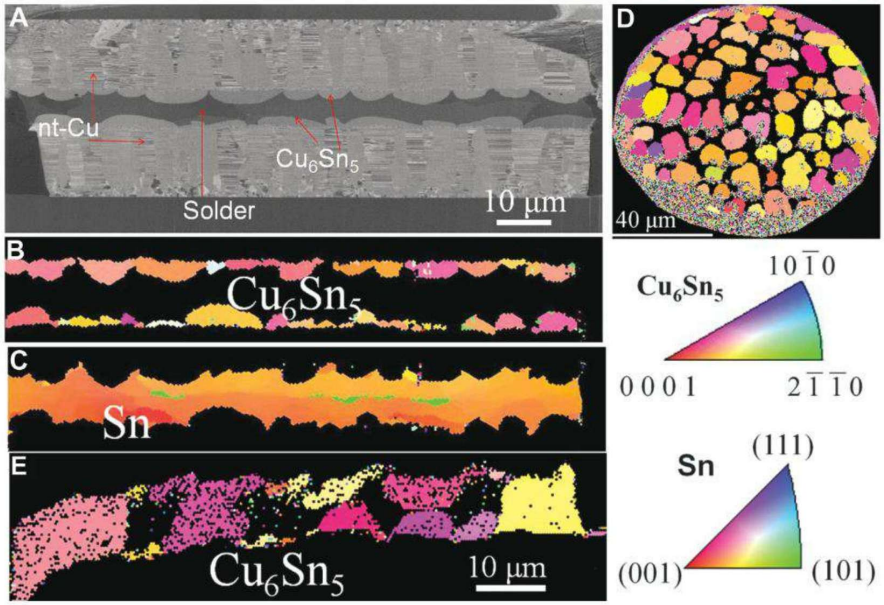

Fig. 3. (**A**) FIB image showing a microbump with 20-μm nt-Cu under-bump metallizations on both sides. (**B**) EBSD orientation image maps in the rolling direction for the Cu_6Sn_5 intermetallic compounds. (**C**) Orientation image maps for the remaining Sn2.5Ag in the rolling direction. (**D**) Plan-view orientation image maps in the normal direction for a microbump reflowed at 260°C for 5 min. (**E**) Another microbump reflowed for 5 min at 260°C.

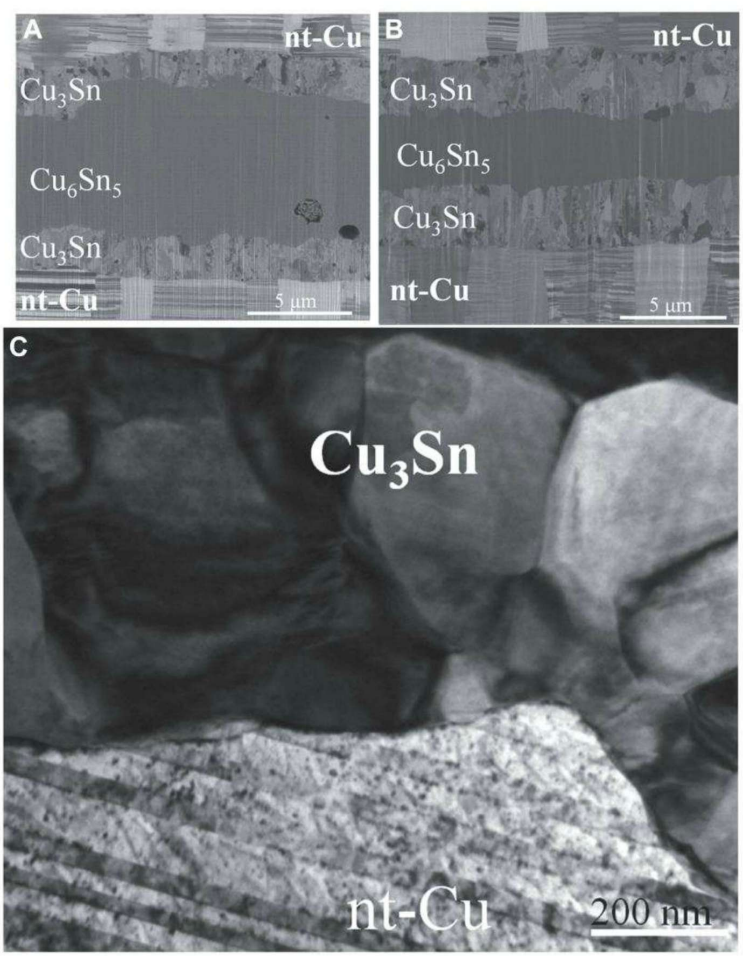

Fig. 4. Cross-sectional FIB image showing a microbump aged at 150°C (**A**) for 500 hours and (**B**) for 1000 hours. (**C**) Cross-sectional TEM image showing the interface of Cu_3Sn and nt-Cu.

microbumps on [111]-oriented nanotwin Cu. The [111] single crystals of Cu are replaced by [111]-oriented nt-Cu in every microbump. The small diameter of the microbump enables the growth of only a few oriented grains, and smaller and misoriented grains will be eliminated by ripening. The prerequisite is the preparation of oriented (111) nt-Cu as the under-bump metallization in each of thousands of microbumps. We have achieved this by introducing a rapid rotation of the electrolyte in the electroplating of Cu and by adding surfactants in the electrolyte solution.

Randomly oriented nt-Cu has been fabricated by using pulsed electroplating (*5*–*7*), and it possesses excellent mechanical strength (*8*–*11*). It also exhibits a higher electromigration resistance than regular Cu grains (*12*). For these reasons, nt-Cu has drawn a great deal of recent attention. Anderoglu *et al.* reported that nt-Cu with a [111] preferred orientation can be deposited via magnetron sputtering (*13*). However, in interconnect and packaging technology, Cu interconnects are deposited by electroplating.

In this report, [111]-oriented Cu grains with nt-Cu have been fabricated by dc electroplating with sulfuric acid as the electrolyte. Surfactants are added to the electrolyte, and the stirring speed of the electrolyte, ranging from 600 to 1200 revolutions per min (rpm), is critical to the outcome of the electroplating (*14*).

Highly oriented nt-Cu can be fabricated by specific current densities and stirring rates in electrolyte (supplementary materials and figs. S2 and S3). Figure 1A shows the cross-sectional focused ion beam (FIB) image for the nt-Cu electroplated with a current density of 80 mA/cm^2 at 1200 rpm for 30 min. The thickness of the Cu film is greater than 20 μm, and columnar Cu grains with unidirectional nanotwins are obtained (figs. S4 and S5). The normal of all the [111]-oriented nanotwins are aligned nearly parallel to the film growth direction. X-ray diffraction indicates that these Cu grains possess a very strong [111] preferred orientation (Fig. 1B and fig. S4). We note that many cones appear on the film surface. Spots from twins were observed in

the cross-sectional transmission electron microscopy (TEM) image and the corresponding electron diffraction pattern for the cone microstructure (Fig. 1C). The spacing of the nanotwins ranges from 10 to 100 nm. Figure 1D shows the plan-view FIB image of the cones on the Cu film surface. The nanotwins may have nucleated at the tips of the cones. The plan-view TEM and electron diffraction images of one of the cones have been examined to confirm the [111] orientation, and the edges of the cone exhibit sixfold symmetry. Figure 1E presents the plan-view TEM image for three neighboring (111) grains: A, B, and C in the middle of the sample, prepared by FIB polishing. The corresponding selected area diffraction pattern is shown in Fig. 1F. The rotation angle between grains A and B is 22°, whereas it is 15° between grains A and C.

Electron backscatter diffraction (EBSD) was used to analyze the statistical distributions of the grain orientations and the grain boundaries (fig. S1). The orientation image maps of the film surface after polishing by FIB show that the Cu film has a strong {111} texture (Fig. 2A). The corresponding color in the inverse pole figure (Fig. 2) represents the out-of-plane direction, indicating a very strong preferred orientation of [111]. The statistical data for the misalignment angles of the Cu (111) grains indicate that 96% of the columnar Cu grains have less than 10° of misalignment with respect to the [111] direction (Fig. 2B). In addition, Fig. 2C shows the fraction with the ⟨111⟩ out-of-plane direction in terms of the intensity of the central pole. The high density at the central pole reveals that a very high fraction of the electroplated Cu grains have a ⟨111⟩ preferred orientation. Figure 2D shows the grain boundaries, including the low, high, and twin boundaries. Here, we define low-angle grain boundaries as those with a misorientation angle less than 15° and high-angle boundaries as those with a misorientation angle between 15° and 65°. A twin boundary is categorized by a 60° angle grain boundary. The results indicate that most of the grain boundaries analyzed can be characterized as high-angle boundaries.

Suh reported the orientation relationship between a [001]-oriented Cu single crystal and the Cu_6Sn_5 grains (*15*). Zou studied the orientation relationships between the Cu_6Sn_5 grains and [111]-oriented Cu single crystals (*16*, *17*). We can fabricate oriented nt-Cu in patterned openings and have applied the very strongly oriented [111] nt-Cu to control the orientations of the Cu_6Sn_5 grains in a large number of microbumps (figs. S5 and S6). Figure 3A shows the cross-sectional FIB image of a microbump between two chips with a 10.5-μm-thick Sn2.5Ag solder after a reflow of 3 min at 260°C. The solder thickness is close to that found in 3D IC packaging. The Cu_6Sn_5 compounds grew on the (111) planes of the nt-Cu under-bump metallization. The EBSD orientation image maps for the Cu_6Sn_5 compounds indicate a preferred orientation near the (0001) plane of the Cu_6Sn_5 (Fig. 3B). Figure 3C presents the orientation image maps for the remaining Sn2.5Ag. A plan-view EBSD analysis was also performed to confirm the preferred orientation of all the Cu_6Sn_5 compounds on a microbump (Fig. 3D). Almost all the Cu_6Sn_5 grains have a preferred orientation close to (0001) (fig. S7). In another sample reflowed for 5 min at 260°C, some of the Cu_6Sn_5 grains on the top chip nearly touched the Cu_6Sn_5 grains on the bottom chip (Fig. 3E). Upon closer inspection, some have merged into one grain. We observe that two misoriented Cu_6Sn_5 grains on the top and bottom always merge into one single Cu_6Sn_5 grain, as indicated by the arrows in the figure.

Lastly, we note that the metallization on oriented nt-Cu forms very few or no Kirkendall (or Frenkel) voids during solid-state aging (*18*). It has been reported that severe Kirkendall voids form in the Cu_3Sn/Cu interface after solid-state aging in solder joints and greatly weaken the mechanical properties of the joint (*19*, *20*). The cross-sectional FIB image of a microbump after solid-state aging at 150°C for 500 hours (Fig. 4A) shows that the solder has been transformed completely into Cu_6Sn_5 and Cu_3Sn. The Cu_3Sn layer is 2.14 μm thick, yet only a few voids are observed in the Cu_3Sn/Cu interface. After aging at 150°C for 1000 hours, the Cu_3Sn layer thickness grew to 3.12 μm (Fig. 4B), and no obvious Kirkendall voids were found (fig. S8). Figure 4C shows the cross-sectional TEM image of the interface of Cu_3Sn/nt-Cu; some nanotwins end in Cu_3Sn grains. In transforming one molecule of Cu_6Sn_5 into two molecules of Cu_3Sn, the remaining three Sn atoms will attract nine Cu atoms to form three Cu_3Sn molecules, and the vacancies required for the Cu diffusion may condense to form voids. Although the twin boundaries are coherent, there are steps and kinks that can serve as vacancy sinks. In addition, Xu *et al.* reported that there are butt twins in the electroplated Cu and that they serve as vacancy sinks (*21*). The high density of nanotwins will provide high density of vacancy sinks. Therefore, no supersaturation of vacancies or nucleation of Kirkendall voids occurs. We expect that the electrical and mechanical properties of the microbumps without Kirkendall voids will be better.

Copper pillars without nanotwins have been implemented in microprocessors to increase the electromigration resistance and the performance of heat dissipation (*22*). The mechanically strong nanotwinned microbumps may cause a reliability concern because of chip-packaging interaction. In the traditional flip-chip technology, Si dies are bonded to polymer substrates, and large thermal stress thus occurs because of the mismatch in thermal expansion coefficients between the two materials. However, in 3D IC, Si dies are bonded to Si substrates of TSV interposers. Therefore, the chip-packaging interaction because of thermal stress is minimized in the microbumps.

By electroplating, we have fabricated highly oriented [111] nt-Cu in columnar [111]-oriented Cu grains in a large number of patterned under-bump metallizations of 20 μm diameter on Si wafers. The oriented nt-Cu can induce the unidirectional growth of [0001] Cu_6Sn_5 grains in solder reflow reactions. In subsequent solid-state aging, the nanotwin boundaries serve as vacancy sinks and prevent the supersaturation of vacancies at the interface of Cu_3Sn/Cu, leading to the formation of very few Kirkendall voids.

References and Notes

1. J. C. Lin *et al.*, paper presented at IEEE International Electron Devices Meeting, San Francisco, CA, 6 December 2010.
2. M. Lu, D. Y. Shih, P. Lauro, C. Goldsmith, D. W. Henderson, *Appl. Phys. Lett.* **92**, 211909 (2008).
3. C. Chen, H. M. Tong, K. N. Tu, *Annu. Rev. Mater. Res.* **40**, 531 (2010).
4. D. R. Flack, *Fundamentals of Jet Propulsion with Applications* (Cambridge Univ. Press, New York, 2005), chap. 8.
5. L. Lu, Y. Shen, X. Chen, L. Qian, K. Lu, *Science* **304**, 422 (2004); 10.1126/science.1092905.
6. L. Lu, X. Chen, X. Huang, K. Lu, *Science* **323**, 607 (2009).
7. X. Li, Y. Wei, L. Lu, K. Lu, H. Gao, *Nature* **464**, 877 (2010).
8. J. Schiøtz, K. W. Jacobsen, *Science* **301**, 1357 (2003).
9. S. J. Zhou, D. L. Preston, P. S. Lomdahl, D. M. Beazley, *Science* **279**, 1525 (1998).
10. L. Lu, M. L. Sui, K. Lu, *Science* **287**, 1463 (2000).
11. K. Lu, L. Lu, S. Suresh, *Science* **324**, 349 (2009).
12. K. C. Chen, W. W. Wu, C. N. Liao, L. J. Chen, K. N. Tu, *Science* **321**, 1066 (2008).
13. O. Anderoglu *et al.*, *Appl. Phys. Lett.* **93**, 083108 (2008).
14. See supplementary materials on *Science* Online.
15. J. O. Suh, K. N. Tu, N. Tamura, *J. Appl. Phys.* **102**, 063511 (2007).
16. H. F. Zou, H. J. Yang, Z. F. Zhang, *Acta Mater.* **56**, 2649 (2008).
17. H. F. Zou, H. J. Yang, Z. F. Zhang, *J. Appl. Phys.* **106**, 113512 (2009).
18. Y. Yin *et al.*, *Science* **304**, 711 (2004).
19. K. Zeng *et al.*, *J. Appl. Phys.* **97**, 024508 (2005).
20. R. Labie *et al.*, paper presented at the 3rd Electronic System-Integration Technology Conference (IEEE Components, Packaging, and Manufacturing Technology Society), Berlin, Germany, 13 September 2010.
21. L. Xu *et al.*, *J. Appl. Phys.* **104**, 113717 (2008).
22. A. Yeoh *et al.*, paper presented at Electronic Components and Technology Conference (IEEE), San Diego, CA, 30 May 2006.

Acknowledgments: The financial support from the National Science Council, Taiwan, under the contract NSC 98-2221-E-009-036-MY3 is acknowledged. The authors thank J.-C. Kuo at National Cheng Kung University for assistance in the EBSD analysis. A patent, "Electrodeposited nano-twins copper layer and method of fabricating the same," is under application. The processing conditions of the (111)-oriented nt-Cu have been submitted for a patent application. The rest of the data and figures in this Report have not been presented or published elsewhere.

Supplementary Materials

www.sciencemag.org/cgi/content/full/336/6084/1007/DC1
Materials and Methods
Figs. S1 to S8

11 November 2011; accepted 19 April 2012
10.1126/science.1216511

Real-Time Imaging of Pt_3Fe Nanorod Growth in Solution

Hong-Gang Liao,[1] Likun Cui,[1] Stephen Whitelam,[1,2] Haimei Zheng[1]*

The growth of colloidal nanocrystal architectures by nanoparticle attachment is frequently reported as an alternative to the conventional growth by monomer attachment. However, the mechanism whereby nanoparticle attachment proceeds microscopically remains unclear. We report real-time transmission electron microscopy (TEM) imaging of the solution growth of Pt_3Fe nanorods from nanoparticle building blocks. Observations revealed growth of winding polycrystalline nanoparticle chains by shape-directed nanoparticle attachment followed by straightening and orientation and shape corrections to yield single-crystal nanorods. Tracking nanoparticle growth trajectories allowed us to distinguish the force fields exerted by single nanoparticles and nanoparticle chains. Such quantification of nanoparticle interaction and understanding the growth pathways are important for the design of hierarchical nanomaterials and controlling nanocrystal self-assembly for functional devices.

Nanocrystals with different shapes and architectures are of considerable interest (*1*–*6*). Uncovering the growth mechanisms responsible for these various architectures has been a topic of intense study. Although nanocrystals have been achieved by a variety of solution growth processes (*1*, *7*–*10*), theories on the growth mechanisms largely fall into one of two categories: growth by monomer attachment or by nanoparticle attachment. According to classical theories of crystal growth, the shape of a nanocrystal is controlled by the relative surface energies of the different crystalline facets, such that higher-energy facets grow faster (*1*, *11*). Growth is assumed to proceed by monomer attachment to the existing nuclei. However, many recent studies suggest that nanoparticles can act as "artificial atoms" and form building blocks for the growth of hierarchical nanostructures. For example, there have been reports of growth by oriented attachment where small nanoparticles interact with each other to form single-crystal lattices (*3*, *7*, *10*, *12*–*14*). Similar growth has been found in the formation of numerous natural crystals by biomineralization processes (*7*, *15*).

Critical questions concerning how nanocrystal architectures grow from nanoparticle building blocks remain unresolved. For instance, it is unclear how the growth process of addition by nanoparticles (instead of monomers) takes place if growth is initiated in a molecular precursor solution. Does the process proceed by nanoparticles attaching one by one to a nucleus, analogous to conventional growth by monomer attachment? Is there a preferred facet or orientation for a nanoparticle to attach to an existing nanoparticle?

Recent developments in transmission electron microscopy (TEM) of imaging through liquids using a liquid environmental cell (*16*–*19*) provide the opportunity to address the above questions. One critical challenge is to maintain the small amount of liquid in the viewing window long enough to allow complete reactions, which is a key to study the growth of colloidal nanocrystals with different shapes and architectures. We overcome this challenge by using an advanced liquid handling technique (*20*) and

[1]Materials Sciences Division, Lawrence Berkeley National Laboratory, Berkeley, CA 94720, USA. [2]The Molecular Foundry, Lawrence Berkeley National Laboratory, Berkeley, CA 94720, USA.

*To whom correspondence should be addressed. E-mail: hmzheng@lbl.gov

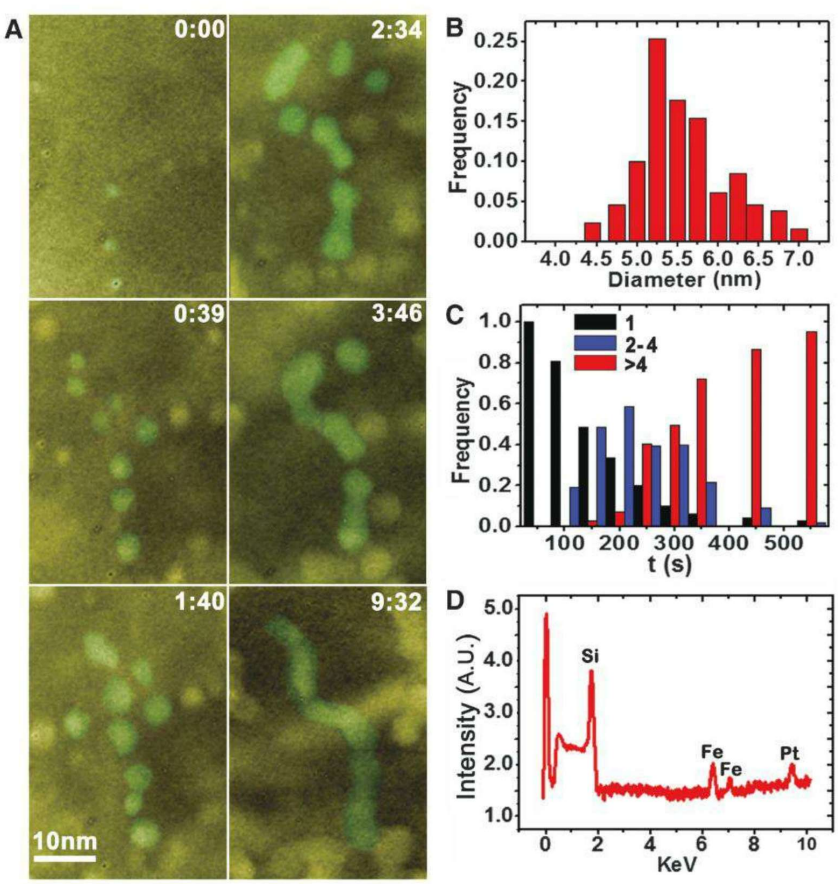

Fig. 1. The growth of Pt_3Fe nanowires in a liquid cell during exposure to the electron beam. A solvent mixture of pentadecane and oleylamine (7:3 vol/vol) was used. (**A**) Sequential color TEM images showing the evolution from the initial nucleation and growth in the molecular precursor solution to a later stage of nanowire formation by shape-directed nanoparticle attachment. Specific nanoparticles that contributed to the nanowire formation are highlighted in green. Time is displayed as minutes:seconds. The initial time is arbitrary. (**B**) Histograms of the particle size distribution when nanoparticle attachment begins. (**C**) Statistics of the length of nanoparticle chain as a function of time. Data are collected in a time window from 1 min 40 s to 9 min 32 s corresponding to (A). (**D**) EDS spectra of Pt_3Fe nanowires obtained ex situ from the same liquid cell. The observed Si signal is from the silicon nitride membrane.

achieve the growth of large–aspect ratio Pt_3Fe nanorods (up to 40:1) by allowing nanoparticles to interact in solution for an extended period of time. We show the real-time imaging of the dynamic growth of Pt_3Fe nanorods by shape-directed nanoparticle attachment.

The growth solution is prepared by dissolving $Pt(acetylacetonate)_2$ (20 mg/ml) and $Fe(acetylacetonate)_2$ (20 mg/ml) in organic solvent. A solvent mixture of pentadecane and oleylamine (7:3 vol/vol) or a mixture of pentadecane, oleylamine, and oleic acid (6:3:1 vol/vol/vol) is used for the comparison of surfactant effects. About 30 pl of growth solution is loaded into one of the reservoirs in a liquid cell. The solution is drawn into the cell by capillary force and forms a liquid layer (120 nm) sandwiched between two silicon nitride membranes (each with a thickness of 13 nm) at the window. The liquid cell is subsequently sealed with epoxy and loaded into the microscope as a standard TEM sample for imaging. A JEOL 3010 TEM operated at 300 kV and a FEI monochromated F20 UT Tecnai operated at 200 kV are used for in situ imaging. A beam current density of 1×10^5 to 8×10^5 A/m^2 is maintained for the study (*20*). However, the intensity can vary briefly at the initial exposure to the electron beam during the time period required to focus for imaging (a few seconds). A CM200 with an energy-dispersive x-ray spectroscopy (EDS) detector is used for elemental analysis following the in situ experiments. An aberration-corrected TEM (TEAM0.5) operated at 300 kV is used for high-angle annular dark field (HAADF) high-resolution scanning TEM (STEM) imaging.

Figure 1A shows sequential images depicting the growth trajectory of a Pt_3Fe nanowire (twisted nanorod) (also see movie S1 for details). Three distinct stages of growth can be identified. During the first stage, many small nanoparticles are formed when the Pt and Fe precursors are reduced by electron beam illumination. Some of them grow by monomer attachment; others undergo coalescence. The nanoparticles merged by coalescence relax into spherical nanoparticles (fig. S1 and movie S1). Eventually, these nanoparticles reach an average size of 5.3 ± 0.9 nm (Fig. 1B). Such growth of monodisperse nanoparticles by parallel monomer attachment and coalescence is similar to the previously observed colloidal Pt nanoparticle growth (*17*). Subsequently, the second stage of growth begins, which is dominated by nanoparticles interacting with each other to form nanoparticle chains. Real-time observation of nanoparticle chain formation by shape-directed nanoparticle attachment and the successive structural relaxation into straight Pt_3Fe nanorods reveals critical mechanisms of the growth of nanocrystal architectures from nanoparticle building blocks. Initially, one nanoparticle meets another, forming a dimer. Unlike in the first stage of growth, the dimer does not relax into a sphere. Instead, a trimer is formed when another particle connects to the dimer end, and additional end-to-end attachments generate a nanoparticle chain. A long nanoparticle chain can also form when short chains of nanoparticles connect to each other. Figure 1C shows the change of chain length as a function of growth time. It is clear that only single nanoparticles exist at the beginning; as growth proceeds, small aggregates (chains of two to four nanoparticles) become dominant. Ultimately, only long chains of nanoparticles are observed. This indicates that not only single nanoparticles but also short nanoparticle chains can be the fundamental building blocks for Pt_3Fe nanowire formation. EDS studies (Fig. 1D) confirm that all the nanocrystals are composed of Pt and Fe with an atomic ratio of roughly 3:1. Further high-resolution TEM (HRTEM) (fig. S1) and electron diffraction studies show a face-centered cubic (fcc) Pt_3Fe crystal structure. Nanocrystals appear with high crystallinity, and a lattice constant of about 0.39 nm (similar to the bulk value) is achieved.

The nanoparticle chains formed during the early stage are winding and markedly flexible. The relative position of the nanoparticles within the chain changes and the orientation of individual nanoparticles also alters, as indicated by the diffraction contrast variations with time (movies S1 to S3). During the final stage of growth, adjacent nanoparticles within the chain contact each other, forming a neck at which, presumably, surfactant molecules are excluded. Subsequently, mass redistribution eliminates the neck, and a smooth nanowire is formed. The diameter of the nanowire is slightly smaller (about 4.0 nm) than that of the individual nanoparticles before attachment (5.3 nm). A bent polycrystalline nanowire can straighten and transform into a single-crystal nanorod with well-defined shape. This final stage of structural relaxation sometimes proceeds in parallel with the second stage of nanoparticle attachment. Notably, most of the nanowires remain twisted and polycrystalline for an extended period of time.

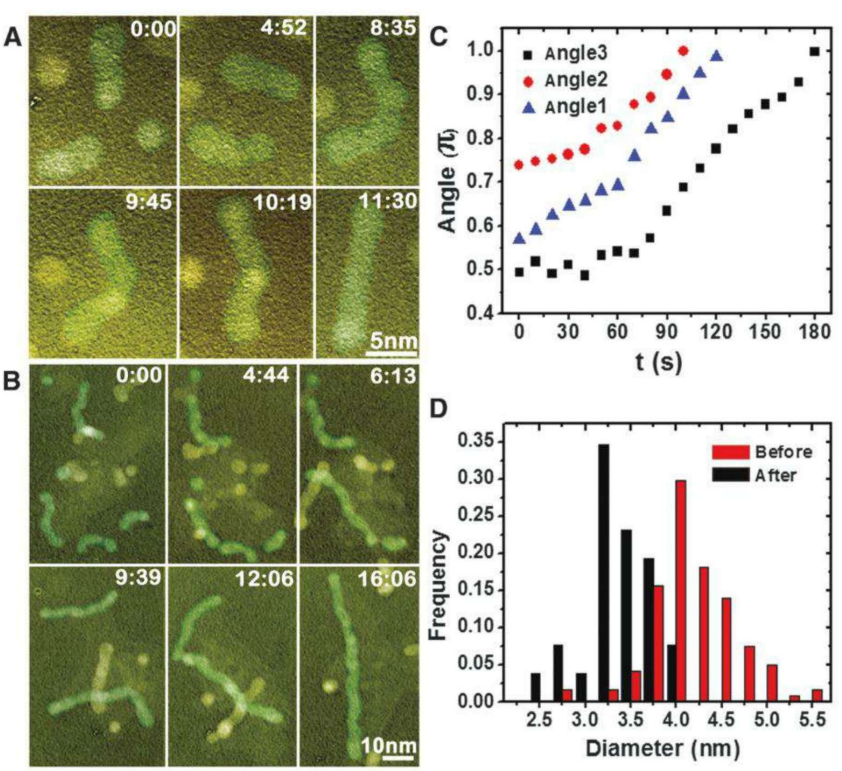

Fig. 2. Formation of twisted Pt_3Fe nanorods and the subsequent straightening process. A solvent mixture of pentadecane, oleylamine, and oleic acid (6:3:1 vol/vol/vol) was used. (**A**) Sequential color TEM images of the growth of a short Pt_3Fe nanorod. (**B**) Sequential color TEM images showing the growth of a long Pt_3Fe nanorod. In both (A) and (B), time is displayed as minutes:seconds. Initial time is arbitrary. Nanorods and the specific particles as building blocks for nanorod formation are highlighted in green. (**C**) The change in contact angle as a function of time after two nanorod building blocks join together. (**D**) Histograms of particle size distribution at the beginning of Pt_3Fe nanorod formation and nanorod diameter distribution after structural relaxation.

Straight nanorods are produced when additional surfactant (10% oleic acid) is added to the growth solution. In this case, the growth solution possesses a solvent mixture of pentadecane, oleylamine, and oleic acid (6:3:1 vol/vol/vol), which differs from that of the above solvent mixture of pentadecane and oleylamine (7:3 vol/vol). First, winding nanoparticle chains are formed following the same growth pathways as shown in Fig. 1A. Chains subsequently straighten and form single-crystal nanorods within a short period of time. Figure 2, A and B, shows the formation of two individual straight nanorods by nanoparticle attachment (also see movies S2 and S3). Nanoparticles or short nanoparticle chains move in liquid by translational and rotational motion. Their preference of adhering to the end instead of the side of a chain strongly suggests the predominance of dipolar forces, as discussed below. Nanorods with different lengths straighten with a similar rate. We measured the change in the contact angle between two short nanorods after they connected as a function of time (Fig. 2C; see images of the three selected nanorods in fig. S2). A higher rate of straightening process is observed at later times when the "neck" between nanoparticles is eliminated. It is likely that different mechanisms are involved in different stages of the straightening process. The slower straightening process at the early stage may arise from the predominance of mass redistribution through the nanoparticle surface to eliminate the neck.

We believe the straightening process is driven by the decrease in total system energy by reducing surface energy and eliminating crystal defects. In the presence of oleic acid, the average diameter of individual nanoparticles at the beginning of nanoparticle chain formation is 4.0 nm (5.3 nm in the absence of oleic acid). The average diameter of a straight nanorod becomes 3.3 nm after structural relaxation (Fig. 2D). The coabsorption of oleylamine and oleic acid on the nanoparticle surface may stabilize the nanoparticles at a smaller size than their counterparts in the absence of oleic acid (*10*, *21*). As the size of the nanoparticle decreases, the higher surface energy arising from the higher surface-to-volume ratio expedites the straightening process. The surfactant effects on the growth of Pt_3Fe nanocrystals have also been observed in our additional experiments. As shown in fig. S3, when surfactant concentration changes drastically, the growth of Pt_3Fe nanocrystals follows a different shape evolution process under the same electron beam conditions. These results demonstrate that the growth is highly influenced by surfactant absorption on the nanocrystal surface and not by TEM imaging mechanisms.

After a nanorod straightens, it takes additional time to form a single-crystal structure. It also takes longer to form a long single-crystal nanorod than a short one. A Pt_3Fe nanorod imaged using HAADF STEM (Fig. 3A) shows that although the rod is straight with a smooth surface, polycrystalline features remain. There are dispersed iron-rich regions in the Pt_3Fe nanorod as well as in individual nanoparticles and dimers, as indicated by the dark spots in the images (examples are marked by arrows in Fig. 3A). The composition nonuniformity across an alloy nanocrystal is commonly observed in flask synthesis (*22*), which agrees with our results. By comparing a Pt_3Fe nanorod with an individual nanoparticle or a dimer, it is clear that the sizes of iron-rich regions are smaller at the later stage as structure relaxation proceeds. This suggests that diffusion and mass redistribution are not limited to the nanocrystal surface during the structural relaxation.

It is notable that a twisted polycrystalline Pt_3Fe nanoparticle chain assembled by imperfect nanoparticle attachment can straighten and correct the orientation to yield a single-crystal nanorod with a perfectly straight shape. We conducted additional in situ studies and obtained snapshot images along the growth trajectory with higher resolution. Figure 3B shows a chain of three connected nanoparticles possessing different orientations from imperfect attachment. Lattice rotation accompanied by mass redistribution and straightening is observed afterward. A single-crystal nanorod is formed shortly after the chain straightens.

To distinguish the force fields exerted by nanoparticles and higher-order structures, we measured the velocity, v, of a spherical nanoparticle as it approached (I) another spherical nanoparticle or (II) a nanoparticle chain. The distance considered is the nearest surface distance between two nanoparticles. We tracked four pairs in either case and used an average chain length of five nanoparticles for case (II) (fig. S4). The average velocity plotted as a function of interparticle distance (Fig. 4A) shows that nanoparticle movements are random when the nanoparticle is above a critical distance from the receiving

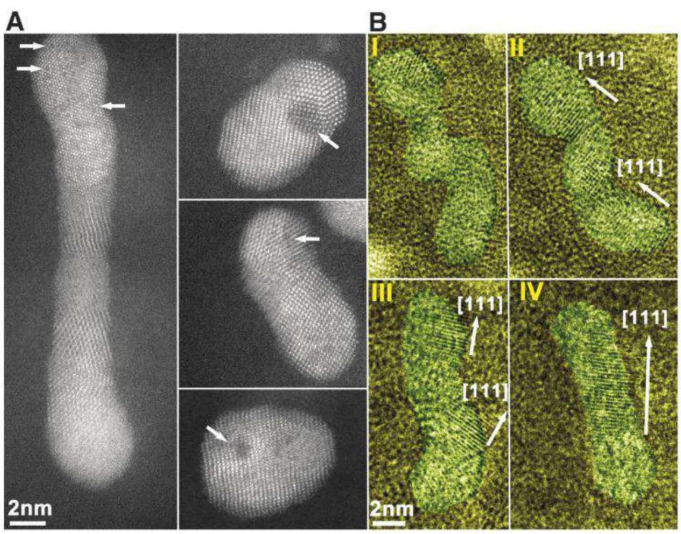

Fig. 3. High-resolution STEM images of Pt_3Fe nanorods and the dynamic shape and orientation changes during structural relaxation. (**A**) HAADF STEM image of a polycrystalline Pt_3Fe nanorod, dimers, and nanoparticles obtained in a liquid cell. The dark spots (examples highlighted by arrows) indicate the iron-rich regions. (**B**) Sequential HRTEM images (I to IV) show both crystal orientation and shape changes during the straightening of a twisted nanoparticle chain. Nanoparticles are highlighted in green.

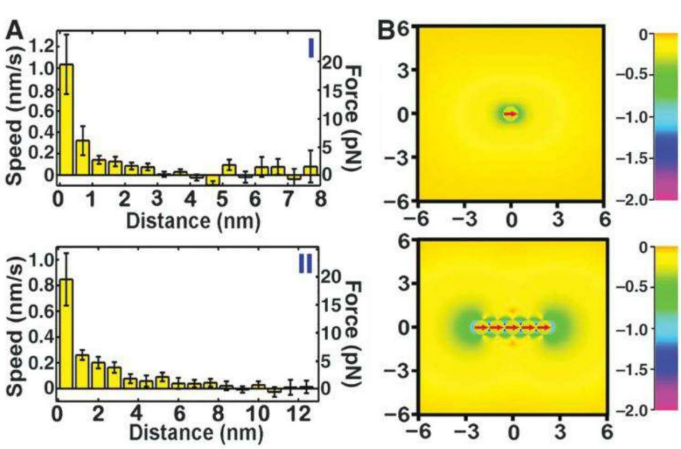

Fig. 4. Nanoparticle interaction as a function of interparticle distance. (**A**) Velocity of a nanoparticle when it approaches (I) another nanoparticle or (II) a nanoparticle chain versus interparticle distance. Error bars show the standard deviation. The right-hand axis shows forces exerted on the approaching nanoparticle. (**B**) Contour maps of the minimum electrostatic interaction energy exerted by a nanoparticle or a nanoparticle chain as a nanoparticle is approaching (a unit of E/k_BT has been used, where k_B is Boltzmann's constant). Each nanoparticle is assumed to be a point electronic dipole. It illustrates that our observation of nanoparticles preferring to attach to the ends of a chain is consistent with dipolar forces mediating nanoparticle attachment.

nanoparticle or nanoparticle chain. As the nanoparticle separation decreases to a critical distance of L_0 = 3 nm when it approaches a spherical nanoparticle or L_0 = ~6 to ~8 nm when it approaches a nanoparticle chain, the nanoparticle acquires a drift velocity, which increases with the decrease in distance. The drift velocity increases greatly at very close approach, indicating the strong attractive forces at short ranges. The right-hand axis of the plot shows the interstructure forces responsible for these drift velocities, calculated assuming the fluctuation dissipation theorem holds (*20*).

Interactions between nanoparticles during the formation of Pt_3Fe nanorods are complex and likely include van der Waals forces, hydrophobic attractions, and charge-charge interactions (*23*–*25*). However, our observation that nanoparticles prefer to attach to nanoparticle chains at their ends, and not in their middle, is strongly suggestive of dipolar interactions (*26*). To illustrate this point, we computed the contour maps of the interaction energy between two nanoparticles and that between a nanoparticle and a nanoparticle chain, assuming each nanoparticle is a distinct point electric dipole. In Fig. 4B, we show the lowest interaction energy of (I) a nanoparticle with another nanoparticle and (II) a nanoparticle with a nanoparticle chain, allowing the approaching nanoparticle to rotate freely. Compared with the interaction potential energy between two nanoparticles (I), the potential energy between a nanoparticle and nanoparticle chain (II) is strongly anisotropic, favoring the end attachment over attachment in the middle of a nanoparticle chain. Previous work has shown that electrostatic dipole moments can be generated by particle faceting (*13*) or surfactants on the nanoparticle surface forming certain patterns (*23*, *27*, *28*). It is also possible that Pt_3Fe nanoparticles possess magnetic dipole moments (*13*, *29*); thus, both electrostatic and magnetic dipole moments may be present in this system [calculation results of magnetic dipolar interaction are similar to those of electrostatic dipolar interaction (*20*)]. However, our experiments show that pure Pt nanorods (unlikely magnetic nanorods) can also grow by nanoparticle attachment following pathways similar to those for Pt_3Fe nanorod formation (fig. S5). These results suggest that the nonmagnetic dipolar interaction (i.e., electrostatic interaction) plays a key role in nanorod growth from nanoparticle building blocks. It also implies that the shape-directed nanoparticle attachment might be an important mechanism for the formation of a variety of one-dimensional nanocrystals.

We have observed the dynamic growth of Pt_3Fe nanorods in solution using TEM. We have identified a range of intricate processes in the growth of nanorods from nanoparticle building blocks, including shape-directed nanoparticle attachment, straightening, orientation correction, and mass redistribution. Visualization of Pt_3Fe nanorod growth trajectories strongly suggests the prominence of dipolar nanoparticle interactions and allows us to quantify the interactions between nanostructures. Understanding the mechanism of one-dimensional colloidal nanocrystal growth using nanoparticles as building blocks provides a link between the world of single molecules and hierarchical nanostructures and paves the way to rational design of nanomaterials with controlled properties.

References and Notes

1. L. Manna, E. C. Scher, A. P. Alivisatos, *J. Am. Chem. Soc.* **122**, 12700 (2000).
2. Y. G. Sun, Y. N. Xia, *Science* **298**, 2176 (2002).
3. C. Pacholski, A. Kornowski, H. Weller, *Angew. Chem. Int. Ed.* **41**, 1188 (2002).
4. D. J. Milliron *et al.*, *Nature* **430**, 190 (2004).
5. N. Tian, Z. Y. Zhou, S. G. Sun, Y. Ding, Z. L. Wang, *Science* **316**, 732 (2007).
6. B. Lim *et al.*, *Science* **324**, 1302 (2009).
7. J. F. Banfield, S. A. Welch, H. Z. Zhang, T. T. Ebert, R. L. Penn, *Science* **289**, 751 (2000).
8. A. B. Panda, G. Glaspell, M. S. El-Shall, *J. Am. Chem. Soc.* **128**, 2790 (2006).
9. Z. Li *et al.*, *Colloids Surf. A Physicochem. Eng. Asp.* **313–314**, 40 (2008).
10. C. Schliehe *et al.*, *Science* **329**, 550 (2010).
11. Y. Yin, A. P. Alivisatos, *Nature* **437**, 664 (2005).
12. R. L. Penn, J. F. Banfield, *Science* **281**, 969 (1998).
13. K. S. Cho, D. V. Talapin, W. Gaschler, C. B. Murray, *J. Am. Chem. Soc.* **127**, 7140 (2005).
14. M. Niederberger, H. Cölfen, *Phys. Chem. Chem. Phys.* **8**, 3271 (2006).
15. A. P. Alivisatos, *Science* **289**, 736 (2000).
16. M. J. Williamson, R. M. Tromp, P. M. Vereecken, R. Hull, F. M. Ross, *Nat. Mater.* **2**, 532 (2003).
17. H. M. Zheng *et al.*, *Science* **324**, 1309 (2009).
18. J. E. Evans, K. L. Jungjohann, N. D. Browning, I. Arslan, *Nano Lett.* **11**, 2809 (2011).
19. N. de Jonge, F. M. Ross, *Nat. Nanotechnol.* **6**, 695 (2011).
20. Supplementary materials are available on *Science* Online.
21. N. Shukla, C. Liu, P. M. Jones, D. Weller, *J. Magn. Magn. Mater.* **266**, 178 (2003).
22. Y. W. Zhang *et al.*, *J. Phys. Chem. C* **112**, 12092 (2008).
23. Y. J. Min, M. Akbulut, K. Kristiansen, Y. Golan, J. Israelachvili, *Nat. Mater.* **7**, 527 (2008).
24. K. J. M. Bishop, C. E. Wilmer, S. Soh, B. A. Grzybowski, *Small* **5**, 1600 (2009).
25. Z. Y. Tang, Z. L. Zhang, Y. Wang, S. C. Glotzer, N. A. Kotov, *Science* **314**, 274 (2006).
26. J. Y. Ku, D. M. Aruguete, A. P. Alivisatos, P. L. Geissler, *J. Am. Chem. Soc.* **133**, 838 (2011).
27. Z. Y. Tang, N. A. Kotov, M. Giersig, *Science* **297**, 237 (2002).
28. K. Liu *et al.*, *Science* **329**, 197 (2010).
29. S. H. Sun, C. B. Murray, D. Weller, L. Folks, A. Moser, *Science* **287**, 1989 (2000).

Acknowledgments: We thank P. Geissler (University of California, Berkeley) for helpful discussions. We are also grateful to the comments of B. Sadtler and G. Reinhard. This work was performed using the facility at National Center for Electron Microscopy (NCEM), Lawrence Berkeley National Laboratory (LBNL), and portions of this work were performed at the Molecular Foundry (MF), LBNL. NCEM and MF were supported by the Office of Science, Office of Basic Energy Sciences (BES), Scientific User Facilities Division of the U.S. Department of Energy (DOE) under contract no. DE-AC02-05CH11231. This project was supported by the Office of Basic Energy Sciences, Division of Materials Sciences and Engineering, of the U.S. DOE under contract no. DE-AC02-05CH11231. H.-G.L. thanks J. Park for help on the initial experimental setup. H.Z. thanks the U.S. DOE Office of Science Early Career Research Program for support and gratefully acknowledges partial funding support from LDRD LBNL.

Supplementary Materials

www.sciencemag.org/cgi/content/full/336/6084/1011/DC1
Materials and Methods
Figs. S1 to S10
References (*30*–*39*)
Movies S1 to S3

16 January 2012; accepted 10 April 2012
10.1126/science.1219185

Direction-Specific Interactions Control Crystal Growth by Oriented Attachment

Dongsheng Li,[1] Michael H. Nielsen,[1,2] Jonathan R. I. Lee,[3] Cathrine Frandsen,[4] Jillian F. Banfield,[5,6] James J. De Yoreo[1,7]*

The oriented attachment of molecular clusters and nanoparticles in solution is now recognized as an important mechanism of crystal growth in many materials, yet the alignment process and attachment mechanism have not been established. We performed high-resolution transmission electron microscopy using a fluid cell to directly observe oriented attachment of iron oxyhydroxide nanoparticles. The particles undergo continuous rotation and interaction until they find a perfect lattice match. A sudden jump to contact then occurs over less than 1 nanometer, followed by lateral atom-by-atom addition initiated at the contact point. Interface elimination proceeds at a rate consistent with the curvature dependence of the Gibbs free energy. Measured translational and rotational accelerations show that strong, highly direction-specific interactions drive crystal growth via oriented attachment.

The growth of crystals through the aggregation and coalescence of nanoparticles is now recognized as a widespread phenomenon in biomineral (*1*, *2*), biomimetic (*3*, *4*), and natural systems (*5*) and during the synthetic production of nanoparticles and nanowires (*6*–*8*).

The resulting crystals often exhibit complex forms ranging from quasi–one-dimensional (1D) chains to 3D hierarchical and self-similar superstructures. Yet the final structure typically diffracts as a single crystal, implying that the primary particles aligned during growth (*4*, *9*). When coalignment is accompanied by coalescence, this growth process is often referred to as oriented attachment (OA) (*10*, *11*). However, the pathway by which OA occurs has not been established. Although the preservation of primary particle morphology and the formation of twins and stacking faults at particle-particle boundaries strongly suggest a sequence of whole-particle alignment followed by interface elimination (*10*, *12*), atom-by-atom reorientation via dislocation and grain-boundary migration after attachment are another potential mechanism (*13*, *14*). If indeed the primary particles align before attachment, the dynamics of that process and the forces that drive it have yet to be revealed.

We used a liquid cell mounted within a high-resolution transmission electron microscope (TEM) for the direct in situ observation of iron oxide nanoparticle growth (fig. S1) (*15*). Previous studies have inferred that OA is important in the early crystal growth of iron oxyhydroxide nanoparticles (*8*, *16*–*18*), which are abundant and play important roles in biogeochemical processes that shape Earth's near-surface environments (*19*–*21*). Images were recorded with lattice fringe resolution, enabling us to track particle orientations throughout the experiments. Selected area electron diffraction pattern analysis indicates that the nanoparticles formed in the fluid cell through re-precipitation from akaganeite nanoparticle precursors are closely related to six-line ferrihydrite ($5Fe_2O_3{\cdot}9H_2O$) (fig. S2).

Low-resolution TEM images showed that after nucleation, the ferrihydrite nanoparticles grew both through monomer addition from solution and particle attachment events (fig. S3 and movie S1), as observed previously with Pt nanoparticles (*22*). We recorded several high-resolution movies that revealed the dynamics of the attachment process (movies S2 to S5): The particles continuously diffused and rotated,

[1]Materials Science Division, Lawrence Berkeley National Laboratory (LBNL), Berkeley, CA 94720, USA. [2]Department of Materials Science and Engineering, University of California, Berkeley, CA 94720, USA. [3]Physical Sciences Directorate, Lawrence Livermore National Laboratory, Livermore, CA 94551, USA. [4]Department of Physics, Technical University of Denmark, 2800 Kongens Lyngby, Denmark. [5]Earth Science Division, LBNL, Berkeley, CA 94720, USA. [6]Department of Earth and Planetary Science, University of California, Berkeley, CA 94720, USA. [7]The Molecular Foundry, LBNL, Berkeley, CA 94720, USA.

*To whom correspondence should be addressed. E-mail: jjdeyoreo@lbl.gov

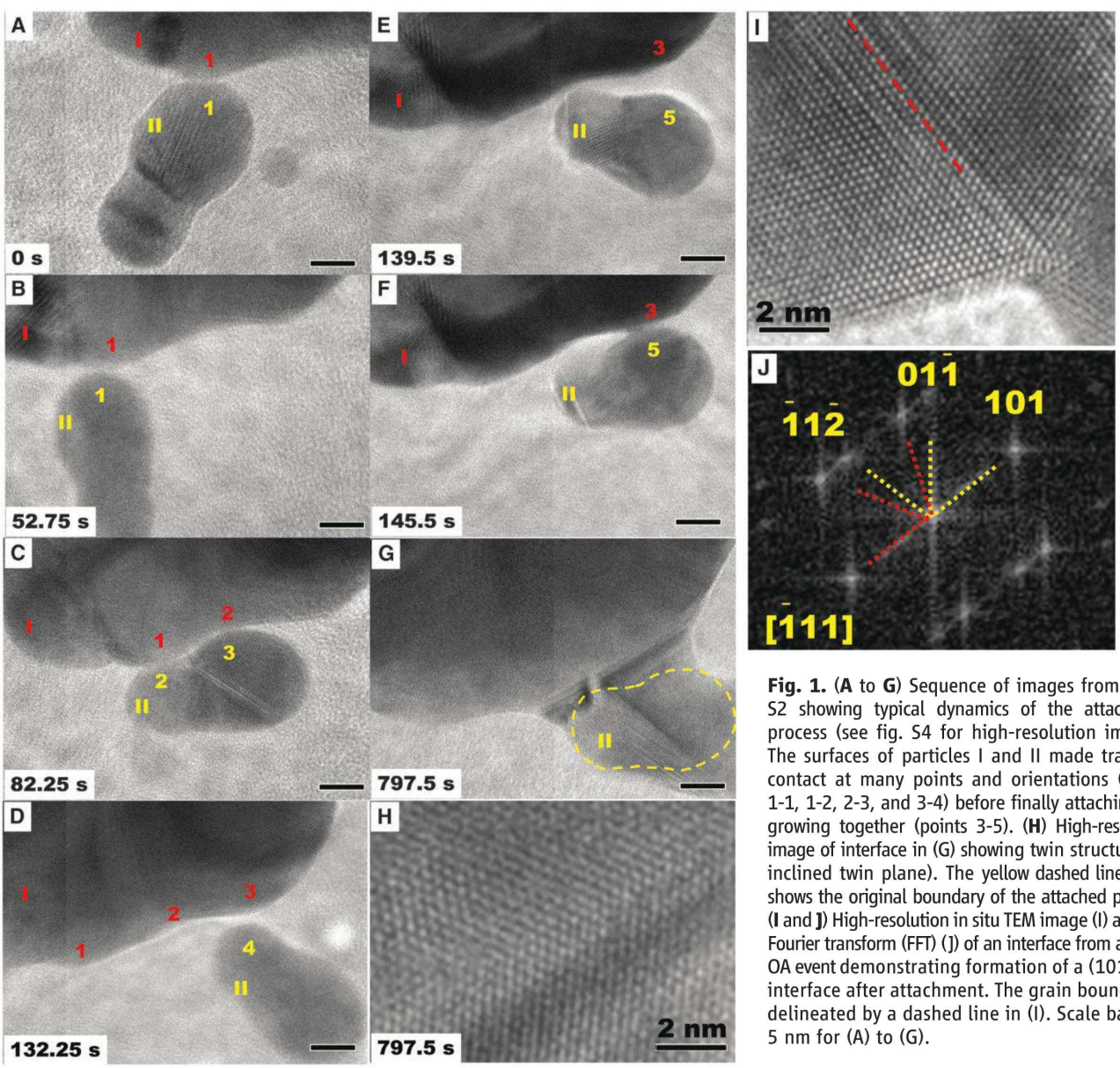

Fig. 1. (**A** to **G**) Sequence of images from movie S2 showing typical dynamics of the attachment process (see fig. S4 for high-resolution images). The surfaces of particles I and II made transient contact at many points and orientations (points 1-1, 1-2, 2-3, and 3-4) before finally attaching and growing together (points 3-5). (**H**) High-resolution image of interface in (G) showing twin structure (an inclined twin plane). The yellow dashed line in (G) shows the original boundary of the attached particle. (**I** and **J**) High-resolution in situ TEM image (I) and fast Fourier transform (FFT) (J) of an interface from another OA event demonstrating formation of a (101) twin interface after attachment. The grain boundary is delineated by a dashed line in (I). Scale bars are 5 nm for (A) to (G).

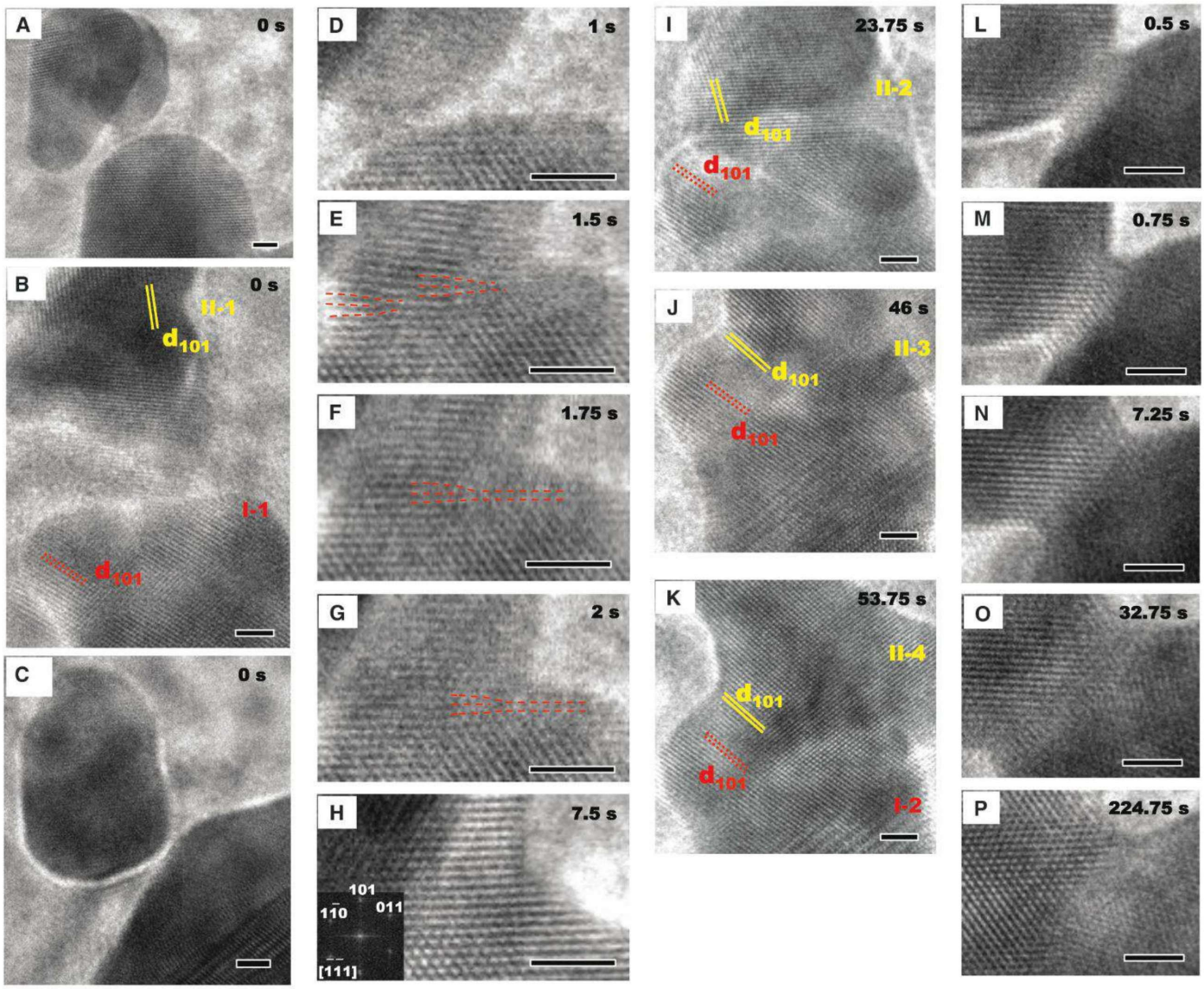

Fig. 2. Sequences of in situ TEM images show the details of the attachment process. (**A**) and (**D** to **H**) Sequence from movie S3 showing attachment at a lattice-matched interface. (A) shows the arrangement of particles before attachment. The asymmetric particle in front of the smaller spherical particle is not involved in the attachment process. (D) to (G) show formation of the interface. Two edge dislocations denoted in (E) to (G) by red dashed lines translate to the right, leaving a defect-free structure in (H). (**B**) and (**I** to **K**) Sequence of images showing relative rotations of particles during the attachment process, leading to a lattice-matched interface. Particles I and II have their [–121] zone axes perpendicular to the viewing plane. FFT patterns are given in fig. S5. (**C**) and (**L** to **P**) Sequence from movie S4 showing how the interface expands laterally after attachment. All scale bars are 2 nm.

repeatedly contacting one another until attachment finally occurred. The surfaces of two adjoining particles made transient contact at many points and orientations before finally attaching and growing together (Fig. 1). Similar behavior was observed for smaller, 5- to 10-nm particles typical of six-line ferrihydrite (*23*) (movie S5).

Lattice fringe images recorded in situ revealed that, irrespective of how many times particles made contact, at the time of attachment they either shared the same crystallographic orientation or their orientations were twin-related (fig. S4). Either way, after attachment, atoms filled the interface region on a time scale on the order of 10 to 100 s, beginning at the point of contact. Interface elimination resulted either in larger defect-free crystals (Fig. 2A and D to H, B and I to K, and movie S3) or crystals that contained a twin plane (Fig. 1, H and I). In all cases analyzed, twinning was on (101) ferrihydrite (Fig. 1J). This interface structure is consistent with studies demonstrating that periodic matching of the Bravais lattice geometry is associated with reduced boundary energy (*24*, *25*), as well as the coincident-site lattice model, which relates the boundary energy to the number of coincident lattice sites (*26*).

Sequences of lattice fringe images also provide direct insight into the dynamics of processes leading to growth and microstructure development, confirming some inferences from ex situ studies (*10*, *27*, *28*) and providing information about the forces involved. As the particles approached, they typically rotated until the lattice planes were close to a perfect match (Fig. 2, E and K). For example, particles initially misaligned by 54° (particles I and II in Fig. 2B), as shown by the orientations of their (101) planes, rotated in opposite directions by +45° and –9°, respectively (Fig. 2, I to K), leading to attachment with perfect crystallographic alignment (Fig. 2K). In some cases, a slight misalignment at the time of attachment led to defect formation at the interface, as in Fig. 2E where the lattice planes near the boundary are slightly

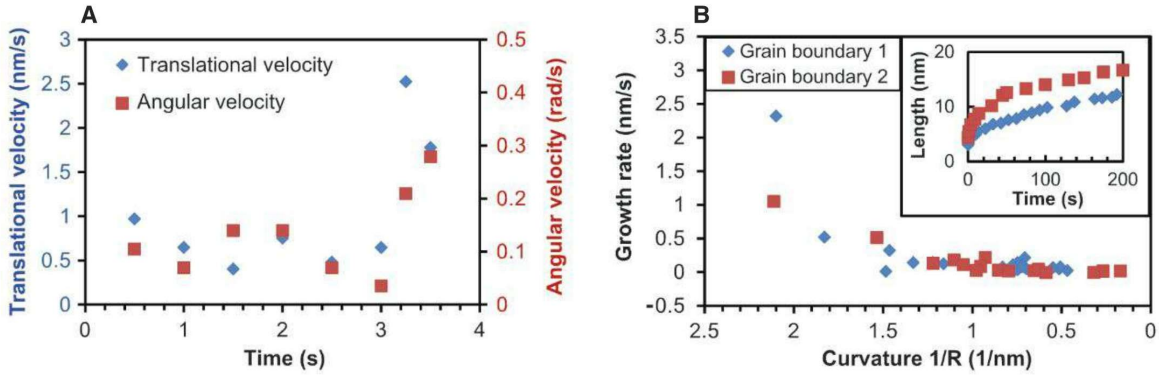

Fig. 3. (**A**) Relative translational and angular speeds leading up to the attachment process in sequence (L) to (P) of Fig. 2. (**B**) Dependence of the interface growth rate on curvature derived from the dependence of interface length on time (inset) for sequence (L) to (P) of Fig. 2 (grain boundary 1) and the sequence in movie S2 (grain boundary 2). The maximum error from delocalization is estimated to be less than 1 nm, and the error bars for each data point are shown in fig. S5.

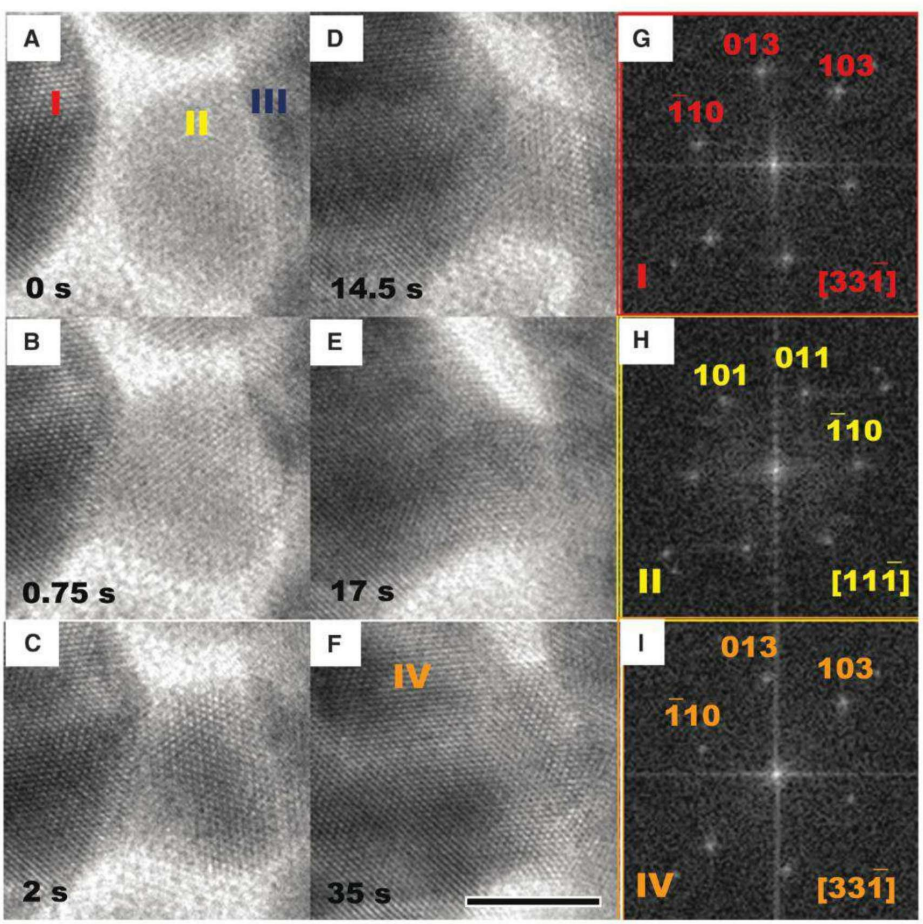

Fig. 4. (**A** to **F**) Sequence of in situ TEM images from movie S6 showing a rare example of attachment across a mismatched interface due to trapping between two adjacent particles. (**G** to **I**) FFT diffraction patterns of particle I [in (C)], particle II [in (C)], and the fused product particle IV [in (F)], respectively. The 5-nm scale bar in (F) applies to all high-resolution TEM images.

bent because of the formation of two edge dislocations. Nonetheless, within 2 s, these dislocations translated laterally across the interface (Fig. 2, E to G), leaving behind perfectly flat planes and eliminating any trace of the interparticle boundary (Fig. 2H).

Analysis of particle motion leading to attachment shows that the translational and rotational speeds increased by factors of 2 to 4 as the particles approached one another. For example, the smaller particle in Fig. 2C diffused with a relatively constant translational speed of approximately 0.6 to 0.8 nm s^{-1} and a rotational speed of approximately 0.09 rad s^{-1} (Fig. 3A). Within the last 0.5 s before attachment, the translational component jumped to 1.8 to 2.5 nm s^{-1} and the rotational component increased to 0.21 to 0.28 rad s^{-1}.

In order to investigate the post-attachment kinetics, we measured the lateral growth rate at the grain boundary. Image sequences (Fig. 2C and L to P, from movie S4) show that after attachment, the boundary advanced by monomer addition. (Also see fig. S4, which shows the attachment event in Fig. 1 at higher resolution.) The lateral growth rate decreased from an initial value of 13.1 nm s^{-1} to 0.14 nm s^{-1} within the first 2 s, and to a constant value of 0.034 nm s^{-1} after approximately 20 s (Fig. 3B). The dependence of the speed of the growth front on the curvature of the interface is consistent with the well-known exponential dependence of chemical potential on interface curvature (*29*). However, a detailed form of the dependence cannot be determined, because the 3D shape of the interface is unknown, as is the variation in attachment and detachment kinetics with interface orientation.

In contrast to freely diffusing nanoparticles, those that were flanked by two adjacent particles (such as particle II in Fig. 4A) became trapped and then fused across a mismatched interface (Fig. 4C and movie S6). At the time of attachment, particles aligned along different zone axes (Fig. 4, G and H). Grain boundaries then migrated toward the adjacent particle, leading to the growth of one orientation at the expense of the other, which was quickly consumed (Fig. 4, A to F). This post-attachment behavior of misaligned particles is consistent with strain-induced grain boundary migration, through which the energy stored in dislocations and point defects at the grain boundary of a highly strained nanoparticle drives recrystallization (*13*, *14*). In close proximity to large particles, some <5-nm particles undergo dissolution even though these particles are stable before their encounter with the larger one (movie S6). As expected from the curvature dependence of the free energy, the dissolution rate increases rapidly with decreasing size. These two phenomena—attachment and recrystallization of a misaligned particle and dissolution of small particles in the vicinity

of larger ones—show that, even in systems where OA is dominant, Ostwald ripening can play a role.

In all examples, nanoparticles explored multiple configurations before attachment occurred. This was possible because the primary particles tended to aggregate into clusters where they interacted in close proximity for sufficient periods of time to become nearly aligned through Brownian motion (fig. S3 and movie S1). This tendency implies the existence of a long-range attractive force that is necessary to keep them in proximity. Osmotic forces, which largely drive colloidal stabilization (*30*), are most likely responsible. Previous ex situ studies of OA also proposed this as a source of initial aggregation (*5*); however, this colloidal stabilization must be sufficiently weak to allow the nanoparticles to approach each other within the primary minimum of the interaction potential, where van der Waals interactions could lead to further attraction. In addition, the diffusional dynamics must be sufficiently rapid to allow rearrangement into low-energy configurations. Because the OA event is accompanied by a jump to contact only after orientation is established (Fig. 1), OA is ultimately driven by a short-range force that acts over <1 nm and is highly sensitive to orientation. The orientation dependence would seem to argue for Coulomb interactions as the source of this force, although one cannot rule out van der Waals interactions with anisotropic polarizability. The observation that the acceleration phase occurs over the last 0.5 to 1 nm is consistent with the expected Debye length for a 50 mM 3:1 electrolyte solution (*30*). In addition, the fact that the particles tend to remain separated by nanometer-scale distances until a correct configuration is reached implies the existence of a slight energetic barrier. This provides further support for the importance of electrostatic interactions, which, in the case of molecular crystals such as iron oxides, would produce cation-cation and anion-anion repulsion when the lattices are mismatched.

Irrespective of its source, to estimate the strength of this short-range attraction, we determined the translational and angular acceleration by measuring the frame-to-frame velocity and rotation rate (Fig. 3A). Using the density of ferrihydrite and the measured particle size to determine the mass and moment of inertia for spherical particles, we calculated that the forces and torques acting on the approaching particle arising from particle-attraction are almost completely offset by the resistance of the solution (supplementary text). Even so, the potential energy for the particle-particle interaction, which equals 1.6×10^{-19} J, far exceeds the initial kinetic energy of 7.5×10^{-40} J. In addition, if we assume that this interaction energy is due to the electrostatic force, we find that the particles interact with an effective number of fundamental charges (1.6×10^{-19} C) on the order of unity (supplementary text).

References and Notes

1. Y. Politi *et al.*, *Science* **306**, 1161 (2004).
2. C. E. Killian *et al.*, *J. Am. Chem. Soc.* **131**, 18404 (2009).
3. H. Cölfen, M. Antonietti, *Angew. Chem. Int. Ed.* **44**, 5576 (2005).
4. H. Cölfen, M. Antonietti, *Mesocrystals and Non-classical Crystallization* (Wiley, San Francisco, CA, 2008).
5. J. F. Banfield *et al.*, *Science* **289**, 751 (2000).
6. Y. Yadong, P. Alivisatos, *Nature* **437**, 7059 (2005).
7. K. S. Cho *et al.*, *J. Am. Chem. Soc.* **127**, 7140 (2005).
8. J. Zhang *et al.*, *Nanoscale* **2**, 18 (2010).
9. S. Mann, *Biomineralization: Principles and Concepts in Bioinorganic Materials Chemistry* (Oxford Univ. Press, Oxford, 2001).
10. R. L. Penn, J. F. Banfield, *Science* **281**, 969 (1998).
11. V. M. Yuwono *et al.*, *J. Am. Chem. Soc.* **132**, 2163 (2010).
12. R. L. Penn, J. F. Banfield, *Am. Mineral.* **83**, 1077 (1998).
13. S. A. Hackney, F. S. Biancaniello, D. N. Yoon, C. A. Handwerker, *Scr. Metall.* **20**, 937 (1986).
14. C. W. Passchier, R. A. J. Trouw, *Microtectonics* (Springer, Sturtz, Wurzburg, Germany, 1998).
15. Materials and methods are available as supplementary materials on *Science* Online.
16. R. L. Penn *et al.*, *J. Phys. Chem. B* **105**, 2177 (2001).
17. C. Frandsen *et al.*, *Phys. Rev. B* **72**, 214406 (2005).
18. Y. Yang *et al.*, *Inorg. Chem.* **50**, 10143 (2011).
19. J. C. Joubert, *Anal. Quim.* **93**, S70 (1997).
20. N. Deo, K. A. Natarajan, *Int. J. Miner. Process.* **55**, 41 (1998).
21. R. L. Penn *et al.*, *Geology* **29**, 843 (2001).
22. H. Zheng *et al.*, *Science* **324**, 1309 (2009).
23. D. E. Janney *et al.*, *Clays Clay Miner.* **48**, 111 (2000).
24. R. W. Balluffi *et al.*, *Surf. Sci.* **31**, 68 (1972).
25. G. Hasson *et al.*, *Surf. Sci.* **31**, 115 (1972).
26. V. Randle, *Role of the Coincidence Site Lattice in Grain Boundary Engineering* (Maney Materials Science, London, 1996).
27. R. L. Penn, *J. Phys. Chem. B* **108**, 12707 (2004).
28. C. Ribeiro *et al.*, *ChemPhysChem* **6**, 690 (2005).
29. G. Cao, *Nanostructures and Nanomaterials: Synthesis, Properties and Applications* (Imperial College Press, London, 2004).
30. J. N. Israelachvili, *Intermolecular and Surface Forces* (Academic Press, Waltham, MA, 2011).

Acknowledgments: We thank V. Altoe and S. Aloni for their assistance with electron microscopy and L. Zhang for his help with analysis of the data. This research was supported by the U.S. Department of Energy, Office of Basic Energy Sciences (OBES), by LBNL under contract no. DE-AC02-05CH11231 and Lawrence Livermore National Laboratory (LLNL) under contract DE-AC52-07NA27344. Development of the TEM fluid cell was supported by the OBES, Division of Chemical, Biological and Geological Sciences; analysis of iron oxide formation was supported by the OBES, Division of Materials Science and Engineering; and cell fabrication and TEM analysis were performed at the Molecular Foundry, LLNL, which is supported by the OBES, Scientific User Facilities Division. M.H.N. acknowledges government support under and awarded by the Department of Defense, the Air Force Office of Scientific Research, and a National Defense Science and Engineering Graduate Fellowship, 32 CFR 168a. C.F. acknowledges support from The Danish Council for Independent Research. Data are available in the supplementary materials.

Supplementary Materials

www.sciencemag.org/cgi/content/full/336/6084/1014/DC1
Materials and Methods
Supplementary Text
Figs. S1 to S5
Table S1
References (*31*–*33*)
Movies S1 to S6

25 January 2012; accepted 27 March 2012
10.1126/science.1219643

Large-Pore Apertures in a Series of Metal-Organic Frameworks

Hexiang Deng,[1]* Sergio Grunder,[2]* Kyle E. Cordova,[1] Cory Valente,[2] Hiroyasu Furukawa,[1] Mohamad Hmadeh,[1] Felipe Gándara,[1] Adam C. Whalley,[2] Zheng Liu,[3] Shunsuke Asahina,[4] Hiroyoshi Kazumori,[4] Michael O'Keeffe,[1] Osamu Terasaki,[5,6,7] J. Fraser Stoddart,[2,7] Omar M. Yaghi[1,7]†‡

We report a strategy to expand the pore aperture of metal-organic frameworks (MOFs) into a previously unattained size regime (>32 angstroms). Specifically, the systematic expansion of a well-known MOF structure, MOF-74, from its original link of one phenylene ring (I) to two, three, four, five, six, seven, nine, and eleven (II to XI, respectively), afforded an isoreticular series of MOF-74 structures (termed IRMOF-74-I to XI) with pore apertures ranging from 14 to 98 angstroms. All members of this series have non-interpenetrating structures and exhibit robust architectures, as evidenced by their permanent porosity and high thermal stability (up to 300°C). The pore apertures of an oligoethylene glycol–functionalized IRMOF-74-VII and IRMOF-74-IX are large enough for natural proteins to enter the pores.

Porous crystals are useful because they allow access of molecules through their pore apertures for storage, separation, or conversion. The pore apertures dictate the size of the molecules that may enter the pores, which provide the surface and space to carry out these functions. A long-standing challenge is to make crystals whose pore apertures are of a size suitable for the inclusion of large organic, inorganic, and biological molecules. The largest reported pore aperture is 32 by 24 Å, and the largest reported internal pore diameter is 47 Å, both of which are found in metal-organic frameworks (MOFs) (*1*, *2*). In principle, it should be possible to use longer links in the synthesis of MOFs so as to provide for even larger pore apertures. However, attempts to do so often yield either interpenetrating structures (*3*, *4*), restricting the size of the pore aperture, or fragile frameworks that collapse upon removal of guests (*1*, *3*).

Here, we report that these challenges are overcome by the expansion of a well-known MOF structure, MOF-74 (*5*, *6*), M_2(2,5-DOT) (where M is Zn^{2+},Mg^{2+} and DOT is dioxidoterephthalate) (Fig. 1, I), from the original DOT link of one phenylene ring to two (II), three (III), four (IV), five (V), six (VI), seven (VII), nine (IX), and eleven (XI) to give an isoreticular (having the same topology) series of MOF-74 structures (termed IRMOF-74-I to -XI), with the dimension of the pore apertures ranging from 14 to 98 Å. Six members of this series (IRMOF-74-IV to -XI) have the largest pore apertures reported to date for a crystalline material, and one member (IRMOF-74-XI), in its guest-free form, has the lowest density (0.195 g cm^{-3}) known thus far for a crystal at room temperature. All members of this series have noninterpenetrating structures and exhibit robust architectures, as evidenced by their permanent porosity and high thermal stability (up to 300°C). We further report experiments indicating that large molecules—such as vitamin B_{12}, metal-organic polyhedron-18, myoglobin, and green fluorescent protein (GFP)—can pass through the pore apertures of IRMOF-74-IV, V, VII, and IX, respectively.

Mesoporous silica, porous carbon, and other related materials are known to have very large apertures (up to 100 nm), and their pore size can be varied in the scale of a few nanometers (*7*–*10*). Unlike these mesoporous materials, the formation of MOFs is governed by the precise linkage of organic struts with the metal atoms to form the secondary building unit (SBUs) (*11*). The formation of the SBUs imposes the precise disposition of the links. In this way, the pore aperture of MOFs can be controlled on the angstrom level through the gradual increase in the number of atoms in the organic links used in the MOF design. These features, coupled with the flexibility in which the MOFs' composition and structure metrics can be varied (*11*–*19*), make them highly desirable for well-defined inclusion processes and indeed distinguish them from other mesoporous materials.

Our strategy for making MOFs with large-pore apertures and avoiding the problem of interpenetration is to start with a framework in which one can maintain a short axis with the long organic links inclined to that axis. The short axis effectively eliminates the possibility of interpenetration because it is the distance between the links along that axis joining the SBUs (*20*, *21*). Ideal in this regard are the frameworks built from infinite rod-shaped metal oxide SBUs, as exemplified in the structure of MOF-74 (Fig. 1A) (*5*, *6*). Here, the metal oxide rod SBUs are in a hexagonal arrangement, joined along the short and long axes by metal-oxygen bonds and organic DOT links, respectively. The formation of the short axis is ensured by the coordination of the metal to the carboxylic and the *ortho*-positioned hydroxyl functionalities of the DOT links, which in turn generates tight packing of the links at an intersecting angle to this axis (fig. S1) (*22*). The resulting product is an extended framework composed of channels along the direction of the short axis that are isolated by walls formed by the aforementioned packing of the organic links, a construct that forbids interpenetration regardless of the organic link's length [(*22*), section S1].

Initially, we produced models of a MOF-74 structure with progressively longer links II to XI. Considering that the composition of the inorganic SBU remains unaltered throughout the entire series, we used the atomic coordinates of the already known MOF-74 structure (*6*) and simply added the appropriate number of phenylene units for each respective member of the series in order to develop the crystal models. All members of this isoreticular series inherit the **etb** net of the parent MOF-74 topology (*23*). The models for IRMOF-74-II and -III were built in $R\bar{3}$, the same space group as for the original MOF-74, whereas for the other members of the series we created the models in *R*3 to better describe the torsion angles

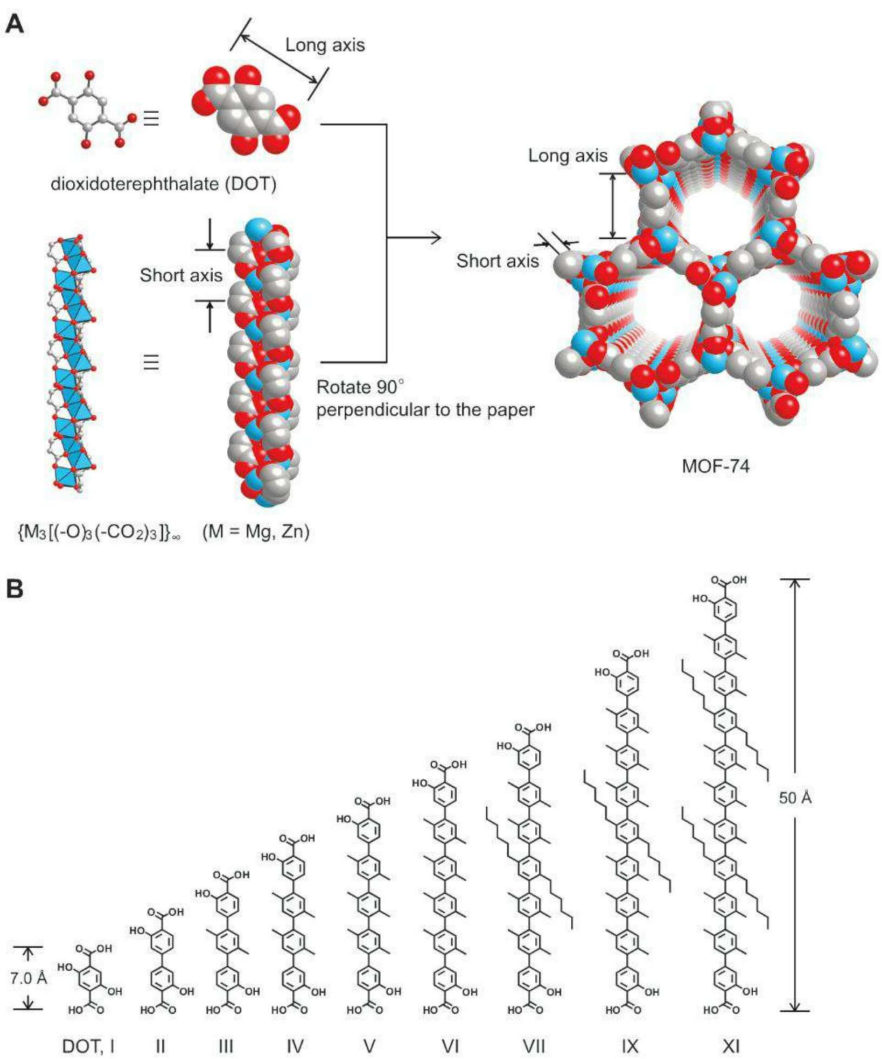

Fig. 1. (**A**) Crystal structure of MOF-74. DOT link is joined by a metal oxide SBU to make the three-dimensional MOF-74 structure with one-dimensional hexagonal channels. C atoms are shown in gray, O atoms are shown in red, 5-coordinate Mg or Zn atoms with open metal sites are shown in blue, and H atoms and terminal ligands protruding into the pores are omitted for clarity. (**B**) Chemical structure of organic links used in the synthesis of a series of nine IRMOFs.

[1]Center for Reticular Chemistry, Center for Global Mentoring, University of California, Los Angeles (UCLA)–U.S. Department of Energy (DOE) Institute for Genomics and Proteomics, and the Department of Chemistry and Biochemistry, UCLA, Los Angeles, CA 90095, USA. [2]Center for the Chemistry of Integrated Systems, Department of Chemistry, Northwestern University, Evanston, IL 60208, USA. [3]Nanotube Research Center, National Institute of Advanced Industrial Science and Technology (AIST), Tsukuba 305-0046, Japan. [4]SMBU, JEOL, Akishima, Tokyo 196-8558, Japan. [5]Department of Materials and Environmental Chemistry, Stockholm University, Stockholm 10691, Sweden. [6]EXSELENT, Stockholm University, Stockholm 10691, Sweden. [7]NanoCentury KAIST Institute and Graduate School of Energy, Environment, Water, and Sustainability (World Class University), Daejeon 305-701, Republic of Korea.

*These authors contributed equally to this work.
†Present address: Department of Chemistry, University of California and The Molecular Foundry at Lawrence Berkeley National Laboratory, Berkeley, CA 94720, USA.
‡To whom correspondence should be addressed. E-mail: yaghi@berkeley.edu

that are now present in the links. A molecular mechanics energy minimization was then performed to optimize the geometry of the links within the framework. This approach allowed us to calculate for the IRMOF series the powder x-ray diffraction patterns (PXRDs), their expected cell parameters, pore aperture, and other related porosity information (table S1) (*22*). This initial analysis was followed by the preparation of the links as well as by carrying out the synthesis and characterization of the IRMOFs and comparing the observed and calculated structural data to verify that the entire IRMOF series has the original MOF-74 topology.

In our design of the organic links, a homologous series of palindromic oligophenylene derivatives terminated with α-hydroxy-carboxylic acid functions were targeted to afford linear and robust building blocks for expanding the MOF-74 structure. The notoriously low solubilities of the parent oligophenylenes (*24*) were circumvented by introducing (III to VI) pairs of methyl substituents with *para* dispositions onto all but the terminal phenylene rings in order to introduce torsional twists between the planes of the rings. This stereoelectronic control breaks interring conjugation and reduces π-π stacking (*25*), enhancing the solubilities of the building blocks for IRMOF production [(*22*), section S2]. In the syntheses of the longer links (VII to XI), solubilities were maintained by replacing, in a constitutionally symmetrical manner, selected pairs of methyl groups with hexyl substituents on appropriate phenylene rings. These crucial design criteria, coupled with a modular synthetic strategy, based on transition-metal catalyzed cross-coupling reactions, enabled the efficient elaboration of a series of slender and robust organic links with lengths ranging from 7 (I) to 50 Å (XI) (Fig. 1B). Gram quantities of soluble organic links II to XI were synthesized in 5 to 16 steps [(*22*), section S2].

The synthetic procedures for the IRMOF-74 series were developed on the basis of conditions previously used in the synthesis of the parent MOF-74 (*5*, *6*). As an illustrative example, colorless microcrystalline powder of IRMOF-74-II was isolated from the reaction of a mixture containing $Mg(NO_3)_2{\cdot}6H_2O$, link II, *N*,*N*-dimethylformamide, ethanol, and water at 120°C for 24 hours (90% yield based on the organic link). Similar conditions, with some adopted changes, were used to

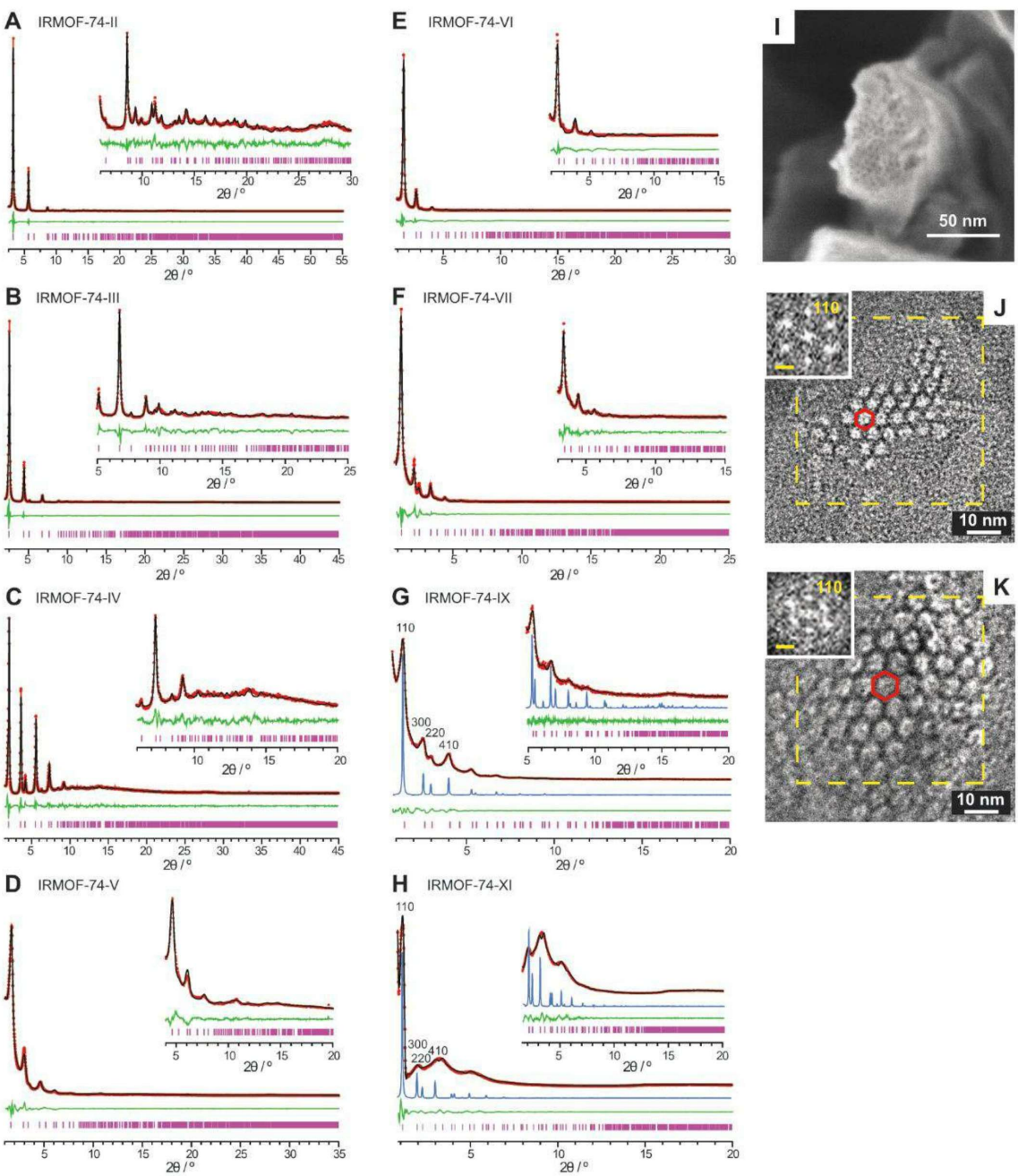

Fig. 2. X-ray diffraction patterns of IRMOF-74 series. (**A** to **F**) The Rietveld refinements of IRMOF-74-II to -VII. (**G** and **H**) The Pawley refinements of IRMOF-74-IX and -XI. Shown are the experimental (red), refined (black), and difference (green) patterns. The Bragg positions are marked as pink bars, and the patterns calculated from the crystal models are shown in blue in (G) and (H). (**I**) HRSEM image of a crystal of IRMOF-74-VII. (**J** and **K**) HRTEM images of IRMOF-74-VII and -IX, respectively. (Insets) The corresponding FFT diffraction patterns of the dashed square area in the original images. Scale bar, 0.2 nm^{-1}.

synthesize the rest of the series in gram quantities and 50 to 95% yield [(*22*), section S3]. The phase purity of each material was confirmed by the singular nature of its needle-like crystal morphology as observed in the scanning electron microscopy (SEM) images [(*22*), section S3]. The materials are highly crystalline, as demonstrated by their sharp powder x-ray diffraction peaks (Fig. 2). However, repeated attempts to produce crystals of the IRMOFs sufficiently large for single-crystal x-ray analysis were unsuccessful. Comparison of the experimental PXRD patterns with those calculated from the crystal models is in good agreement with regard to both positions and the relative intensities of the peaks. The predicted IRMOF-74 structures were ultimately validated with the Rietveld refinements performed for IRMOF-74-II to -VII (Fig. 2, A to H, respectively). The structural parameters were refined against the PXRD patterns collected with a synchrotron source, resulting in satisfactory residuals (table S2) [(*22*), section S4]. IRMOF-74-IX and -XI display broad peaks in their PXRD patterns—indicative of small crystals—a situation that precludes distinguishing the peaks with low intensities in the high-angle area. Furthermore, a possible lessening in the extent of order within the pore walls cannot be ruled out because these members of the series are constructed from extremely long organic links with long alkyl chains in which disorder and flexibility of the links are more pronounced. Although the quality of the diffraction patterns for these members does not allow us to perform a meaningful full structural refinement (Rietveld), the patterns clearly show the most intense diffraction peaks, corresponding to the largest *d*-spacings, at their expected 2θ positions. Accordingly, we carried out Pawley refinements in order to obtain their unit cell information. Low convergence residuals were achieved in the refinements of both compounds, and the agreement of the measured and model-calculated cell parameters indicated the formation of the targeted crystal structures (tables S2 and S3) (*22*).

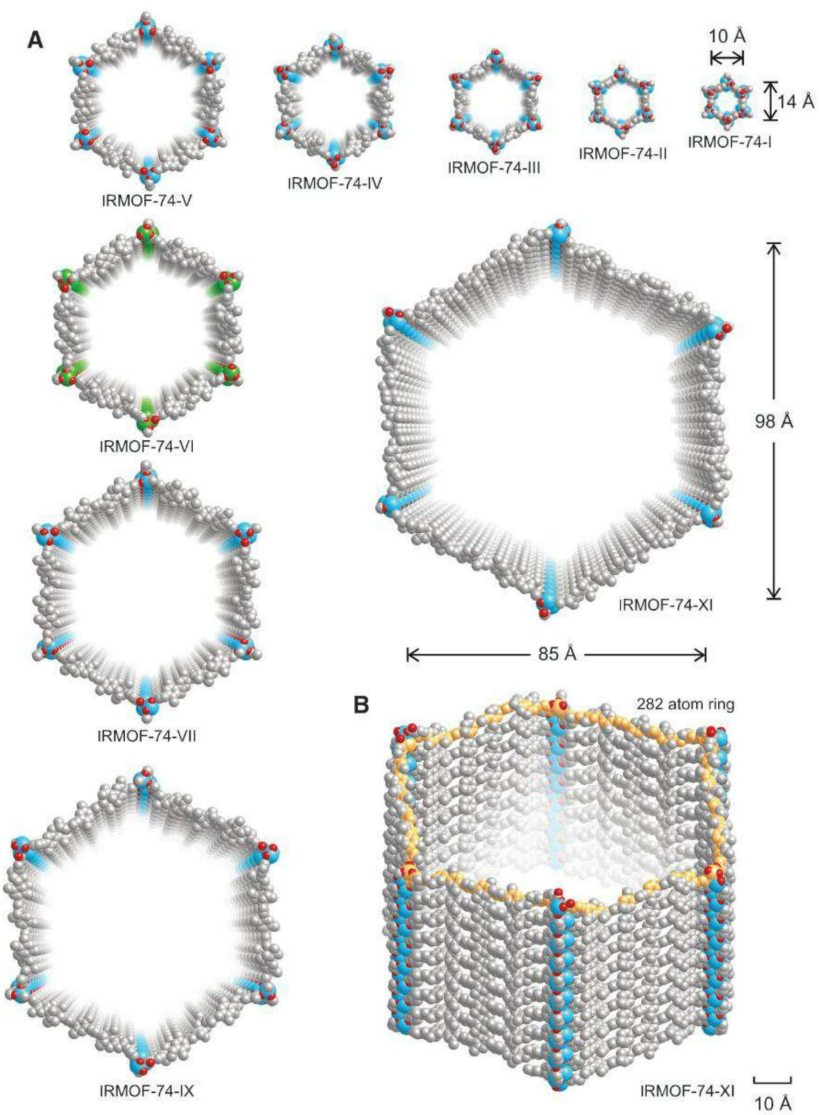

Fig. 3. Crystal structures of IRMOF-74 series. (**A**) Perspective views of a single one-dimensional channel shown for each member of IRMOF series, starting from the smallest (top right). Pore aperture is described by the length of the diagonal and the distance between the two opposite edges in the regular hexagonal cross section. Hexyl chains as well as hydrogen atoms are omitted for clarity. C atoms are shown in gray, O atoms in red, Mg atoms in blue, and Zn atoms in green. (**B**) Perspective side view of the hexagonal channel, showing the ring of 282 atoms (highlighted in gold) that define the pore aperture of the largest member of the series, IRMOF-74-XI.

Visualizing the pores of MOFs by means of EM presents a considerable challenge because of their sensitivity to the electron beam. We examined members of this IRMOF-74 series with low-voltage high-resolution SEM (LV-HRSEM) (IRMOF-74-VII) and high-resolution transmission EM (HRTEM) (IRMOF-74-VII and IX). Preliminary results showed that we could clearly visualize the arrangement and the size of the pores in specimens of the crystals of those IRMOFs (Fig. 2, I to K). Ordered pores arranged in a hexagonal formation were resolved through both techniques, and the pore metrics are in agreement with those determined from x-ray crystallography. Through the HRTEM experiments, six-sided rings were observed when the incident electron beam was positioned along the *c* axis and thus parallel to the pore channels. Fast Fourier transform (FFT) analysis was performed on the centered square areas in the HRTEM images of IRMOF-74-VII and -IX (Fig. 2, J and K, insets). Six reflection spots corresponding to the 110 reflections were resolved from the FFT patterns, from which the *d*-spacing was measured (3.95 and 5.57 nm for IRMOF-74-VII and -IX, respectively). These values are in good agreement with the *d*-spacing values derived from the x-ray crystal structure analysis (4.59 and 5.69 nm for IRMOF-74-VII and -IX, respectively). The small deviations from x-ray crystal analysis can be attributed to the broad spot in the FFT analysis and the ultra-high vacuum condition used in the HRTEM experiment. Furthermore, through the HRTEM analysis images of the channel direction (*c* axis) were observed by placing the incident electron beam perpendicular to the channels [(*22*), section S5].

The unit cell, void volume, and pore aperture cover a wide range as the size of the organic link is increased (table S4). The void volume calculated by using the crystal structure data increased from 49 to 85% for the parent IRMOF-74-I to -XI. The pore aperture is defined as the length of the diagonal and the distance between the two opposite edges in the regular hexagonal cross section (Fig. 3A, atom-to-atom distance). This method is consistent with that previously used for referring to the pore aperture, and it was deployed here to facilitate comparison with reported values (*2*, *26*). The diagonal dimension of the pore aperture, based on the refined unit cell, increased from 19 Å in IRMOF-74-II to 98 Å in IRMOF-74-XI, with a discrete increment of nearly 6 Å as each phenylene unit was added. Furthermore, upon the addition of each phenylene

unit there was an increase of 24 atoms in the ring size defining the pore aperture, leading to rings of 282 atoms in IRMOF-74-XI (Fig. 3B). This number of atoms far exceeds that defining the most open zeolites. In this series of IRMOFs, eight out of nine members (IRMOF-74-II to XI) have pore dimensions falling in the mesoporous region (>20 Å). Several other MOFs have been reported whose pore sizes are in this mesoporous region (*1*–*3*, *26*–*31*); however, their pore apertures are all exceeded by six members of this IRMOF series (IRMOF-74-IV to XI).

In order to assess the porosity of the IRMOFs and their architectural stability, Ar gas adsorption measurements at 87 K were performed. Initially, we carried out the activation procedures and characterization so as to ensure that the pores have been activated and free of guests. The solids of the IRMOFs were subjected to solvent exchange followed by evacuation, and in some cases treated with supercritical carbon dioxide, to obtain porous samples [(*22*), section S6]. These samples were studied by means of thermal gravimetric analysis, which showed no weight loss up to 300°C, confirming the high thermal stability of all the IRMOFs and indicating the absence of organic solvents from their pores. Successful removal of unreacted starting materials and organic solvent was further confirmed through ^{13}C cross-polarization/magic angle–spinning nuclear magnetic resonance [(*22*), section S6], elemental analysis, and Fourier transform infrared spectroscopy [(*22*), section S5]. Ar adsorption isotherms were measured on the activated samples of IRMOF-74-II to -XI (Fig. 4, A to D) [(*22*), section S7], each of which displays a Type IV isotherm that is typical of mesoporous materials (*8*). The magnitude of the relative pressure of the second step in the type IV isotherm is attributed to the increase in the effective energy of adsorption (pore-filling or condensation), in which higher pressures (P/P_0) are required for progressively larger pore sizes. Indeed, the starting point of the second step for IRMOF-74-II to -XI is observed at $P/P_0 = 0.03, 0.12, 0.21, 0.30, 0.38, 0.46, 0.55$, and 0.64, respectively. This gradual shift of the step position corresponds closely to the pore size expansion trend in the series. In addition, the pore sizes of these IRMOFs were examined by fitting nonlocal density functional theory models to the Ar adsorption isotherms. The estimated values are in line with the pore aperture metrics derived from the crystal structures [(*22*), section S7].

The pore volume in the frameworks is reflected in their Ar uptake capacity, which increases systematically from IRMOF-74-I to -XI as longer organic links are incorporated (440, 800, 990, 1310, 1520, 1320, 1680, 2000, and 2580 $cm^3\ g^{-1}$ at $P/P_0 = 0.9$, respectively; slightly lower uptake is observed in IRMOF-74-VI because of the use of Zn instead of Mg). The largest calculated pore volume in the series is for IRMOF-74-XI (3.3 $cm^3\ g^{-1}$), which is near that of the recently reported ultrahighly porous MOF-210 (3.6 $cm^3\ g^{-1}$) (*27*). In contrast, the highest Brunauer-Emmett-Teller (BET) surface area among the IRMOFs was observed in IRMOF-74-II, and the BET surface areas for IRMOFs with longer organic links showed even lower values because of the smaller geometric surface per volume (1350, 2510, 2440, 2480, 2230, 1600, 1800, 1920, and 1760 $m^2\ g^{-1}$ for IRMOF-74-I to -XI, respectively). Nevertheless, the surface areas are still much higher as compared with those found in mesoporous silica, porous carbon, and zeolites, thus providing more readily available surfaces for interaction with large guest molecules. The low density, which was also achieved in this IRMOF series, is not only attributable to the increase of open space but is a consequence of

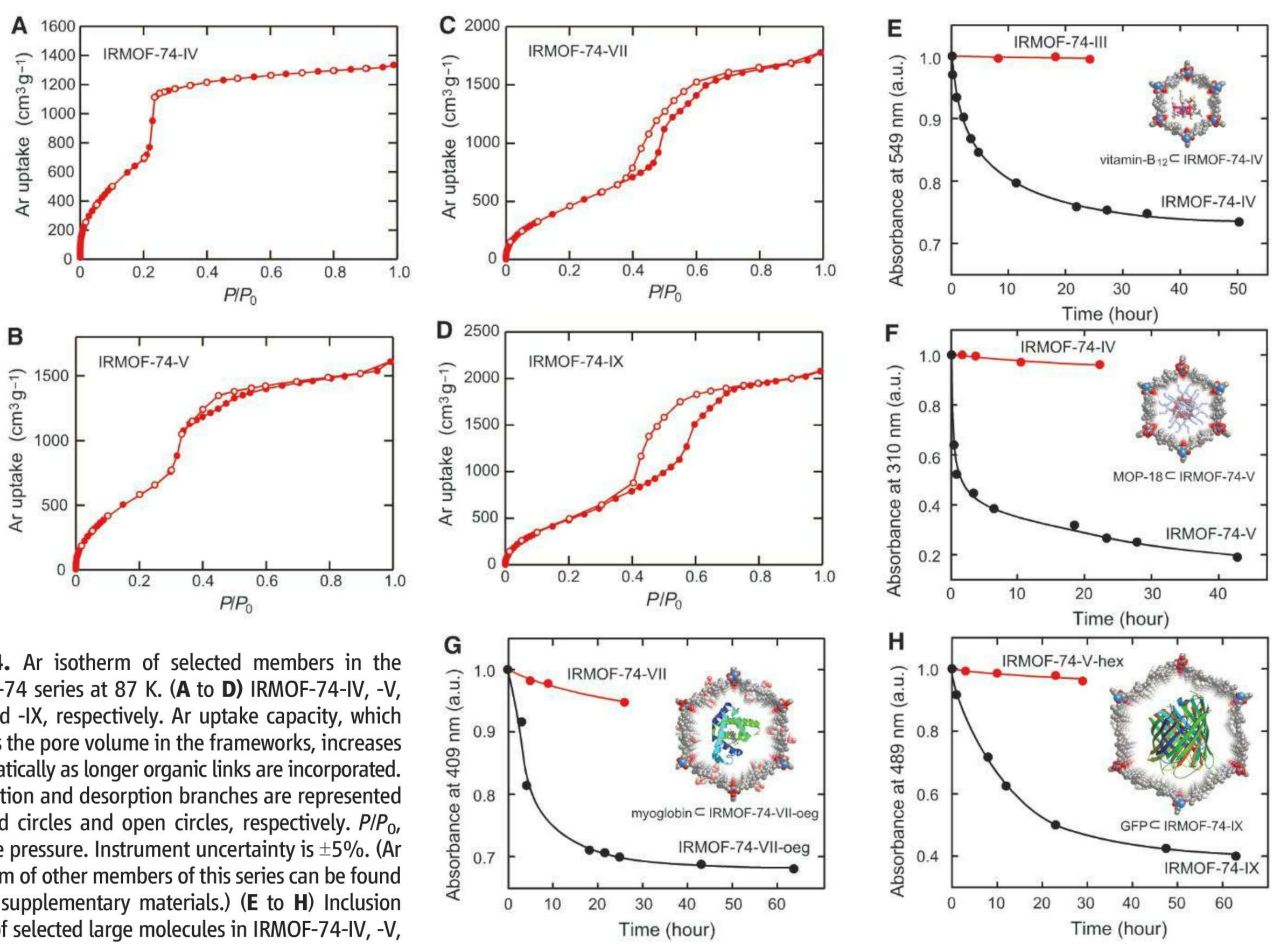

Fig. 4. Ar isotherm of selected members in the IRMOF-74 series at 87 K. (**A** to **D**) IRMOF-74-IV, -V, -VII and -IX, respectively. Ar uptake capacity, which reflects the pore volume in the frameworks, increases systematically as longer organic links are incorporated. Adsorption and desorption branches are represented by solid circles and open circles, respectively. P/P_0, relative pressure. Instrument uncertainty is ±5%. (Ar isotherm of other members of this series can be found in the supplementary materials.) (**E** to **H**) Inclusion study of selected large molecules in IRMOF-74-IV, -V, -VII-oeg and -IX series, respectively. This process was monitored through the decrease in absorbance at a selected wavelength as a function of contact time. For each measurement, the initial absorbance was normalized to 1.0. (Insets) Illustrations of the inclusion complex for each study.

the use of Mg, a metal with light weight, for the formation of the SBU. Seven of the eight new IRMOFs were constructed with Mg, including IRMOF-74-XI, which has the crystal density of 0.195 g cm^{-3}, the lowest known so far for a guest-free crystal at room temperature. There are several examples of crystalline materials reported with slightly lower framework density; however, they have not been proved to exist in their guest-free form (*32*, *33*).

Given the remarkable stability, ultrahigh porosity, and extremely large-pore-aperture characteristic of the IRMOF-74 series, we now have the ability to access a new size regime for the inclusion of large organic, inorganic, and biological molecules inside the pores of these IRMOF crystals. Preliminary measurements demonstrate the inclusion of large molecules into IRMOFs with appropriate pore apertures—specifically, vitamin B_{12} (largest size dimension of 27 Å) in IRMOF-74-IV, MOP-18 (inorganic spherical cluster with a diameter of 34 Å) (*34*) in IRMOF-74-V, myoglobin (globular protein with spherical dimensions of 21 by 35 by 44 Å) in IRMOF-74-VII-oeg, and GFP (barrel structure with diameter of 34 Å and length of 45 Å) in IRMOF-74-IX.

Typically, crystals of the desired IRMOF-74 were immersed in a solution containing the particular guest compound to be included. Activated crystals of IRMOF-74-IV were immersed in a 0.11 mM solution of vitamin B_{12}. The amount of vitamin B_{12} in the supernatant was measured with ultraviolet-visible (UV-Vis) spectrophotometry, and the characteristic absorbance at 480 nm was monitored over a period of 48 hours. The results are plotted in Fig. 4E, which clearly shows a continuous decrease of the amount of vitamin B_{12} in the supernatant. The same experiment was carried out, as a control, with IRMOF-74-III, whose pore aperture is smaller than IRMOF-74-IV and was not expected to show any uptake of vitamin B_{12}. This result was confirmed in that no decrease in absorbance was observed (Fig. 4E). Similar experiments were done for the inclusion of MOP-18 in IRMOF-74-V, myoglobin in IRMOF-74-VII-oeg, and GFP in IRMOF-74-IX (Fig. 4, F to H, respectively). For the solid resulting from the inclusion of MOP-18, an Ar adsorption isotherm at 87 K of a dried sample displayed a decrease in the step pressure as a result of inclusion into the pore [(*22*), section S8]. In the case of myoglobin, we functionalized the pores with a hydrophilic group (triethylene glycol mono-methyl ether, oeg) and observed substantial uptake by the corresponding IRMOF-74-VII-oeg because of myoglobin's hydrophilic surface. However, a negligible amount of myoglobin inclusion was observed in the control experiment, in which the pores were functionalized by hydrophobic hexyl chains, IRMOF-74-VII (Fig. 4F). For the control experiment in the GFP inclusion study, we used the hexyl chain functionalized IRMOF-74-V, termed IRMOF-74-V-hex, to provide a similarly hydrophobic pore environment to IRMOF-74-IX (Fig. 4G). Furthermore, GFP retained its folded structure when included in IRMOF-74-IX, as evidenced through confocal microscopy, which showed an unaltered characteristic fluorescence of GFP [(*22*), section S8]. It is remarkable that the crystallinity of the IRMOF materials is fully maintained throughout the inclusion process; the diffraction lines in the PXRD patterns of the included samples are coincident with those of the starting materials [(*22*), section S8].

References and Notes

1. Y. K. Park *et al.*, *Angew. Chem. Int. Ed.* **46**, 8230 (2007).
2. L. Ma *et al.*, *Nat. Chem.* **2**, 838 (2010).
3. M. Eddaoudi *et al.*, *Science* **295**, 469 (2002).
4. X. Lin *et al.*, *J. Am. Chem. Soc.* **131**, 2159 (2009).
5. N. L. Rosi *et al.*, *J. Am. Chem. Soc.* **127**, 1504 (2005).
6. P. D. C. Dietzel *et al.*, *Eur. J. Inorg. Chem.* **2008**, 3624 (2008).
7. S. A. Bagshaw *et al.*, *Science* **269**, 1242 (1995).
8. D. Zhao *et al.*, *Science* **279**, 548 (1998).
9. S. H. Joo *et al.*, *Nature* **412**, 169 (2001).
10. S. Inagaki *et al.*, *Nature* **416**, 304 (2002).
11. O. M. Yaghi *et al.*, *Nature* **423**, 705 (2003).
12. S. Kitagawa *et al.*, *Angew. Chem. Int. Ed.* **43**, 2334 (2004).
13. D. Bradshaw *et al.*, *Acc. Chem. Res.* **38**, 273 (2005).
14. J. S. Seo *et al.*, *Nature* **404**, 982 (2000).
15. Z. Wang, S. M. Cohen, *J. Am. Chem. Soc.* **129**, 12368 (2007).
16. B. D. Chandler *et al.*, *Nat. Mater.* **7**, 229 (2008).
17. O. Shekhah *et al.*, *Chem. Soc. Rev.* **40**, 1081 (2011).
18. M. Dincă *et al.*, *J. Am. Chem. Soc.* **128**, 16876 (2006).
19. V. Lykourinou *et al.*, *J. Am. Chem. Soc.* **133**, 10382 (2011).
20. N. L. Rosi *et al.*, *Angew. Chem. Int. Ed.* **114**, 294 (2002).
21. M. Lin *et al.*, *CrystEngComm* **13**, 776 (2011).
22. Materials and methods are available as supplementary materials on *Science* Online.
23. M. O'Keeffe, O. M. Yaghi, *Chem. Rev.* **112**, 675 (2012).
24. D. Hanss, O. S. Wenger, *Eur. J. Inorg. Chem.* **2009**, 3778 (2009).
25. S. T. Pasco, G. L. Baker, *Synth. Met.* **84**, 275 (1997).
26. X.-S. Wang *et al.*, *J. Am. Chem. Soc.* **128**, 16474 (2006).
27. H. Furukawa *et al.*, *Science* **329**, 424 (2010).
28. A. Sonnauer *et al.*, *Angew. Chem. Int. Ed.* **48**, 3791 (2009).
29. O. K. Farha *et al.*, *Nat. Chem.* **2**, 944 (2010).
30. X. Zhang *et al.*, *Angew. Chem. Int. Ed.* **50**, 5729 (2011).
31. B. Wang *et al.*, *Nature* **453**, 207 (2008).
32. H. M. El-Kaderi *et al.*, *Science* **316**, 268 (2007).
33. H. Furukawa *et al.*, *Inorg. Chem.* **50**, 9147 (2011).
34. H. Furukawa *et al.*, *J. Am. Chem. Soc.* **128**, 8398 (2006).

Acknowledgments: The research at UCLA was funded by BASF SE (Ludwigshafen, Germany) (synthesis of MOFs), the Center for Gas Separations Relevant to Clean Energy Technologies, an Energy Frontier Research Center (EFRC) funded by the DOE, Office of Science, Office of Basic Energy Sciences (U.S. DOE–BES) for adsorption (DE-SC0001015), and the U.S. Department of Defense, Defense Threat Reduction Agency for inclusion studies (HDTRA11-1-0018). The research conducted at Northwestern University was supported in part by the Non-equilibrium Energy Research Center, which is an EFRC funded by the U.S. DOE–BES (DE-SC0000989). We acknowledge the World Class University Program (R-31-2008-000-10055-0). We thank M. Zhao and D. Li from D. S. Eisenberg's group at UCLA for providing GFP and helpful discussions. Portions of this research were carried out at the Stanford Synchrotron Radiation Laboratory, a national user facility operated by Stanford University on behalf of the U.S. DOE–BES. Confocal laser scanning microscopy was performed at the California NanoSystems Institute Advanced Light Microscopy/Spectroscopy Shared Resource Facility at UCLA, supported with funding from NIH–National Center for Research Resources shared resources grant (CJX1-443835-WS-29646) and NSF Major Research Instrumentation grant (CHE-0722519). We acknowledge JEOL for providing their latest LV-HRSEM instrument. We thank M. Schibler, S. Wan, L. Wang, A. Sue, C. Stevens, C. Knobler, and J. Brown for their invaluable assistance. Z.L. acknowledges K. Suenaga at AIST, Tsukuba, Japan, for his encouragement. S.G. acknowledges the Swiss National Science Foundation for financial support. F.G. acknowledges funding by the Spanish Ministry of Education through the "Programa de Movilidad de Recursos Humanos del Plan Nacional de I-D+i 2008-2011." All data and images are available in the body of the paper or as supplementary materials. Crystallographic data for the reported crystal structures have been deposited at the Cambridge Crystallographic Data Centre via www.ccdc.cam.ac.uk with codes 841642 to 841651 (IRMOF-74-II to -XI, respectively).

Supplementary Materials

www.sciencemag.org/cgi/content/full/336/6084/1018/DC1
Materials and Methods
Figs. S1 to S51
Tables S1 to S6
References (*35*–*38*)

6 February 2012; accepted 6 April 2012
10.1126/science.1220131

Linking Petrology and Seismology at an Active Volcano

Kate Saunders,[1]* Jon Blundy,[1] Ralf Dohmen,[2] Kathy Cashman[1]

Many active volcanoes exhibit changes in seismicity, ground deformation, and gas emissions, which in some instances arise from magma movement in the crust before eruption. An enduring challenge in volcano monitoring is interpreting signs of unrest in terms of the causal subterranean magmatic processes. We examined over 300 zoned orthopyroxene crystals from the 1980–1986 eruption of Mount St. Helens that record pulsatory intrusions of new magma and volatiles into an existing larger reservoir before the eruption occurred. Diffusion chronometry applied to orthopyroxene crystal rims shows that episodes of magma intrusion correlate temporally with recorded seismicity, providing evidence that some seismic events are related to magma intrusion. These time scales are commensurate with monitoring signals at restless volcanoes, thus improving our ability to forecast volcanic eruptions by using petrology.

Zoned volcanic crystals preserve a record of magmatic processes over the lifetime of the crystal, from initial nucleation to final quenching upon eruption (*1*–*3*). Perturbations in magmatic variables (such as composition, volatile content, temperature, pressure, and oxidation state) can cause crystal zonation. The interplay of volatile loss through degassing and heating due to magma chamber recharge can result in complex textural patterns of crystal growth and dis-

solution, with associated changes in crystal chemistry. If the response of crystal chemistry to changes in magmatic variables is known, through experimental or thermodynamic models, the textural appearance and chemical composition of discrete crystal zones can be used to discriminate between different magmatic processes responsible for the zonation. By modeling the individual perturbations (crystal zones) with diffusion chronometry, it is possible to temporally link petrologically constrained magmatic processes to the contemporaneous monitoring record, greatly enhancing our ability to interpret monitoring signals (*3*).

Mount St. Helens (MSH) is a composite stratovolcano in the Cascades volcanic arc in the United States. MSH produced a series of well-monitored and -studied explosive and dome-forming eruptions during 1980–1986. Dacite, with relatively little chemical variation, was the dominant magma erupted, although historically MSH has erupted a whole spectrum of magmas, from basalt to andesite and high-silica dacite (*4*). A detailed picture of the temporal evolution of the subvolcanic magmatic system at MSH has been inferred from geophysical studies coupled with in situ microanalytical studies of melt inclusions and crystals from the 1980–1986 sequence (*5*–*8*). The volatile saturation pressures of melt inclusions reveal that crystal growth occurred at a range of depths during 1980 that were consistent with the spread of earthquake depths (*7*), whereas post-1980 crystallization is limited to the upper 3 km of the volcanic plumbing system (*7*). Orthopyroxene (opx) is a ubiquitous crystal and groundmass phase at MSH throughout the eruption sequence (Fig. 1).

We analyzed opx from nine MSH samples by backscattered electron (BSE) imaging and analyzed major element chemistry by electron probe microanalyzer (EPMA) and Fe-Mg diffusion modeling (*9*) (Fig. 1B). Opx composition typically spans a compositional range of Mg# [molar $Mg/(Mg+Fe^{2+})$] from 0.54 to 0.76, with a predominance of values in the range 0.6 to 0.7 (table S1). Maximum variation in Mg# within a single crystal is 0.15, but typically ranges from 0.06 to 0.09. Overall, the range of major element compositions of opx crystals displays no systematic differences between samples, irrespective of zoning type (zoned or unzoned), location of analysis (rim or core), or size (phenocryst or microlite). The compositional heterogeneity of opx crystals increases over the course of the eruption sequence, with opx crystals erupted between 1984 and 1986 (dome-forming eruptions) displaying the greatest compositional range.

Of 579 opx crystals examined, 98 displayed Fe-Mg zoning suitable for diffusion modeling, whereas 165 displayed no discernible Fe-Mg zoning (table S2). The number of unzoned crystals observed per sample sharply decreased between the 8 August 1980 and the 14 May 1982 eruption, coincident with the last known intrusion of deep magma deduced from seismicity (*8*). Zoned crystals were subdivided into four categories: (i) concentric reverse-zoned (with Fe-rich cores and Mg-rich rims); (ii) concentric normal-zoned (Mg-rich cores and Fe-rich rims); (iii) multiply zoned (with two or more reversals in Mg#); and (iv) patchy (with zoning that does not fall into any other category) (Fig. 1A). The abundance of Fe-rich cores decreases toward May 1986 (table S2). The outer interface of the outermost zone of suitable opx from the categories (*1*–*3*) was modeled diffusively (*9*) (table S3) to determine the time scales of magmatic processes in the lead-up to eruption. The zones are classed as either normal- or reverse-zoned as identified by the relative compositional change in the outermost zones only. Calculated time scales are generally <12 months, a time period commensurate with the monitoring recorded at MSH, suggesting that temporal links can be made between petrology and monitoring.

Before the calculated time scales can be interpreted, it is important to evaluate the causal mechanism for the opx zoning. Crystal zonation results from changes in magmatic temperature, water content, pressure variation, or magma differentiation. Major element compositions of opx crystals show that cores and rims of crystals grew from similar, if not the same, melt batches (table S1). The only exceptions being the high-Mg# zones of opx in 7 August 1980 and the later dome-forming eruptions of 7 February 1983, 17 June 1984, and 8 May 1986, which form a distinct grouping at high Mg# but with concentrations of TiO_2, Al_2O_3, and CaO that are indistinguishable from those in the other zones (fig. S1 and table S1). Comparison of natural MSH opx to opx generated in experimental studies (*10, 11, 12*) reveals that only one set of experiments can reproduce opx with the distinct high Mg# zones. These are the experiments of (*11*), which were conducted at the most-oxidized conditions [log of oxygen fugacity (fO_2) = –11.5]. In order to evaluate whether a change in fO_2 can cause the variation in opx Mg#, we calculated the amount of ferrous iron required to change the opx Mg# by 0.09 at a fixed temperature and a fixed Fe-Mg exchange coefficient (table S4). This requires a change of 26% in the proportion of the total iron that is ferrous, which corresponds to a change in fO_2 relative to NNO (ΔNNO) of ~2.5, log units (table S4). However, the maximum observed variation in ΔNNO in any one eruption is only +0.8 (*7*), indicating that a change of fO_2 alone cannot be responsible for the variation in Mg#. It has been proposed that higher melt concentrations of H_2O can increase the Fe content of opx crystals (*13*), and (*13*) used the experimental data of (*10*) to show that a 1 weight % (wt %) change in H_2O concentration could cause the Mg# variation observed, which melt inclusion studies (*7*) indicate is plausible for MSH 1980–1986 eruptions. Thus, a combination of variation in fO_2 and H_2O concentration of the melt could generate the observed differences in opx Mg#, although we must consider the affects of this on other chemical components.

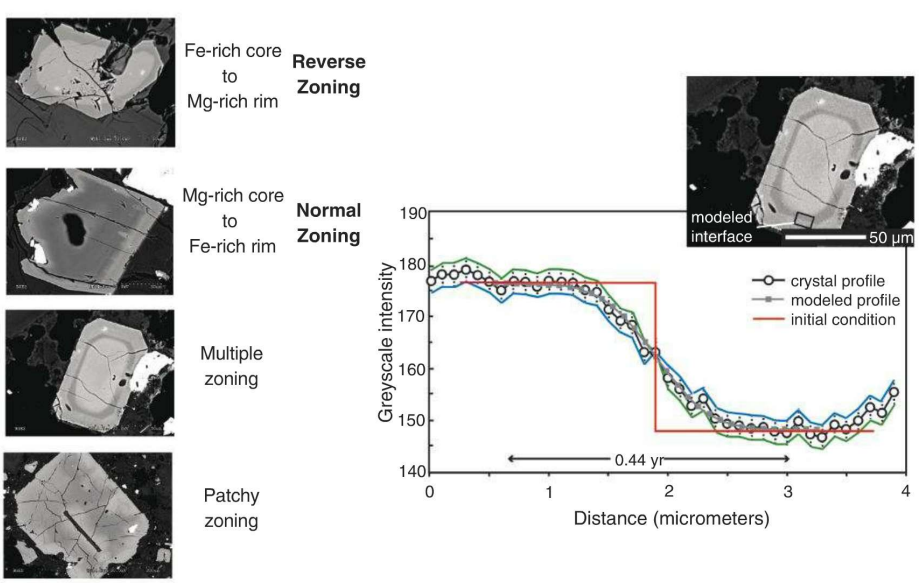

Fig. 1. Crystal zoning in MSH opx crystals. (**Left**) Examples of the different types of zoning observed. (**Right**) Modeled diffusion profile extracted from the BSE image (*9*) at 884°C (*7*), using a Fe-Mg interdiffusion coefficient of 4.72×10^{-21} m^2 s^{-1} (*18*). The profile is extracted from the highlighted area and rotated for modeling. The blue and green lines indicate the maximum uncertainty in the measured profiles due to the 2 SD errors of EPMA analyses (error bars) propagated through the BSE calibration (*9*). This results in calculated time scales of 0.51 year and 0.37 year for the blue and green profiles, respectively.

[1]Department of Earth Sciences, University of Bristol, Bristol BS8 2TU, UK. [2]Institut für Geologie, Mineralogie und Geophysik, Ruhr-Universität Bochum, Bochum, Germany.

*To whom correspondance should be addressed. E-mail: Kate.Saunders@bristol.ac.uk

We observed two styles of opx Fe-Mg zonation: (i) rare relatively smooth (diffused) boundaries and (ii) comparatively sharp boundaries (Fig. 2 and additional data S1). In opx crystals with smooth Fe-Mg boundaries, Al_2O_3 and TiO_2 are decoupled from the Mg#, whereas they correlate with Mg# in crystals with sharp interfaces (Fig. 2). This suggests that Fe-Mg interdiffusion occurs on a much faster time scale than Al_2O_3 and TiO_2, effectively smoothing the original Mg# profile while retaining variations in Al_2O_3 and TiO_2. Al diffusion in clinopyroxenes is known to be very slow (*14*), therefore it is reasonable to assume that this is also true for opx. Thus, the Al_2O_3 and TiO_2 concentrations of opx crystals can be used to reconstruct the original magmatic zoning in opx composition before its modification by the interdiffusion of Fe and Mg and so investigate the magmatic processes responsible for the original zonation.

TiO_2 and Al_2O_3 profiles of individual opx crystals reveal that the majority of opx growth occurred within a restricted compositional region with only a few excursions, most notably to high TiO_2 (fig. S2). These excursions are typically found in crystal cores with subsequent rimward migration to the tightly constrained region occupied by the majority of crystals. This behavior suggests that these opx cores have an "antecrystic" origin; that is, they were entrained from ancestral, partially crystallised magmas. In order to reconstruct the melt composition responsible for the growth of the crystal zones, we developed an empirical transfer function using experimental data on MSH dacites (*10, 12*), conducted over a wide range of temperature (850° to 1060°C), pressure (100 – 250 MPa), and water fugacity (46 to 165 MPa) appropriate to the subvolcanic magma reservoir (*7*). The transfer functions relate the experimental partitioning coefficients ($K_{di} = [i]_{opx}/[i]_{melt}$, where square brackets denote the weight fraction concentration) of Ti and Al between opx and melt to the Al_2O_3 content of the opx as follows

$$K_{dAl} = 0.0835\ Al_2O_3\ (\text{wt \% in opx}) - 0.0123\ (\pm 0.014,\ R^2 = 0.8727,\ n = 29) \quad (1)$$

$$K_{dTi} = 4.961\ K_{dAl} + 0.0186\ (\pm\ 0.15,\ R^2\ 0.5996,\ n = 29) \quad (2)$$

where R^2 is the correlation coefficient and n is the number of individual experiments fitted.

We compare the reconstructed melt compositions, using Eqs. 1 and 2, to magmas erupted historically from MSH and elsewhere in the Cascades (Fig. 3). The bulk of calculated melt compositions overlap the spectrum of whole rock, melt inclusion, and groundmass glass data of samples erupted from MSH during the 1980–1986 sequence as well as dominantly dacitic rocks from elsewhere in the Cascades. The observed close correspondence strongly suggests that the opx zones that we observe were generated through crystallization from a diversity of broadly cogenetic melts observed, or inferred, to have been present at some stage in the sub-MSH magma plumbing system. Calculated melt compositions for opx from Goat Rocks andesites [1800 to 1857 (*4*)] plot (*15*) at higher TiO_2 concentrations (Fig. 3) than other MSH magmas, revealing a possible source of the high-Ti opx crystal cores. Thus, we consider opx with high TiO_2 (0.39 wt % at 0 to 2 wt % Al_2O_3) to be antecrysts derived from preexisting plutonic bodies created during earlier periods of magmatic activity. A small proportion of opx crystals with highly diffused core-rim interfaces (Fig. 2), but TiO_2 concentrations of 0.1 to 0.3 wt %, return magmatic residence times of 43 to 878 years (*9*). These opx crystals are also interpreted as antecrysts that were entrained into the 1980–1986 magma system from the subvolcanic plutonic complex (*4*) generated during earlier periods of magmatism.

The close correspondence between calculated melt compositions and volcanic magmas at MSH, and the fact that the trends converge on the composition of matrix glasses of MSH dacites, provide insights into the changing chemical environments to which the opx crystals were exposed. For example, individual opx crystals were probably held in a subvolcanic magma reservoir that was periodically perturbed by incursions of chemically related magma that differed from the bulk resident magma either in temperature, volatile content, fO_2, or bulk composition, or all four (Fig. 3). Fluctuations in fO_2 are not large enough to affect the observed Mg#. However, the effect on Al and Ti concentration from changing H_2O content is unclear. Figure 3 suggests that the most ready explanation for the observed opx zoning is variations in magma chemistry. The style of zoning reflects the nature of the magmatic perturbation involving these different magmas. Normal zoning may be a consequence of rapid cooling of crystals suspended in new magma pulses as they intrude into the reservoir or of rapid crystallization induced by fluxing with CO_2-rich gas, for which there is evidence in MSH melt inclusions (*16*). Conversely, reverse zoning can be produced as crystals resident in the chamber are subjected to heating by the intruding magma, resulting in crystals first becoming partially resorbed, then overgrown with a more Mg-rich zone in equilibrium with the hotter, adjacent melt. Unzoned crystals are ambiguous: They could represent (i) remote parts of the magma chamber unaffected by new magma intrusions, (ii) new growth from fully homogenized hybrid magmas, or (iii) old crystals from the preexisting resident body. Typically, only

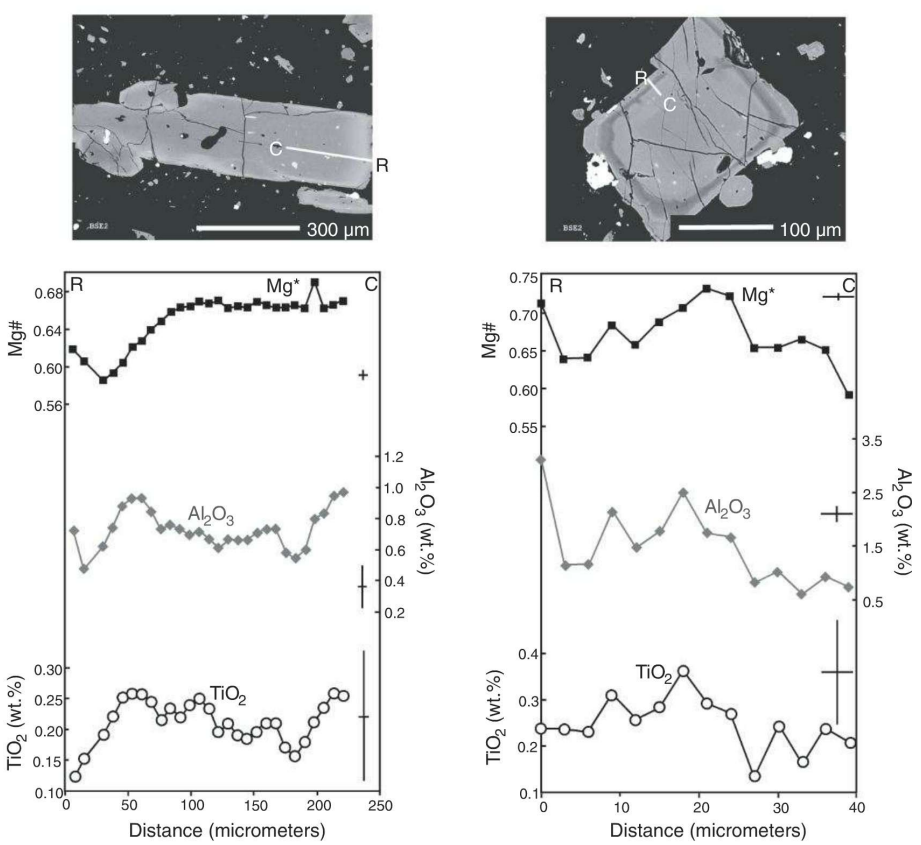

Fig. 2. Sharp and diffuse boundaries of opx crystals. (**Left**) Crystal SH135_KS22 has a diffuse core-rim (C-R) interface. Al_2O_3 and TiO_2 are decoupled from Mg#. (**Right**) Crystal SH135_KS24 displays sharp compositional boundaries at the rim where Al_2O_3, TiO_2, and Mg# all correlate. Errors bars (crosses) represent 2 SD analytical errors of Al_2O_3 and TiO_2 analyses (*19*) of propagated errors on Mg# calculation from the 2 SD error of FeO and MgO analyses on the *y* axis and an excitation area of analysis of 2 µm on the *x* axis.

core and rim analyses of these opx crystals were measured. However, a profile through an opx that is homogenous in Mg# from May 1980 (fig. S3) reveals zonation in Al_2O_3 and TiO_2, within 30 μm of the rim, indicating that originally this opx would also have been zoned, before the zoning was eliminated by diffusion. The time scale for this to occur can be estimated from the characteristic diffusion length $\{x = (Dt)^{1/2}$, where x is distance, D is the diffusion coefficient [see (*9*)], and t is time$\}$. If a diffusion length of 50 μm (a typical rim width) is assumed, reequilibrium would take between 220 and 16,000 years at 1100° and 886°C, respectively. These time scales are consistent with the crystals being plutonic relics of the Kalama eruption (1480 to 1778) and older eruptions (Swift Creek and Cougar) (*4*). In that case, both options (i) and (iii) are both plausible. The proportion of the different zoning types (table S2) potentially contains information about the relative volumes of resident (plutonic) and new magma throughout the eruptive sequence.

Fe-Mg diffusion chronometry (*9*) (Fig. 1B) yields the time elapsed between the final rim growth of zoned opx crystals and their eruption. Both normal and reverse rims appear to have grown contemporaneously. Integrating the diffusion time series with the seismic and SO_2-flux record of the eruption sequence reveals that the predominant episodes of rim crystallization (normal and reverse) correlate remarkably well with episodes of increased seismicity and flux of SO_2 gas during the eruption sequence (Fig. 4). Some Mg-rich rims formed during the months before 18 May 1980 (from October 1978), whereas both Fe-rich and Mg-rich rims grew simultaneously from February 1980, typically less than 1 year before eruption (tables S3). There is a peak in Fe-rich rim growth in April 1980 (Fig. 4), with the dominance of Fe-rich rims increasing through the eruption sequence.

Detectable seismic activity beneath MSH commenced on 20 March 1980 and may have been episodic in nature (*8, 17*). Long-period earthquakes that began in April 1980 represent the degassing of magma accumulated at shallow depths (*8*), thus providing evidence for the movement of volatiles (such as H_2O and CO_2) through the system. This is coincident with the growth of Fe-rich opx rims that grow preferentially under H_2O-rich (or reducing) conditions (*13*). Melt inclusion volatile-saturation pressures indicate that crystallization between April 1982 and May 1986 is shallow (at a depth of 0 to 3 km) (*7*). Hence some of this normal zoning may have originated through the fluxing of CO_2-rich gas (Fig. 4) triggering copious crystallization (*16*) rather than the intrusion of new hot magma, for which there is only limited monitoring evidence at this time (*7, 8*).

The predominance of Mg-rich rims in the early part of the eruption sequence, where seismicity indicates the input of new deeper magma (8 to 12 km) (*5, 8*) and the volatile-saturation pressures of melt inclusions are higher (*7*), leads us to interpret the Mg-rich rims as the result of recharge or convective overturn of the magmatic system just before 18 May 1980. The preponderance of reverse-zoned opx rims in the explosive eruptive periods of May 1980 (Fig. 4) is consistent with rejuvenation by hotter, less-evolved magma. The absence of conspicuous blobs of mixed magma in MSH eruptives argues against a substantial compositional gap between resident and rejuvenating magma. Normal zoning peaks in early 1982 and mid-1985 may also record the intrusions of new magma into the system.

The peaks in normal opx zonation (Fe-rich rims) observed in post-1980 samples (Fig. 4D) reflect crystallization of the magma body. In the absence of vigorous hydrothermal cooling, crystallization can be achieved by CO_2 gas fluxing through the volcanic system or rapid cooling of the rejuvenating magmas. Both possibilities are plausible. The simultaneous growth of Mg-rich and Fe-rich rims throughout the eruption sequence may indicate continued inputs of small batches of magma into the MSH magmatic system that were not detected by the external monitoring network, as suggested from a detailed analysis of the seismicity (*8*). In this case, crystals would have originated in both the resident (Fe-rich cores) and intruding (Mg-rich cores) magmas and in any regions of the magma system affected by CO_2-rich gas fluxing. Correlations between peaks in normal zoning and enhanced SO_2 flux (Fig. 4) support this possibility. Unzoned crystals were resident beneath MSH before rejuvenation in the late 1970s, From 1980 to 1986, the volume of older, resident magma would have become diminished through eruption, which is consistent with the decreasing volume of unzoned crystals (table S2).

Our results show that the development of opx crystal zones occurred on time scales commensurate with the monitoring record. The growth of these zones is consistent, petrologically, with perturbations of the magmatic reservoir. The preponderance of rim-growth episodes during times of elevated seismic activity suggests that earthquake swarms faithfully record the arrival of new magma pulses. These pulses are co-genetic with the resident magma in the subvolcanic reservoir (*2*) and were probably generated from a common parent at greater depths. Mixing of new pulses into the reservoir produced a range of normal and reverse zones in opx crystals located close to the point of injection and along any pathways of CO_2 degassing. Vestigial crystals from older eruptive episodes, or remote from the injection point, did not develop zoning. The mixing of older magmas into new, hotter pulses may have triggered convective overturn in the reservoir, bringing together crystals with different histories, and hence zoning patterns, shortly before eruption. Our results support the idea that there was pulsatory growth of the sub-MSH magma reservoir, in accord with models of incremental growth emerging from studies of intrusive bodies of silica-rich magma, and they

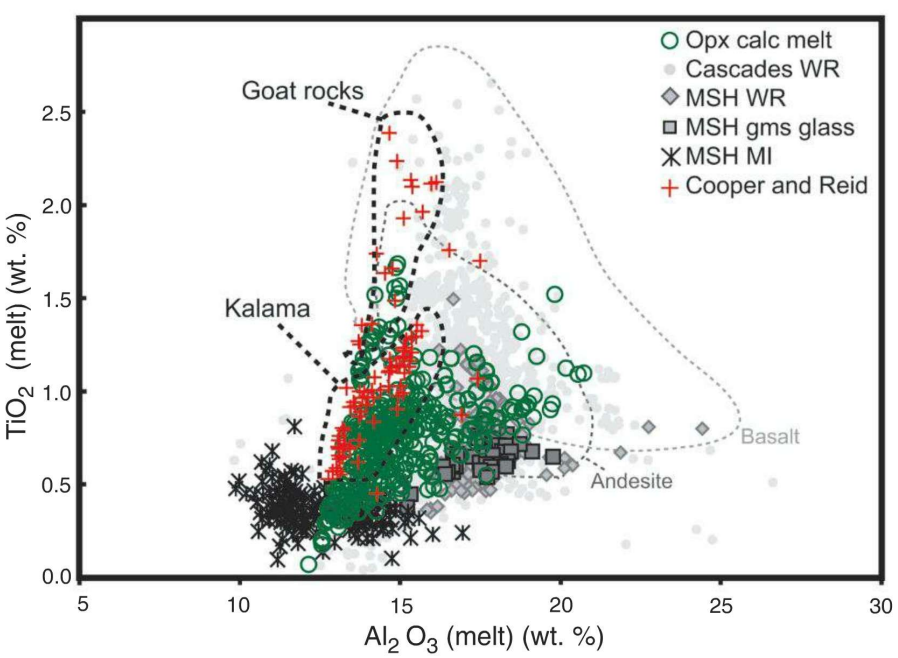

Fig. 3. Comparison of calculated melt compositions from 1980–1986 opx, using Eqs. 1 and 2, to bulk rock, groundmass glass (gms glass), and melt inclusion (MI) compositions of volcanics from the Cascades (*20*) and MSH (*4, 7, 10, 20–27*). Fields that correspond to basalt (<58 wt % SiO_2) and andesite (58 to 64 wt % SiO_2) whole-rock (WR) compositions (based on SiO_2 content) are highlighted by light gray dashed lines. The majority of opx-derived melt compositions lie in the dacite field (not highlighted, >64 wt % SiO_2) located at low Al_2O_3 and TiO_2 concentrations on the lower left side of the plot.

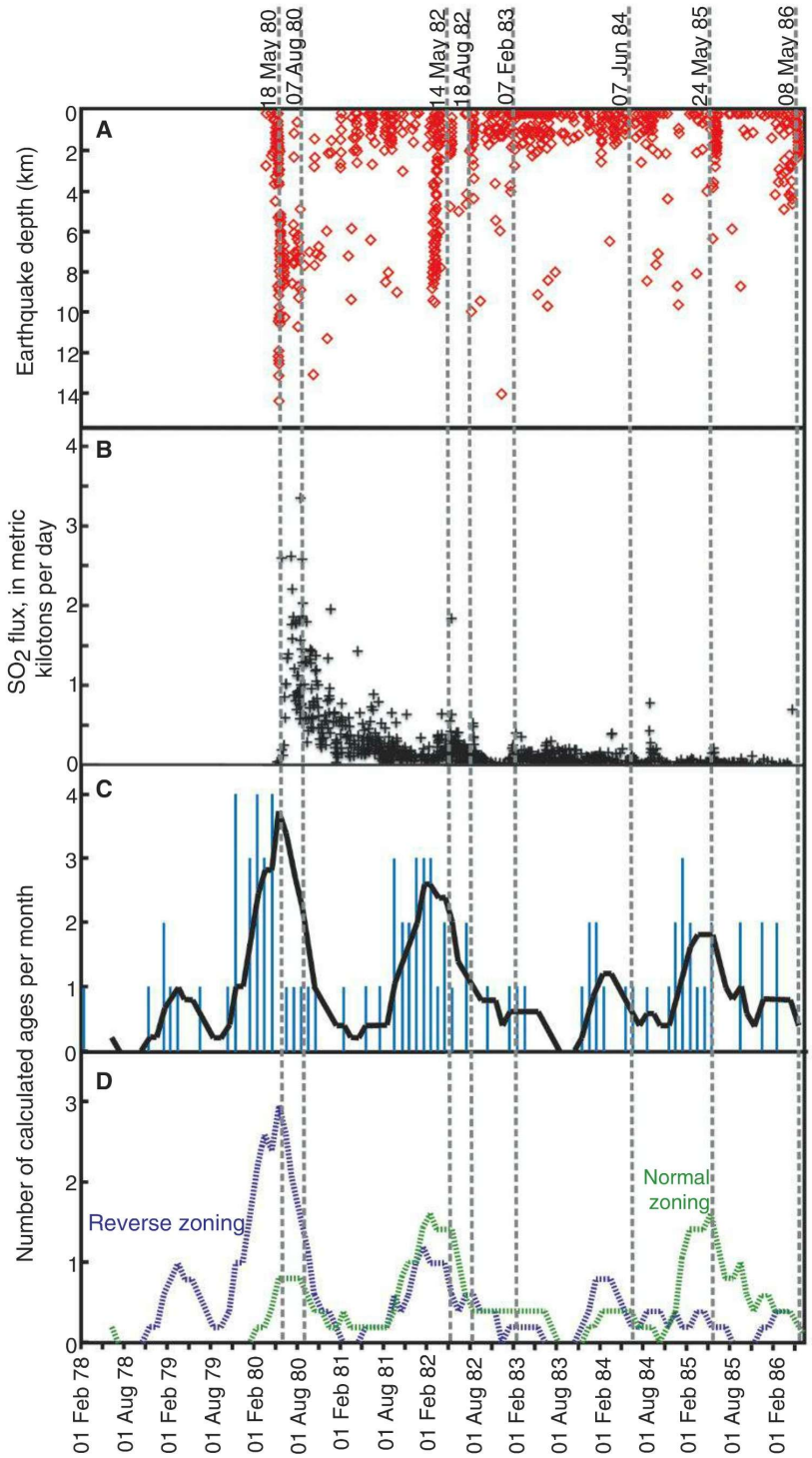

Fig. 4. Calculated Fe-Mg diffusion time scales of MSH opx crystals compared to monitoring data for the same eruptive period. (**A**) Seismic record of the 1980–1986 eruption sequence (*5*). No seismic record is available before 1980. (**B**) Measured flux of SO_2 gas from MSH (*28*). (**C**) Calculated age of opx rim growth (that is, the date of eruption minus the calculated diffusion time scale), binned by month for the entire opx population. Thus, the age recorded is the month in which the opx rim growth was triggered by magmatic perturbation. The black line displays the running average (over five points, equivalent to the average calculated uncertainty in calculated time scales) of all the data (*9*). The peaks in the diffusion time series correspond to episodes of deep seismicity in 1980 and 1982 and to elevated SO_2 flux in 1980 and possibly 1982. (**D**) Running average of the opx rim time scales, displaying reverse zonation (Mg-rich rims) in blue and normal zonation (Fe-rich rims) in green (table S3). There are reverse zonation peaks in the early 1980, probably due to rejuvenation of the magma system by hotter pulses, whereas Fe-rich rims are more dominant from 1982 on. Vertical dashed gray lines represent the eruptions studied here.

provide an independent petrological framework in which to interpret monitoring data.

References and Notes

1. D. J. Morgan *et al.*, *Earth Planet. Sci. Lett.* **222**, 933 (2004).
2. K. Berlo, J. Blundy, S. Turner, C. Hawkesworth, *Contrib. Mineral. Petrol.* **154**, 291 (2007).
3. M. Kahl, S. Chakraborty, F. Costa, M. Pompilio, *Earth Planet. Sci. Lett.* **308**, 11 (2011).
4. J. S. Pallister, R. P. Hoblitt, D. W. Crandell, D. R. Mullineaux, *Bull. Volcanol.* **54**, 126 (1992).
5. Pacific Northwest Seismic Network, http://old.pnsn.org/HELENS/welcome.html.
6. K. Cashman, S. M. McConnell, *Bull. Volcanol.* **68**, 57 (2005).
7. J. Blundy, K. Cashman, K. Berlo, *U.S. Geol. Surv. Prof. Pap.* **1750**, 755 (2008).
8. R. Scandone, K. V. Cashman, S. D. Malone, *Earth Planet. Sci. Lett.* **253**, 513 (2007).
9. Materials and methods are available as supplementary materials on *Science* Online.
10. J. E. Gardner, M. Rutherford, S. Carey, H. Sigurdsson, *Bull. Volcanol.* **57**, 1 (1995).
11. M. J. Rutherford, J. D. Devine, *J. Geophys. Res.* **93**, 11949 (1988).
12. M. J. Rutherford, H. Sigurdsson, S. Carey, A. Davis, *J. Geophys. Res.* **90**, 2929 (1985).
13. H. M. Frey, R. A. Lange, *Contrib. Mineral. Petrol.* **162**, 415 (2011).
14. V. Sautter, O. Jaoul, F. Abel, *Earth Planet. Sci. Lett.* **89**, 109 (1988).
15. K. M. Cooper, M. R. Reid, *Earth Planet. Sci. Lett.* **213**, 149 (2003).
16. J. D. Blundy, K. V. Cashman, A. Rust, F. Witham, *Earth Planet. Sci. Lett.* **290**, 289 (2010).
17. E. Endo, S. D. Malone, L. S. Noson, C. S. Weaver, *U.S. Geol. Surv. Prof. Pap.* **1250**, 93 (1981).
18. C. S. Schwandt, R. T. Cygan, H. R. Westrich, *Contrib. Mineral. Petrol.* **130**, 390 (1998).
19. K. Saunders *et al.*, *Am. Mineral.* **97**, 532 (2012).
20. E. A. Du Bray *et al.*, USGS Data Series 155: Geochemical database for volcanic rocks of the Western Cascades, Washington, Oregon, and California (2006).
21. J. S. Fruchter *et al.*, *Science* **209**, 1116 (1980).
22. P. R. Hooper, I. W. Herrick, E. R. Laskowski, C. R. Knowles, *Science* **209**, 1125 (1980).
23. A. M. Sarna-Wojcicki, C. E. Meyer, M. J. Woodward, P. J. Lamothe, *U.S. Geol. Surv. Prof. Pap.* **1250,** 667 (1981).
24. K. V. Cashman, J. E. Taggart, *Science* **221**, 1385 (1983).
25. W. G. Melson, *Science* **221**, 1387 (1983).
26. C. W. Criswell, *J. Geophys. Res.* **92**, 10237 (1987).
27. D. R. Smith, W. P. Leeman, *J. Volcanol. Geotherm. Res.* **55**, 271 (1993).
28. K. A. McGee, T. J. Casadevall, *U.S. Geol. Surv. Open File Rep. 94-212* (1994).

Acknowledgments: This work was supported by a National Environment Research Council postdoctoral fellowship (NE/G0129X/1) to K.S. and an ERC Advanced Grant (CRITMAG) to J.B. We thank S. Kearns and B. Buse for help with analyses and are grateful to K. Berlo for access to their MSH samples. The three reviewers are thanked for their comments. The data reported in this paper are tabulated in the supplementary materials.

Supplementary Materials

www.sciencemag.org/cgi/content/full/336/6084/1023/DC1
Materials and Methods
Figs. S1 to S3
Tables S1 to S4
References (*29–35*)
Additional Data S1

3 February 2012; accepted 6 April 2012
10.1126/science.1220066

Temperature-Dependent Alterations in Host Use Drive Rapid Range Expansion in a Butterfly

Rachel M. Pateman,[1,2]* Jane K. Hill,[1]* David B. Roy,[2] Richard Fox,[3] Chris D. Thomas[1]*

Responses of species to climate change are extremely variable, perhaps because of climate-related changes to interactions among species. We show that temperature-related changes in the dependence of the butterfly *Aricia agestis* on different larval host plants have facilitated rapid range expansion. Historically, the butterfly was largely restricted to a single plant species, *Helianthemum nummularium*, but recent warmer conditions have enabled the butterfly to increasingly use the more widespread plant species *Geranium molle*. This has resulted in a substantial increase in available habitat and rapid range expansion by the butterfly (79 kilometers northward in Britain in 20 years). Interactions among species are often seen as constraints on species' responses to climate change, but we show that temperature-dependent changes to interspecific interactions can also facilitate change.

Many species are altering their ranges in response to climate warming (*1*), but patterns of expansion vary greatly among species (*2*, *3*). Some species have retreated where they might have been expected to expand, whereas others have expanded considerably faster than expected, based on the rate of climate change (*3*). There are many potential explanations for variation in patterns of range change, including habitat availability (*4*), land-use change (which can cause retractions), and dispersal ability (*2*). Laboratory and modeling studies also suggest that altered interspecific interactions could represent a major source of variation in determining range changes (*5*–*10*). Specifically, such interactions with other species are most commonly regarded as additional constraints because they may limit species to a narrower set of physical conditions (and hence narrower geographic ranges) than their fundamental, climatic niches might otherwise allow. Here, we provide field evidence of responses within individual populations and across geographic ranges to show that changing biotic interactions can accelerate rather than constrain distribution change.

Our study species is the brown argus butterfly, *Aricia agestis*, which has spread northward in Great Britain by ~79 km in 20 years (Fig. 1A) (*11*), which is 2.3 times faster than the average expansion rate documented for species globally (median 16.9 km per decade) (*3*). The butterfly reaches its northern range boundary in Britain, where it was scarce and declining in the 1980s (*12*) and largely restricted to using rockrose (Cistaceae, *Helianthemum nummularium*) as its larval host plant, in calcareous grasslands (*13*). Since then, the butterfly has rapidly extended its distribution northward (Fig. 1A) (*14*, *15*), which is unusual for a species previously considered to be relatively specialized and sedentary (*2*), and colonized large areas where rockrose is absent. We report here how temperature-dependent changes in the butterfly's association with a different larval host plant species underpin this unexpectedly rapid range expansion.

Plant species in the Geraniaceae family are used by the butterfly in continental Europe (*16*) but were rarely used historically in Britain (*13*), despite them being widespread. Using data on the distribution of brown argus collected by amateur

[1]Department of Biology, University of York, York YO10 5DD, UK. [2]Natural Environment Research Council (NERC) Centre for Ecology and Hydrology, Wallingford, Maclean Building, Benson Lane, Crowmarsh Gifford, Wallingford, Oxon OX10 8BB, UK. [3]Butterfly Conservation, Manor Yard, East Lulworth, Wareham, Dorset BH20 5QP, UK.

*To whom correspondence should be addressed. E-mail: rmp502@york.ac.uk (R.M.P.); jane.hill@york.ac.uk (J.K.H.); chris.thomas@york.ac.uk (C.D.T.)

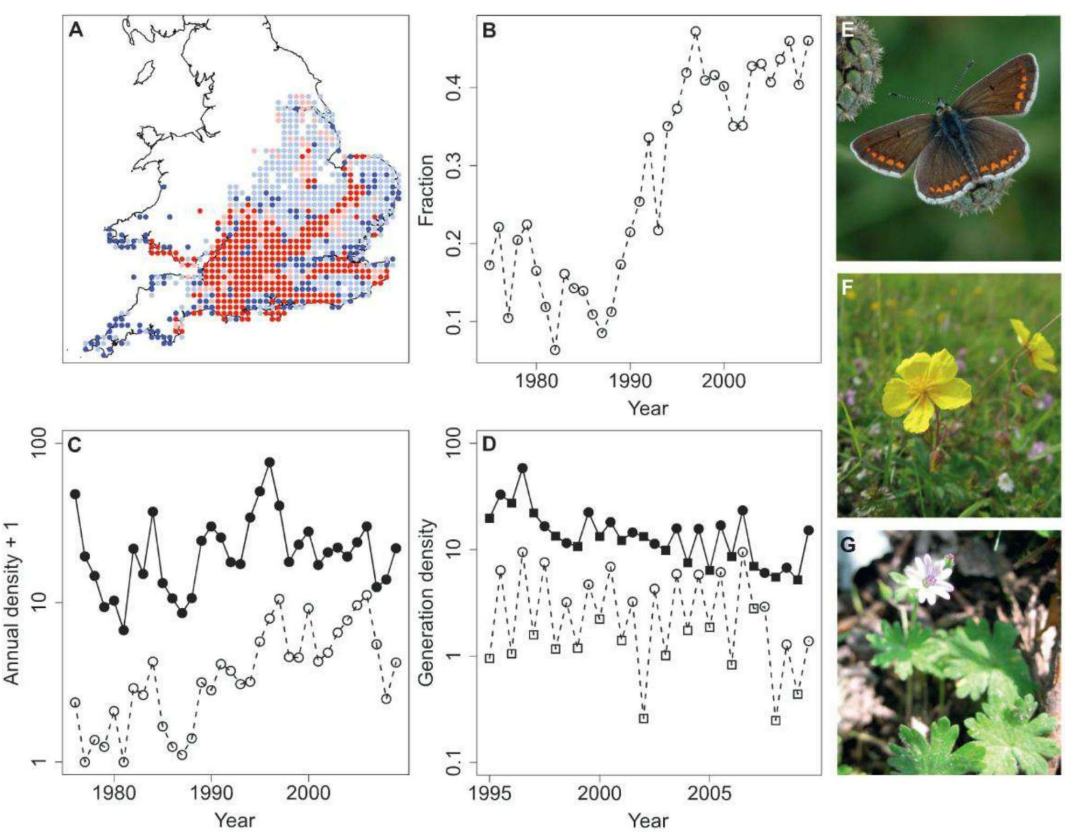

Fig. 1. Distribution and density changes of the brown argus butterfly. (**A**) Occurrence of brown argus in 10 × 10 km grid squares that contain rockrose (red) and Geraniaceae only (blue). Records from the period 1970–1987 [before the increase in use of Geraniaceae (B)] are in dark shades; new 10 × 10 km squares colonized in the period 1988–2009 are in light shades. (**B**) Increase in the fraction of brown argus distributional records from 10 × 10 km grid squares where only Geraniaceae hosts are present. (**C**) Mean annual density (count per kilometer) of brown argus in rockrose (solid line, solid symbols) and Geraniaceae (dashed line, open symbols) sites from 1976–2009. (**D**) Same as for (C), but separating 1995 to 2009 population counts into numbers for first (squares) and second (circles) adult flight periods each year. Photographs are (**E**) Brown argus [Jim Asher/Butterfly Conservation]; (**F**) rockrose [Rachel Pateman]; and (**G**) dove's-foot cranesbill [Alison Jukes].

butterfly recorders over the past four decades, we found that during the 1990s there was an increase in the fraction of all occurrences of the butterfly in locations where the only available host plants were in the family Geraniaceae (Spearman's rank correlation between year and fraction of 10 × 10 km resolution observation records in Geraniaceae-only areas: $r_s = 0.82$, $n = 35$ years, $P < 0.001$) (Fig. 1B) (*11*). This has been achieved through an increase in occurrence in Geraniaceae-only areas because occurrence on rockrose does not appear to have declined. Increases in the occurrence of brown argus in Geraniaceae-only areas were associated with warm summers [linear regression of the between-year change in the fraction of brown argus records in Geraniaceae-only grid squares versus mean summer temperature (MST): equation 1, change = (0.03 × MST) − 0.47; Pearson $r = 0.45$, $F_{1,32} = 8.35$, $P = 0.007$] (*11*).

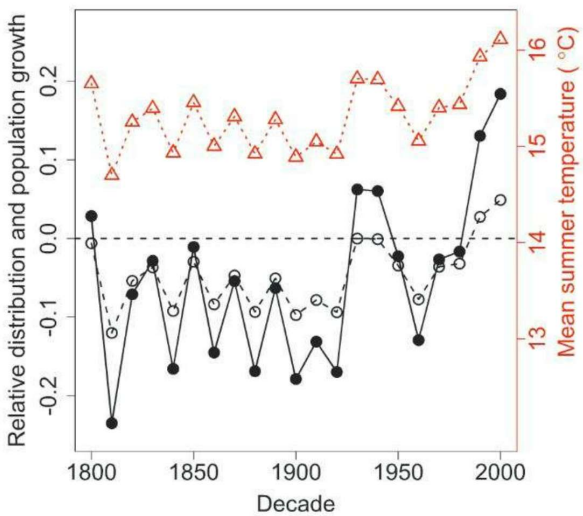

Fig. 2. Estimated decadal net increase (positive) or decrease (negative) in the fraction of all brown argus occurrences associated with Geraniaceae sites in the past (solid line, solid circles). Difference in estimated annual population growth rates, averaged across decades, between Geraniaceae and rockrose sites (mean for Geraniaceae sites minus mean for rockrose sites) (long dashed line, open circles; positive values indicate higher relative population growth on Geraniaceae, and negative values indicate higher performance on rockrose). MST for each decade (short red dashed line and triangles). Dates on scale bar refer to first year of each decade for which estimates have been calculated.

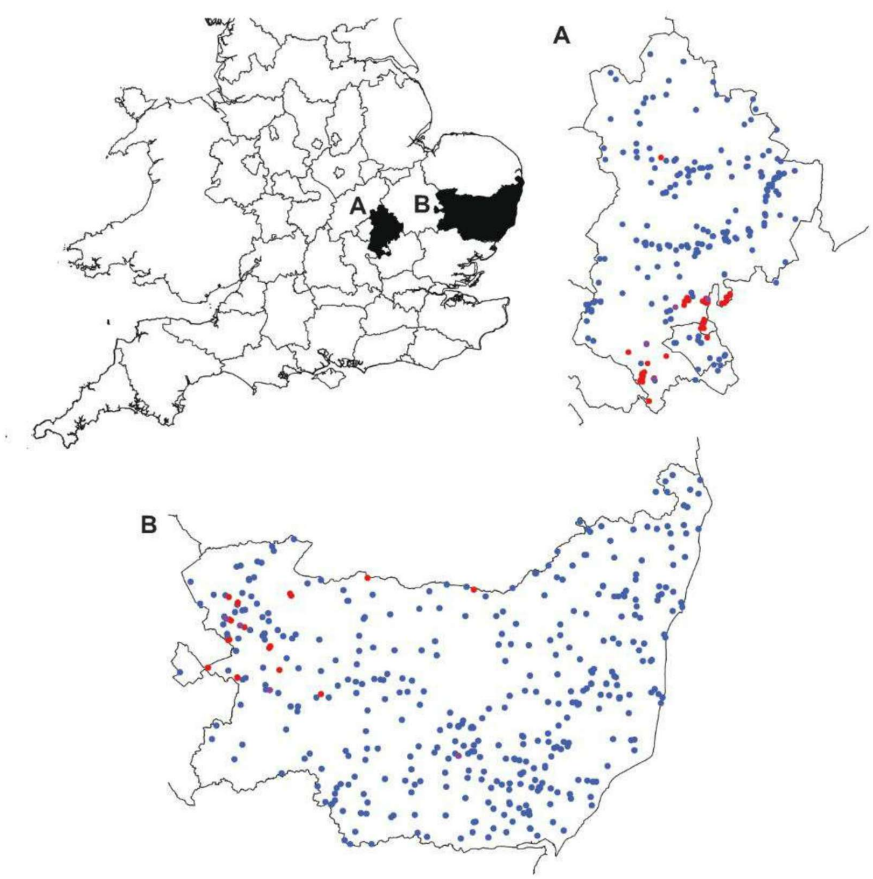

Fig. 3. Availability of rockrose and cranesbill in the landscape. 100 × 100 m grid squares with records of rockrose (red symbols), dove's-foot cranesbill (blue symbols), or both species (purple symbols) in two well-recorded counties: (**A**) Bedfordshire and (**B**) Suffolk. Rapid range expansion took place in Bedfordshire and Suffolk, associated with the increased use of dove's-foot cranesbill and other Geraniaceae.

To establish the population-dynamic basis for this distributional change in host plant use, we analyzed the effect of climate on brown argus populations associated with different larval host plants, on the basis of count data by volunteers from over 200 fixed transects in Britain (*17*). Warmer summers result in higher brown argus population densities on both rockrose and Geraniaceae [analysis of covariance, relationship between annual population growth rate and MST, with host as categorical variable: $F_{1,35} = 6.85$, $P = 0.013$; equation 2, population growth on rockrose = (0.21 × MST) − 3.30; equation 3, population growth on Geraniaceae = (0.33 × MST) − 5.18], with no effect of mean annual temperature and little or no effect of winter temperature (*11*). Thus, butterfly populations on both host plant types have benefited from the recent increase in frequency of warm summers.

We used the relationships described above between temperature and butterfly distribution (equation 1) and abundance (equations 2 and 3) to hindcast changes in the relative use of different host plants (from distribution data) and in relative annual population growth rates on different host plants (from transect counts) for the 19th and 20th centuries in Britain, the period for which fine-scale historical climate data are available (Fig. 2) (*11*). The climate over most of this period was cooler than at present, and our models predict a retraction in the distribution of brown argus away from Geraniaceae in most decades and lower relative population growth rates on Geraniaceae. Both the distribution and population growth rate analyses indicate that the rockrose host plant was more favorable than was Geraniaceae under these cooler conditions. Historical records of brown argus support this prediction, with only 19% of occurrences in Geraniaceae-only areas during the cool beginning of the 20th century (1900–1929), increasing to 30% during the warmer 1930s and 1940s and dropping back down to 16% during the cooler period from 1950 to 1989 (insufficient records are available from the 19th century to assess the relative occurrence in Geraniaceae-only areas) (*11*). In the past two decades, as the frequency of warm summers has increased, our models (equations 1 to 3) lead to the expectation that brown argus will have experienced higher population performance on Geraniaceae than on rockrose and have expanded in its distribution onto Geraniaceae (Fig. 2), as has been observed (Fig. 1).

The brown argus is likely to have survived past, cooler periods predominantly as localized populations in warm sites that contain large rockrose populations. Rockrose achieves high local densities compared with the annual dove's-foot cranesbill (*Geranium molle*) (*18*, *19*), the most frequently used of the Geraniaceae host plants

(*15*) [rockrose averages 23 times greater ground cover than dove's-foot cranesbill per 100 × 100 m sample area that contains host plants (fig. S1) (*11*)]. The long-lived perennial rockrose also has more stable populations than does the annual and ruderal dove's-foot cranesbill. These differences between the plants enable rockrose to support larger (Fig. 1, C and D) and more stable brown argus populations [Levene's test for equality of variances: $W = 10.97$, $n = 2$ 30-generation sequences, $P = 0.002$ (Fig. 1D)]. Moreover, rockrose frequently grows in areas of short turf on southerly facing slopes (fig. S2) (*11*, *20*), which provide warm microclimates [southerly aspects receive greater direct radiation and achieve higher maximum summer temperatures (*21*)]. As recently as the early 1980s, the brown argus was mainly associated with rockrose populations on sheltered south-facing slopes (*12*). The few historical records of Geraniaceae-feeding populations from this period were predominantly in sand dunes (*13*), which also provide warm microclimates.

Summer temperatures in Britain from 1990 to 2009 were on average 0.78°C warmer than between 1800 and 1989, and this is likely to have increased the thermal suitability of sites for brown argus, especially those that are not southerly facing. This would have increased the ability of Geraniaceae-containing sites to support brown argus population growth; there was a 5.3-fold increase in brown argus population density in Geraniaceae sites between 1976–1985 and 2000–2009 (Spearman's rank correlation between year and density on Geraniaceae: $r_s = 0.76$, $n = 34$ years, $P < 0.001$) (Fig. 1C). In contrast, no increase in overall population density occurred at rockrose sites (Spearman's rank correlation between year and density on rockrose: $r_s = 0.25$, $n = 34$ years, $P = 0.162$; 1.1-fold density increase from 1976–1985 to 2000–2009) (Fig. 1C), even though butterfly abundance increased temporarily during warm summers. This suggests that other factors limit population density on rockrose (supplementary text).

Based on 100 × 100 m grid squares with records of host plants, dove's-foot cranesbill is 4 to 17 times more widespread than is rockrose in counties where rapid expansion has taken place (Fig. 3) (*11*). Once the brown argus can establish populations on cranesbill, the high frequency of cranesbill populations in the landscape permit it to spread between populations of this host plant without the need for long-distance dispersal. The butterfly's capacity to use Geranicaeae has been aided by the spread of butterfly phenotypes that readily select Geraniaceae plants for egg-laying (*15*) and by a degree of escape from natural enemies (parasitoids) associated with historical rockrose sites (*22*). These processes have come together to generate an unexpectedly rapid transformation in the metapopulation dynamics of the butterfly from a highly localized distribution associated with southerly facing rockrose-containing calcareous grasslands to widespread use of virtually any grassland with rockrose or Geranicaeae host plants. Ecological and evolutionary adjustments by the butterfly, interacting with alternative host plants that differ in their niches and life-history traits, have resulted in rapid range expansion of this previously rare and declining butterfly. We suggest that altered interactions among species do not necessarily constrain distribution changes but can facilitate expansions.

References and Notes

1. R. Hickling *et al.*, *Glob. Change Biol.* **12**, 450 (2006).
2. M. S. Warren *et al.*, *Nature* **414**, 65 (2001).
3. I. C. Chen *et al.*, *Science* **333**, 1024 (2011).
4. J. K. Hill *et al.*, *Ecol. Lett.* **4**, 313 (2001).
5. T. Park, *Physiol. Zool.* **27**, 177 (1954).
6. A. J. Davis *et al.*, *Nature* **391**, 783 (1998).
7. A. J. Davis *et al.*, *J. Anim. Ecol.* **67**, 600 (1998).
8. W. H. Van der Putten, M. Macel, M. E. Visser, *Philos. Trans. R. Soc. London Ser. B* **365**, 2025 (2010).
9. M. B. Araújo, M. Luoto, *Glob. Ecol. Biogeogr.* **16**, 743 (2007).
10. O. Schweiger *et al.*, *Ecology* **89**, 3472 (2008).
11. Materials and methods are available as supplementary materials on *Science* Online.
12. N. A. D. Bourn, J. A. Thomas, *Biol. Conserv.* **63**, 67 (1993).
13. J. Heath, E. Pollard, J. A. Thomas, *Atlas of Butterflies in Britain and Ireland* (Viking, Harmondsworth, 1984).
14. J. Asher *et al.*, *The Millennium Atlas of Butterflies in Britain and Ireland* (Oxford Univ. Press, Oxford, 2001).
15. C. D. Thomas *et al.*, *Nature* **411**, 577 (2001).
16. T. Tolman, *Collins Field Guide to the Butterflies of Britain and Europe* (HarperCollins, London, 1997).
17. E. Pollard, T. J. Yates, *Monitoring Butterflies for Ecology and Conservation* (Chapman & Hall, London, 1993).
18. M. C. F. Proctor, M. E. Griffiths, *J. Ecol.* **44**, 675 (1956).
19. J. P. Grime, J. G. Hodgson, R. Hunt, *Comparative Plant Ecology: A Functional Approach to Common British Species* (Unwin Hyman, London, 1988).
20. K. H. Lakhani, B. N. K. Davis, *J. Appl. Ecol.* **19**, 621 (1982).
21. R. B. Hutchins *et al.*, *Soil Sci.* **121**, 234 (1976).
22. R. Menéndez *et al.*, *Ecol. Entomol.* **33**, 413 (2008).

Acknowledgments: Work was funded through NERC Ecology and Hydrology Funding Initiative grant NE/E012035. Butterfly distribution data were derived from a database of records submitted by volunteers (www.butterfly-conservation.org/text/64/butterfly_distribution.html), and densities were derived from UK Butterfly Monitoring Scheme data (www.ukbms.org/obtaining.htm). Both schemes are operated by Butterfly Conservation and the Centre for Ecology & Hydrology and funded by a consortium of government agencies. Plant data were derived from a database of volunteer records managed by the Botanical Society for the British Isles (www.bsbi.org.uk/research.html). We are grateful to the volunteers who collected the original butterfly and plant data. Temperature data were derived from the Central England Temperature (CET) data set (www.metoffice.gov.uk/hadobs). Digital Elevation Models were provided by the NERC Earth Observation Data Centre (www.neodc.rl.ac.uk/browse/neodc/nextmap). Original data collected by authors is presented in the supplementary materials.

Supplementary Materials

www.sciencemag.org/cgi/content/full/336/6084/1028/DC1
Materials and Methods
Supplementary Text
Figs. S1 to S4
Tables S1 and S2
References (*23*–*28*)

22 November 2011; accepted 6 April 2012
10.1126/science.1216980

Linking Crystallographic Model and Data Quality

P. Andrew Karplus[1] and Kay Diederichs[2]*

In macromolecular x-ray crystallography, refinement *R* values measure the agreement between observed and calculated data. Analogously, R_{merge} values reporting on the agreement between multiple measurements of a given reflection are used to assess data quality. Here, we show that despite their widespread use, R_{merge} values are poorly suited for determining the high-resolution limit and that current standard protocols discard much useful data. We introduce a statistic that estimates the correlation of an observed data set with the underlying (not measurable) true signal; this quantity, CC*, provides a single statistically valid guide for deciding which data are useful. CC* also can be used to assess model and data quality on the same scale, and this reveals when data quality is limiting model improvement.

Accurately determined protein structures provide insight into how biology functions at the molecular level and also guide the development of new drugs and protein-based nanomachines and technologies. The large majority of protein structures are determined by x-ray crystallography, where measured diffraction data are used to derive a molecular model. It is surprising that, despite decades of methodology development, the question of how to select the resolution cutoff of a crystallographic data set is still controversial, and the link between the quality of the data and the quality of the derived molecular model is poorly understood. Here, we describe a statistical quantity that addresses both of these issues and will lead to improved molecular models.

The measured data in x-ray crystallography are the intensities of reflections, and these yield structure factor amplitudes each with unique *h*, *k*, and *l* indices that define the lattice planes. The standard indicator for assessing the agreement of

[1]Department of Biochemistry and Biophysics, Oregon State University, Corvallis, OR 97331, USA. [2]Department of Biology, University of Konstanz, Box 647, D-78457 Konstanz, Germany.

*To whom correspondence should be addressed. E-mail: kay.diederichs@uni-konstanz.de

a refined model with the data is the crystallographic R value, defined as

$$R = \frac{\sum_{hkl} |F_{obs}(hkl) - F_{calc}(hkl)|}{\sum_{hkl} F_{obs}(hkl)} \quad (1)$$

where $F_{obs}(hkl)$ and $F_{calc}(hkl)$ are the observed and calculated structure factor amplitudes, respectively. R is 0.0 for perfect agreement with the data, and R is near 0.59 for a random model (*1*). Because R can be made arbitrarily low for models having sufficient parameters to overfit the data, Brünger (*2*) introduced R_{free} as a cross-validated R on the basis of a small subset of reflections not used during refinement. The R for the larger "working" set of reflections is then referred to as R_{work}.

Crystallographic data quality is commonly assessed by an analogous indicator R_{merge} [originally (*3*) R_{sym}], which measures the spread of n independent measurements of the intensity of a reflection, $I_i(hkl)$, around their average, $\bar{I}(hkl)$:

$$R_{merge} = \frac{\sum_{hkl} \sum_{i=1}^{n} |I_i(hkl) - \bar{I}(hkl)|}{\sum_{hkl} \sum_{i=1}^{n} I_i(hkl)} \quad (2)$$

In 1997, it was discovered that because $I_i(hkl)$ values influence $\bar{I}(hkl)$, the R_{merge} definition must be adjusted by a factor of $\sqrt{n/(n-1)}$ to give values that are independent of the multiplicity (*4*). The multiplicity-corrected version, called R_{meas}, reliably reports on the consistency of the individual measurements. A further variant, R_{pim} (*5*), reports on the expected precision of $\bar{I}(hkl)$ and is lower by a factor of $1/\sqrt{n}$ factor compared with R_{meas}. Because the strength of diffraction decreases with resolution, a high-resolution cutoff is applied to discard data considered so noisy that their inclusion might degrade the quality of the resulting model. Data are typically truncated at a resolution before the R_{merge} (or R_{meas}) value exceeds ~0.6 to 0.8 and before the empirical signal-to-noise ratio, $\langle \bar{I}/\sigma(\bar{I}) \rangle$, drops below ~2.0 (*6*) (fig. S1). The uncertainty associated with these criteria is illustrated by a recent review that concluded "an appropriate choice of resolution cutoff is difficult and sometimes seems to be performed mainly to satisfy referees" (*6*).

That these criteria result in high-resolution cutoffs that are too conservative is illustrated here using an example data set (***EXP***) collected for a cysteine-bound complex of cysteine dioxygenase (CDO); the ***EXP*** data have an average intensity about 7% as strong as the data originally used to determine the structure at 1.42 Å resolution (PDB 3ELN; R_{work}/R_{free} = 0.135/0.177) (*7*, *8*). Standardized model refinements starting with a 1.5 Å resolution unliganded CDO structure (PDB code 2B5H) (*9*) were carried out against the ***EXP*** data for a series of high-resolution cutoffs between 2.0 and 1.42 Å resolution (table S1). As R value comparisons are only meaningful if calculated at the same resolution, we evaluated paired refinements made with adjacent resolution limits using R_{work} and R_{free} values calculated at the poorer resolution limit. Improvement is indicated by drops in R_{free} or increases in R_{work} at the same R_{free} (meaning the model is less overfit). This analysis revealed that every step of added data improved the resulting model (Fig. 1). Consistent with this, difference Fourier maps show a similar trend in signal versus resolution (fig. S2), and geometric parameters of the resulting models improve with resolution (table S2).

The proven value of the data out to 1.42 Å resolution contrasts strongly with the R_{meas} and $\langle \bar{I}/\sigma(\bar{I}) \rangle$ values at that resolution (>4.0 and ~0.3, respectively) (Fig. 2), which are far beyond the limits currently associated with useful data. Applying the typical standards described above, this data set would have been truncated at ~1.8 Å resolution, which would halve the number of unique reflections in the data set (table S1) and would yield a worse model.

It is striking to observe the different behavior at high resolution of the crystallographic versus the data-quality R values, with the one remaining below 0.40 and the other diverging toward infinity (Fig. 2). Consideration of the R_{merge} formula rationalizes this divergence, because the denominator (the average net intensity) approaches zero at high resolution, but the numerator becomes dominated by background noise and is essentially constant. Thus, despite their similar names and mathematical definitions, data-quality

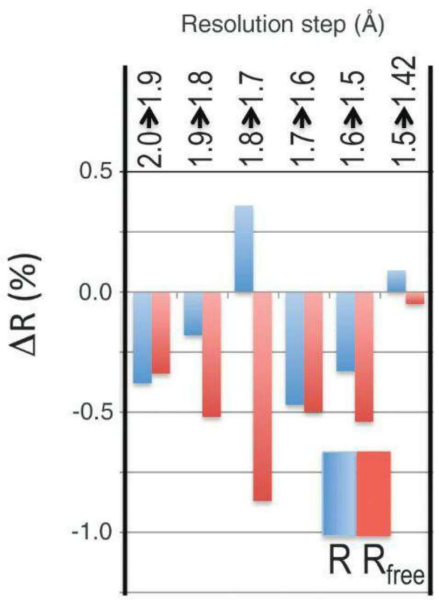

Fig. 1. Higher-resolution data, even if weak, improves refinement behavior. For each incremental step of resolution from $X \rightarrow Y$ (top legend), the pair of bars gives the changes in overall R_{work} (blue) and R_{free} (red) for the model refined at resolution Y with respect to those for the model refined at resolution X, with both R values calculated at resolution X. The first pair of bars shows that R_{work} and R_{free} dropped 0.38% and 0.34%, respectively, upon isotropic refinement when the refinement resolution limit was extended from 2.0 to 1.9 Å; the other pairs of bars show the improvement upon anisotropic refinement.

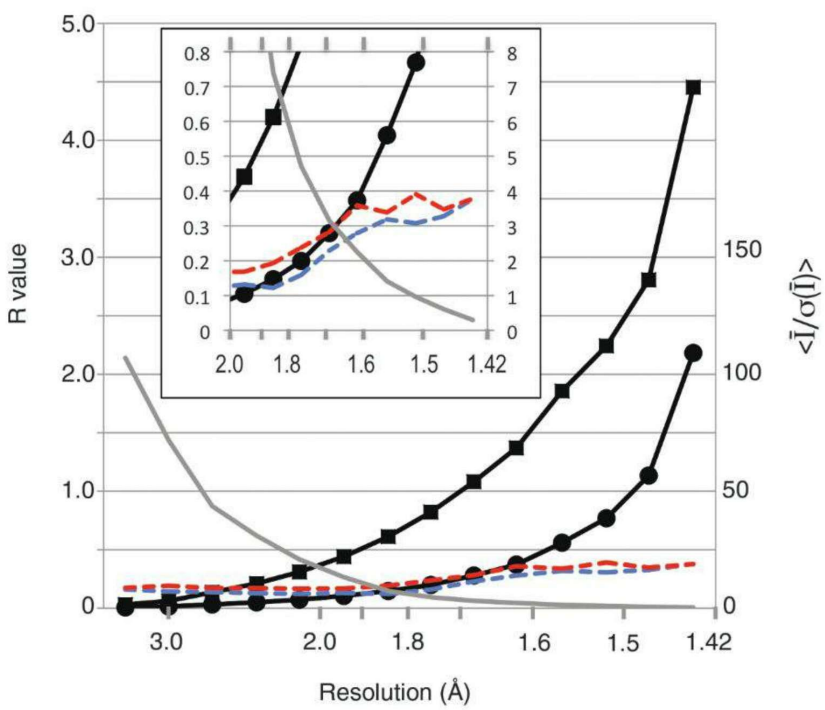

Fig. 2. Data quality R values behave differently than those from crystallographic refinement, and useful data extend well beyond what standard cutoff criteria would suggest. R_{meas} (squares) and R_{pim} (circles) are compared with R_{work} (blue) and R_{free} (red) from 1.42 Å resolution refinements against the ***EXP*** data set. $\langle \bar{I}/\sigma(\bar{I}) \rangle$ (gray) is also plotted. (**Inset**) A close-up of the plot beyond 2 Å resolution.

R values are not comparable to R values from model refinement, and there is no valid basis for the commonly applied criterion that data are not useful beyond a resolution where R_{meas} (or R_{merge} or R_{pim}) rises above ~0.6. As suggested by Wang (*10*), $\langle \bar{I}/\sigma(\bar{I}) \rangle$ at a much lower level than generally recommended could be used to define the cutoff, but this has the problem that $\sigma(\bar{I})$ values can be misestimated (*6*, *11*).

With current standards not serving as reliable guides for selecting a high-resolution cutoff, we investigated the use of the Pearson correlation coefficient (CC) (*12*) as a parameter that could potentially assess both data accuracy and the agreement of model and data on a common scale. Pearson's CC is already used in crystallography, in that a CC value of 0.3 between independent measurements of anomalous signals has become the recommended criterion for selecting the high-resolution cutoff of the data to be used for defining the locations of the anomalous scatterers (*13*). Following a procedure suggested earlier (*4*), we divided the unmerged ***EXP*** data into two parts, each containing a random half of the measurements of each unique reflection. Then, the CC was calculated between the average intensities of each subset. This quantity, denoted $CC_{1/2}$, is near 1.0 at low resolution and drops to near 0.1 at high resolution (Fig. 3). According to Student's t test (*12*), the $CC_{1/2}$ of 0.09 for the ~2100 reflection pairs in the highest resolution bin is significantly different from zero ($P = 2 \times 10^{-5}$).

This high significance occurs even though $CC_{1/2}$ should be expected to underestimate the information content of the data. This is because for weak data, $CC_{1/2}$ measures the correlation of one noisy data set (the first half-data set) with another noisy data set (the other half-data set), whereas the true level of signal would be measured by what could be called CC_{true}, the correlation of the averaged data set (less noisy because of the extra averaging) with the noise-free true signal. Although the true signal would normally not be known, for the ***EXP*** test case, the 3ELN data provide a reference that has much lower noise and should be much closer to the underlying true data. The CC calculated between the ***EXP*** and 3ELN data sets is indeed uniformly higher than $CC_{1/2}$ (Fig. 3), dropping only to 0.31 in the highest resolution bin (Student's t test $P = 10^{-64}$).

We next sought an analytical relation between $CC_{1/2}$ and CC_{true}. Using only the assumption that errors in the two half-data sets are random and, on average, of similar size (see supplementary text), we derived the relation

$$CC^* = \sqrt{\frac{2CC_{1/2}}{1 + CC_{1/2}}} \qquad (3)$$

where CC* estimates the value of CC_{true}, based on a finite-size sample. Equation 3 has been used in electron microscopy studies for a similar purpose (*14*) and is also related to the Spearman-Brown prophecy formula used in psychometrics to predict what test length is required to achieve a certain level of reliability (*15*). CC*, when computed with Eq. 3, agrees reasonably well with the CC for the ***EXP*** data compared with the 3ELN reference data, which shows that systematic factors influencing a real data set are not large enough to greatly perturb this relation (Fig. 4A). CC* provides a statistic that not only assesses data quality but also allows direct comparison of crystallographic model quality and data quality on the same scale. In particular, CC_{work} and CC_{free}—the standard and cross-validated correlations of the experimental intensities, with the intensities calculated from the refined molecular model—can be directly compared with CC* (Fig. 4B). A CC_{work} larger than CC* implies overfitting, because, in that case, the model agrees better with the experimental data than the true signal does. A CC_{free} smaller than CC* (such as is seen at low resolution) indicates that the model does not account for all of the signal in the data. A CC_{free} closely matching CC*, such as at high resolution in Fig. 4B, implies that data quality is limiting model improvement. In this high-resolution region, the model, which was refined against ***EXP***, correlates much better with the more accurate 3ELN than with the ***EXP*** data (Fig. 4B). This shows that, as is common for parsimonious models (*16*), the constructed molecular model is a better predictor of the true signal than are the experimental data from which it was derived. On a related point, because current estimates of a model's coordinate error do not take the data errors into account (*17*–*19*), the model accuracy is actually better than these methods indicate.

We verified, using a simulated data set (*20*) and two further test cases, that these findings are

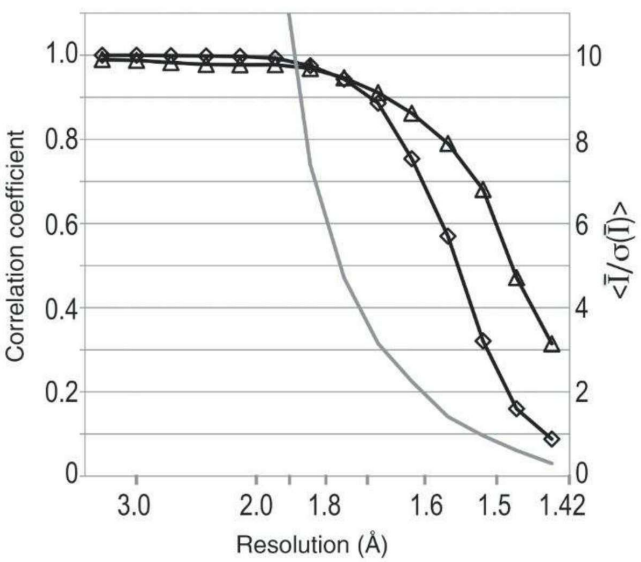

Fig. 3. Signal as a function of resolution as measured by correlation coefficients. Plotted as a function of resolution for the ***EXP*** data are $CC_{1/2}$ (diamonds) and the CC for a comparison with the 3ELN reference data set (triangles). $\langle \bar{I}/\sigma(\bar{I}) \rangle$ (gray) is also shown. All determined $CC_{1/2}$ values shown have expected standard errors of <0.025 (*21*, *22*).

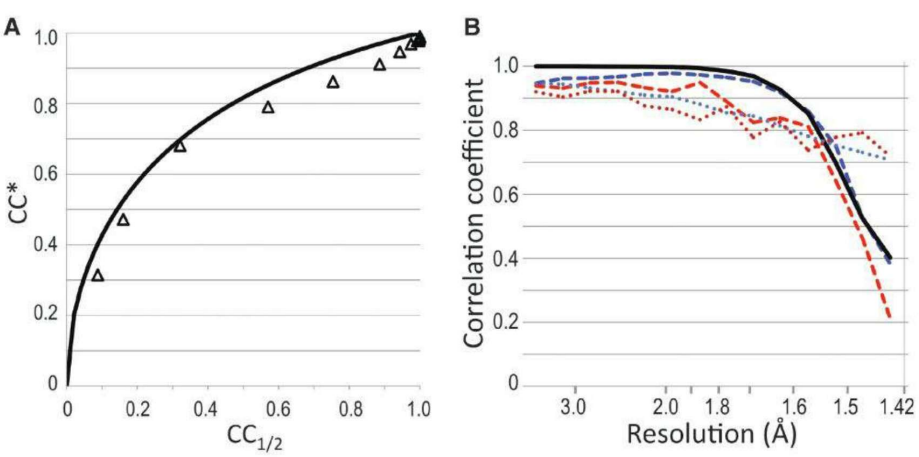

Fig. 4. The $CC_{1/2}$/CC* relation and the utility of comparing CC* with CC_{work} and CC_{free} from a refined model. (**A**) Plotted is the analytical relation (Eq. 3) between $CC_{1/2}$ and CC* (black curve). Also roughly following the CC* curve are the CC values for the ***EXP*** data compared with 3ELN (triangles) as a function of $CC_{1/2}$. (**B**) Plotted as a function of resolution are CC* (black solid) for the ***EXP*** data set, as well as CC_{work} (blue dashed) and CC_{free} (red dashed) calculated on intensities from the 1.42 Å refined model. Also shown are values for CC_{work} (blue dotted) and CC_{free} (red dotted) between the 1.42 Å refined model and the 3ELN data set.

not specific to the ***EXP*** data (tables S3, S4, and S5, and fig. S3). Thus, CC* (or $CC_{1/2}$) is a robust, statistically informative quantity useful for defining the high-resolution cutoff in crystallography. These examples show that with current data reduction and refinement protocols, it is justified to include data out to well beyond currently employed cutoff criteria (fig. S4), because the data at these lower signal levels do not degrade the model, but actually improve it. Advances in data-processing and refinement procedures, which until now have not been optimized for handling such weak data, may lead to further improvements in model accuracy. Finally, we emphasize that the analytical relation (Eq. 3) between $CC_{1/2}$ and CC* is general, and thus, CC* may have similar applications for data- and model-quality assessment in other fields of science involving multiply measured data.

References and Notes

1. A. J. C. Wilson, *Acta Crystallogr.* **3**, 397 (1950).
2. A. T. B. Brünger, *Nature* **355**, 472 (1992).
3. U. W. Arndt, R. A. Crowther, J. F. W. Mallett, *J. Phys. E Sci. Instrum.* **1**, 510 (1968).
4. K. Diederichs, P. A. Karplus, *Nat. Struct. Biol.* **4**, 269 (1997).
5. M. S. Weiss, *J. Appl. Cryst.* **34**, 130 (2001).
6. P. R. Evans, *Acta Crystallogr. D Biol. Crystallogr.* **67**, 282 (2011).
7. C. R. Simmons *et al.*, *Biochemistry* **47**, 11390 (2008).
8. Materials and methods are available as supplementary materials on *Science* Online.
9. C. R. Simmons *et al.*, *J. Biol. Chem.* **281**, 18723 (2006).
10. J. Wang, *Acta Crystallogr. D Biol. Crystallogr.* **66**, 988 (2010).
11. P. Evans, *Acta Crystallogr. D Biol. Crystallogr.* **62**, 72 (2006).
12. N. A. Rahman, *A Course in Theoretical Statistics* (Griffin, London, 1968).
13. T. R. Schneider, G. M. Sheldrick, *Acta Crystallogr. D Biol. Crystallogr.* **58**, 1772 (2002).
14. P. B. Rosenthal, R. Henderson, *J. Mol. Biol.* **333**, 721 (2003).
15. P. Bobko, *Correlation and Regression: Applications for Industrial Organizational Psychology and Management* (Sage Publications, Thousand Oaks, 2001).
16. H. G. Gauch Jr., *Am. Sci.* **81**, 468 (1993).
17. V. Luzzati, *Acta Crystallogr.* **6**, 142 (1953).
18. D. W. J. Cruickshank, *Acta Crystallogr. D Biol. Crystallogr.* **55**, 583 (1999).
19. R. A. Steiner, A. A. Lebedev, G. N. Murshudov, *Acta Crystallogr. D Biol. Crystallogr.* **59**, 2114 (2003).
20. K. Diederichs, *Acta Crystallogr. D Biol. Crystallogr.* **65**, 535 (2009).
21. R. Fisher, *Statistical Methods for Research Workers* (Oliver and Boyd, Edinburgh, 1925), §33–34.
22. Ten independent random partitionings of the data into the two subsets for calculating $CC_{1/2}$ yielded standard deviations of <0.02 in all resolution ranges, and agreed reasonably with the expected standard error as calculated by $\sigma(CC) = (1 - CC^2)/\sqrt{n - 1}$ where n is the number of observations contributing to the CC calculation (*21*).

Acknowledgments: This work was supported in part by the Alexander von Humboldt Foundation, the Konstanz Research School Chemical Biology, and NIH grants GM083136 and DK056649. We thank R. Cooley for providing the EXP data images, V. Lunin for help with deriving Eq. 3, and A. Gittleman for help with mathematical notation. We also thank M. Junk, W. Kabsch, K. Schäfer, D. Tronrud, M. Wells and W. Welte for critically reading the manuscript. The program HIRESCUT is available upon request. P.A.K. and K.D. designed and performed the research and wrote the paper. The authors declare no competing financial interests.

Supplementary Materials

www.sciencemag.org/cgi/content/full/336/6084/1030/DC1
Materials and Methods
Supplementary Text
Figs. S1 to S4
Tables S1 to S5
References (*23*–*29*)

20 December 2011; accepted 16 March 2012
10.1126/science.1218231

Structures from Anomalous Diffraction of Native Biological Macromolecules

Qun Liu,[1] Tassadite Dahmane,[2] Zhen Zhang,[2] Zahra Assur,[2] Julia Brasch,[2] Lawrence Shapiro,[2] Filippo Mancia,[3] Wayne A. Hendrickson[1,2,3,4]*

Crystal structure analyses for biological macromolecules without known structural relatives entail solving the crystallographic phase problem. Typical de novo phase evaluations depend on incorporating heavier atoms than those found natively; most commonly, multi- or single-wavelength anomalous diffraction (MAD or SAD) experiments exploit selenomethionyl proteins. Here, we realize routine structure determination using intrinsic anomalous scattering from native macromolecules. We devised robust procedures for enhancing the signal-to-noise ratio in the slight anomalous scattering from generic native structures by combining data measured from multiple crystals at lower-than-usual x-ray energy. Using this multicrystal SAD method (5 to 13 equivalent crystals), we determined structures at modest resolution (2.8 to 2.3 angstroms) for native proteins varying in size (127 to 1148 unique residues) and number of sulfur sites (3 to 28). With no requirement for heavy-atom incorporation, such experiments provide an attractive alternative to selenomethionyl SAD experiments.

Crystallographic structure determinations for biomolecules require the retrieval of phases, which are lost when measuring x-ray diffraction patterns. For the first protein crystal structures, phase evaluation was by the method of multiple isomorphous replacement (MIR) with derivatives incorporating mercury [atomic number (Z) = 80] or other heavy atoms. Once many structures were known, phases could often be estimated by the method of molecular replacement; however, de novo structure determination remained essential for molecules without adequately close structural relatives. Multiwavelength anomalous diffraction (MAD) analyses (*1*), which exploit element-specific scattering from x-ray resonance with atomic orbitals, came to be used increasingly for de novo structures as tunable synchrotron beamlines developed (*2*). Whereas MAD gives definitive phase information, its single-wavelength counterpart, SAD, is ambiguous in defining only trigonometric sines of phases. This phase ambiguity could be resolved once density-modification procedures, based largely on molecular boundaries and symmetry, were devised (*3*, *4*); and SAD then surged (*5*). MAD and SAD now dominate de novo phasing, as they have the advantage that lighter atoms can be effective sources of phasing signals. Selenomethionine is easily incorporated into proteins (*6*), and selenium (Z = 34) is now by far the most-used phasing element (*2*). With MAD and SAD, metal atoms such as iron (Z = 26) present in some native proteins can also suffice.

Sulfur (Z = 16) is the heaviest element in most native proteins. Its K-shell resonance at 2.47 keV (λ = 5.02 Å) is inaccessible to standard MAD experiments, and its anomalous scattering at conventional wavelengths is slight; nevertheless, sulfur anomalous scattering can suffice for SAD phasing. The structure of crambin was the first to be determined from sulfur SAD phasing (*7*), although the experiment was not then identified as SAD. Later, broader effectiveness of sulfur SAD was demonstrated with tests on lysozyme (*8*) and in solving the structure of obelin (*9*). Similarly, the feasibility of phosphorous SAD was demonstrated for nucleic acids (*10*). The motivation for truly routine native SAD is great, because heavy-atom incorporations are often problematic, even for the most reliable selenomethionine. Subsequent optimization of native-SAD experiments has included developments for low-energy measurements (*11*), assessments of the impact of high data redundancy (*10*, *11*), optimal wavelength selection (*12*), control of complications from radiation damage (*13*, *14*), and the use of home-source CrKα radiation (*15*).

Besides test cases and technical developments, some novel protein structures beyond crambin and obelin have been determined by sulfur SAD analyses. As compared with the swelling numbers of SAD structures in general, however, the

[1]New York Structural Biology Center, National Synchrotron Light Source (NSLS) X4, Building 725, Brookhaven National Laboratory, Upton, NY 11973, USA. [2]Department of Biochemistry and Molecular Biophysics, Columbia University, New York, NY 10032, USA. [3]Department of Physiology and Cellular Biophysics, Columbia University, New York, NY 10032, USA. [4]Howard Hughes Medical Institute, Columbia University, New York, NY 10032, USA.

*To whom correspondence should be addressed. E-mail: wayne@convex.hhmi.columbia.edu

sulfur SAD component is small and not growing. Our February 2012, compilation of light-only SAD structures (all atoms with $Z \leq 20$) as reported in the Protein Data Bank (PDB, www.pdb.org) reveals 57 novel structures determined since 1981 (table S1). Although more than 30 novel native-SAD structures were reported between 2004 and 2007, there have been only six after 2009 (not counting deposits reported here). Most of the table S1 native-SAD structures (42 of 57) are at high resolution ($d_{min} < 2.0$ Å); only two have $d_{min} > 2.3$ Å. Native-SAD numbers are to be compared with overwhelming SAD and MAD PDB deposits overall (>5000 each since 1996). Why is the sulfur SAD contribution so meager? Surely a major factor is the low strength of anomalous scattering signals from sulfur as compared with selenium, the mainstay of SAD and MAD experiments. With one sulfur atom for every 30 residues, the average metal-free protein will produce a Bijvoet diffraction ratio ($\langle|\Delta F_{\pm h}|\rangle/\langle|F|\rangle$) (*1*) of only ~1.0% even for 7 keV x-rays as compared with ~6.5% for a corresponding average selenomethionyl protein at the Se-K edge (12.658 keV). When compounded with noise from counting statistics, diffuse scattering, absorption, radiation damage, and many other sources, such feeble signals are difficult to measure with sufficient accuracy to place the dozens of atomic positions in a typical sulfur substructure and then to obtain phases for full structure analysis.

The ratio of signal to noise in diffraction measurements can be enhanced by increasing data multiplicity; however, radiation damage is the enemy of multiplicity, as crystal deterioration limits useful redundancy (*16*). We previously devised a procedure for combining the SAD data from multiple crystals to increase multiplicity without added radiation damage, whereby we were able to solve a relatively large and poorly diffracting selenomethionyl protein structure (*17*). For light-only native-SAD phasing, the anomalous signals are much weaker than those from Se; thus, sample preparation, data collection, and data analysis require much more care. Here, we describe procedures for robust structure evaluation from the small anomalous signals of light-atom–only molecules and apply these procedures in determining four protein structures.

Anomalous signals for light elements increase steadily with decreasing energy; notably, f'' (the determinative, imaginary component of anomalous scattering) for sulfur increases from 0.24 electrons (e) at the Se-K edge (12.658 keV) to 0.73 e at 7 keV and to 1.93 e at 4 keV (table S2). Thus, native-SAD analyses benefit from low-energy experiments. Enhanced f'' comes at the expense of increased x-ray absorption and incoherent scattering, however, which also increases with decreasing energy (table S2). All materials in all beam paths contribute, including the sample itself and gases between the sample and detector. Absorption diminishes diffracted signals, and incoherent scattering dramatically increases the

Table 1. Summary of native-SAD structure determinations, $\langle|\Delta F_{\pm h}|\rangle/\langle|F|\rangle$ is estimated at zero scattering angle from a priori contents (*6*). *SHELXD* substructure success rate from 100 tries for $HK9_s$ and netrin G2, 1000 tries for CysZ, and 2000 tries for TorT/$TorS_S$. MapCC is the correlation coefficient between density-modified (DM, no averaging) experimental- and model-phased maps. Auto-built residues are model building (successes/refined as ordered) by *ARP/wARP* except by Buccaneer for TorT/$TorS_S$.

	$HK9_s$	CysZ	Netrin G2	TorT/$TorS_s$
Number of crystals	6	7	5	13
Resolution (Å)	2.3	2.3	2.3	2.8
Unique residues	157	492	332	1162
Unique sulfur atoms	3	22	26	28
$\langle|\Delta F_{\pm h}|\rangle/\langle|F|\rangle$(%)	0.74	1.12	1.49	0.83
Diffraction statistics	Table S3	Table S4	Table S5	Table S6
Substructure success (%)	35.0	3.4	11.0	0.7
MapCC after DM (%)	65.5	72.3	80.8	71.3
Auto-built residues	98/127	408/453	291/312	965/1148
R	0.187	0.200	0.203	0.184
R_{free}	0.227	0.238	0.241	0.242
PDB code*	3VA9	3TX3	3TBD	3O1I

*PDB code 3TBD was refined at a higher resolution, and 3O1I was refined previously from other data.

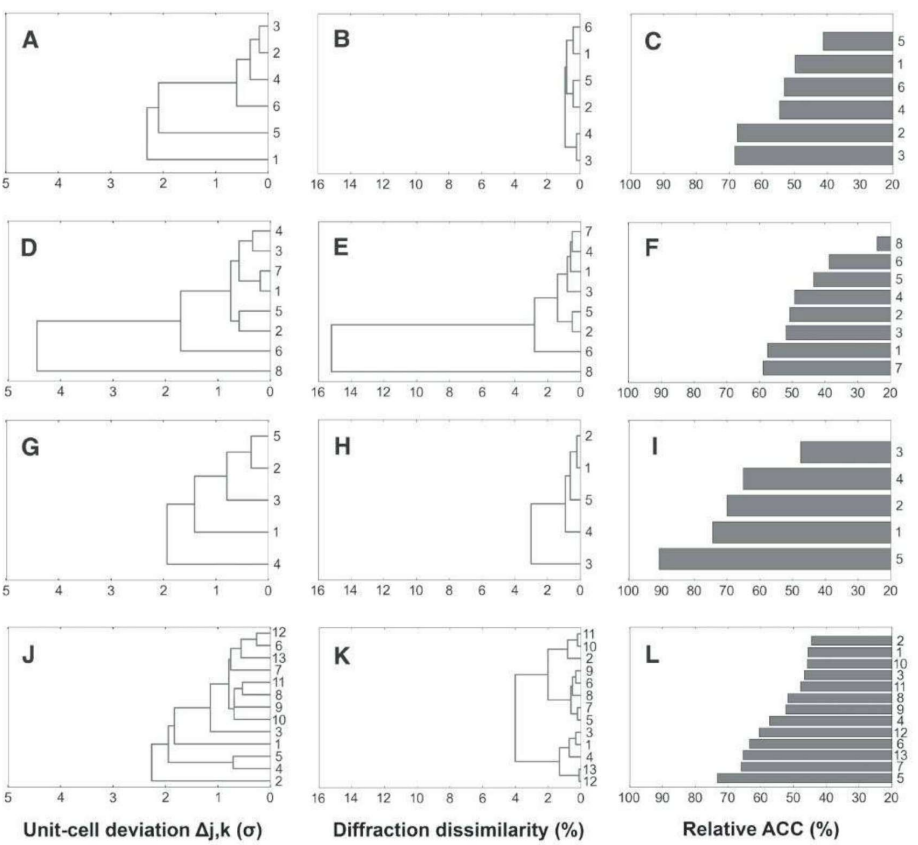

Fig. 1. Variations among crystals from multicrystal data sets. (Left) Cluster analyses of unit cell variations. (Center) Cluster analyses of overall diffraction dissimilarity. (Right) Relative anomalous correlation coefficient. (**A**, **B**, and **C**) $HK9_S$. (**D**, **E**, and **F**) CysZ. (**G**, **H**, and **I**) netrin G2. (**J**, **K**, and **L**) TorT/$TorS_S$. Unit cell variations are standard Euclidean distances normalized by population variances, i.e., the distance between j and k of among N crystals is $\Delta_{j,k} = \{\Sigma_i [(u_{i,j} - u_{i,k})^2/V_i]\}^{1/2}$ where u_i includes all variable-unit cell parameters i, each having a variance of $V_i = \sigma_i^2 = \Sigma_k (u_k - \bar{u}_k)^2/N$, $k = 1 \rightarrow N$. Overall diffraction dissimilarity between crystals j and k is defined as $D_{i,j} = 1.0 - C_{ij}$, where C_{ij} is the correlation coefficient between all Bragg intensities in common between the two diffraction patterns. For C_{ij} calculations, high-angle data cutoffs were at 3.0 Å for $HK9_S$, CysZ, and netrin G2 and 3.9 Å for TorT/$TorS_S$. Clustering calculations were made in a single-linkage (minimum) mode for unit cell analyses and in a complete-linkage (maximum) mode for diffraction analyses. The linkage line connecting any two clusters defines the "distance" between those clusters. The RACC compares Bijvoet differences from an identified individual data set with those in the data set merged from all crystals.

background beneath integrated Bragg intensities; both reduce the signal-to-noise ratio. To optimize the experimental design, we estimated transmitted anomalous signals as a function of x-ray energy and sample size (fig. S1). For samples of the sizes used in these studies (100 to 300 μm), the optimal x-ray energy is at 6 to 7 keV, and we chose to use 7.112 keV x-rays as defined by the Fe-K edge; for smaller samples and microbeams, lower energies become optimal if one assumes appropriate detector geometry. To minimize diffuse scattering, we introduced a helium-filled cone in the sample-to-detector beam path and conscribed the beam size to match crystal size. To enhance signal-to-noise ratios, we adopted an inverse-beam data collection strategy (*18*), which reduces systematic errors by measuring Friedel mates with equivalent geometry, and we used a multicrystal strategy (*17*) to mitigate random errors by greatly increasing data multiplicity. To avoid crystal variation, we devised measures to assure statistical equivalence of all included crystals. To minimize effects of radiation damage, we merged data in successive wedges and excluded highly deteriorated wedges.

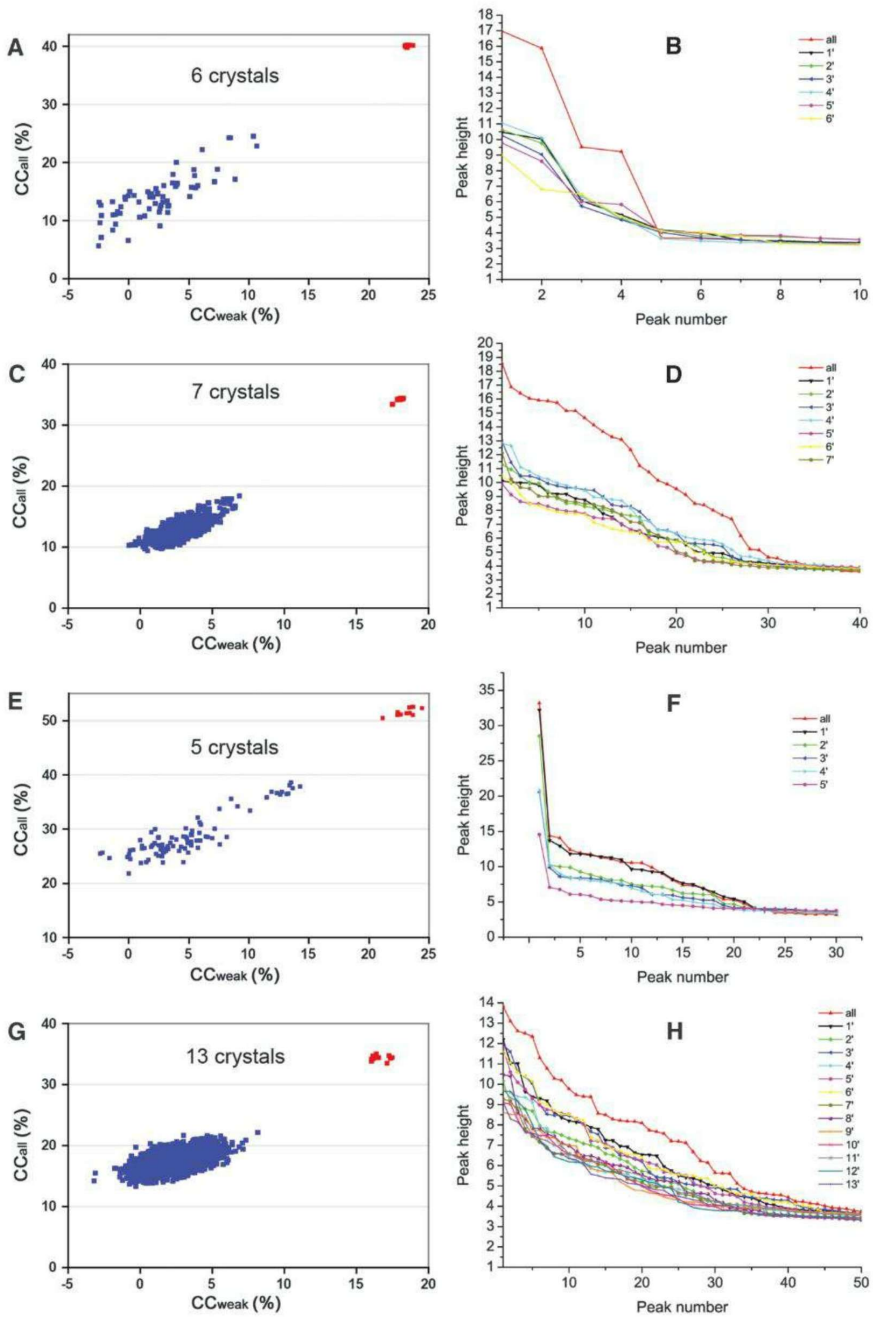

Fig. 2. Analysis of anomalously scattering substructures. (Left) Profiles of *SHELXD* correlation coefficients (CC) between observed and calculated Bijvoet differences. (**A**) $HK9_S$, 35 solutions in 100 tries. (**C**) CysZ, 34 solutions in 1000 tries. (**E**) Netrin G2, 11 solutions in 100 tries. (**G**) $TorT/TorS_S$, 14 solutions in 2000 tries. Successful solutions are colored in red; random solutions are colored in blue. (Right) Bijvoet-difference Fourier peak profiles. (**B**) $HK9_S$, 10 highest peaks. (**D**) CysZ, 40 highest peaks. (**F**) Netrin G2, 30 highest peaks. (**H**) $TorT/TorS_S$, 50 highest peaks. For each experiment, ordered peak-height profiles are shown for maps from each single-crystal data set (identified by inset keys) and for the map from the merged data set (red in all cases). Peak heights are given in units of root-mean-squared deviation over the entire respective Fourier syntheses.

We undertook to develop our multicrystal native-SAD procedures by determining four crystal structures; experimental details are given in Table 1 and in the materials and methods section in the supplementary materials. Three of these applications solved protein structures without homologs of known structure ($HK9_S$, CysZ, and netrin G2) and one ($TorT/TorS_S$) "re-solved" a challenging test problem solved previously by other methods. One (CysZ) is an integral membrane protein and the others are domains of membrane receptors.

Crystal variation is always a concern for structure determination from multiple crystals, especially because variations may arise upon rapid freezing (*19*); nevertheless, we did not observe adverse effects in our earlier eight-crystal mergings (*17*). Here, as before, the crystals did differ somewhat in various parameters, including unit cell dimensions, $I/\sigma(I)$, R_{merge}, anomalous correlation coefficient (ACC), and $\Delta F/\sigma(\Delta F)$ (tables S3 to S6). We evaluated these crystal variations, testing for statistical equivalence in three characteristics: unit cell variations, overall diffraction dissimilarity (1.0–pairwise intensity correlation coefficient), and the relative anomalous correlation coefficient (RACC). RACC correlates the Bijvoet differences from an individual data set with those of the data merged from all crystals. Note that we found evidence for rejecting only one data set (CysZ data set 8) as an outlier.

Analyses of unit cell variations (left), overall diffraction variations (center), and anomalous differences (right) are shown in Fig. 1 for 6 crystals of $HK9_S$ (A, B, and C); 8 crystals of CysZ (D, E, and F); 5 crystals of netrin G2 (G, H, and I); and 13 crystals of $TorT/TorS_S$ (J, K, and L). Variations among crystals within an experiment were small except for data set 8 of CysZ, which deviated from other CysZ crystals both for unit cell parameters (>4 σ) and diffracted intensities (>15%). The next biggest deviations were from data 2 of $TorT/TorS_S$, where deviations were within 2.2 σ for unit cell parameters and within 5% for overall diffraction patterns, which indicated their compatibility.

Although the anomalous correlation coefficient (ACC) was a most effective measure of SAD phasing efficacy in our previous SeMet study (*17*), ACC proved to be unreliable for many single native-SAD data sets, with overall ACC values approaching zero. Thus, we devised the RACC to provide a more robust measure of anomalous signals. As shown in tables S3 to S6, typical RACC values are at or above 40%; CysZ outlier data set 8 was the one exception (RACC =

24.1%). For the four crystal systems in this study, we found that rejection criteria of unit cell deviations of >3σ, overall diffraction dissimilarity of >5%, and RACC of <35% were satisfactory and consistent with one another for outlier identification. A combinatorial criterion could be more robust, and appropriate rejection criteria could vary with characteristics of specific native-SAD experiments. Populated subclusters of data sets might be identified to yield satisfactorily valid but nonisomorphous structures.

Individual data sets from accepted crystals were further checked for exclusion of radiation-damaged wedges and for individual outlier rejections upon scaling and merging with the program *SCALA* (*20*). For each application, individual data sets were reordered according to overall RACC, and mergings were made by successively adding one data set at a time, both best to worst (tables S7A to S10A) and worst to best (tables S7B to S10B), followed by attempts at structure determination. In general, substructures were determined at reduced resolution (3.0 to 3.9 Å) and then used for phasing at the data limit. In each case, assessment parameters improved with successive mergings once substructure determination was feasible, and measures of anomalous signal strength (fig. S2) and diffracted intensity precision (fig. S3) were appreciably enhanced for merged data versus individual data sets. Most important, substructure determinations by *SHELXD* (*21*) were robust in all cases after data merger (Fig. 2, A, C, E, and G) and resulting phases were accurate as evidenced by Bijvoet-difference peak profiles (Fig. 2, B, D, F, and H) and electron density maps (fig. S4). Each of the multicrystal electron density distributions supported automated chain tracing at a high level of completion (77 to 93%) (Table 1). Phasing efficacy increased with the number of crystals and with multiplicity ordered by data wedges, but it appeared to reach an asymptotic limit (Fig. 3). Map quality continued to improve even at 150-fold data multiplicity.

The four crystal structures determined here are shown as ribbon diagrams in Fig. 4, including the sulfur, chlorine, calcium, and sulfate substructures identified and used in the SAD analyses. These structures range from 127 to 1148 ordered residues, are in crystal symmetries from monoclinic to tetragonal, and have resolution limits from 2.8 to 2.3 Å. Full descriptions of the structures and associated biology are being published elsewhere, including the structure of netrin G2 as refined at higher resolution (*22*) and the prior structure of TorT/TorS$_S$ (*23*). Each structure was unknown previously; both HK9$_S$ and netrin G2 had resisted structure determination by other methods; CysZ is an unprecedented kind of membrane protein; and the TorT/TorS$_S$ complex is both large and at modest resolution (2.8 Å). The range of these applications indicates substantial generality and robustness.

Although the multicrystal native-SAD procedure was effective as implemented here, our experimental setup was not ideal. These results are from a bending-magnet beamline on a second-generation synchrotron source. As suggested by fig. S1 and table S1, substantially better performance can be expected by microdiffraction at an advanced undulator beamline that is optimized for low-energy experiments, including the provision of a detector designed to capture high-angle diffraction effectively. Improvements in scaling and weighting procedures can also be anticipated.

Notwithstanding prospects for improvement, we suggest that multicrystal-SAD phasing can facilitate robust de novo determination of native proteins and nucleic acids at a level rivaling that from the use of selenomethionyl proteins at present. The TorT/TorS$_S$ complex has a size

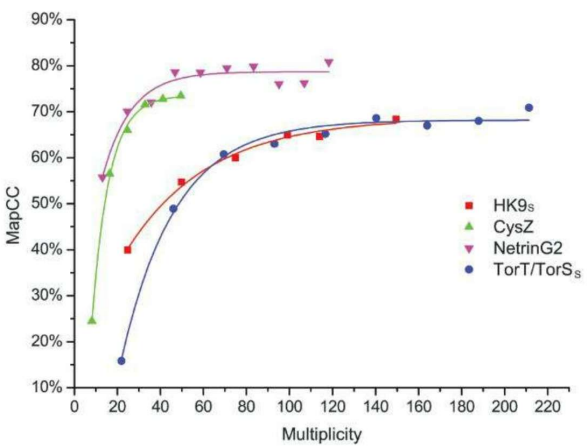

Fig. 3. Phasing efficacy dependence on data multiplicity. Phasing efficacy is measured here by the map correlation coefficient (mapCC), and average data multiplicity is given in the order of wedges of accumulated diffraction data. Each individual data set was divided into wedges of sequentially measured frames (6 wedges for HK9$_S$, 6 wedges for CysZ, 10 wedges for netrin G2, and 9 wedges for TorT/TorS$_S$), and these data were then merged wedge by wedge. Accumulations from these wedges were then used for native-SAD phasing based on substructures obtained before from all data. For each accumulation, experimental electron densities after density modification were compared with model electron densities. Resultant mapCCs for these wedge structures are plotted with respect to multiplicity for the respective accumulations: HK9$_S$ (red), CysZ (green), netrin G2 (magenta), and TorT/TorS$_S$ (blue). Fittings are with an asymptotic formula described in supplementary text.

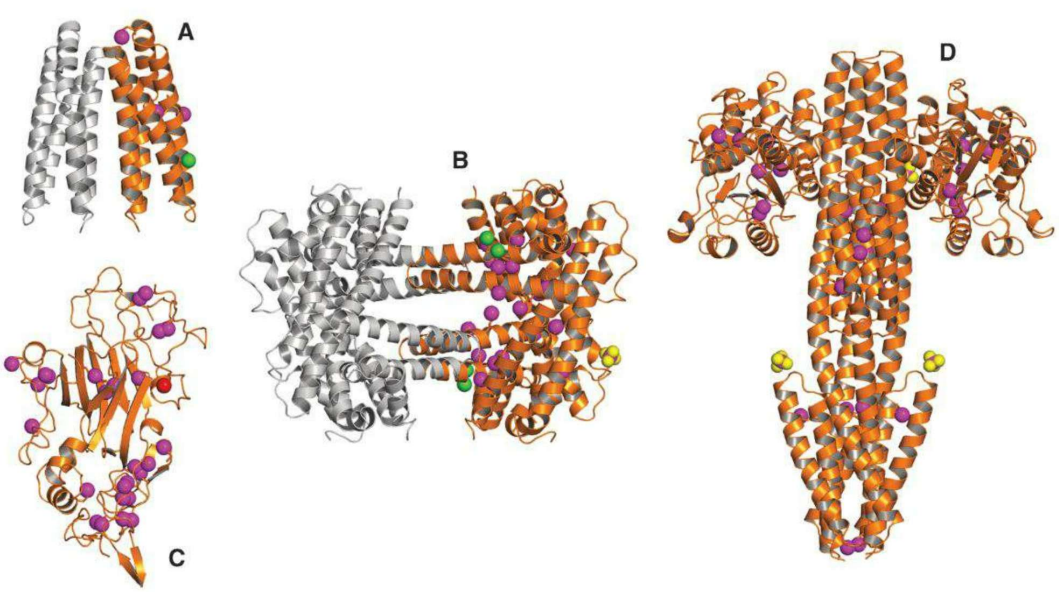

Fig. 4. Native-SAD crystal structures. (**A**) HK9$_S$, a substructure of 3 S atoms and 1 Cl atom defined 127 ordered residues at 2.3 Å resolution. (**B**) CysZ, a substructure of 20 S atoms, 4 Cl atoms, and 1 SO_4 defined 453 ordered residues at 2.3 Å resolution. (**C**) Netrin G2, a substructure of 26 S atoms, and 1 Ca atom defined 312 ordered residues at 2.3 Å resolution. (**D**) TorT/TorS$_S$, a substructure of 28 S atoms and 3 SO_4 defined 1148 ordered residues at 2.8 Å resolution. Each molecular oligomer or complex is shown as a ribbon diagram with those residues in the asymmetric unit colored orange. Anomalously scattering substructures are shown as spheres with sulfur atoms in magenta, chloride atoms in green (HK9$_S$ and CysZ), sulfate ions in yellow and magenta (CysZ and TorT/TorS$_S$), and the one calcium ion in red (netrin G2).

(~1200 residues) and a resolution limit (2.8 Å) that are at a complexity level exceeding more than 90% of entries in the current PDB. Although difficulties may arise in obtaining sufficient numbers of adequate crystals to support multicrystal determinations, advantages will accrue in being liberated from the need for derivatization or selenomethionine incorporation.

References and Notes

1. W. A. Hendrickson, *Science* **254**, 51 (1991).
2. W. A. Hendrickson, *J. Synchrotron Radiat.* **6**, 845 (1999).
3. B.-C. Wang, *Methods Enzymol.* **115**, 90 (1985).
4. K. D. Cowtan, P. Main, *Acta Crystallogr. D Biol. Crystallogr.* **49**, 148 (1993).
5. Z. Dauter, M. Dauter, E. Dodson, *Acta Crystallogr. D Biol. Crystallogr.* **58**, 494 (2002).
6. W. A. Hendrickson *et al.*, *EMBO J.* **9**, 1665 (1990).
7. W. A. Hendrickson, M. M. Teeter, *Nature* **290**, 107 (1981).
8. Z. Dauter *et al.*, *J. Mol. Biol.* **289**, 83 (1999).
9. Z. J. Liu *et al.*, *Protein Sci.* **9**, 2085 (2000).
10. Z. Dauter, D. A. Adamiak, *Acta Crystallogr. D Biol. Crystallogr.* **57**, 990 (2001).
11. M. S. Weiss, T. Sicker, R. Hilgenfeld, *Structure* **9**, 771 (2001).
12. C. Mueller-Dieckmann, S. Panjikar, P. A. Tucker, M. S. Weiss, *Acta Crystallogr. D Biol. Crystallogr.* **61**, 1263 (2005).
13. M. S. Weiss, S. Panjikar, C. Mueller-Dieckmann, P. A. Tucker, *J. Synchrotron Radiat.* **12**, 304 (2005).
14. M. Cianci, J. R. Helliwell, A. Suzuki, *Acta Crystallogr. D Biol. Crystallogr.* **64**, 1196 (2008).
15. C. Yang *et al.*, *Acta Crystallogr. D Biol. Crystallogr.* **59**, 1943 (2003).
16. E. F. Garman, *Acta Crystallogr. D Biol. Crystallogr.* **66**, 339 (2010).
17. Q. Liu, Z. Zhang, W. A. Hendrickson, *Acta Crystallogr. D Biol. Crystallogr.* **67**, 45 (2011).
18. W. A. Hendrickson *et al.*, *Proc. Natl. Acad. Sci. U.S.A.* **86**, 2190 (1989).
19. E. Garman, *Acta Crystallogr. D Biol. Crystallogr.* **55**, 1641 (1999).
20. P. Evans, *Acta Crystallogr. D Biol. Crystallogr.* **62**, 72 (2006).
21. T. R. Schneider, G. M. Sheldrick, *Acta Crystallogr. D Biol. Crystallogr.* **58**, 1772 (2002).
22. J. Brasch *et al.*, *J. Mol. Biol.* **414**, 723 (2011).
23. J. O. Moore, W. A. Hendrickson, *Structure* **20**, 729 (2012).

Acknowledgments: We thank R. Abramowitz and J. Schwanof for help with synchrotron data collection. This work was supported in part by cooperative agreement GM095315 from the Protein Structure Initiative (CysZ), and by NIH grants GM034102 ($HK9_S$ and $TorT/TorS_S$) and GM062270 (netrin G2). Beamline X4A of the NSLS at Brookhaven National Laboratory, a U.S. Department of Energy facility, is supported by the New York Structural Biology Center. Accession codes for PDB deposits are listed in Table 1. DNA constructs and cell lines may require a material transfer agreement with Columbia University.

Supplementary Materials

www.sciencemag.org/cgi/content/full/336/6084/1033/DC1
Materials and Methods
Supplementary Text
Figs. S1 to S4
Tables S1 to S10
References (*24*–*43*)

5 January 2012; accepted 16 March 2012
10.1126/science.1218753

The Crystal Structure of Human Argonaute2

Nicole T. Schirle and Ian J. MacRae*

Argonaute proteins form the functional core of the RNA-induced silencing complexes that mediate RNA silencing in eukaryotes. The 2.3 angstrom resolution crystal structure of human Argonaute2 (Ago2) reveals a bilobed molecule with a central cleft for binding guide and target RNAs. Nucleotides 2 to 6 of a heterogeneous mixture of guide RNAs are positioned in an A-form conformation for base pairing with target messenger RNAs. Between nucleotides 6 and 7, there is a kink that may function in microRNA target recognition or release of sliced RNA products. Tandem tryptophan-binding pockets in the PIWI domain define a likely interaction surface for recruitment of glycine-tryptophan-182 (GW182) or other tryptophan-rich cofactors. These results will enable structure-based approaches for harnessing the untapped therapeutic potential of RNA silencing in humans.

RNA silencing processes, such as the RNA interference (RNAi) and microRNA (miRNA) pathways, are mediated by a specialized family of RNA-binding proteins named Argonaute. Argonaute proteins bind small regulatory RNAs [21 to 23 nucleotides (nt)] and use the encoded sequence information to locate and silence complementary target RNAs. Targeted RNAs are silenced either by direct cleavage via the endonucleolytic "slicing" reaction catalyzed by some Argonaute proteins (*1*, *2*) or by Argonaute-mediated recruitment of additional silencing factors (*3*–*5*). Structural studies of prokaryotic homologs, which use DNA guides to recognize and cleave target oligonucleotides, revealed a bilobed architecture composed of four globular domains (N, PAZ, MID, and PIWI) connected through two structured linker domains (L1 and L2) (*6*). The two lobes form the walls of a central cleft that cradles guide DNAs and complementary targets (*7*–*9*). An ribonuclease H-like active site in the PIWI domain catalyzes the cleavage of target nucleic acids (*6*, *10*, *11*). Although structures of isolated PAZ, MID, and MID-PIWI domains from several eukaryotic Argonaute proteins have been reported (*12*–*18*), the extent to which the structures and mechanisms of full-length Argonautes resemble those of their prokaryotic cousins is not known.

We determined the crystal structure of full-length human Argonaute2 (Ago2) to a resolution of 2.3 Å (table S1). Ago2 has a bilobed structure reminiscent of that seen in prokaryotes (Fig. 1 and fig. S1). However, the lobes of Ago2 do no align with the corresponding lobes derived from prokaryotic structures, revealing large structural differences between Argonautes from different kingdoms of life (Fig. 2A and fig. S2). In contrast, the individual domains of Ago2 superimpose reasonably well with their prokaryotic counterparts (Fig. 2B). Therefore, the major architectural differences between prokaryotic and eukaryotic Argonautes appear mainly in the relative positions of well-conserved core domain structures (figs. S3 and S4). The core domains in Ago2 also have extended loops and additional secondary structures, not present in bacteria, that

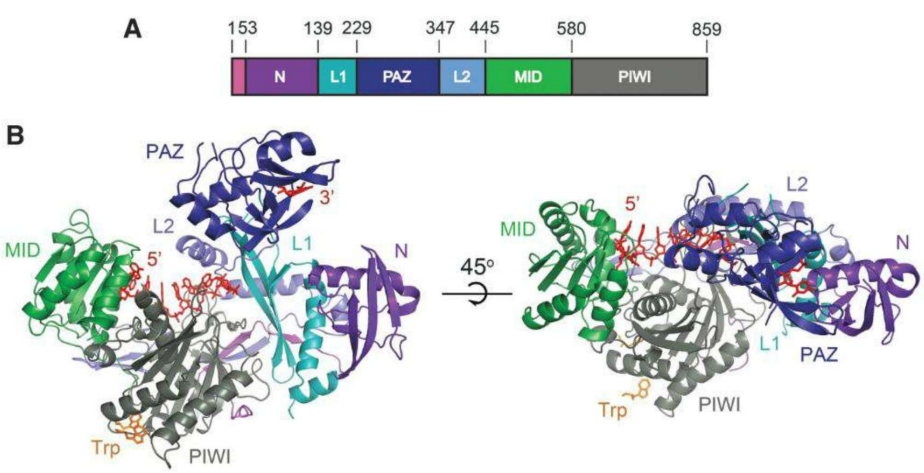

Fig. 1. Structure of human Ago2. (**A**) Schematic of the Ago2 primary sequence. (**B**) Front and top views of Ago2 with the N (purple), PAZ (navy), MID (green), and PIWI (gray) domains and linkers L1 (teal) and L2 (blue). A generic guide RNA (red) can be traced for nucleotides 1 to 8 and 21. Tryptophan molecules (orange) bind to tandem hydrophobic pockets in the PIWI domain.

Department of Molecular Biology, The Scripps Research Institute, La Jolla, CA 92037, USA.

*To whom correspondence should be addressed. E-mail: macrae@scripps.edu

are likely to play roles in guide binding, target RNA recognition, and recruitment of Ago2-associated protein factors (figs. S5 and S6).

We observed electron density for an eight-nucleotide stretch of single-stranded RNA extending across the MID/PIWI/L2/L1 interface (Fig. 3). This density likely arises from heterogeneous, small cellular RNAs (~10 to 20 nt in length) that accompany Ago2 in our preparations (fig. S7). The RNA is bound in a conformation similar to that of guide DNAs in bacterial structures. The electron density for nucleotides 1 to 7 is well defined, indicating that Ago2 positions this segment of guide RNAs in a uniform conformation that is largely sequence independent. We modeled the guide RNA as polyadenosine because the experimental electron density accommodated purine bases (fig. S8). The 5′ base of the RNA stacks against Y529, which also forms a hydrogen bond to the 5′ phosphate along with side chains of Y529, K533, N545, and K566 (Fig. 3A), as seen in the structure of the isolated MID domain (*18*). Additional water-mediated contacts to the 5′ phosphate are made by K570, R812, and the carboxyl terminus (A859). In contrast to prokaryotic structures, we did not observe a magnesium ion in the 5′ phosphate-binding site. Ago2 contacts the guide RNA primarily through hydrogen bonds and salt linkages to the phosphate backbone and Van der Waals interactions with the body of the ribose sugar. Residues K566, K709, H753, Y790, R792, S798, and Y804 in the MID and PIWI domains contact phosphates 3 to 6 of the guide (Fig. 3B). Residues S220, R357, R714, and R761 of L1, L2, and the PIWI domain contact phosphates 7 to 9 (Fig. 3C). The 3′ binding pocket of the PAZ domain contained some weak electron density, which we modeled as a single nucleotide with a refined occupancy of 0.75.

Ago2 does not appear to rely heavily on direct hydrogen bonds to the 2' hydroxyls of the guide for RNA recognition. We observe only two hydrogen bonds between the protein and 2' hydroxyls of the guide: Nucleotide 5 hydrogen bonds to the main chain amide of I756, and nucleotide 7 hydrogen bonds to the main chain carbonyl of A221 (fig. S9). The 2' hydroxyl of nucleotide 2 makes a water-mediated contact to main-chain carbonyls of N562 and R792. However, we observe no hydrogen-bond acceptors or donors less than 3.8 Å away from the 2' hydroxyls of nucleotides 1, 3, 4, 6, and 8. This may explain why DNA bases and 2' fluoro substitutions are tolerated in the antisense strand of small interfering RNAs (siRNAs) (*19*, *20*). We also note that the guide-binding pocket of the bacterial Argonaute is more hydrophobic than the same region of human Ago2 and may not accommodate several 2' hydroxyls (fig. S10). These observations may explain why the prokaryotic enzyme prefers guide DNAs over RNAs (*10*).

Nucleotides 2 to 6 of the guide RNA are splayed out, with Watson-Crick faces exposed to the bulk solvent, in an A-form conformation (Fig. 3D). This observation supports the "seed-pairing" model of miRNA targeting, in which Argonaute is proposed to prearrange miRNA nucleotides 2 to 7 in an A-form configuration, thereby reducing the entropic cost associated with forming a stable duplex with target RNAs (*21*, *22*). However, there is a distinct kink between nucleotides 6 and 7 of the RNA that breaks the A-form structure in this region of the guide. The kink appears to be introduced by Ile-365, which is inserted between the faces of bases 6 and 7. The position of nucleotide 7 is further stabilized by Met-364, which interacts with the minor-grove edge of the base. Met-364 and Ile-365 reside on α-helix 7 in a region of L2 that is conserved in eukaryotic Argonautes (Fig. 3D and fig. S11). The archeal Argonaute from the *Pyrococcus furiosus* has a similar helix (fig. S1). In contrast, *Thermus thermophilus* Argonaute, the best structurally characterized member of the superfamily, lacks an analogous helix.

Docking an A-form duplex onto the guide RNA reveals that helix 7 would have to shift to accommodate target pairing to nucleotides 6 and 7 of the guide (fig. S12). A shift in helix 7 would also likely release the constraints on nucleotide 7, allowing the guide to form a contiguous A-form helix. These types of conformational changes may relate to the importance of pairing to nucleotide 7 for effective miRNA targeting (*23*) and could possibly be used as a readout for recognition of miRNA target sites. The ability of Ago2 to kink guide RNAs may also facilitate release of

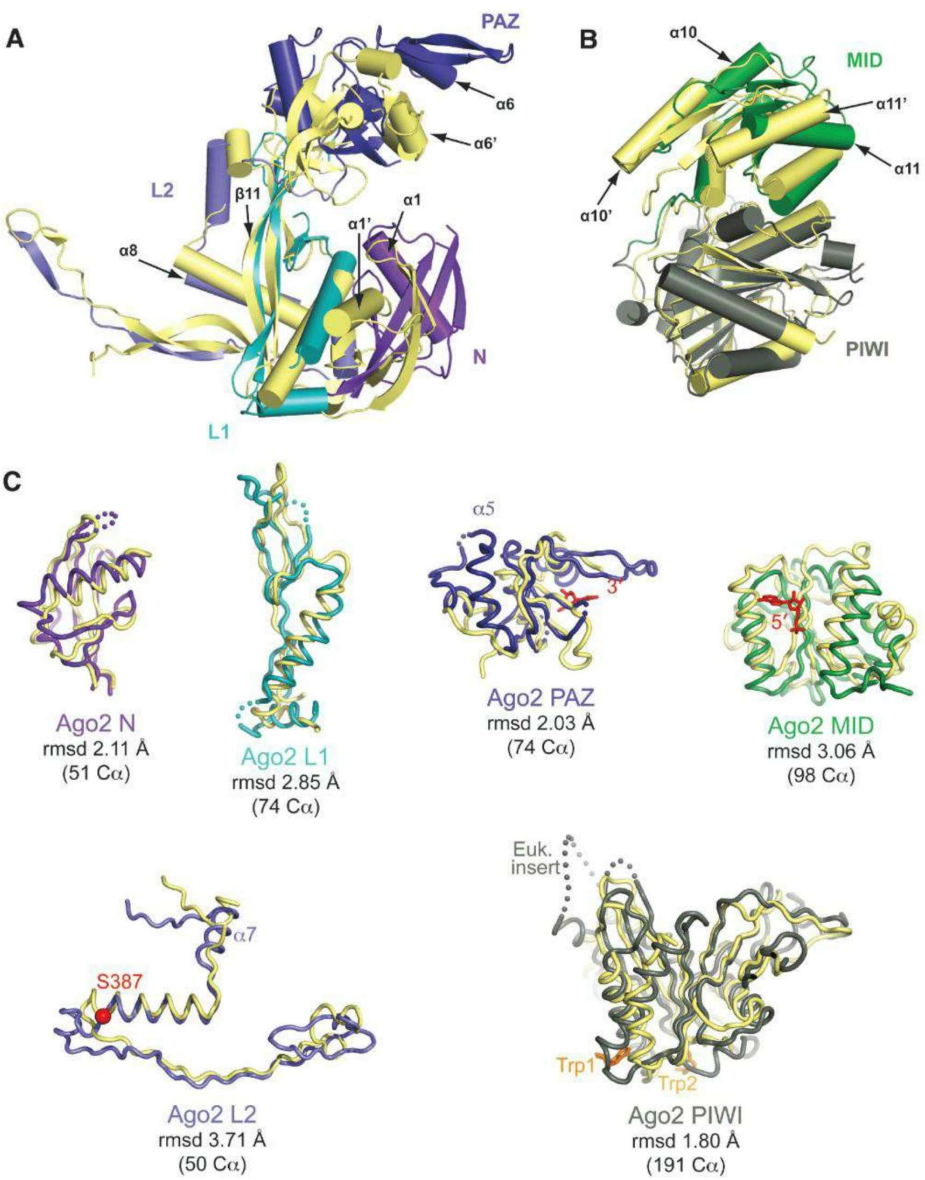

Fig. 2. Comparison of bacterial and human Argonaute structures. (**A**) Superposition of N-PAZ and (**B**) superposition of MID-PIWI lobes of Ago2 (colored as in Fig. 1) onto corresponding lobes from *T. thermophilus* (yellow). (**C**) Individual domains of Ago2 superimposed on the corresponding domains from *T. thermophilus* with root mean square deviation (rmsd) values for equivalent alpha-carbons indicated. Functional points of interest in Ago2 are labeled.

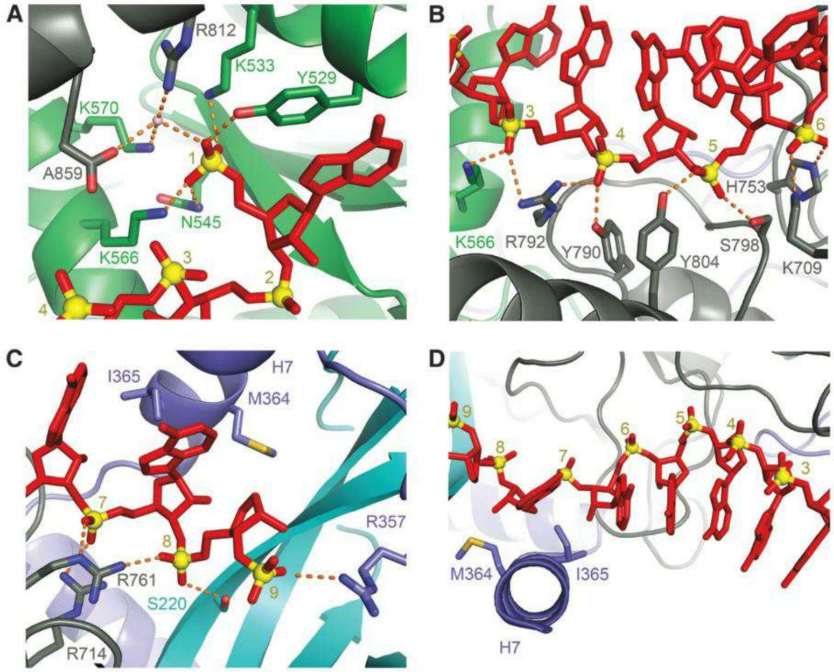

Fig. 3. Conformation of bound guide RNAs. (**A**) The 5′ nucleotides of guide RNAs are recognized by extensive interactions with the MID and PIWI domains. An ordered water molecule is shown as a pink sphere. Hydrogen bonds are shown as dashed orange lines. (**B** and **C**) Ago2 organizes the seed region in an A-form helix by extensive interactions with the phosphate backbone. (**D**) Helix 7 introduces a kink in the guide RNA between bases 6 and 7 that disrupts helical stacking. Single-letter abbreviations for the amino acid residues are as follows: A, Ala; C, Cys; D, Asp; E, Glu; F, Phe; G, Gly; H, His; I, Ile; K, Lys; L, Leu; M, Met; N, Asn; P, Pro; Q, Gln; R, Arg; S, Ser; T, Thr; V, Val; W, Trp; and Y, Tyr.

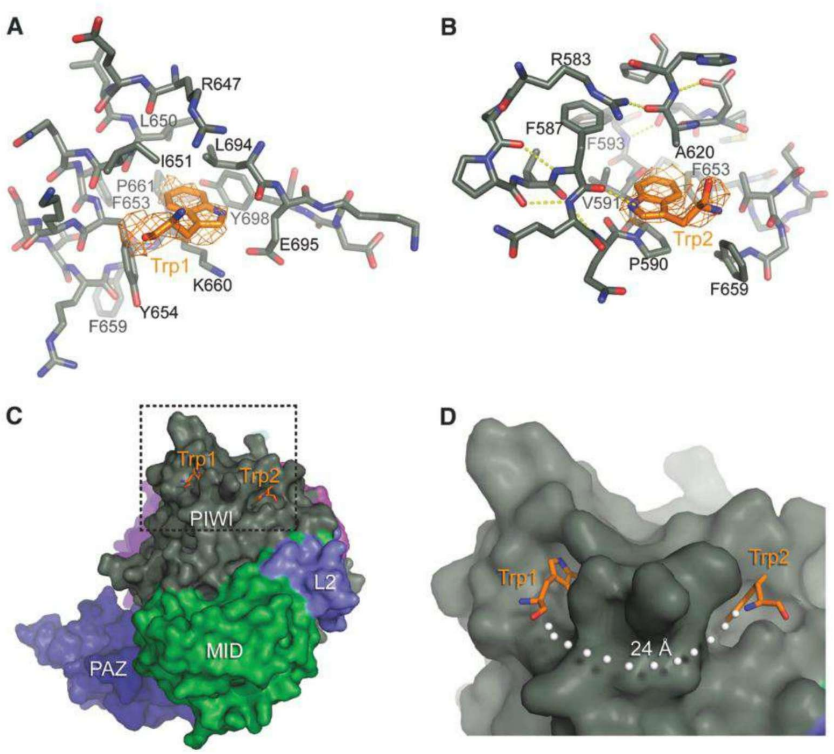

Fig. 4. Tandem tryptophan-binding pockets in the PIWI domain. (**A** and **B**) Residues forming the binding pockets of tryptophan 1 and 2 are shown, with hydrogen bonds indicated (dashed yellow lines). Tryptophan molecules are shown with surrounding unbiased difference maps (with tryptophan structure factors minus without) contoured at two sigma (orange). (**C**) Surface representation showing the tryptophan-binding pockets. (**D**) Close-up view of boxed area in (C). White dots indicate the shortest direct path connecting the two sites along the surface of Ago2.

sliced RNA products by disrupting guide-target pairing in this region.

Argonaute-associated proteins often contain glycine-tryptophan (GW)–rich regions, which are believed to interact with the Argonaute PIWI domain (*3*, *17*, *24*–*27*). The tryptophan residues in GW proteins are essential for mediating protein-Argonaute interactions (*25*, *28*, *29*). To identify possible GW interaction sites, we determined the structure of Ago2 crystallized in the presence of free tryptophan (table S2). Unambiguous electron density for tryptophan molecules was observed in two adjacent hydrophobic pockets in the PIWI domain (Fig. 4). Tryptophan 1 stacks over the aliphatic segment of K660 and packs against the side chains of L650, I651, Y654, L694, and Y698. Tryptophan 2 stacks against P590, forms a hydrogen bond to the main-chain carbonyl of F587 through the amine group in its indole ring, and packs against the side chains of F659, F587, V591, A620, and F653. In the absence of tryptophan, phenol (present at 100 mM in the minus-tryptophan crystallization conditions) was observed in tryptophan-binding site 1 (fig. S13).

Both tryptophan molecules bound with indole side chains inserted into Ago2 and main-chain atoms extended out toward the bulk solvent, as would be expected for binding tryptophans attached to a polypeptide. We therefore suggest that the observed tryptophan-binding pockets are interaction sites for binding to GW motifs in Argonaute-associated proteins. Consistent with this idea, mutations that disrupt these binding sites in Ago2 and *Drosophila* Ago1 specifically reduce binding to GW182 without disrupting miRNA binding (fig. S14) (*17*, *25*).

We note that tryptophan residues in various GW proteins often occur in pairs, separated by a flexible linker of 8 to 14 amino acid residues (*25*, *28*, *29*). An extended 8–amino acid peptide spans a distance of about 24 Å, which closely matches the distance between the two tryptophan-binding sites, when measuring along the surface of Ago2 (Fig. 4C). Based on these observations, we hypothesize that Argonaute may specifically recognize GW proteins by binding to tandem tryptophan residues that are separated by an appropriately sized flexible linker. Consistent with this notion, the carboxylic acid of tryptophan 1 is oriented toward the amino group of tryptophan 2, as would be expected for tryptophan residues aligned on a single polypeptide chain (Fig. 4C).

A major motivation for previous studies of prokaryotic forms of Argonaute was that understanding their structures might provide mechanistic insights relevant to Argonaute in humans (*1*, *6*, *9*). The data presented here validate this assumption, showing that the active site structure is conserved (fig. S15), and the seed region of the guide is preordered for pairing to targets. The structure of Ago2 also reveals new features not present in bacteria. The rearrangement of domains within the bilobed structure likely influences how the protein interacts with guide and target molecules. Indeed, helix 7 influences the

conformation of guide RNAs in a manner that is not seen for guide DNAs in bacteria. Moreover, the tryptophan-binding sites in the PIWI domain form a likely interaction surface for additional RNA-induced silencing complex components for which no known homologs exist in the prokaryotic kingdom. The structures presented here extend studies of the prokaryotic into understanding Argonaute in humans. Bridging this gap is an essential step toward leveraging structural information for design and delivery strategies for silencing human disease factors using RNAi.

References and Notes

1. J. Liu *et al.*, *Science* **305**, 1437 (2004).
2. G. Meister *et al.*, *Mol. Cell* **15**, 185 (2004).
3. I. Behm-Ansmant *et al.*, *Genes Dev.* **20**, 1885 (2006).
4. J. E. Braun, E. Huntzinger, M. Fauser, E. Izaurralde, *Mol. Cell* **44**, 120 (2011).
5. M. R. Fabian *et al.*, *Nat. Struct. Mol. Biol.* **18**, 1211 (2011).
6. J. J. Song, S. K. Smith, G. J. Hannon, L. Joshua-Tor, *Science* **305**, 1434 (2004).
7. Y. Wang *et al.*, *Nature* **456**, 921 (2008).
8. Y. Wang *et al.*, *Nature* **461**, 754 (2009).
9. Y. Wang, G. Sheng, S. Juranek, T. Tuschl, D. J. Patel, *Nature* **456**, 209 (2008).
10. Y. R. Yuan *et al.*, *Mol. Cell* **19**, 405 (2005).
11. J. B. Ma *et al.*, *Nature* **434**, 666 (2005).
12. J. B. Ma, K. Ye, D. J. Patel, *Nature* **429**, 318 (2004).
13. A. Lingel, B. Simon, E. Izaurralde, M. Sattler, *Nature* **426**, 465 (2003).
14. J. J. Song *et al.*, *Nat. Struct. Biol.* **10**, 1026 (2003).
15. K. S. Yan *et al.*, *Nature* **426**, 468 (2003).
16. A. Boland, F. Tritschler, S. Heimstädt, E. Izaurralde, O. Weichenrieder, *EMBO Rep.* **11**, 522 (2010).
17. A. Boland, E. Huntzinger, S. Schmidt, E. Izaurralde, O. Weichenrieder, *Proc. Natl. Acad. Sci. U.S.A.* **108**, 10466 (2011).
18. F. Frank, N. Sonenberg, B. Nagar, *Nature* **465**, 818 (2010).
19. Y. L. Chiu, T. M. Rana, *RNA* **9**, 1034 (2003).
20. G. F. Deleavey *et al.*, *Nucleic Acids Res.* **38**, 4547 (2010).
21. D. P. Bartel, *Cell* **116**, 281 (2004).
22. B. P. Lewis, C. B. Burge, D. P. Bartel, *Cell* **120**, 15 (2005).
23. D. P. Bartel, *Cell* **136**, 215 (2009).
24. S. L. Lian *et al.*, *RNA* **15**, 804 (2009).
25. A. Eulalio, S. Helms, C. Fritzsch, M. Fauser, E. Izaurralde, *RNA* **15**, 1067 (2009).
26. M. El-Shami *et al.*, *Genes Dev.* **21**, 2539 (2007).
27. N. Bies-Etheve *et al.*, *EMBO Rep.* **10**, 649 (2009).
28. D. Baillat, R. Shiekhattar, *Mol. Cell. Biol.* **29**, 4144 (2009).
29. S. Till *et al.*, *Nat. Struct. Mol. Biol.* **14**, 897 (2007).

Acknowledgments: We thank the laboratories of D. Stout, E. O. Saphire, and I. Wilson for sharing synchrotron time and for helpful discussions. Crystallization screens were carried out at the Joint Center for Structural Genomics, supported by the National Institute of General Medical Sciences (NIGMS) Protein Structure Initiative (U54 GM074898). Diffraction data were collected on beamlines 24-ID-E at the Advanced Photon Source and 11-1 at the Stanford Synchrotron Radiation Lightsource. This work was supported by NIGMS grant R01 GM086701 to I.J.M. I.J.M. is a Pew Scholar in the Biomedical Sciences. Coordinates of Ago2 and Ago2 bound to tryptophan have been deposited in the Protein Data Bank (4EI1 and 4EI3).

Supplementary Materials

www.sciencemag.org/cgi/content/full/science.1221551/DC1
Materials and Methods
Figs. S1 to S15
Tables S1 and S2
References (*30*–*38*)

6 March 2012; accepted 17 April 2012
Published online 26 April 2012;
10.1126/science.1221551

Metabolite Profiling Identifies a Key Role for Glycine in Rapid Cancer Cell Proliferation

Mohit Jain,[1,2,3,4]* Roland Nilsson,[1,2,3,5]* Sonia Sharma,[6] Nikhil Madhusudhan,[1,2,3] Toshimori Kitami,[1,2,3] Amanda L. Souza,[1] Ran Kafri,[2] Marc W. Kirschner,[2] Clary B. Clish,[1] Vamsi K. Mootha[1,2,3]†

Metabolic reprogramming has been proposed to be a hallmark of cancer, yet a systematic characterization of the metabolic pathways active in transformed cells is currently lacking. Using mass spectrometry, we measured the consumption and release (CORE) profiles of 219 metabolites from media across the NCI-60 cancer cell lines, and integrated these data with a preexisting atlas of gene expression. This analysis identified glycine consumption and expression of the mitochondrial glycine biosynthetic pathway as strongly correlated with rates of proliferation across cancer cells. Antagonizing glycine uptake and its mitochondrial biosynthesis preferentially impaired rapidly proliferating cells. Moreover, higher expression of this pathway was associated with greater mortality in breast cancer patients. Increased reliance on glycine may represent a metabolic vulnerability for selectively targeting rapid cancer cell proliferation.

Malignant transformation results from mutations that alter cellular physiology to confer a proliferative advantage (*1*, *2*). Despite the genetic heterogeneity and complexity of cancer (*3*), transformed cells exhibit a limited number of proposed common hallmarks, including metabolic reprogramming, which manifests as altered nutrient uptake and use (*2*, *4*). Although metabolic reprogramming is thought to be essential for rapid cancer cell proliferation, a systematic characterization of the metabolic pathways active in transformed cells is lacking, and the contribution of these pathways in promoting rapid cancer cell proliferation remains unclear (*4*). Existing studies of cancer metabolism have examined relatively few cell lines, and have largely focused on the measurement of intracellular metabolite pools (*5*)—from which it is difficult to infer metabolic pathway activity—or have relied on isotope tracing to estimate metabolic flux through a limited number of reactions (*6*).

To systematically characterize cancer cell metabolism, we used liquid chromatography–tandem mass spectrometry (LC-MS/MS) to create cellular consumption and release (CORE) profiles of 219 metabolites (table S1) spanning the major pathways of intermediary metabolism, in the NCI-60 panel, a collection of 60 well-characterized primary human cancer cell lines established from nine common tumor types (*7*). CORE profiling builds on metabolic footprinting or exometabolomics (*8*, *9*), and provides a systematic and quantitative assessment of cellular metabolic activity by relating metabolite concentrations in spent medium from cultured cells to metabolite concentrations in baseline medium, resulting in a time-averaged CORE profile for each metabolite on a per-cell basis over a period of exponential growth (Fig. 1). Using CORE profiling, we identified 140 metabolites that were either present in fresh medium or released by at least one cancer cell line, of which 111 metabolites demonstrated appreciable variation across the 60 cell lines, with excellent reproducibility between biological replicates (Fig. 2). About one-third of the 111 metabolites were consumed by all cell lines, whereas most of the remaining two-thirds of metabolites were consistently released into the medium; only a handful of metabolites exhibited consumption in certain cell lines and release by others (Fig. 2). A larger, fully annotated version of Fig. 2 is provided in fig. S1.

This CORE atlas of cancer metabolism (Fig. 2 and fig. S1) can be used to explore metabolic phenotypes of cancer cells and to discover relationships between metabolites. For example, ornithine was released from leukemia cells, and adenosine and inosine were released from melanoma cells (fig. S2), reflecting metabolic activities that may be unique to these cancers. Unsupervised cluster analysis of metabolite

[1]Broad Institute, Cambridge, MA 02142, USA. [2]Department of Systems Biology, Harvard Medical School, Boston, MA 02115, USA. [3]Center for Human Genetic Research and Department of Molecular Biology, Massachusetts General Hospital, Boston, MA 02114, USA. [4]Division of Cardiovascular Medicine, Department of Medicine, Brigham and Women's Hospital, Boston, MA 02115, USA. [5]Unit of Computational Medicine, Department of Medicine, Karolinska Institutet, 17176 Stockholm, Sweden. [6]La Jolla Institute for Allergy & Immunology, La Jolla, CA 92037, USA.

*These authors contributed equally to this work.
†To whom correspondence should be addressed. E-mail: vamsi@hms.harvard.edu

CORE data identified leukemia cells as a distinct group but did not more generally distinguish between tumor cell lines according to tissue of origin (fig. S3). Functionally related metabolites demonstrated similar patterns of consumption and release across the 60 cell lines. For example, major nutrients including glucose, essential amino acids, and choline formed a single cluster, as did metabolites representing glycolysis, the citric acid cycle, nucleotides, and polyamines (Fig. 2 and fig. S1). Consumption of major nutrients also correlated with release of their by-products; for example, glucose consumption correlated to lactate release (Fig. 1B), consistent with the well-documented Warburg effect in transformed cells (*4*). A similar pattern of nutrient consumption and by-product release was also observed with other nutrients. Glutamine consumption, quantitatively the greatest among amino acids, was closely mirrored by glutamate release (Fig. 1B). An analysis of all monitored metabolites revealed that total measured carbon consumption was also closely correlated with total measured carbon release (Fig. 1B), which suggests that transformed cells share a common metabolic phenotype: incomplete catabolism of major nutrients followed by release of by-products.

We next sought to determine whether any metabolite CORE profiles were associated with cancer cell proliferation. Previously reported doubling times across the 60 cancer cell lines ranged from 17.0 to 79.5 hours and were highly reproducible (*10*) (fig. S4). From the 111 metabolite CORE profiles, two metabolites—phosphocholine and glycine—were significantly correlated (Bonferroni-corrected $P < 0.01$) with proliferation rate across the 60 cell lines (Fig. 3A). Phosphocholine, which was released from all cells, correlated with consumption of the essential nutrient choline (fig. S5) and has been reported to accumulate in transformed cells as a substrate for phospholipid biosynthesis (*11*). In contrast, the relation between glycine consumption and proliferation rate was unanticipated, because glycine is a non-essential amino acid that can be endogenously synthesized. Glycine exhibited an unusual CORE profile, being consumed by rapidly proliferating cells and released by slowly proliferating cells (Fig. 3B), which suggests that glycine demand may exceed endogenous synthesis capacity in rapidly proliferating cancer cells, whereas in slowly proliferating cells, glycine synthesis may exceed demand. Increasing glycine consumption with faster proliferation rate was observed across all 60 cell lines (Fig. 3B) and was even more pronounced within specific tumor types, including ovarian, colon, and melanoma cells (Fig. 3B and fig. S6), but was not evident in nonadherent leukemia cells (fig. S6).

To determine whether glycine consumption is specific to transformed cells or a general feature of rapid proliferation, we measured glycine consumption in cultured primary human mammary epithelial cells (HMECs), human bronchial epithelial (HBE) cells, human umbilical vein endothelial cells (HUVECs), and human activated $CD4^+$ T lymphocytes. These nontransformed cells had doubling times between 8 and 18 hours, comparable to the most rapidly dividing cancer cells, yet each of these cell types released rather than consumed glycine (HMECs, 3.5 ± 0.8 fmol $cell^{-1}$ $hour^{-1}$; HBE cells, 17.5 ± 3.2 fmol $cell^{-1}$ $hour^{-1}$; HUVECs, 8.4 ± 1.4 fmol $cell^{-1}$ $hour^{-1}$; lymphocytes, 1.9 ± 0.3 fmol $cell^{-1}$ $hour^{-1}$). Thus, glycine consumption appears to be a feature specific to rapidly proliferating transformed cells.

To complement the metabolite CORE analysis, we next examined the gene expression of 1425 metabolic enzymes (*12*) in a previously generated microarray data set across these 60 cell lines (*13*). This independent analysis revealed that glycine biosynthesis enzymes are more highly expressed in rapidly proliferating cancer cell lines (Fig. 3C). Intracellular glycine synthesis is compartmentalized between the cytosol and mitochondria (*14*), providing two separate enzymatic pathways (Fig. 3D). The mitochondrial glycine synthesis pathway consists of the glycine-synthesizing enzyme serine hydroxymethyltransferase 2 (SHMT2), a target of the oncogene c-Myc (*15*), as well as MTHFD2 and MTHFD1L, which regenerate the cofactor tetrahydrofolate (THF) for the SHMT2 reaction (Fig. 3D). The mitochondrial pathway exhibited significant correlation with proliferation, whereas the corresponding cytosolic enzymes did not (Fig. 3C), which suggests a key role for mitochondria in supporting rapid cancer cell proliferation. To assess the relative contributions of glycine consumption and endogenous synthesis to intracellular glycine pools, we used tracer analysis with (^{13}C)glycine in rapidly dividing LOX IMVI cells. Assuming a simple steady-state model (*13*), we estimate from labeling of intracellular glycine and serine pools (Fig. 3E) that about one-third of intracellular glycine originates from extracellular consumption, whereas the remainder is synthesized endogenously. Thus, both metabolite CORE profiling and gene expression analysis independently identify glycine metabolism as closely related to rapid proliferation in cancer cells.

To directly evaluate the contribution of glycine metabolism to rapid cancer cell proliferation, we used a combination of genetic silencing and nutrient deprivation. We stably silenced expression of the glycine-synthesizing enzyme SHMT2 in slowly proliferating A498 cells and in rapidly proliferating LOX IMVI cells (Fig. 3B) with four distinct short hairpin RNA (shRNA) sequences (fig. S7A). Chinese hamster ovary cell strains mutant in SHMT2 were previously shown to be auxotrophic for glycine (*16*). Silencing of SHMT2 in the absence of extracellular glycine halted the proliferation of LOX IMVI cells (Fig. 3F) and was rescued by the addition of glycine to the medium; this indicates that glycine itself, rather than one-carbon units derived from the SHMT2 reaction (Fig. 3D), is critical to proliferation in these cells (Fig. 3F). Supplementation of medium with sarcosine, a glycine-related metabolite (*17*), or formate, a source of cellular one-carbon units (*18*), failed to rescue LOX IMVI cells (fig. S7B). In contrast, slowly proliferating A498 cells (Fig. 3F) were not impaired by SHMT2 depletion and extracellular glycine deprivation, indicating that other means of glycine synthe-

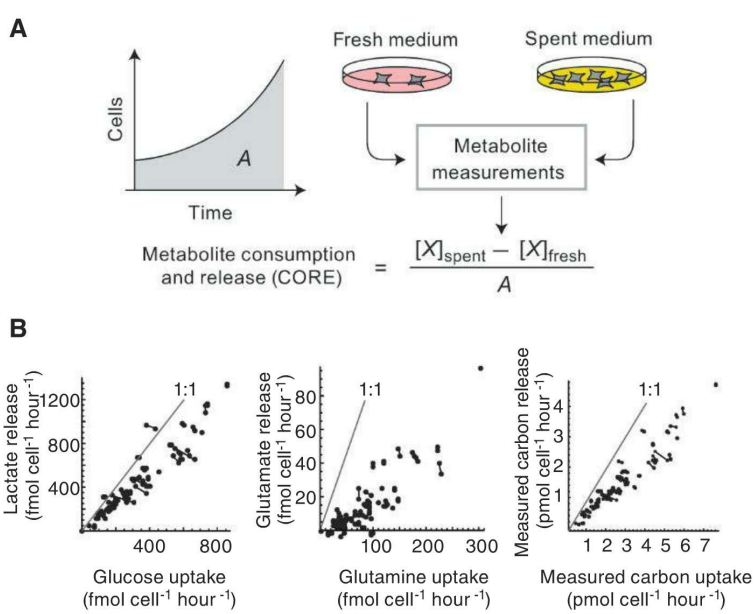

Fig. 1. CORE profiling. (**A**) For determining metabolite CORE (consumption and release) profiles, medium samples taken before (fresh) and after (spent) 4 to 5 days of cell culture are subjected to metabolite profiling by LC-MS/MS. For each metabolite *X*, the CORE value is calculated as the difference in molar abundance normalized to the area *A* under the growth curve. (**B**) Glucose consumption versus lactate release, glutamine consumption versus glutamate release, and total measured carbon consumption versus total measured carbon release across the 60 cell lines. Gray lines indicate the 1:1 molar ratio (carbon consumed/carbon released) for each metabolite pair; joined data points represent biological replicates.

sis can satisfy the requirements in these cells. Withdrawal of extracellular glycine alone also reduced the proliferation of LOX IMVI cells but not A498 cells (fig. S8), although this effect was more subtle. Collectively, our data suggest that mitochondrial production of glycine is critical specifically in rapidly proliferating cancer cells. To determine whether this reliance on glycine for rapid proliferation extends to other cancer cells, we tested silencing of SHMT2 (fig. S7C) and extracellular glycine deprivation in 10 additional primary cancer cell lines from the NCI-60 panel (Fig. 3G). Rapidly proliferating cancer cells exhibited slower proliferation with antagonism of glycine metabolism and were rescued with addition of extracellular glycine, whereas slowly proliferating cells were less sensitive to these perturbations (Fig. 3G), even when assessed at later time points to allow for a comparable number of cellular divisions relative to rapidly proliferating cells (fig. S9).

We next sought to explore the potential mechanisms by which glycine metabolism contributes to rapid cancer cell proliferation. Metabolic tracing with (^{13}C)glycine revealed that consumed glycine was incorporated into purine nucleotides in rapidly proliferating LOX IMVI cells, but less so in slowly proliferating A498 cells (Fig. 4, A and B), which suggests that consumed glycine in part supports de novo purine synthesis in these cells. We also noted the incorporation of labeled glycine into cellular glutathione (fig. S10A). Analysis of previously performed large-scale chemosensitivity profiling across the 60 cancer cell lines (*7*) revealed that sensitivity to an inhibitor of glutathione synthesis, buthionine sulfoximine (*19*), was unrelated to proliferation rate (fig. S10B), whereas sensitivity to inhibitors of de novo purine biosynthesis—mycophenolate, tiazofurin, and alanosine (*20*)—was highly correlated with proliferation rate across the cell lines (fig. S10C). The use of glycine for de novo purine biosynthesis can occur by two mechanisms: direct incorporation into the purine backbone, or further oxidation by the glycine cleavage system (GCS) to yield one-carbon units for nucleotide synthesis and cellular methylation reactions (Fig. 4A). Because only carbon 2 of glycine is converted into one-carbon units by the GCS (Fig. 4A), we cultured LOX cells in 1-(^{13}C)glycine or 2-(^{13}C)glycine to differentiate between these two mechanisms (*21*). Consumed 2-(^{13}C)glycine did not give rise to doubly labeled purines (Fig. 4B), which indicates that the incorporation of consumed glycine into purine nucleotides does not involve oxidation by the GCS.

To better characterize the impact of glycine deprivation on cell cycle progression, we performed cell cycle analysis in HeLa cancer cells expressing a geminin–green fluorescent protein reporter and stained with DAPI (4′,6-diamidino-2-phenylindole). Silencing of SHMT2 (fig. S11A) and deprivation of extracellular glycine slowed proliferation in HeLa cells (fig. S11B), similar to other fast-proliferating cancer cells (Fig. 3G), and resulted in prolongation of the G_1 phase of the cell cycle (Fig. 4C and fig. S11C), whereas protein synthesis remained relatively intact (fig. S11D), consistent with a defect in nucleotide biosynthesis (*20*). Collectively, these results suggest that consumed glycine is used in part for de novo purine nucleotide biosynthesis in rapidly proliferating cells, and that antagonism of glycine metabolism results in prolongation of the G_1 phase, thus slowing proliferation.

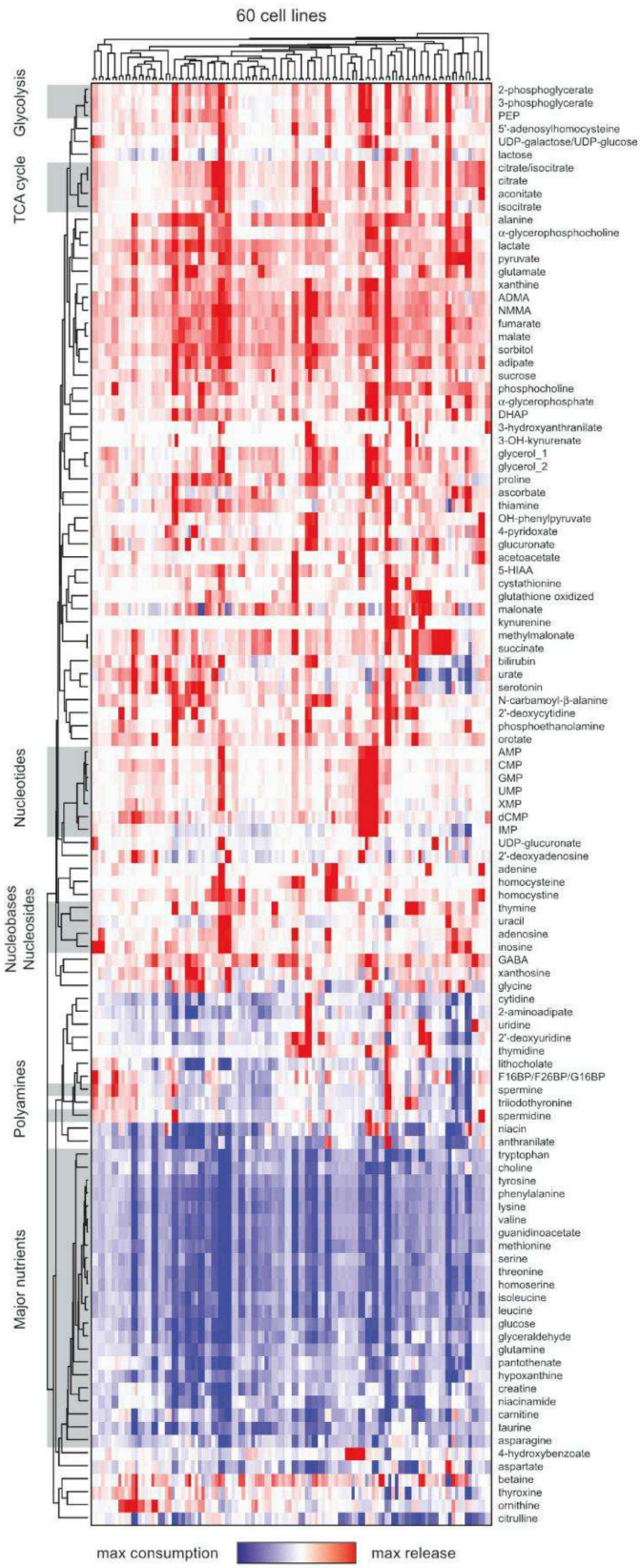

Fig. 2. CORE profiling across the NCI-60 cell lines. Hierarchical clustering of CORE profiles for 111 metabolites across 60 cancer cell lines in duplicate cultures, are shown; blue color indicates consumption, white indicates no change, and red color indicates release. Gray highlights indicate functionally related metabolites. In three rows, metabolites that cannot be distinguished are separated by slashes. Glycerol_1 and glycerol_2 represent independent LC-MS/MS measures.

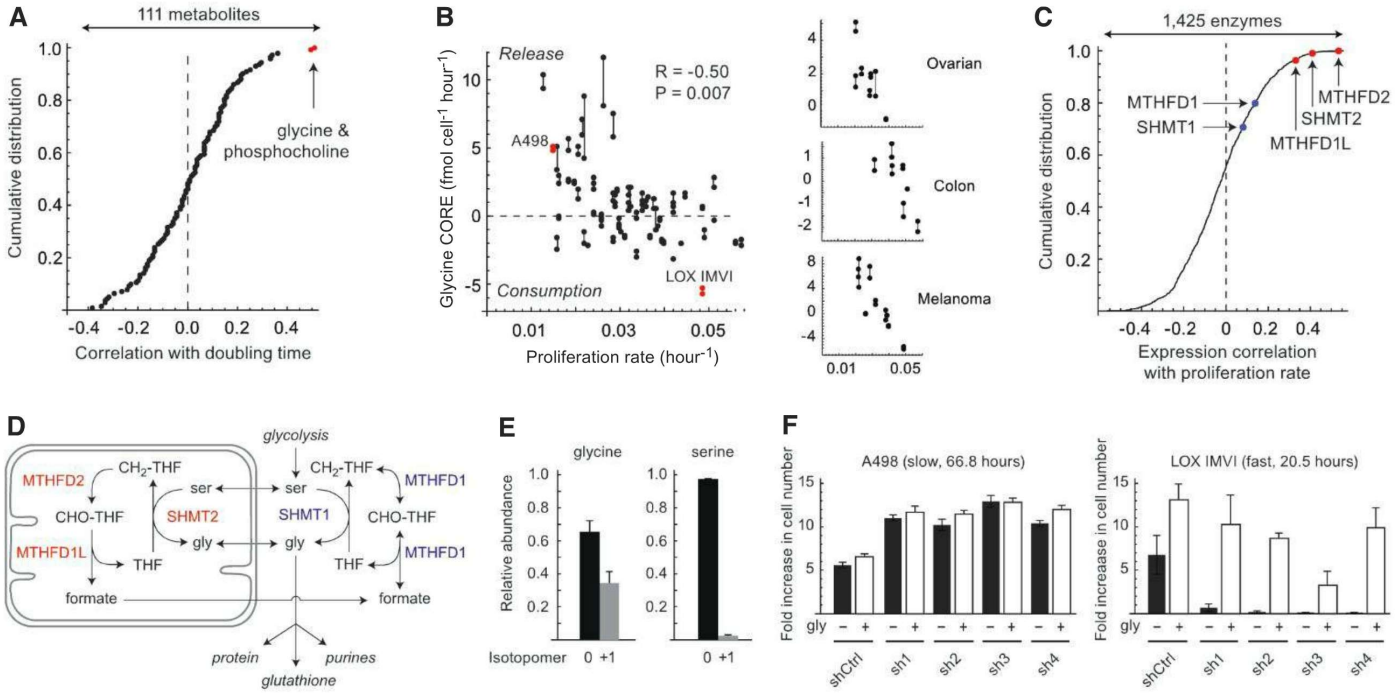

Fig. 3. Glycine consumption and synthesis are correlated with rapid cancer cell proliferation. (**A**) Distribution of Spearman correlations between 111 metabolite CORE profiles and proliferation rate across 60 cancer cell lines. Only metabolites highlighted in red are significant at $P < 0.05$, Bonferroni-corrected. (**B**) Glycine CORE versus proliferation rate across 60 cancer cell lines (left) and selected solid tumor types (right). Cell lines selected for follow-up experiments are highlighted in red. Joined data points represent replicate cultures. *P* values are Bonferroni-corrected for 111 tested metabolites. (**C**) Distribution of Spearman correlations between gene expression of 1425 metabolic enzymes and proliferation rates across 60 cancer cell lines. Highlighted are mitochondrial (red) and cytosolic (blue) glycine metabolism enzymes. (**D**) Schematic of cytosolic and mitochondrial glycine metabolism. (**E**) Abundance of unlabeled (0) and labeled (+1) intracellular glycine and serine in LOX IMVI cells grown on 100% extracellular (^{13}C)glycine. (**F**) Growth of A498 and LOX IMVI cells expressing shRNAs targeting SHMT2 (sh1-4) or control shRNA (shCtrl), cultured in the absence (solid bars) or presence (open bars) of glycine (gly). (**G**) Growth of 10 cancer cell lines expressing shRNA targeting SHMT2 (sh4) after 3 days, cultured in the absence (–gly, solid bars) or presence (+gly, open bars) of glycine. Cell number is presented as a ratio relative to +gly cells. Error bars in (E), (F), and (G) denote SD.

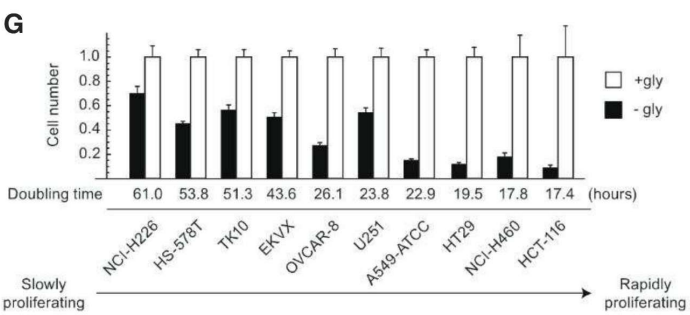

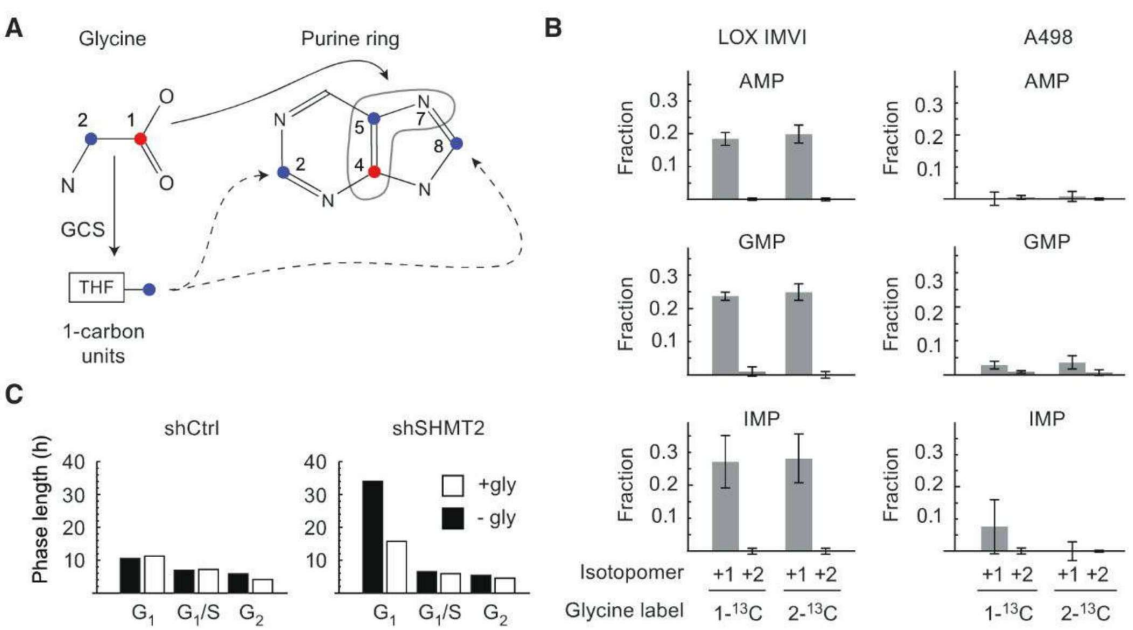

Fig. 4. Glycine metabolism supports de novo purine nucleotide biosynthesis. (**A**) Schematic of carbon incorporation into the purine ring from 1-(^{13}C)glycine or 2-(^{13}C)glycine. THF, tetrahydrofolate; GCS, glycine cleavage system. (**B**) Purine nucleotide +1 and +2 isotopomers in LOX IMVI or A498 cells grown on 100% 1-(^{13}C)glycine or 2-(^{13}C)glycine, as a fraction of the total intracellular metabolite pool. (**C**) Cell cycle analysis in HeLa cells expressing shRNA targeting SHMT2 (shSHMT2) or control shRNA (shCtrl), grown in the absence (–gly, solid bars) or presence (+gly, open bars) of glycine. Cell cycle phase length was calculated from the percentage of cells present in each cell cycle phase by geminin expression and DAPI staining (fig. S11C).

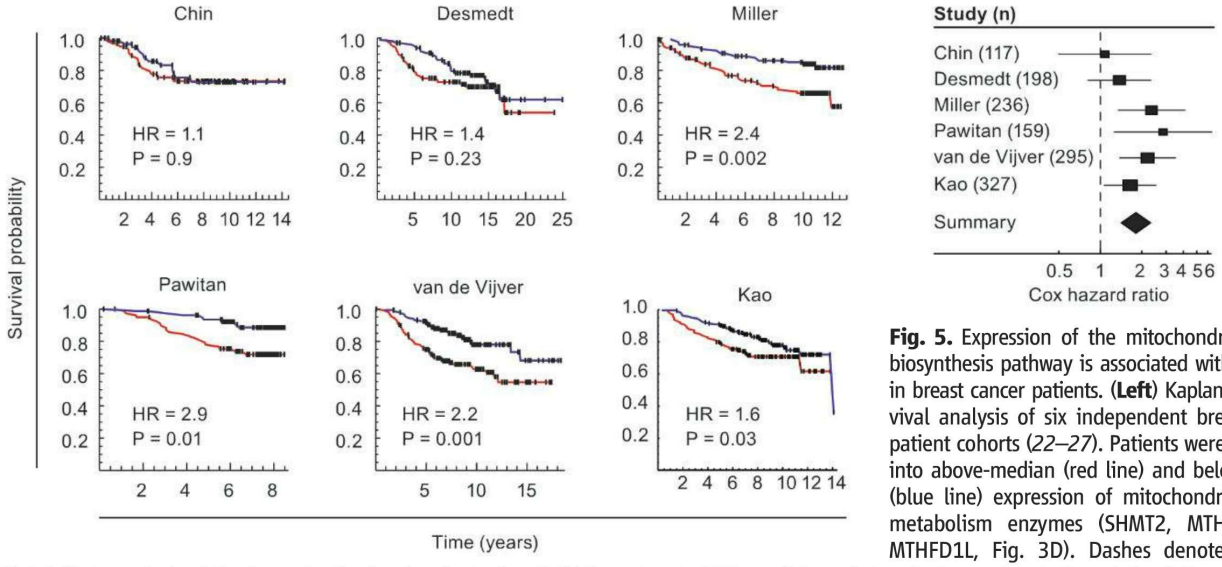

Fig. 5. Expression of the mitochondrial glycine biosynthesis pathway is associated with mortality in breast cancer patients. (**Left**) Kaplan-Meier survival analysis of six independent breast cancer patient cohorts (*22*–*27*). Patients were separated into above-median (red line) and below-median (blue line) expression of mitochondrial glycine metabolism enzymes (SHMT2, MTHFD2, and MTHFD1L, Fig. 3D). Dashes denote censored events. (**Right**) Meta-analysis of Cox hazard ratios for the six studies. Solid lines denote 95% confidence intervals; boxes denote the relative influence of each study over the results (inverse squared SE); diamond marks the overall 95% confidence interval.

To explore the potential relevance of glycine metabolism to cancer, we examined the expression of the mitochondrial glycine synthesis enzymes SHMT2, MTHFD2, and MTHFD1L (Fig. 3D) in previously generated microarray data sets across six independent large cohorts totaling more than 1300 patients with early-stage breast cancer followed for survival (*22*–*27*). We defined two groups of individuals: those with above-median gene expression of the mitochondrial glycine biosynthesis pathway, and those with below-median gene expression. Above-median expression of the mitochondrial glycine biosynthesis pathway was associated with greater mortality (Fig. 5), and a formal meta-analysis of all six data sets indicated an overall hazard ratio of 1.82 (95% confidence interval, 1.43 to 2.31; Fig. 5), comparable to those of other established factors, such as lymph node status and tumor grade, that contribute to poor cancer prognosis (*25*). The mitochondrial glycine synthesis enzyme SHMT2 alone was also significantly associated with mortality, whereas its cytosolic paralog SHMT1 was not (fig. S12). These data highlight the potential importance of mitochondrial glycine metabolism in human breast cancer.

Our atlas of cancer cell metabolism generated by CORE profiling may be broadly useful for investigating cellular metabolism and for identifying metabolite biomarkers of cancer and drug responsiveness. In our study, we used this atlas to probe the relation between metabolism and proliferation, thereby discovering an unexpected increased reliance on glycine metabolism in rapidly proliferating cancer cells—a phenotype that was not observed in rapidly proliferating nontransformed cells. Although we found that glycine is used for de novo purine nucleotide biosynthesis in rapidly proliferating LOX IMVI cells, alternative mechanisms—including the use of one-carbon groups derived from glycine for cellular methylation reactions (*17*)—may be important in other cancer cell types. Glycine and related metabolites (including sarcosine, serine, and threonine), or their associated metabolic pathways, have been identified as central to cancer metastasis (*5*), cellular transformation (*17*, *28*, *29*), and murine embryonic stem cell proliferation (*30*). Glycine metabolism may therefore represent a metabolic vulnerability in rapidly proliferating cancer cells that could in principle be targeted for therapeutic benefit.

References and Notes

1. P. C. Nowell, *Science* **194**, 23 (1976).
2. D. Hanahan, R. A. Weinberg, *Cell* **144**, 646 (2011).
3. M. R. Stratton, P. J. Campbell, P. A. Futreal, *Nature* **458**, 719 (2009).
4. P. P. Hsu, D. M. Sabatini, *Cell* **134**, 703 (2008).
5. A. Sreekumar *et al.*, *Nature* **457**, 910 (2009).
6. R. J. DeBerardinis *et al.*, *Proc. Natl. Acad. Sci. U.S.A.* **104**, 19345 (2007).
7. R. H. Shoemaker, *Nat. Rev. Cancer* **6**, 813 (2006).
8. J. Allen *et al.*, *Nat. Biotechnol.* **21**, 692 (2003).
9. O. Shaham *et al.*, *Proc. Natl. Acad. Sci. U.S.A.* **107**, 1571 (2010).
10. P. M. O'Connor *et al.*, *Cancer Res.* **57**, 4285 (1997).
11. R. Katz-Brull, H. Degani, *Anticancer Res.* **16**, 1375 (1996).
12. N. C. Duarte *et al.*, *Proc. Natl. Acad. Sci. U.S.A.* **104**, 1777 (2007).
13. See supplementary materials on *Science* Online.
14. A. S. Tibbetts, D. R. Appling, *Annu. Rev. Nutr.* **30**, 57 (2010).
15. M. A. Nikiforov *et al.*, *Mol. Cell. Biol.* **22**, 5793 (2002).
16. F. Kao, L. Chasin, T. T. Puck, *Proc. Natl. Acad. Sci. U.S.A.* **64**, 1284 (1969).
17. W. C. Zhang *et al.*, *Cell* **148**, 259 (2012).
18. H. Patel, E. D. Pietro, R. E. MacKenzie, *J. Biol. Chem.* **278**, 19436 (2003).
19. O. W. Griffith, A. Meister, *J. Biol. Chem.* **254**, 7558 (1979).
20. S. P. Linke, K. C. Clarkin, A. Di Leonardo, A. Tsou, G. M. Wahl, *Genes Dev.* **10**, 934 (1996).
21. T. F. Fu, J. P. Rife, V. Schirch, *Arch. Biochem. Biophys.* **393**, 42 (2001).
22. K. Chin *et al.*, *Cancer Cell* **10**, 529 (2006).
23. C. Desmedt *et al.*; TRANSBIG Consortium, *Clin. Cancer Res.* **13**, 3207 (2007).
24. Y. Pawitan *et al.*, *Breast Cancer Res.* **7**, R953 (2005).
25. M. J. van de Vijver *et al.*, *N. Engl. J. Med.* **347**, 1999 (2002).
26. K. J. Kao, K. M. Chang, H. C. Hsu, A. T. Huang, *BMC Cancer* **11**, 143 (2011).
27. L. D. Miller *et al.*, *Proc. Natl. Acad. Sci. U.S.A.* **102**, 13550 (2005).
28. R. Possemato *et al.*, *Nature* **476**, 346 (2011).
29. J. W. Locasale *et al.*, *Nat. Genet.* **43**, 869 (2011).
30. J. Wang *et al.*, *Science* **325**, 435 (2009).

Acknowledgments: We thank T. R. Golub, O. Shaham, S. B. Vafai, and L. Strittmatter for scientific discussions and feedback; X. Cao for assistance with glucose and lactate measurements; the Broad Institute RNAi Platform for shRNA reagents; D. Gomez-Cabrero for assistance with multidimensional scaling; A. Ploner and P. Dickman for assistance with survival analysis; W. C. Kopp, S. L. Holbeck, K. Gill, and P. Sellers of the Developmental Therapeutics Program, National Cancer Institute, for reagents and assistance with cell culture; and T. Hasaka of the Broad Institute for assistance with imaging studies. Supported by NIH grant K08HL107451 (M.J.), a postdoctoral scholarship from the Knut & Alice Wallenberg Foundation and Stockholm County (SLL) grant 01626-2009 (R.N.), a Special Fellow award from the Leukemia & Lymphoma Society (S.S.), and NIH grant R01DK081457 and a gift from the Nestle Research Center (V.K.M.). The full metabolite CORE profiling data set is available in the supplementary materials as well as through the NCI Molecular Targets data repository (http://dtp.nci.nih.gov/mtargets/download.html). M.J. and R.N. conceived and performed all experiments, collected and analyzed experimental data, and prepared the manuscript. S.S. assisted with cell culture, RNAi, and T lymphocyte experiments. N.M. and T.K. assisted with cell culture and imaging-based experiments. A.L.S. and C.B.C. performed LC-MS/MS profiling experiments and provided experimental feedback. R.K. and M.W.K. performed cell cycle studies. V.K.M. conceived all experiments, reviewed all experimental data, and prepared the manuscript. All authors have discussed the results and reviewed the manuscript. All authors declare no competing financial interests.

Supplementary Materials

www.sciencemag.org/cgi/content/full/336/6084/1040/DC1
Materials and Methods
Figs. S1 to S12
Table S1
References (*31*–*43*)
Database S1

8 July 2011; accepted 23 March 2012
10.1126/science.1218595

FKF1 Conveys Timing Information for CONSTANS Stabilization in Photoperiodic Flowering

Young Hun Song,[1] Robert W. Smith,[2] Benjamin J. To,[1] Andrew J. Millar,[2] Takato Imaizumi[1]*

Plants use day-length information to coordinate flowering time with the appropriate season to maximize reproduction. In *Arabidopsis*, the long day–specific expression of CONSTANS (CO) protein is crucial for flowering induction. Although light signaling regulates CO protein stability, the mechanism by which CO is stabilized in the long-day afternoon has remained elusive. Here, we demonstrate that FLAVIN-BINDING, KELCH REPEAT, F-BOX 1 (FKF1) protein stabilizes CO protein in the afternoon in long days. FKF1 interacts with CO through its LOV domain, and blue light enhances this interaction. In addition, FKF1 simultaneously removes CYCLING DOF FACTOR 1 (CDF1), which represses *CO* and *FLOWERING LOCUS T* (*FT*) transcription. Together with *CO* transcriptional regulation, FKF1 protein controls robust *FT* mRNA induction through multiple feedforward mechanisms that accurately control flowering timing.

Plants monitor seasonal day-length changes by sensing light conditions at a specific time of day to regulate flowering (*1*). In *Arabidopsis*, the day length–specific expression of FLOWERING LOCUS T (FT) protein is crucial for the proper timing of flowering (*2*–*4*). *FT* transcription is directly activated by CONSTANS (CO) transcription factor (*5*), which is stabilized only in the afternoon of long days (*6*). The regulation of long day–specific CO protein expression is one of the most crucial mechanisms for photoperiodic flowering (*2*–*4*). Light signals perceived by phytochrome A (phyA) and cryptochrome (cry) photoreceptors stabilize CO protein during long days (*6*). However, the timing mechanism by which CO protein is stabilized specifically in the long-day afternoon was not well understood, as both phyA and cry proteins are expressed at similar levels throughout each long day (*7*). Previously we showed that FKF1 (FLAVIN-BINDING, KELCH REPEAT, F-BOX 1) regulates *CO* transcription (*8*–*10*). Here, we demonstrate that FKF1 also controls *FT* transcription by stabilizing CO protein and simulta-

[1]Department of Biology, University of Washington, Seattle, WA 98195, USA. [2]School of Biological Sciences and SynthSys, University of Edinburgh, Edinburgh EH9 3JD, UK.

*To whom correspondence should be addressed. E-mail: takato@u.washington.edu

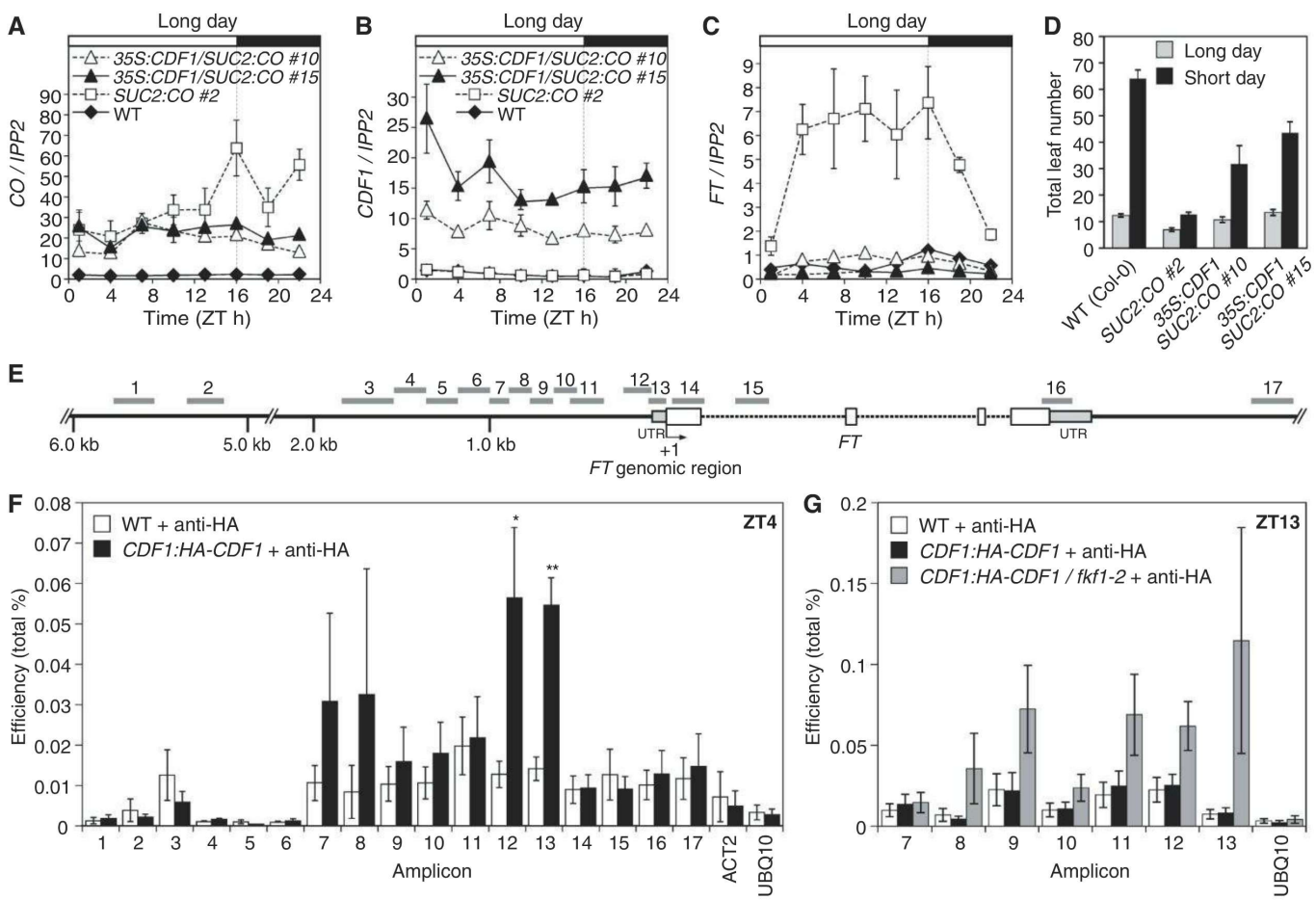

Fig. 1. CDF1 represses *FT* transcription. (**A** to **C**) Gene expression analysis for *CO* (A), *CDF1* (B), and *FT* (C) in wild-type (WT), *SUC2:CO-HA*, and *35S:CDF1/SUC2:CO-HA* plants grown in long days. *IPP2* expression was used as a control. Experiments were repeated three times independently. (**D**) Flowering phenotypes of plants overexpressing *CO* and *CDF1*. Data are means ± SD of 16 plants. (**E**) Schematic drawing of the *FT* genomic region and the amplicon locations for ChIP experiments. (**F** and **G**) ChIP analysis with 10-day-old plants grown in long days. *ACT2* and *UBQ10* loci were used as controls. (F) WT and *CDF1:HA-CDF1* plants were harvested in the morning (ZT4). Means ± SEM were calculated from seven independent replicates. *$P < 0.05$, **$P < 0.01$ (one-tailed *t* test). (G) WT, *CDF1:HA-CDF1*, and *CDF1:HA-CDF1/fkf1-2* plants were harvested in the afternoon (ZT13). Data were calculated from five independent replicates.

neously degrading *FT* repressors in the long-day afternoon.

Our mathematical gene-circuit model (*11*) predicted that FKF1 protein would induce *FT* expression independently of *CO* transcriptional regulation; we therefore examined the possibility of FKF1-dependent *FT* gene regulation. Because FKF1 degrades the transcription factor CDF1 (CYCLING DOF FACTOR 1) (*9*, *10*), we hypothesized that if CDF1 acts as a *FT* transcriptional repressor, the removal of CDF1 protein might regulate *FT* expression. Because FKF1 and CO proteins are known to interact in yeast (*12*), a second possibility was that FKF1 regulates CO protein activity. To investigate additional roles of FKF1 protein in photoperiodic flowering, we tested these two possibilities.

To test whether FKF1 regulates *FT* transcription through CDF1 protein stability regulation, we asked whether CDF1 directly regulates *FT* transcription. *CDF1* mRNA was overexpressed in transgenic *SUC2:CO-HA* plants in which hemagglutinin (HA)–tagged CO was expressed by a phloem-specific *SUCROSE-PROTON SYMPORTER2* (*SUC2*) promoter. Even though *CO* mRNA levels were similar in these lines (Fig. 1A and figs. S1 and S2), *FT* mRNA levels were reduced in the lines that had higher *CDF1* expression (Fig. 1, B and C, and figs. S1 and S2). These plants flowered later than those of the *SUC2:CO-HA* line (Fig. 1D). These results indicate that CDF1 protein represses *FT* transcription independently of *CO* transcription.

We next examined whether CDF1 protein associates with the *FT* promoter. The amplicons of *FT* promoter regions 7, 8, 12, and 13 were enriched in *CDF1:HA-CDF1* samples (*9*) relative to wild-type samples harvested at zeitgeber time ZT4 (i.e., 4 hours after light onset on a given day) (Fig. 1, E and F); these results indicated that CDF1 binds to the *FT* promoter regions in the morning.

As both FKF1 and GIGANTEA (GI) proteins exist on the *FT* promoter (*13*), we speculated that FKF1 could remove CDF1 on the *FT* promoter during the afternoon. We reasoned that in the absence of FKF1, more CDF1 proteins might remain associated with the *FT* promoter in the afternoon. Our chromatin immunoprecipitation (ChIP) assay revealed that HA-CDF1 associated near the *FT* transcription start site in the afternoon only in the *fkf1* mutant background (Fig. 1G).

FKF1 regulates the stability of CDF1 homologs that have overlapping function with CDF1 (*14*); we therefore tested whether other CDF proteins also repress *FT* transcription. Because *CO* mRNA levels in the *cdf1 cdf2 cdf3 cdf5* quadruple mutant are higher than in wild-type plants (*14*), we compared *FT* expression levels between the *cdf* quadruple mutant and the *CO:HA-CO* plant in which *CO* levels were elevated using the *CO* promoter. Even though *CO* mRNA levels in the quadruple mutant were lower than in the *CO:HA-CO* plant, *FT* mRNA levels in the mutant were higher than in the *CO:HA-CO* line (fig. S3). As the *FT* mRNA levels in the *cdf1* single mutant resemble those in wild-type plants (*9*), our results indicate that these CDF proteins may redundantly repress *FT* transcription. Taken together with previous results (*9*, *14*), it is likely that FKF1 degrades CDF1 and possibly other CDF proteins to regulate *FT* expression.

Next, we examined whether there is an interaction between FKF1 and CO proteins. Using a *Nicotiana benthamiana* expression system (*15*), we coimmunoprecipitated HA-FKF1 protein with tandem affinity purification (TAP)–tagged CO (CO-TAP) (Fig. 2A). The FKF1-CO interaction was confirmed by reciprocal coimmunoprecipitation assays (fig. S4). We then analyzed the interaction in transgenic *Arabidopsis* plants expressing functional 3xFLAG and 6xHis-tagged CO (CO-3F6H) and HA-FKF1 (fig. S5). HA-FKF1 proteins were coimmunoprecipitated with CO-3F6H proteins (Fig. 2B), indicating that FKF1 and CO proteins can interact in vivo.

To identify the interaction site of FKF1 with CO, we coexpressed HA-tagged FKF1 domains (LOV, LOV+F, F+Kelch, and Kelch) with CO-TAP in *N. benthamiana*. HA-LOV and HA-LOV+F peptides interacted with CO-TAP protein (Fig. 2C). In addition, a small but reproducible

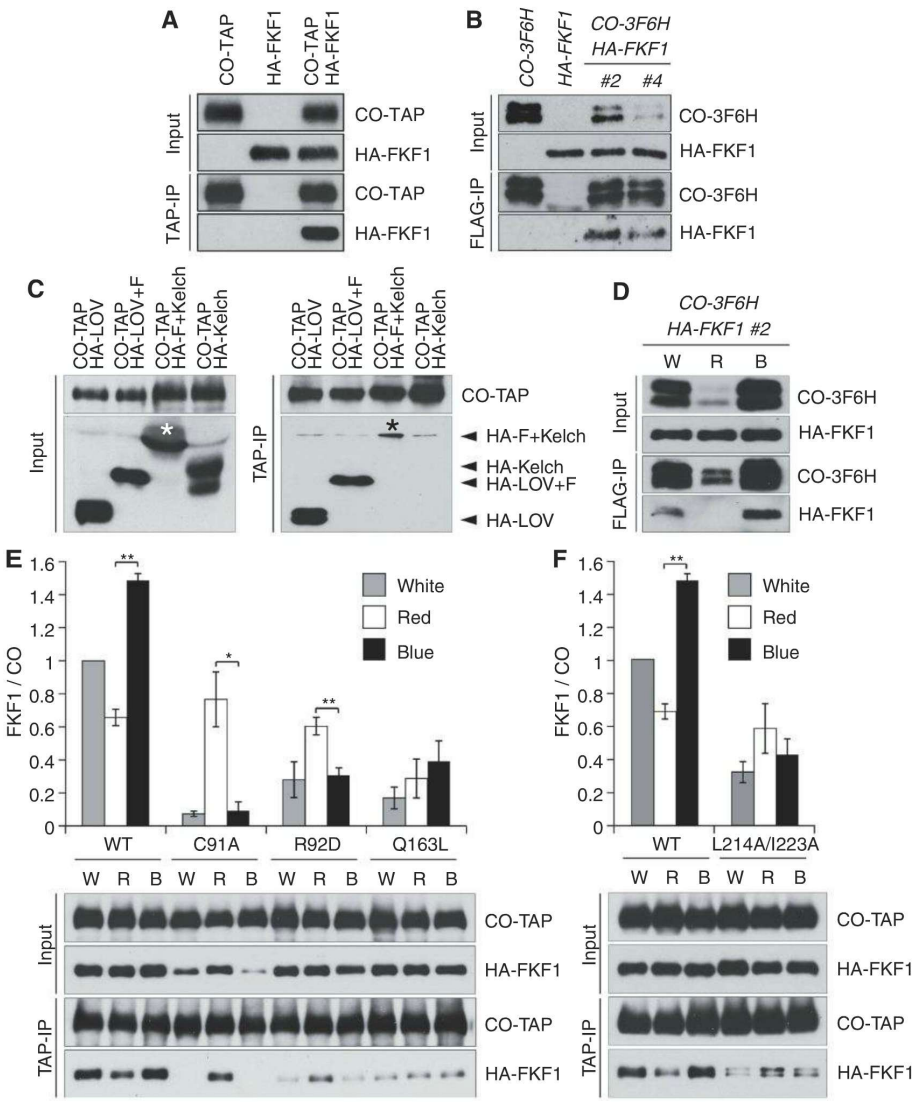

Fig. 2. FKF1 interacts with CO in a blue light–enhanced manner. (**A**) The interaction between FKF1 and CO proteins in *N. benthamiana*. (**B**) In vivo FKF1-CO protein interaction. Long day–grown plants were harvested at ZT13 when they were 10 days old. (**C**) Mapping the CO binding site of FKF1. LOV+F contains LOV and F-box domains; F+Kelch contains F-box and Kelch repeat domains. Asterisks indicate HA-F+Kelch proteins. (**D**) Blue light–enhanced FKF1-CO interaction. Long day–grown plants were transferred to different light conditions at day 10 and harvested at ZT13. (**E** and **F**) FKF1 and CO interaction under different light conditions. Wild-type and mutant forms of HA-FKF1 and CO-TAP were expressed in *N. benthamiana*. Quantified values are relative to the FKF1-CO interaction in white light for each combination. Means ± SEM were calculated from three to six independent samples. $*P < 0.05$, $**P < 0.01$ (one-tailed *t* test).

amount of HA-F+Kelch peptide was coimmunoprecipitated with CO-TAP (Fig. 2C). These results suggest that the LOV domain is sufficient for CO binding and that the F-box region may also participate in this interaction.

Because the interaction of FKF1 and GI occurs in a blue light–dependent manner (*10*), we investigated the blue light dependency of the FKF1-CO protein interaction. More HA-FKF1 was coimmunoprecipitated with CO-3F6H under blue light than red light in vivo (Fig. 2D). However, this could be due to differences in CO protein levels under these conditions (Fig. 2D). As CO and FKF1 protein levels were similar in these conditions in *N. benthamiana*, we assessed the potential light dependency of the interaction. The amount of the FKF1-CO interaction was significantly greater in blue light than red light (Fig. 2E).

If the LOV domain is responsible for blue light–enhanced CO binding, we speculated that the photochemically blind LOV mutations $Cys^{91} \rightarrow$ Ala (C91A), $Arg^{92} \rightarrow$ Asp (R92D), and $Gln^{163} \rightarrow$ Leu (Q163L) should alter the interaction (*10*). These LOV mutations weakened the interaction under blue and white light (Fig. 2E), indicating that blue light perceived by the LOV domain enhanced the interaction. As our results indicated the involvement of F-box with CO binding (Fig. 2C), we analyzed whether a functional F-box is important for binding. Two mutations [$Leu^{214} \rightarrow$ Ala (L214A) and $Ile^{223} \rightarrow$ Ala (I223A)] that eliminate the ability of F-box to bind to *Arabidopsis* Skp1-like (ASK1) proteins (*16*) were introduced to the FKF1 F-box. The F-box mutations also attenuated blue-light effects on the interaction (Fig. 2F), which suggested that the formation of the SCF^{FKF1} complex facilitates the FKF1-CO protein interaction.

To investigate the effect of the FKF1-CO interaction, we analyzed the effect of *fkf1* mutation on CO activity. Because FKF1 affects *CO* transcription (*8*), we used lines in which *CO* mRNA is constitutively expressed (Fig. 3A and figs. S6A and S7). In the *CO*-overexpressing lines, having

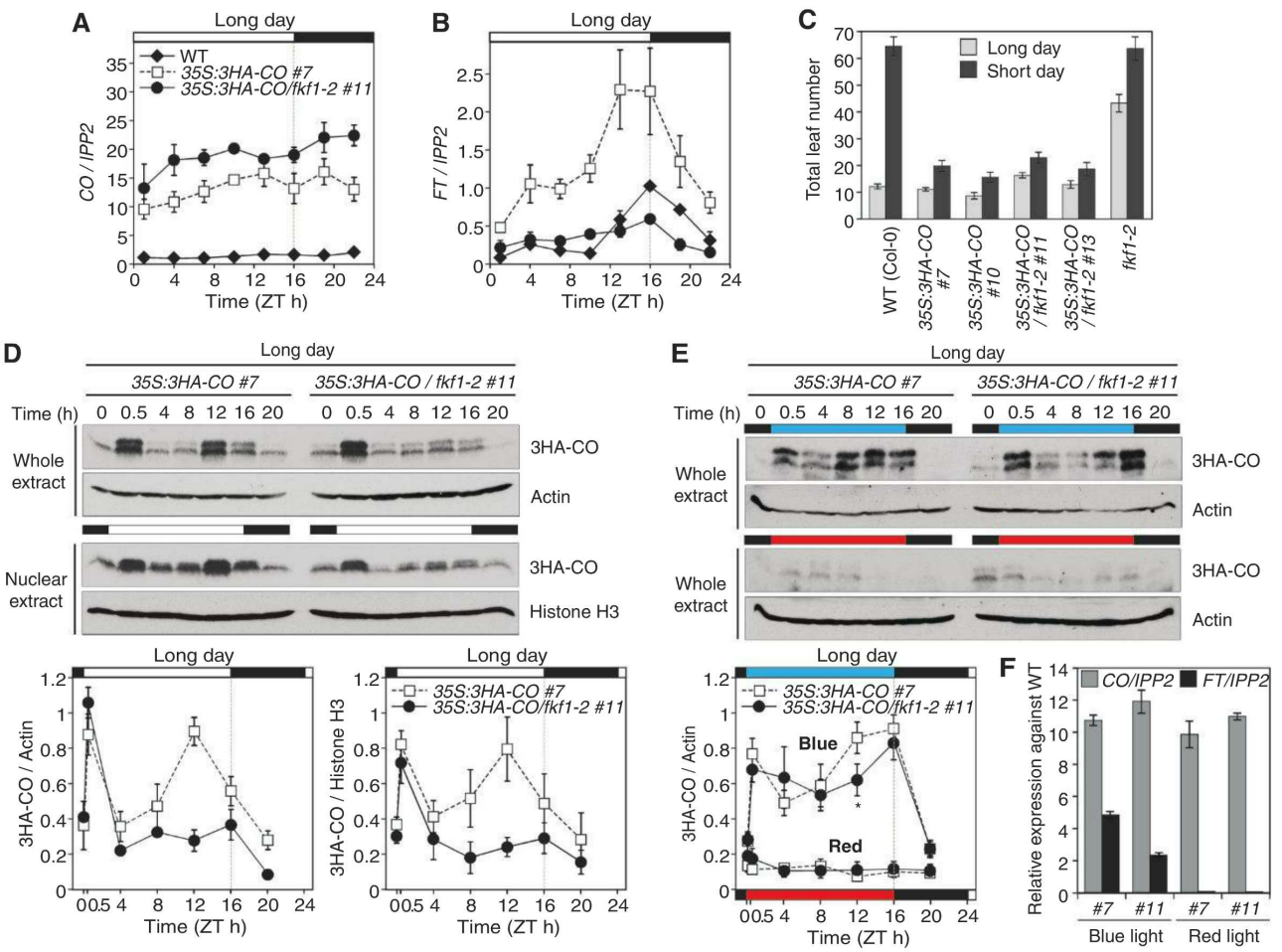

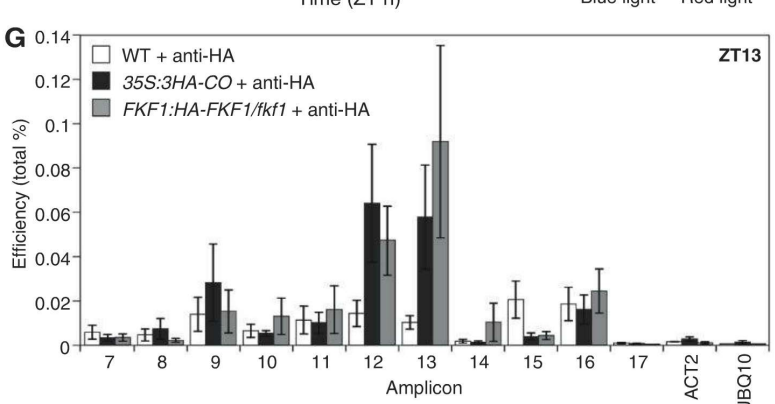

Fig. 3. FKF1 regulates the light phase of CO protein expression. (**A** and **B**) Gene expression levels of *CO* (A) and *FT* (B) in WT, *35S:3HA-CO*, and *35S:3HA-CO/fkf1-2* plants in long days. (**C**) Flowering time of *CO* overexpressors in WT and *fkf1* mutant. Data are means ± SD of at least 13 plants. (**D** and **E**) FKF1 regulates CO protein stability. Actin and histone H3 proteins were used as controls. Plants were grown for 10 days in long days (D) and transferred into blue- and red-light conditions on day 10 (E). (**F**) *CO* and *FT* mRNA levels in plants shown in (E). Experiments in (A), (B), and (D) to (F) were repeated three times independently. (**G**) Association of FKF1 and CO with *FT* promoter. Plants were grown for 10 days in long days and collected in the afternoon (ZT13). Means ± SEM were calculated from five independent replicates.

the *fkf1* mutation reduced *FT* mRNA levels (Fig. 3B and figs. S6B and S7). *CO* overexpressors in the *fkf1* mutant flowered later than *35S:3HA-CO* plants in long days (Fig. 3C). We observed a similar *fkf1* effect on *FT* mRNA expression when *CO* mRNA levels were elevated in the tissues where *CO* is expressed (fig. S8).

The timing of FKF1 protein expression under light coincides with CO protein stabilization (*6*, *8*). Because the *fkf1* mutation reduced CO activity (Fig. 3B), we speculated that FKF1 may stabilize CO protein. We analyzed the diurnal CO protein profiles in *fkf1*. During long days, CO protein peaks at ZT0.5 and ZT12 in *35S:CO* plants (*6*). Our *35S:3HA-CO* lines showed a similar daily CO protein pattern, although there were doublet bands corresponding to the 3HA-CO proteins (Fig. 3D and fig. S6C), as also observed previously (*17*). In *fkf1*, CO protein fell to low levels in the afternoon (ZT12 to ZT16), although the ZT0.5 CO peak was still present (Fig. 3D and fig. S6C). We found FKF1 in both cytosolic and nuclear fractions (fig. S9). The profile of CO abundance in the nucleus was similar to that in the whole protein extracts (Fig. 3D and fig. S6C), demonstrating that FKF1 stabilizes CO protein in both the cytoplasm and nucleus. In short days, CO levels were extremely low (*6*) (fig. S10A), and there were no obvious differences in CO protein expression (fig. S10B) between wild-type and *fkf1* backgrounds. These findings imply that rhythmic FKF1 expression may determine the timing of stabilizing CO in long days.

Blue light stabilizes CO protein in long days (*6*), and our data suggest that blue light enhances the FKF1-CO interaction. We analyzed the daily CO protein profiles under blue- and red-light conditions. CO protein was stable under blue light. The CO protein level was slightly but significantly lower in the *fkf1* background at ZT12 (Fig. 3E), indicating that FKF1's contribution is restricted to the afternoon. The CO protein profiles in blue light resemble those in the white light–grown *phyB* mutant (*6*), which suggests that without phyB-dependent destabilization of CO, blue light perceived by cryptochromes can stabilize CO protein throughout the day. In addition, the *fkf1* mutation reduced *FT* mRNA levels without changing *CO* mRNA levels under blue light (Fig. 3F). Under red light, CO protein was unstable in all *CO* overexpressors (Fig. 3E). This is most likely due to the activation of phyB signaling, which degrades CO protein (*6*). Together with the previous observation (*6*), these results suggest that the antagonistic balance between blue and red light determines CO protein levels.

Because FKF1 stabilizes CO protein even in the nucleus (Fig. 3D), we postulated that FKF1 and CO interactions might also occur on the *FT* promoter. We found that both FKF1 and CO proteins associated near the *FT* transcription start site (*13*) (Fig. 3G), where CORE (CO-responsive element) sequences exist (*18*). These results indicate that FKF1 may interact with CO protein on the *FT* promoter.

Our results imply that FKF1 has at least three different roles in the regulation of *FT* expression (fig. S11): (i) FKF1 regulates *CO* transcription by degrading CDF proteins (*9*, *10*, *14*). (ii) Because CDF proteins are also *FT* repressors, the same FKF1-mediated degradation mechanism may also regulate *FT* transcription. (iii) FKF1 is involved in the stabilization of CO protein in the long-day afternoon, increasing the expression of *FT*.

We refined our previous model (*11*) by including these biochemical functions of FKF1 (*15*). The new mathematical model focuses on the regulation of *CO* and *FT* mRNA and CO protein (Fig. 4A). FKF1 and GI modulate the CDF1 protein, which represses *CO* and *FT* (Fig. 4A) and represents the functions of all CDF proteins in the model. Falling CDF1 protein levels relieve repression of *CO* at the end of long days in the simulated wild type, leading to the characteristic shoulder in the mRNA profile around ZT13 (Fig. 4B and fig. S12). The simulated *fkf1* mutant reduces *CO* transcript levels by 59% at ZT13 (Fig. 4B). In the model, CO is stabilized by FKF1 in a light-dependent manner (fig. S12). The simulated *fkf1* mutant both fails to degrade CDF1 and fails to stabilize CO (fig. S13), reducing the amount of *FT* over one cycle (FT_{area}) by ~78% of wild-type levels in long days (Fig. 4C), similar to the *FT* levels in *fkf1* (*8*). In addition, the model recreated the altered *FT* profiles of *CO* overexpression lines shown in Figs. 1 and 3 (figs. S14 and S15). These results indicate that the two FKF1-dependent mechanisms described are sufficient to explain the observed *CO* and *FT* mRNA profiles.

Using the model, we estimated the importance of each FKF1 function under long-day conditions by simulating partial loss-of-function mutants that are not accessible genetically. If FKF1 could not degrade CDF1 protein but stabilized CO protein [mutant designated Δ(1)], the simulated FT_{area} decreased by ~22% from the wild-type levels (Fig. 4D). If FKF1 degraded CDF1 but could not stabilize CO protein [mutant Δ(2)], the simulated FT_{area} decreased by ~51% (Fig. 4D). Although the exact balance varies among model versions (fig. S16), both mechanisms were required to explain the very low levels of *FT* observed in full *fkf1* mutants (fig. S13H).

Our results suggest that FKF1 regulates *FT* expression through a multiple-feedforward motif (Fig. 4A) that can enhance signal detection (*19*). Photoperiod sensing depends on correctly timed operation of this motif. Our data indicate that the circadian clock conveys time information for stabilizing CO protein through the timing of FKF1 expression. We therefore investigated the impact of removing circadian control from these two components, via constitutive expression of *CO* and *FKF1*, while *GI* and *CDF1* mRNA expression remained rhythmic. Our model predicted that this would stabilize CO protein (fig. S17A) and alter the *FT* mRNA profile, with a near-linear rise during the daytime, and also increase *FT* expression levels depending on FKF1 protein levels (fig. S17B). To verify our model predictions, we analyzed CO protein and *FT* mRNA expression in *35S:3HA-CO/35S:HA-FKF1* lines (fig. S18). Constitutive FKF1 protein expression stabilized CO protein even during the early part of the day (fig. S18). In addition, *FT* expression in these lines increased linearly throughout the day and *FT* levels were higher in the line with a higher *FKF1* level (fig. S18). These results vali-

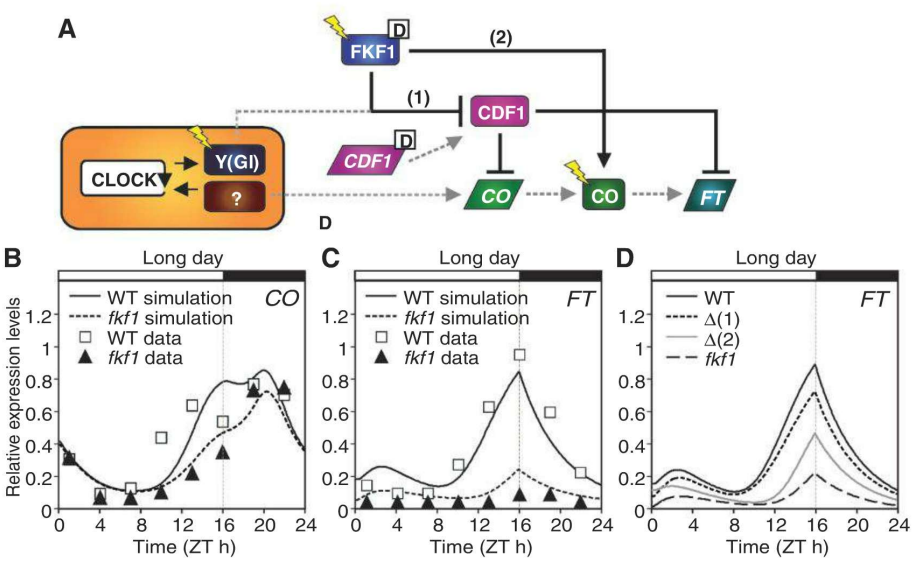

Fig. 4. Simulation of the photoperiod sensor. (**A**) Schematic of the new model incorporating the roles of CDF1 and FKF1 in regulating *FT*. Parallelograms, rectangles, and flashes represent mRNAs, proteins, and light inputs, respectively; D indicates components input as experimental data (*15*) (fig. S19). Solid lines indicate FKF1-dependent mechanisms. The rest of the interactions are shown as dotted lines. (**B** and **C**) Simulations of *CO* (B) and *FT* (C) mRNA are plotted against experimental data (*8*) for wild-type plants and *fkf1* mutants in long days. (**D**) Effects of partial loss of FKF1 function in *FT* induction. The mutants Δ(1) and Δ(2) are numbered according to the two FKF1 functions shown in (A), which were respectively deleted to simulate *FT* patterns.

dated our prediction and indicate the importance of circadian regulation of *FKF1* expression for day length–dependent CO protein stabilization.

The FKF1 photoperiod sensor uses multiple, partially redundant switches to allow strong activation in long days. As the Sun rises higher in the sky each day when spring approaches, plants can sense the increased intensity in the blue-light range of the spectrum each afternoon through multiple photoreceptors, including FKF1. The complexity of this mechanism even in a temperate species such as *Arabidopsis* suggests that it has the flexibility to regulate successful reproduction in a wide range of environments.

References and Notes

1. B. Thomas, D. Vince-Prue, *Photoperiodism in Plants* (Academic Press, San Diego, CA, ed. 2, 1997).
2. Y. Kobayashi, D. Weigel, *Genes Dev.* **21**, 2371 (2007).
3. A. de Montaigu, R. Tóth, G. Coupland, *Trends Genet.* **26**, 296 (2010).
4. R. Amasino, *Plant J.* **61**, 1001 (2010).
5. A. Samach *et al.*, *Science* **288**, 1613 (2000).
6. F. Valverde *et al.*, *Science* **303**, 1003 (2004).
7. T. Mockler *et al.*, *Proc. Natl. Acad. Sci. U.S.A.* **100**, 2140 (2003).
8. T. Imaizumi, H. G. Tran, T. E. Swartz, W. R. Briggs, S. A. Kay, *Nature* **426**, 302 (2003).
9. T. Imaizumi, T. F. Schultz, F. G. Harmon, L. A. Ho, S. A. Kay, *Science* **309**, 293 (2005).
10. M. Sawa, D. A. Nusinow, S. A. Kay, T. Imaizumi, *Science* **318**, 261 (2007).
11. J. D. Salazar *et al.*, *Cell* **139**, 1170 (2009).
12. Y. Fukamatsu *et al.*, *Plant Cell Physiol.* **46**, 1340 (2005).
13. M. Sawa, S. A. Kay, *Proc. Natl. Acad. Sci. U.S.A.* **108**, 11698 (2011).
14. F. Fornara *et al.*, *Dev. Cell* **17**, 75 (2009).
15. See supplementary materials on *Science* Online.
16. L. Q. Han, M. Mason, E. P. Risseeuw, W. L. Crosby, D. E. Somers, *Plant J.* **40**, 291 (2004).
17. Z. Zuo, H. Liu, B. Liu, X. Liu, C. Lin, *Curr. Biol.* **21**, 841 (2011).
18. S. B. Tiwari *et al.*, *New Phytol.* **187**, 57 (2010).
19. U. Alon, *Nat. Rev. Genet.* **8**, 450 (2007).

Acknowledgments: We thank S. Harmer, K. Torii, D. Nusinow, S. Ito, and H. Kinmonth-Schultz for critical reading of the manuscript and G. Coupland for providing *cdf* quadruple mutant. Supported by the Next Generation Biogreen 21 program (SSAC grant PJ008109) (Y.H.S.), UK Biotechnology and Biological Sciences Research Council (BBSRC) grants BB/F59011/1 and BB/F005237/1 (R.W.S.), and NIH grant GM079712 (T.I.). SynthSys is partly supported by BBSRC grant BB/G019621 and by the UK Engineering and Physical Sciences Research Council.

Supplementary Materials

www.sciencemag.org/cgi/content/full/336/6084/1045/DC1
Materials and Methods
Figs. S1 to S20
Table S1
References (*20*–*40*)

25 January 2012; accepted 13 April 2012
10.1126/science.1219644

Kinship Categories Across Languages Reflect General Communicative Principles

Charles Kemp[1]* and Terry Regier[2]

Languages vary in their systems of kinship categories, but the scope of possible variation appears to be constrained. Previous accounts of kin classification have often emphasized constraints that are specific to the domain of kinship and are not derived from general principles. Here, we propose an account that is founded on two domain-general principles: Good systems of categories are simple, and they enable informative communication. We show computationally that kin classification systems in the world's languages achieve a near-optimal trade-off between these two competing principles. We also show that our account explains several specific constraints on kin classification proposed previously. Because the principles of simplicity and informativeness are also relevant to other semantic domains, the trade-off between them may provide a domain-general foundation for variation in category systems across languages.

Concepts and categories vary across cultures but may nevertheless be shaped by universal constraints (*1*–*4*). Cross-cultural studies have proposed universal constraints that help to explain how colors (*5*, *6*), plants, animals (*7*, *8*), and spatial relations (*9*, *10*) are organized into categories. Kinship has traditionally been a prominent domain for studies of this kind, and researchers have described many constraints that help to predict which of the many logically possible kin classification systems are encountered in practice (*11*–*15*). Typically these constraints are not derived from general principles, although it is often suggested that they are consistent with cognitive and functional considerations (*2*, *11*–*13*, *15*). Here, we show that major aspects of kin classification follow directly from two general principles: Categories tend to be simple, which minimizes cognitive load, and to be informative, which maximizes communicative efficiency. Principles like these have been discussed in other contexts by previous researchers (*16*–*19*). For example, Zipf suggested that word-frequency distributions achieve a trade-off between simplicity and communicative precision (*20*, *21*), Hawkins (*22*) has suggested that grammars are shaped by a trade-off between simplicity and communicative efficiency, and Rosch has suggested that category systems "provide maximum information with the least cognitive effort" [p. 190 of (*23*)].

Figure 1A shows a simple communication game that helps to illustrate how kin classification systems are shaped by the principles of simplicity and informativeness. The speaker has a specific relative in mind and utters the category label for that relative. Upon hearing this category label, the hearer must guess which relative the speaker had in mind. The speaker and hearer communicate through a shared system of categories that specifies a category label for each relative. This system is simple to the extent that it can be concisely mentally represented and therefore easily learned and remembered (*11*). The system is informative to the extent that it supports successful communication. The principles of simplicity and informativeness trade off against each other (*20*, *21*, *23*). A system with a single category that includes all possible relatives would be simple but uninformative because this category does not help to pick out specific relatives. A system with a different name for each relative would be complex but highly informative because it picks out individual relatives perfectly.

Understanding how simplicity and informativeness trade off in a particular domain requires assumptions about the structure of that domain. Analyses based on generic assumptions can be productive (Fig. 1B), but in-depth analyses of specific domains will need to formalize simplicity and informativeness in ways that are sensitive to the structural properties of those domains. For example, analyses of kin classification (Fig. 1A) should reflect the fact that kinship categories are defined over relatives embedded within a genealogical system, and analyses of color classification (Fig. 1C) should reflect the fact that colors are embedded within a continuous perceptual space. In order to explore whether kin classification systems are shaped by the trade-off between simplicity and informativeness, we formulate versions of these general constraints that are appropriate for the domain of kinship.

The kin classification systems we consider include terms that refer to the kin types in Fig. 2A, namely, grandparents, parents, aunts, uncles, siblings, children, nieces, nephews, and grandchildren. This is the largest set of kin types for which we have kin naming data and for which our analyses are computationally tractable. Previous studies that chart the space of logically possible classification systems have focused on grandparents (*24*), siblings (*11*), or uncles and aunts (*13*) in isolation, and the classification systems that we consider are large by comparison. The systems in Fig. 2A, however, do not include cousins, which have played a prominent role in previous taxonomies of kin classification systems (*2*). The supplementary materials (*25*) describe how our approach extends to systems in-

[1]Department of Psychology, Carnegie Mellon University, Pittsburgh, PA 15213, USA. [2]Department of Linguistics, Cognitive Science Program, University of California, Berkeley, CA 94720, USA.

*To whom correspondence should be addressed. E-mail: ckemp@cmu.edu

cluding cousins and other more distant relatives in the family tree. Here, we show that our approach accounts for the substantial cross-language variation found in categorizing the kin types shown in Fig. 2.

The first tree in Fig. 2A includes 24 relatives of a woman labeled as Alice (here, we assume one relative per kin type; (*25*) reports analyses with different numbers of relatives per kin type), and the second tree includes 32 relatives of a man labeled as Bob. Only the second tree includes niblings (nieces and nephews), because our data include information about nibling categories for male speakers only. Each possible kin classification system that we consider partitions the 56 relatives in the two trees into a set of nonoverlapping categories. That is, each possible system includes terms that allow Alice and Bob to refer to each of their relatives, and exactly one term is available for each relative. The colors in Fig. 2A show a partition that corresponds to the English kin classification system. In the case of English, the partitions of the two trees are identical, but some other languages include different terms for speakers of different sexes. For example, Fig. 2B illustrates the kin classification system of Northern Paiute, an indigenous language of the western United States, in which men and women use different terms to refer to their grandchildren (*26*). In Northern Paiute, unlike English, the kin terms for grandparents and grandchildren are self-reciprocal; for example, Alice and her maternal grandmother use the same term to refer to each other. We work with a cross-cultural data set compiled by Murdock (*27*) that includes kin classification systems for 566 languages. In compiling these data, Murdock aimed to cover the set of kin classification systems that had been described in the literature and took care not to include closely related languages with similar classification systems. Some of the kin classification systems in Murdock's data are incomplete and do not specify kin categories for all kin types in Fig. 2A, but the data set specifies complete systems for 487 languages in total. These systems include 410 distinct types, of which the most frequent occurs six times, and these 410 types represent only a tiny fraction of the 10^{55} systems that are possible in theory.

We hypothesized that the trade-off between simplicity and informativeness can help to explain which of the many possible systems are attested, or found to exist in actuality. Intuitively, a kin classification system is complex if it includes many terms that must be learned and remembered and if each of those terms has a complex definition. We formalize this idea by assuming that kin classification systems are mentally encoded in a representation language and that the complexity of a system corresponds to the length of its shortest description in this language. The representation language is assumed to be universal, but kin classification systems for different cultures can be created by combining elements of this language in different ways (*28*). Figure 2C shows the shortest description of the English system in a representation language that we now describe. The representation language includes a small set of primitives, all drawn from previous accounts of kinship classification (*29*–*31*), including features like FEMALE(·) and relations like PARENT(·,·). The full set of primitives is shown in Fig. 3A. Rules for combining these primitives are again based on previous formal accounts (*30*, *32*–*34*) and are shown in Fig. 3B. The first six rules indicate that a new relation C(·,·) can be defined as a conjunction or disjunction involving two relations or a relation and a feature. For example, Fig. 2C uses the first rule in Fig. 3B to define mother(·, ·) as the conjunction of PARENT(·,·) and FEMALE(·). The seventh rule indicates that a new relation C(·,·) can be defined as the relative product of two existing relations. For example, Fig. 2C defines grandmother(·,·) as the relative product of mother(·,·) and PARENT(·,·). The final three rules indicate that a new relation can be the inverse, symmetric closure [$A^{\leftrightarrow}(\cdot,\cdot)$] or transitive closure [$A^{+}(\cdot,\cdot)$] of an existing relation. Figure 2D uses the inverse rule to define the child of a man's sister [mansisterchild(·,·)] as the inverse of maternaluncle(·,·). The symmetric closure rule is used in Fig. 2D to define the four self-reciprocal terms that refer to grandparents and grandchildren. The transitive closure rule can capture systems where the same term is used to refer to a parent and a grandparent or to a child and a grandchild. Given the conceptual resources in Fig. 3, the complexity of a system is the smallest number of rules needed to define all terms in the system. For example, the complexity of the English system (Fig. 2C) is 15, and the complexity of the Northern Paiute system (Fig. 2D) is 24. The complexity of a system can exceed the number of terms in the system: The Northern Paiute system includes 18 terms, but Fig. 2D requires 24 rules in order to define these 18 terms. Our algorithm for computing the complexity of a system is described in (*25*).

Consider now the dimension of informativeness (*35*, *36*). Suppose that the 24 individuals in Alice's family tree are numbered from left to right and top to bottom, and let **z** be a vector that represents a partition of the 24 individuals into categories, where z_i represents the kinship category used to label individual *i*. For example, if Alice is an English speaker, then z_1 will equal z_3 because individuals 1 and 3 are both grandmothers. Suppose now that Alice wants to refer to individual 1 (her maternal grandmother) and uses the phrase "my grandmother." Because Alice has two grandmothers, some additional information must be specified to pick out the individual she has in mind. Information theory holds that the additional cost c_i in bits when referring to individual *i* is

$$c_i = -\log_2\left(\frac{p_i}{\sum_{z_j=z_i} p_j}\right) \quad (1)$$

where p_i is the probability that Alice will need to refer to individual *i*. For example, if Alice is equally likely to refer to her maternal and paternal grandmothers, then one extra bit must be communicated in addition to the phrase "my grandmother" to indicate which grandmother she has

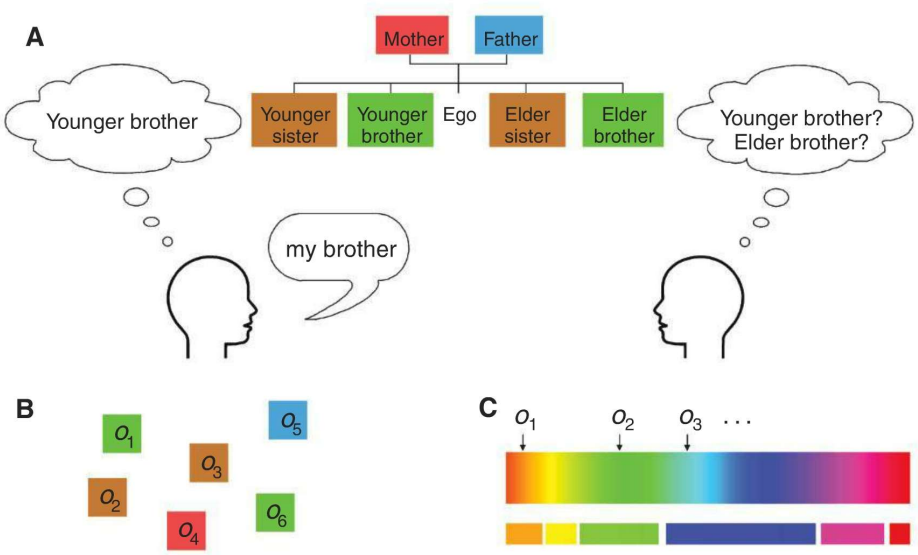

Fig. 1. Communication games can be used to study the trade-off between simplicity and informativeness. (**A**) A communication game for the kinship domain. The objects in the domain are six relatives of the speaker, who is labeled as "Ego" in the family tree. The speaker and hearer have both learned category labels for all of the relatives, and the colors shown here represent English category labels. For example, a single term, "brother," is used for both younger and elder brother. The speaker uses a category label to refer to one of her relatives, and the hearer must infer which relative she has in mind. (**B**) A similar communication game can be formulated within a generic domain that has no structure except for the fact that objects are grouped into categories (*21*). The colors again represent category labels. (**C**) A similar communication game can be formulated within the domain of color, where the "objects" are now points in a continuous perceptual space, shown here for simplicity as a one-dimensional spectrum. The colored bars below the spectrum indicate ranges of color that belong to the same English color categories.

in mind. The communicative cost C for Alice is defined as the expected cost when Alice needs to refer to one of the individuals in her family tree:

$$C = \sum_{i=1}^{24} p_i c_i \quad (2)$$

The communicative cost for Bob is defined similarly, and we define the communicative cost of an entire kin classification system as the average of the costs for Alice and Bob.

The need probabilities p_i play an important role in Eqs. 1 and 2 and can in principle capture the fact that different cultures impose different communicative requirements (*2*, *37*). Because we lack data that would allow us to estimate need probabilities on a per-language basis, we provisionally assume a universal distribution of need probabilities. We estimated these probabilities by computing the relative frequencies of kin expressions of the form "my grandmother," "my mother," "my daughter," "my granddaughter," and the like across corpora for two languages: the Corpus of Contemporary American English (*38*) and the German Reference Corpus (*39*). Relative frequencies were similar for English and German, and Fig. 3C is based on combined results across these two languages. Although the need probabilities in Fig. 3C are based on English and German, some of the same qualitative patterns may apply to many cultures. For example, because every member of a society has parents but some members do not have children, it follows that references to parents should tend to be more common across the whole society (*40*). We will use the probabilities in Fig. 3C for all analyses to follow, but future studies can explore whether our results can be improved by using different sets of need probabilities for different cultures.

Given our definitions of complexity and communicative cost, we will say that one kin classification system dominates another if it is superior along one dimension and no worse along the other. For example, Northern Paiute does not dominate English (English is simpler), and English does not dominate Northern Paiute (Northern

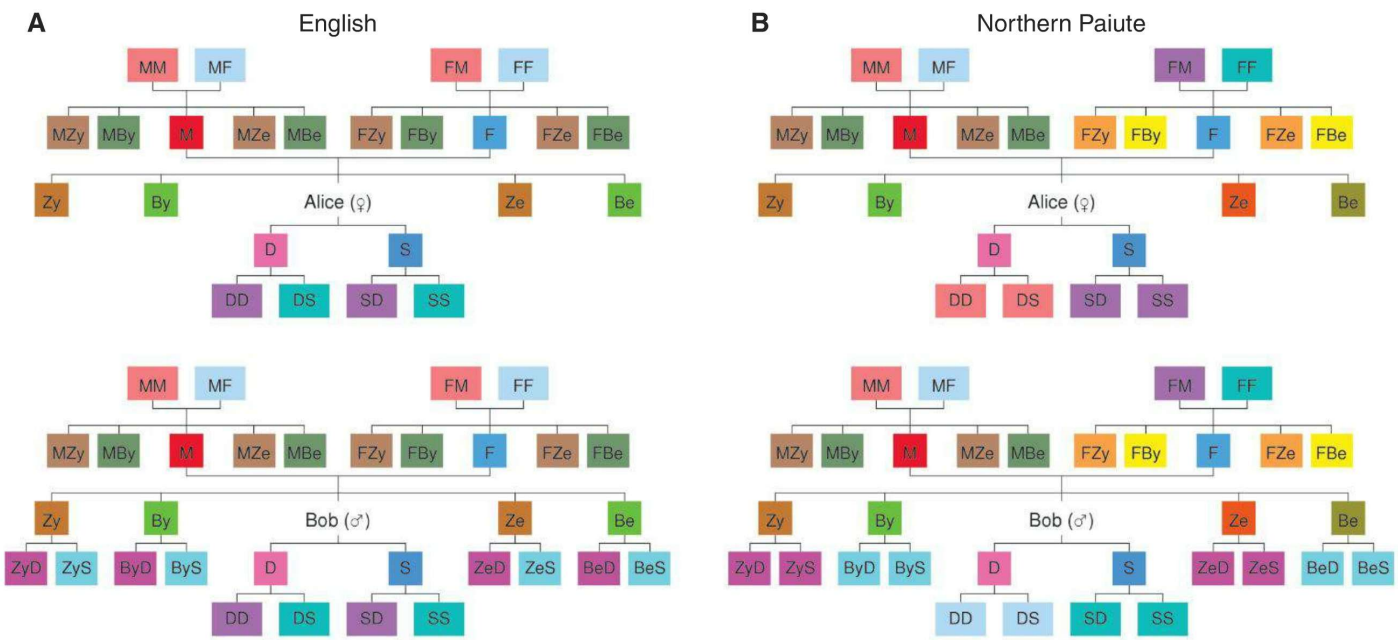

C

mother(x, y)	↔ PARENT(x, y) ∧ FEMALE(x)
father(x, y)	↔ PARENT(x, y) ∧ MALE(x)
daughter(x, y)	↔ CHILD(x, y) ∧ FEMALE(x)
son(x, y)	↔ CHILD(x, y) ∧ MALE(x)
sister(x, y)	↔ ∃z daughter(x, z) ∧ PARENT(z, y)
brother(x, y)	↔ ∃z son(x, z) ∧ PARENT(z, y)
sibling(x, y)	↔ ∃z CHILD(x, z) ∧ PARENT(z, y)
aunt(x, y)	↔ ∃z sister(x, z) ∧ PARENT(z, y)
uncle(x, y)	↔ ∃z brother(x, z) ∧ PARENT(z, y)
niece(x, y)	↔ ∃z daughter(x, z) ∧ sibling(z, y)
nephew(x, y)	↔ ∃z son(x, z) ∧ sibling(z, y)
grandmother(x, y)	↔ ∃z mother(x, z) ∧ PARENT(z, y)
grandfather(x, y)	↔ ∃z father(x, z) ∧ PARENT(z, y)
granddaughter(x, y)	↔ ∃z daughter(x, z) ∧ CHILD(z, y)
grandson(x, y)	↔ ∃z son(x, z) ∧ CHILD(z, y)

D

mother(x, y)	↔ PARENT(x, y) ∧ FEMALE(x)
father(x, y)	↔ PARENT(x, y) ∧ MALE(x)
daughter(x, y)	↔ CHILD(x, y) ∧ FEMALE(x)
son(x, y)	↔ CHILD(x, y) ∧ MALE(x)
sister(x, y)	↔ ∃z daughter(x, z) ∧ PARENT(z, y)
brother(x, y)	↔ ∃z son(x, z) ∧ PARENT(z, y)
youngersister(x, y)	↔ sister(x, y) ∧ YOUNGER(x, y)
oldersister(x, y)	↔ sister(x, y) ∧ OLDER(x, y)
youngerbrother(x, y)	↔ brother(x, y) ∧ YOUNGER(x, y)
olderbrother(x, y)	↔ brother(x, y) ∧ OLDER(x, y)
maternalaunt(x, y)	↔ ∃z sister(x, z) ∧ mother(z, y)
maternaluncle(x, y)	↔ ∃z brother(x, z) ∧ mother(z, y)
paternalaunt(x, y)	↔ ∃z sister(x, z) ∧ father(z, y)
paternaluncle(x, y)	↔ ∃z brother(x, z) ∧ father(z, y)
mansisterchild(x, y)	↔ maternaluncle(y, x)
manbrotherchild(x, y)	↔ paternaluncle(y, x)
maternalgrandmother(x, y)	↔ ∃z mother(x, z) ∧ mother(z, y)
maternalgrandfather(x, y)	↔ ∃z father(x, z) ∧ mother(z, y)
paternalgrandmother(x, y)	↔ ∃z mother(x, z) ∧ father(z, y)
paternalgrandfather(x, y)	↔ ∃z father(x, z) ∧ father(z, y)
selfreciprocal1(x, y)	↔ maternalgrandmother^{-1}(x, y)
selfreciprocal2(x, y)	↔ maternalgrandfather^{-1}(x, y)
selfreciprocal3(x, y)	↔ paternalgrandmother^{-1}(x, y)
selfreciprocal4(x, y)	↔ paternalgrandfather^{-1}(x, y)

Fig. 2. Kin classification systems and their shortest descriptions in the representation language that we use. (**A**) The English kin classification system. Individuals with the same color [e.g., Alice's mother's mother (MM) and father's mother (FM)] are assigned to the same category (in this case, "grandmother"). (**B**) The Northern Paiute system. Note that Alice and Bob use different kinship terms for their grandchildren. (**C** and **D**) The shortest descriptions of the English and Northern Paiute systems in the representation language that we use.

Paiute enables more informative communication). A system is "near-optimal" (*6*, *10*) if it is dominated by few alternatives, and we can now explore whether attested systems are near-optimal with respect to the space of possible systems.

We tested the near-optimality hypothesis by using a series of analyses that range in scope from broad to focused. Because the complete space of possible systems is too large to enumerate, we began by exploring a large subset of this space that is likely to include all of the near-optimal candidates. We began by enumerating around 71,000 distinct kinship categories that can be defined by starting with the primitives in Fig. 3A and applying the rules in Fig. 3B up to three times. Each of these categories corresponds to a subset of the 56 individuals in Fig. 2A. The number of kin classification systems that can be built from these categories is extremely large, and we therefore sampled a representative subset of these systems. Figure 4A plots these systems along our two dimensions. The best systems according to our account are located along the optimal frontier, also known as the Pareto frontier, which corresponds to the bottom left boundary of the space. The majority of attested systems (black circles) are found near the optimal frontier. Whereas Fig. 4A explores a sample from the space of all possible kin classification systems, Fig. 4B shows the results of a more focused analysis that includes all and only the 8.3×10^8 systems that can be created by combining categories that appear in more than two attested systems. Again the attested systems tend to fall near the optimal frontier, indicating that they tend to dominate other systems built from the same collection of categories.

Figure 4, A and B, is based on partitions of the full family tree in Fig. 2, but Fig. 4C shows results for analyses that focus separately on grandparents, grandchildren, siblings, mother and aunts, father and uncles, and children and niblings (nieces and nephews). Attested systems are again shown in black, and the size of each black circle indicates its frequency. The results are consistent with the near-optimal pattern observed for the entire family tree. The results also support a related prediction of our account: that frequent systems should tend to lie closer to the optimal frontier than rare systems.

Our analyses so far have tested the near-optimality claim relative to large spaces of possible competitors. We now test this claim relative

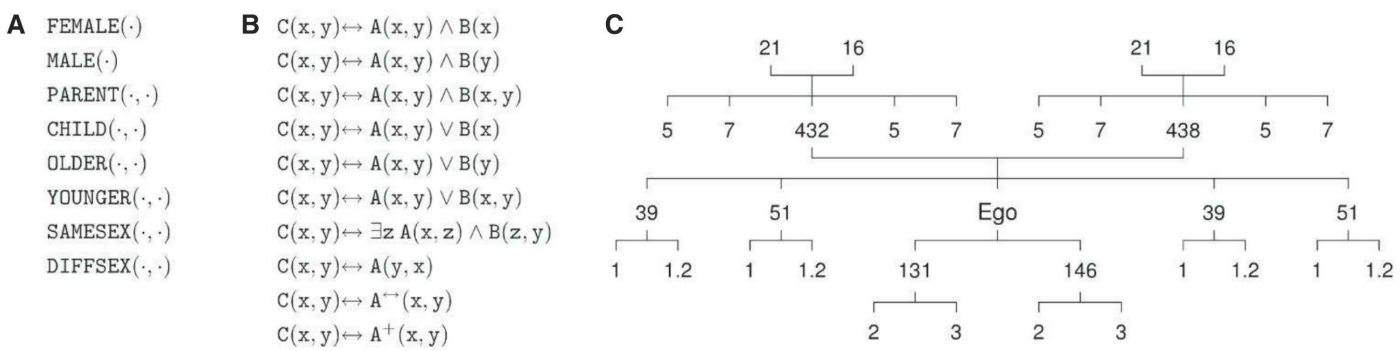

Fig. 3. Components used to formalize the notions of cognitive complexity and communicative cost. (**A**) Primitive concepts. (**B**) Rules for combining these concepts. Each rule allows a new concept C() to be defined in terms of at most two concepts A() and B(), which must be either primitive or previously defined. (**C**) Need probabilities for individuals in the family trees of Fig. 2. The actual probabilities are derived from English and German corpus statistics and are proportional to the numbers shown here.

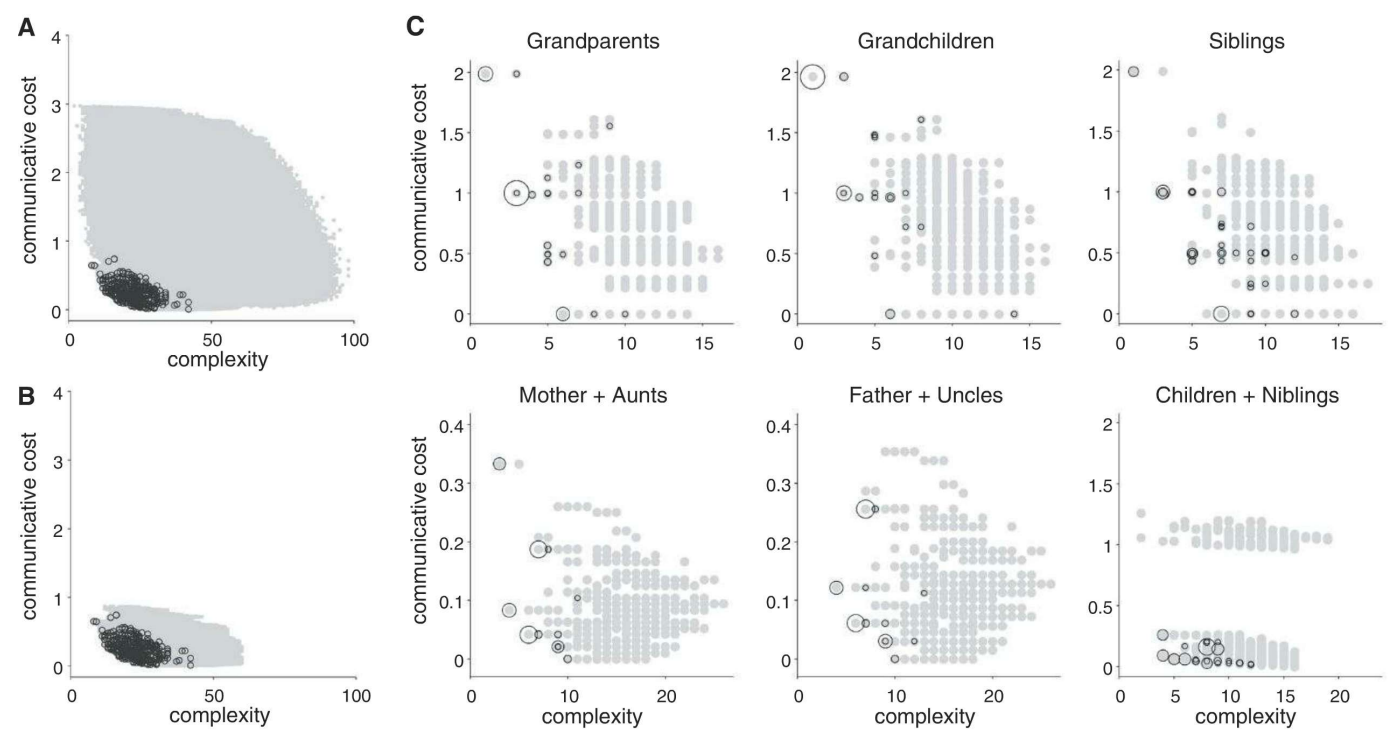

Fig. 4. The optimal frontier. (**A**) Communicative cost versus complexity for a large space of possible kin classification systems. Attested systems are shown as black circles. (**B**) Communicative cost versus complexity for systems built from attested categories that appear more than twice in the Murdock data. (**C**) Optimality analyses for six subsets of the full family tree in Fig. 2. In each plot, the black circles represent real-world systems, and the sizes of these circles represent frequencies within the Murdock data set.

to smaller sets of competitors that might be expected to perform especially well: simple transformations of attested systems (*6*). If attested systems are near-optimal, then each attested system should tend to dominate transformations of that system. The transformations that we consider are based on permutations defined over five chunks of the family tree, each comprising four individuals: grandparents, grandchildren, siblings, maternal siblings, and paternal siblings. These chunks are shown in Fig. 5A. For example, if we permute the system in Fig. 2B by exchanging the category labels of the grandparents chunk with those of the grandchildren chunk, then Alice will use one term for her maternal grandparents, a second term for her paternal grandparents, and four distinct terms for her grandchildren. We considered all such permutations that respected category boundaries: that is, permutations that moved entire categories and did not move only parts of categories. Figure 5B summarizes the results when the full set of permutations is applied to the attested systems in the Murdock data set. In most cases, attested systems dominate permutations of these systems, suggesting that attested systems tend to be near-optimal with respect to a focused set of related systems, not just the full space.

Previous researchers have described constraints that help to predict which kin classification systems are encountered in practice (*2*, *11*, *15*, *35*–*37*, *41*–*50*), and we now show that some of these constraints emerge as consequences of our account. Greenberg (*13*, *24*) focused on markedness constraints, including the constraint that near relatives (e.g., siblings) are more likely than distant relatives (e.g., parent's siblings) to be split into multiple categories and the constraint that ascending generations (e.g., grandparents) are more likely to be split than descending generations (e.g., grandchildren) (*13*). As Greenberg (*24*) and others (*51*, *52*) have argued, markedness constraints can often be usefully formulated in terms of probabilities, and some of Greenberg's specific constraints can be explained as a consequence of the nonuniform distribution of need probabilities over the tree in Fig. 3C. In particular, need probabilities are higher for near relatives than distant relatives and higher for ascending generations than descending generations. To demonstrate that our theory is sensitive to Greenberg's constraints, we show results for three specific permutations (Fig. 5C). The first and second permutations exchange near relatives (siblings) with distant relatives (maternal or paternal siblings), and the third exchanges an ascending generation (grandparents) with a descending generation (grandchildren). In all three cases, attested systems tend to score better than permuted systems, illustrating that violations of Greenberg's constraints are penalized by our account.

Another commonly invoked constraint is that kinship categories tend to have conjunctive definitions (e.g., parent AND female) rather than disjunctive definitions (e.g., parent OR female) (*11*–*13*). Because conjunctive definitions lead to smaller categories and disjunctive definitions lead to broader categories, our communicative cost measure predicts that conjunctive definitions will tend to be preferred. To test this prediction, we developed a ranking measure that reflects the optimality of individual categories (*25*). By this measure, smaller ranks are better: Categories that belong to systems on the optimal frontier have ranks of zero, and categories that belong only to systems that lie far from the optimal frontier have large ranks. We computed the rank of every category that belongs to one of the hypothetical systems shown as light gray circles in the subtree analyses of Fig. 4C. Figure 5D shows that for each subtree, conjunctive categories have smaller (i.e., better) ranks on average than disjunctive categories. Although our theory tends to penalize disjunctive systems, fig. S9 (*25*) shows that the near-optimality results in Fig. 4 are driven by more than just this fact.

We have argued that kin classification systems in the world's languages exhibit a near-optimal trade-off between simplicity and informativeness. We have also argued that the trade-off between these general principles accounts for some specific constraints on kin classification systems. Even so, kin classification is clearly shaped by factors that go beyond the account presented here. For example, kin classification systems tend to correlate with, and are presumably shaped by, local social patterns of marriage and residence (*2*). Our account places substantial constraints on kin classification systems, explaining several previously documented constraints, and we propose that social forces supply further constraints, such that kin classification systems are both near-optimal with respect to general communicative constraints and well-suited for local social purposes.

Although our theory predicts that kin classification systems achieve a near-optimal trade-off between simplicity and informativeness, it does not capture the process of cultural evolution (*41*, *53*, *54*) that presumably led to this result. Previous researchers have developed models of cultural evolution that may help to explain how near-optimal kin classification systems emerge as a consequence

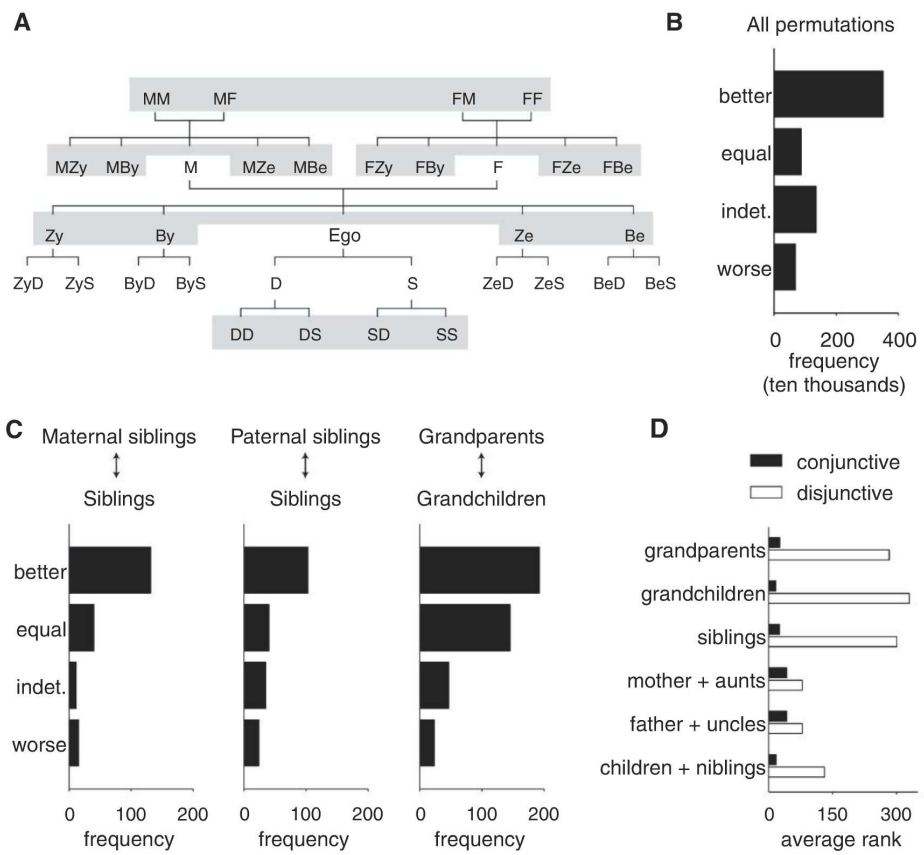

Fig. 5. Fine-grained optimality analyses. (**A**) The gray bars indicate the five chunks used for the permutation analysis. (**B**) Results of the permutation analysis. Attested systems typically score better than permuted versions of these systems and rarely score worse. In some cases, the attested and permuted systems are equal in both cost and complexity; in others, the attested system is superior along one dimension but inferior along the other, and the comparison is indeterminate. (**C**) Results for three specific permutations that exchange near relatives (siblings) with more distant relatives (maternal and paternal siblings) and that exchange ascending relatives (grandparents) with descending relatives (grandchildren). Attested systems dominate those that permute near and distant relatives, or ascending and descending relatives, which explains specific markedness constraints proposed previously. (**D**) Comparison between conjunctive and disjunctive categories. Conjunctive categories contribute to systems of greater optimality, which may help to explain the cross-cultural predominance of conjunctive categories.

of selective pressure for simplicity and informativeness (*55*–*57*). Studying the evolution of kin classification systems may reveal additional constraints on attested systems; for example, there may be systems that are near-optimal according to our analysis but unattested because they are not the outcomes of plausible evolutionary sequences (*41*).

We have relied here on kinship-specific realizations of the principles of simplicity and informativeness. Appropriate realizations of the same general principles may apply to semantic domains other than kinship, and some evidence suggests that they do. It has been proposed that color naming systems in the world's languages reflect partitions of perceptual color space that are near-optimally informative (*58*), and recent analyses support this view (*6*), including an analysis of lightness terms (*59*) that relies on a variant of the communication game in Fig. 1. A similar analysis of color terms should be possible within our framework, where communication is considered successful to the extent that the color inferred by the hearer is close in perceptual space to that intended by the speaker. The domains of kinship and color are different in fundamental respects: Kin terms describe relations between discrete individuals, whereas color terms pick out regions of a continuous perceptual space. The fact that the same general principles help to explain semantic category systems in such dissimilar domains opens up the possibility of a domain-general foundation for categorization across cultures.

References and Notes

1. A. A. Goldenweiser, *J. Am. Folkl.* **26**, 259 (1913).
2. G. P. Murdock, *Social Structure* (Macmillan, New York, 1949).
3. D. E. Brown, *Human Universals* (McGraw Hill, Boston, 1991).
4. M. D. Hauser, *Nature* **460**, 190 (2009).
5. B. Berlin, P. Kay, *Basic Color Terms: Their Universality and Evolution* (Univ. of California Press, Berkeley, CA, 1969).
6. T. Regier, P. Kay, N. Khetarpal, *Proc. Natl. Acad. Sci. U.S.A.* **104**, 1436 (2007).
7. B. Berlin, *Ethnobiological Classification: Principles of Categorization of Plants and Animals in Traditional Societies* (Princeton Univ. Press, Princeton, NJ, 1992).
8. S. Atran, in *Thinking: An Invitation to Cognitive Science*, E. E. Smith, D. N. Osherson, Eds. (MIT Press, Cambridge, MA, 1995), vol. 3, pp. 131–174.
9. S. Levinson, S. Meira, *Language* **79**, 485 (2003).
10. N. Khetarpal, A. Majid, T. Regier, in *Proceedings of the 31st Annual Conference of the Cognitive Science Society*, N. Taatgen, H. van Rijn, Eds. (Cognitive Science Society, Austin, TX, 2009), pp. 2396–2401.
11. S. B. Nerlove, A. K. Romney, *Am. Anthropol.* **69**, 179 (1967).
12. D. B. Kronenfeld, *Am. Ethnologist* **1**, 489 (1974).
13. J. Greenberg, in *On Language: Selected Writings of Joseph Greenberg*, K. Denning, S. Demmer, Eds. (Stanford Univ. Press, Stanford, CA, 1990), pp. 310–327.
14. R. E. Valdés-Peréz, V. Pericliev, *Cross-Cultural Res.* **33**, 162 (1999).
15. D. Jones, *Behav. Brain Sci.* **33**, 367 (2010).
16. A. Martinet, *A Functional View of Language* (Oxford Univ. Press, London, 1962).
17. P. Grice, *Studies in the Way of Words* (Harvard Univ. Press, Cambridge, MA, 1989).
18. S. Pinker, P. Bloom, *Behav. Brain Sci.* **13**, 707 (1990).
19. N. Evans, S. C. Levinson, *Behav. Brain Sci.* **32**, 429 (2009).
20. G. K. Zipf, *Human Behavior and the Principle of Least Effort* (Addison-Wesley, Cambridge, MA, 1949).
21. R. Ferrer i Cancho, R. V. Solé, *Proc. Natl. Acad. Sci. U.S.A.* **100**, 788 (2003).
22. J. Hawkins, *Efficiency and Complexity in Grammars* (Oxford Univ. Press, Oxford, 2004).
23. E. Rosch, in *Cognition and Categorization*, E. Rosch, B. B. Lloyd, Eds. (Lawrence Erlbaum, New York, 1978), pp. 27–48.
24. J. H. Greenberg, *Language Universals* (Mouton de Gruyter, The Hague, Netherlands, 1966).
25. Materials and methods are available as supplementary materials on *Science* Online.
26. A. L. Kroeber, *California Kinship Systems* (Univ. of California Press, Berkeley, CA, 1917).
27. G. P. Murdock, *Ethnology* **9**, 165 (1970).
28. A. Wierzbicka, *Semantics, Culture and Cognition: Universal Human Concepts in Culture-Specific Configurations* (Oxford Univ. Press, New York, 1992).
29. A. L. Kroeber, *J. R. Anthropol. Inst. Great Britain Ireland* **39**, 77 (1909).
30. J. H. Greenberg, *Philos. Sci.* **16**, 58 (1949).
31. S. Gould, *A New System for the Formal Analysis of Kinship* (University Press of America, Lanham, MD, 2000).
32. A. F. C. Wallace, J. Atkins, *Am. Anthropol.* **62**, 58 (1960).
33. E. Woolford, *Am. Ethnologist* **11**, 771 (1984).
34. D. W. Read, C. A. Behrens, *J. Quant. Anthropol.* **2**, 353 (1990).
35. A. F. C. Wallace, *Proc. Natl. Acad. Sci. U.S.A.* **47**, 458 (1961).
36. E. J. Hedican, *Ethnology* **25**, 229 (1986).
37. R. G. D'Andrade, in *Explorations in Mathematical Anthropology*, P. Kay, Ed. (MIT Press, Cambridge, MA, 1971), pp. 60–75.
38. M. Davies, The Corpus of Contemporary American English (COCA): 400+ million words, 1990-present (2008); available at www.americancorpus.org.
39. M. Kupietz, H. Keibel, in *Working Papers in Corpus-Based Linguistics and Language Education* (2009), pp. 53–59. Corpus is available at www.ids-mannheim.de/cosmas2/.
40. H. H. Clark, E. V. Clark, *Psychology and Language: An Introduction to Psycholinguistics* (Harcourt Brace Jovanovich, New York, 1977).
41. P. J. Epling, J. Kirk, J. P. Boyd, *Am. Anthropol.* **75**, 1596 (1973).
42. D. B. Kronenfeld, *Plastic Glasses and Church Fathers: Semantic Extension from the Ethnoscience Tradition* (Oxford Univ. Press, New York, 1996).
43. P. Hage, *Am. Ethnologist* **24**, 652 (1997).
44. M. Godelier, T. R. Trautmann, F. E. Tjon Sie Fat, in *Transformations of Kinship*, M. Godelier, T. R. Trautmann, F. E. Tjon Sie Fat, Eds. (Smithsonian Institution Press, Washington, DC, 1998), pp. 1–26.
45. F. K. Lehman, *Anthropol. Theory* **1**, 212 (2001).
46. M. de l'Etang, P. J. Bancel, *Mother Tongue* **IX**, 133 (2005).
47. D. B. Kronenfeld, *Anthropos* **101**, 203 (2006).
48. M. J. Leaf, *Ethnology* **45**, 305 (2006).
49. D. W. Read, *Ethnology* **46**, 329 (2007).
50. B. Milicic, in *Kinship, Language and Prehistory: Per Hage and the Renaissance in Kinship Studies*, D. Jones, B. Milicic, Eds. (Univ. of Utah Press, Salt Lake City, 2010), pp. 212–222.
51. M. Haspelmath, *J. Linguist.* **42**, 25 (2006).
52. E. Hume, *Phonological Stud.* **11**, 295 (2008).
53. V. Pericliev, *Profiling Language Families by Their Kin Term Patterns: A Computational Approach* (Lincom Europa, München, Germany, 2011).
54. F. M. Jordan, *Hum. Biol.* **83**, 297 (2011).
55. L. Steels, T. Belpaeme, *Behav. Brain Sci.* **28**, 469 (2005).
56. T. L. Griffiths, M. L. Kalish, *Cogn. Sci.* **31**, 441 (2007).
57. T. C. Scott-Phillips, S. Kirby, *Trends Cogn. Sci.* **14**, 411 (2010).
58. K. A. Jameson, R. G. D'Andrade, in *Color Categories in Thought and Language*, C. L. Hardin, L. Maffi, Eds. (Cambridge Univ. Press, Cambridge, 2010), pp. 295–319.
59. R. Baddeley, D. Attewell, *Psychol. Sci.* **20**, 1100 (2009).

Acknowledgments: Code and data are available at www.charleskemp.com/kinship. We thank S. Gahl, A. Garrett, M. Just, A. Kemp, B. MacWhinney, Y. Xu, Y. Zhang, two anonymous reviewers, and especially P. Kay for valuable suggestions. This work was supported by the NSF under awards CDI-0835797 and SBE-0541957 and by the Pittsburgh Life Sciences Greenhouse Opportunity Fund.

Supplementary Materials

www.sciencemag.org/cgi/content/full/336/6084/1049/DC1
Materials and Methods
Figs. S1 to S9
Tables S1 to S6
References (*60*–*64*)

6 January 2012; accepted 9 April 2012
10.1126/science.1218811

Neural Correlates of a Magnetic Sense

Le-Qing Wu and J. David Dickman*

Many animals rely on Earth's magnetic field for spatial orientation and navigation. However, how the brain receives and interprets magnetic field information is unknown. Support for the existence of magnetic receptors in the vertebrate retina, beak, nose, and inner ear has been proposed, and immediate gene expression markers have identified several brain regions activated by magnetic stimulation, but the central neural mechanisms underlying magnetoreception remain unknown. Here we describe neuronal responses in the pigeon's brainstem that show how single cells encode magnetic field direction, intensity, and polarity; qualities that are necessary to derive an internal model representing directional heading and geosurface location. Our findings demonstrate that there is a neural substrate for a vertebrate magnetic sense.

Behavioral studies have shown that many animals derive geopositional information using cues from Earth's magnetic field (*1*–*5*). Geomagnetic inclination varies from 0° at the magnetic equator to ±90° at the magnetic poles (Fig. 1), and these direction angle variations could be used to derive latitude information (*6*). Geomagnetic intensity also varies uniformly from the equator to the poles (Fig. 1), and local intensity variations exist that seem to be used by some animals for positional determination (*7*). To be functional, a neural system subserving magnetoreception must be sensitive to both of these magnetic field qualities. Although several regions of the central nervous system are activated by magnetic stimulation (*8*–*12*), until now there has been no clear evidence for magnetic sense neural correlates in the vertebrate brain.

A number of studies have suggested that retinal (*13*, *14*), beak (*15*, *16*), and possibly inner ear receptors (*17*, *18*) all transduce magnetic field information in birds. Thus, we recently delivered a rotating magnetic field to alert pigeons and used an early-release gene marker for neural activation

Department of Neuroscience, Baylor College of Medicine, Houston, TX 77024, USA.

*To whom correspondence should be addressed. E-mail: dickman@bcm.edu

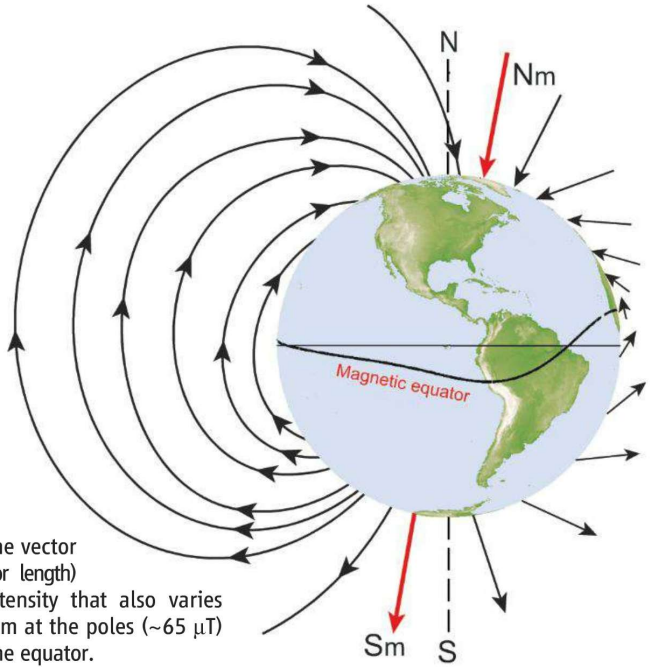

Fig. 1. Schematic illustration of Earth's geomagnetic field. View of American continents with the north (Nm) and south (Sm) magnetic poles (red vectors), magnetic equator (thick line), Earth spin axis (N-S dashed line), and hemispheric equator (thin line). Magnetic force lines (left field arrows) exit through the Sm pole and enter into the Nm pole. The magnetic field vector (right arrows) direction represents the magnetic inclination angle (relative to gravity) that varies uniformly between ±90° at the poles (Sm and Nm) and 0° at the magnetic equator. The vector magnitude (shown as vector length) represents geomagnetic intensity that also varies uniformly between maximum at the poles (~65 μT) and minimum (~20 μT) at the equator.

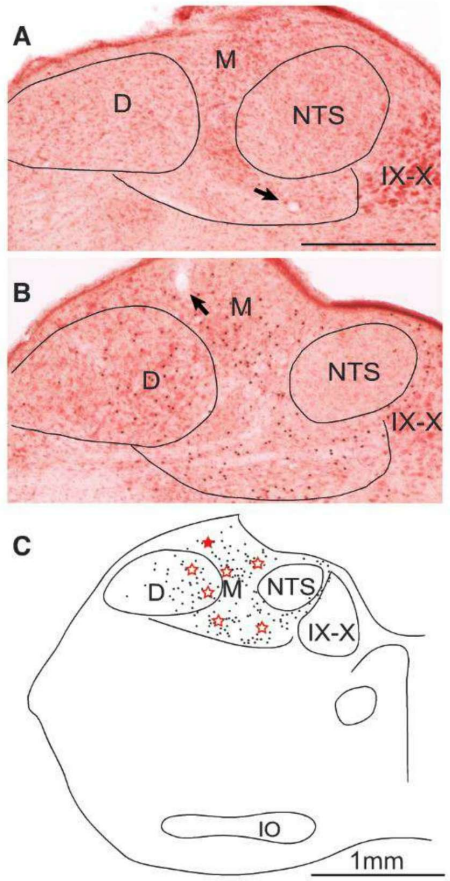

Fig. 2. Recording site verification and c-Fos expression in response to magnetic field stimulation. (**A** and **B**) Vestibular brainstem sections from two pigeons, each with an electrolytic lesion (arrows) made from a recording electrode on the last experimental day. In (B), the brain was processed to show c-Fos transcription factor (black dots), a marker for neural activation, after 72 min of magnetic field stimulation (*18*). (**C**) Anatomical reconstruction of section B, with c-Fos–positive cell locations (black dots) and recording site lesion locations (red stars) for all seven birds (collapsed onto one representative section). D, descending vestibular nucleus; IO, inferior olivary nucleus; M, medial vestibular nucleus; NTS, nucleus of the solitary tract; IX-X, glossopharyngeal-vagal nuclei. Scale bar = 1 mm.

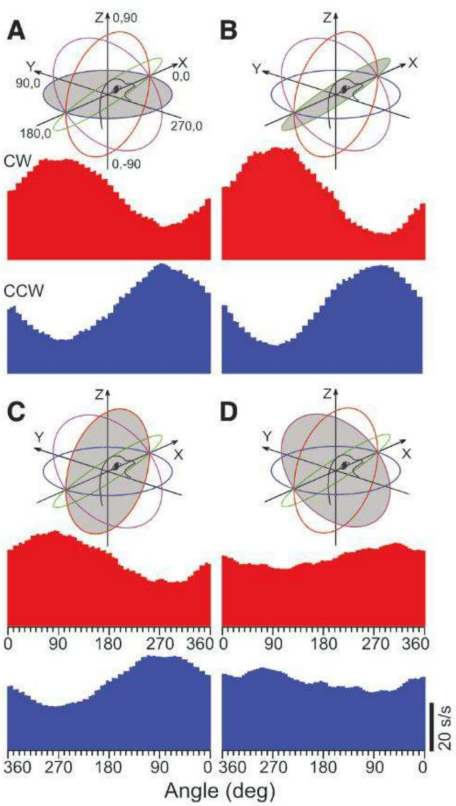

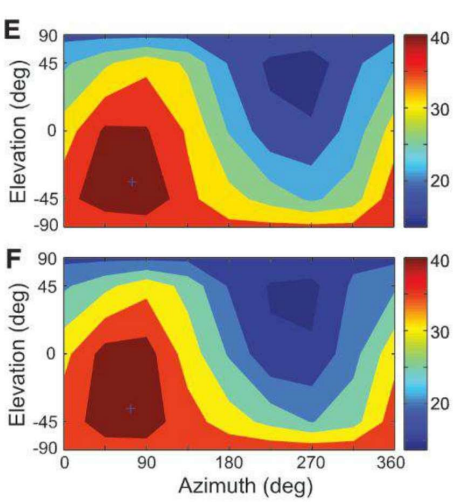

Fig. 3. Stimulus protocol and neural responses to magnetic field stimulation. (**A** to **D**) Schematic illustration of rotating magnetic field vector stimulation for the four great planes tested (top). Azimuth and elevation values [shown in (A)] were referenced to rotations about the positive *x* (0,0), *y* (90,0), and *z* (0,90) axes, corresponding to nasal area, left ear, and vertex, respectively. Zero degrees azimuth and elevation corresponds to a vector directed along the positive *x* axis, whereas an azimuth of 0 and elevation of –90 was a downward- (–*z*) directed stimulus vector. At the base of each panel, response post-stimulus time histograms (mean firing rate as a function of vector orientation) for an example MR neuron to CW (red) and CCW (blue) magnetic vector rotations for each great plane (gray) are shown. (**E** and **F**) Directional tuning contour map (Lambert cylindrical equal-area projection) computed for CW (E) and CCW (F) responses in (A) to (D). Each color contour corresponds to the mean firing rate in spikes per second (s/s) as a function of magnetic field vector elevation and azimuth. The blue cross corresponds to the spatial location of the 3D preferred direction vector.

(the c-Fos transcription factor) to delineate where in the pigeon's brain magnetic field information is processed (*18*). Four main magnetoreception brain regions were identified, including the lateral hyperpallium, hippocampus, dorsal thalamus, and caudal vestibular nuclei, which are all known to be involved in spatial orientation and navigation functions. We also found that lesions of the inner ear lagena receptor (a vestibular otolith organ) eliminated magnetic field activation in several of these regions (*18*), including the vestibular nuclei, where lagena afferents terminate (*19*). We used these findings to hypothesize that this vestibular brainstem region serves as a primary magnetoreception processing center and to begin our search for a neural substrate encoding the avian magnetic sense.

We recorded single-cell extracellular responses from vestibular neurons in seven awake pigeons during magnetic field stimulation. The birds' heads were fixed in place in order to eliminate transient vestibular activation (*20*), and the birds were

placed in total darkness to minimize possible retinal photopigment activation (*13*, *14*). We histologically verified the recording sites (electrolytic lesions) in all seven animals and found them to be located in the caudal descending (D) and medial (M) vestibular nuclei (Fig. 2, A to C). In one pigeon (Fig. 2B), both a marking lesion and c-Fos expression after magnetic field stimulation (*18*) were colocalized, which verified that the recording site was among magnetically activated cells.

To stimulate magnetoreception neurons, a three-dimensional (3D) coil system was used to actively cancel the natural geomagnetic field and then generate an artificial magnetic field, with a vector whose elevation, azimuth, and magnitude could be independently manipulated. The magnetic field vector was stepped in 10° direction-angle increments (100 ms per step) through 360° to complete one revolution (a 3.6-s period) in one of four great circle planes (horizontal, sagittal, and 45° tilts) relative to the center of the bird's head (Fig. 3). For each great circle plane, both clockwise (CW; increasing inclination angle) and counterclockwise (CCW; decreasing inclination angle) magnetic field vector rotations were presented at multiple repetitions. We recorded from 53 vestibular brainstem neurons [magnetic response (MR) cells] that exhibited significant response modulations above the baseline firing rate to magnetic stimulation [analysis of variance (ANOVA), $P < 0.001$]. An additional 276 cells were unresponsive to magnetic stimulation. Figure 3 and fig. S1 show a representative brainstem neuron that responded to the eight CW and CCW magnetic vector rotations (Fig. 3, A to D) by modulating most in one great circle plane (Fig. 3B) and least to an orthogonal plane (Fig. 3D). Further, there was a smooth modulation in firing rate for each stimulus plane, with one magnetic vector direction eliciting the maximal neural response and the opposite direction producing the minimum response (movie S1). To determine whether MR cells respond to the spatial orientation of the magnetic field vector, and not to a higher-order derivative (such as vector velocity), responses to both CW and CCW rotation directions were compared for each stimulus plane. We observed that MR cell responses were proportional to the orientation of the magnetic field vector, regardless of rotation direction (Fig. 3, A to D).

To quantify the differences in CW/CCW responses, we computed directional tuning curves separately for rotation direction. The mean firing rates for both CW and CCW responses were then plotted as a function of magnetic field vector azimuth and elevation in color contour maps (Fig. 3, E and F; Lambert equal-area projections). Separate 3D cosine functions were fit to the CW and CCW responses to calculate the mean maximum sensitivity (S_{max}) and preferred direction values. A significant linear regression [Pearson correlation coefficient (R) = 0.996, $P < 0.001$] relating the maximum sensitivity values for CW and CCW vector rotations for all 53 MR cells was observed, with a slope that was not statistically distinguishable from unity [slope = 0.98, coefficient of determination (R^2) = 0.99, 95% confidence interval (CI) = (0.97, 1.01); Fig. 4A]. Because CW and CCW responses were equivalent, a single cosine function was fit to the averaged CW and CCW responses to calculate the total S_{max} and preferred direction measures for each MR cell ($R^2 > 0.82$ for 93% of the cells and $R^2 > 0.62$ for the remaining cells). For the example cell of Fig. 3, a peak modulation of 17.6 spikes/s above and below the baseline occurred when the magnetic field stimulus vector was directed out (azimuth of 74.2°) and below (–33.7° elevation) the left ear. For all MR cells, the maximal sensitivities to magnetic stimulation ranged between ±1.3 and ±22.1 spikes/s, with a mean of ±13.2 spikes/s (SD ± 4.8). The absolute 3D angular difference in preferred tuning directions (excitatory peak) between CW and CCW neural responses was compared, and 89% (47 out of 53) of MR cells had identical preferred directions, with 4% more being within one 10° angle step (Fig. 4B).

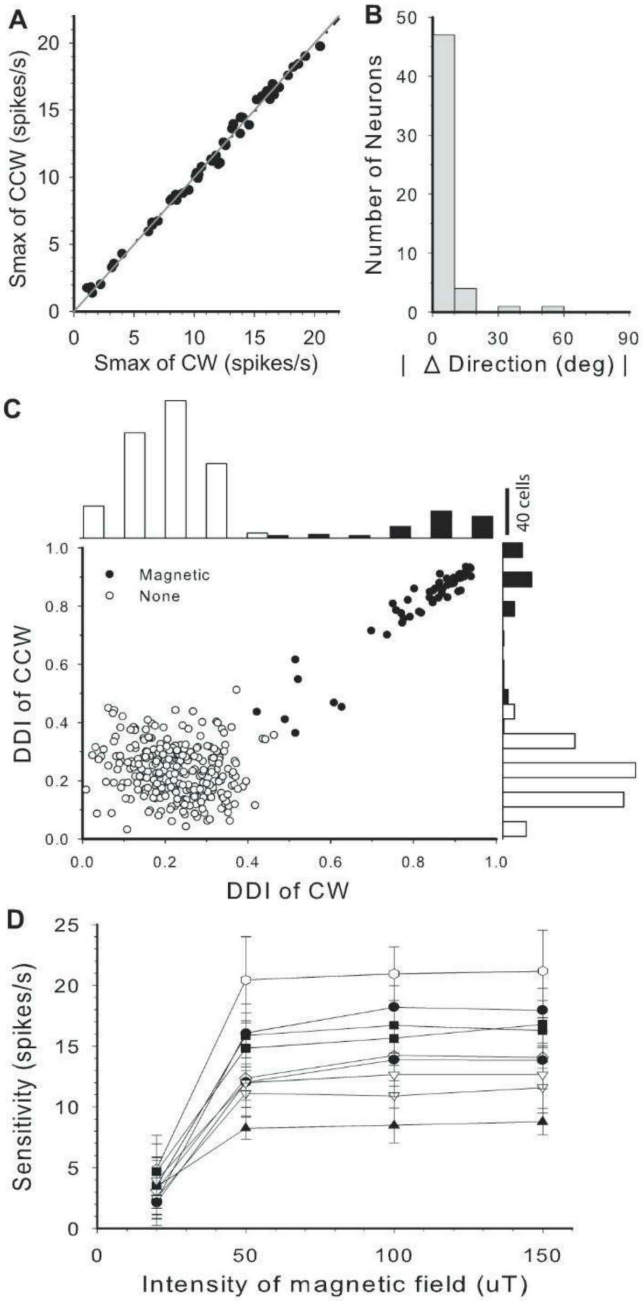

Fig. 4. Sensitivity, preferred direction, tuning strength, and intensity functions for MR cells. (**A**) Maximum sensitivity for MR cells (n = 53) to CW and CCW magnetic field rotation directions. No significant difference between slopes [r^2 = 0.99, 95% CI = (0.97, 1.01)] for ideal unity ratio (black line) and regression (dashed gray line) indicates equivalent cell response for both directions. (**B**) Difference in maximum sensitivity preferred directions for CW and CCW magnetic vector rotations. (**C**) DDI values (peak sensitivity) for nonmagnetic (open circles) and MR cells (solid circles) to CW and CCW magnetic field vector rotation. DDI values range from zero (no significant directional tuning) to 1 (highly tuned). Top and side histograms show marginal distributions. Scale bar = 40 cells. (**D**) MR cell (n = 9) intensity functions for peak sensitivity (CW and CCW combined).

The strength of the preferred direction tuning for each MR cell was quantified with a direction discrimination index (DDI). The DDI ranges from 0 to 1, where larger DDI values indicate a neuron's stronger selectivity for magnetic field vector orientation. MR cells exhibited strongly tuned DDIs that were equivalent (pairwise sign test, P = 0.83) for both CW and CCW vector rotation directions (regression slope 1.05, R^2 = 0.89), whereas cells that exhibited no response to magnetic stimulation did not (Fig. 4C). For the population of MR cells, CW and CCW values were averaged to calculate a mean DDI of 0.82 ± 0.12 (SD, n =

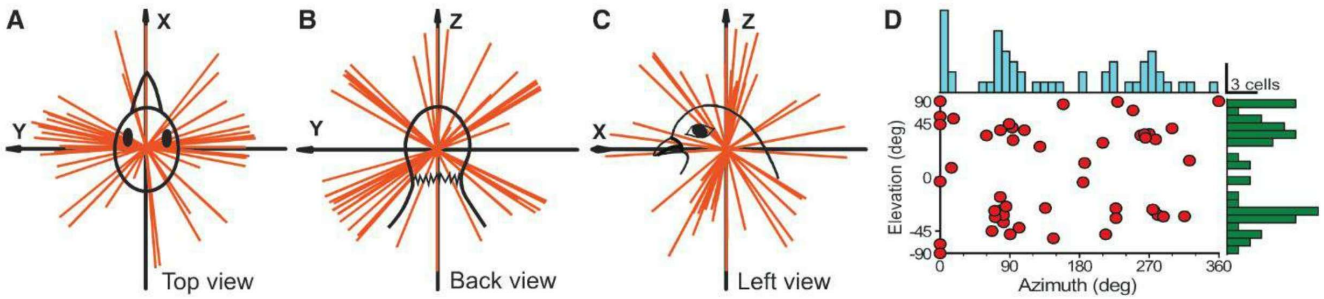

Fig. 5. Spatial orientation of 3D preferred direction vectors and distributions. (**A** to **C**) 3D preferred direction unit vectors plotted in Cartesian coordinate projections onto the *x-y* (top), *y-z* (back), and *x-z* (left) cardinal head planes. (**D**) Distribution of MR cell preferred directions in spherical coordinates plotted as a function of azimuth and elevation (Lambert cylindrical equal-area projection). Histograms on top and right sides show the marginal distributions. Scale bar = 3 cells.

53 cells). Distributions show that 87% of the MR neurons had DDI values above 0.7, indicating highly tuned selectivity. In contrast, none of the nonresponsive cells were selective, with significantly lower DDI values (mean = 0.22, SD ± 0.05, $F_{(1,327)} = 1695$, $P < 0.001$) that were independent of magnetic vector rotation ($R^2 = 0.02$). Taken together, these findings indicate that MR cells respond to magnetic vector direction by encoding the elevation (inclination angle), the azimuth, and the polarity (cosine tuning) of the applied magnetic field.

Earth's geomagnetic field systematically varies between approximately 20 microteslas (μT) at the magnetic equator to more than 60 μT at the magnetic poles (International Geomagnetic Reference Field 11 Model, data year 2010). To determine whether magnetic-responsive neurons were sensitive in that range, we derived intensity functions using four different amplitudes (20 to 150 μT) of the rotating magnetic field vector presented to nine MR neurons in each great circle plane for both CW and CCW rotation directions (Fig. 4D). All neurons had low sensitivity to the 20-μT stimuli (mean ± SD, values for three trials), with significantly increased responses to the 50-μT level (repeated measures ANOVA, $F_{(1,8)} = 475.5$, $P < 0.0001$) and further increases for the 100-μT level ($F_{(1,8)} = 13.3$, $P < 0.006$). Exponential curve fits to each cell indicated that many MR neurons reach response saturation between 70 and 120 μT, and there were no significant differences between neural responses at the 100- and 150-μT levels ($P = 0.335$). These intensity functions show that MR cells have a sensitivity bandwidth that spans the current range of Earth's geomagnetic field.

Because we found that MR cells are selectively tuned to magnetic field vector direction, we examined the population spatial distribution by plotting each cell's preferred direction as a unit vector in spherical Cartesian coordinates (three cardinal head planes; Fig. 5, A to C). Although the preferred directions were widely distributed, they were not uniform. For example, many MR cells' preferred vectors were directed at 45° increments above or below the interaural axis (Fig. 5, B and C). Others had preferred directions aligned with either the naso-occipital (Fig. 5, A and C), or dorsal-ventral (Fig. 5, B and C) axes. When viewed in magnetic stimulus space as a function of azimuth and elevation (Fig. 5D), the preferred direction elevations were significantly bimodal, with peaks at 35° and –30° (Silverman's multimodality test, $P < 0.05$). In contrast, the azimuth data were unimodal ($P = 0.284$).

We have shown that single vestibular brainstem neurons encode the direction, intensity, and polarity of an applied magnetic field, which is consistent with a ferrimagnetic particle receptor (*21*), as opposed to a radial-pair cryptochrome mechanism (*14*). Our findings demonstrate that MR neurons are most sensitive within an intensity range that is naturally produced by Earth's magnetic field, a necessary condition for a magnetoreception system to be useful in the derivation of geopositional information. However, Earth's magnetic field varies over time (for instance, there has been a 35% decrease in its strength over the past 2000 years), so it would seem likely that magnetoreception systems adapt to the slowly changing fields through evolution and/or developmental plasticity in order to maximize magnetic sense perception. It is likely that MR neurons receive magnetic information from the inner ear lagena (*18*, *19*); however, signals from the beak and/or retina are also possible (*13*–*16*). Because MR neurons are located in the vestibular nuclei, multimodal integration of magnetic and linear acceleration cues could provide geomagnetic information relative to the fixed constant of gravity (*18*, *22*, *23*). If so, magnetoreception neural constructs would remain stable in a space-fixed reference frame, regardless of head position. We suggest that MR cells encode a geomagnetic vector that could be used by the neural population to computationally derive the bird's position and directional heading. The geomagnetic vector elevation component could provide the bird's latitude (Fig. 1), the vector azimuth component could be used as a magnetic compass to provide heading direction, and the vector magnitude could provide spatial position cues through local variations in intensity (Fig. 1) relative to a learned internal model of geomagnetic space (*4*, *7*, *24*). How MR cell information is used for orientation and navigation remains to be discovered, but our findings demonstrate that there is a direct neural substrate underlying a magnetic sense in the avian brain.

References and Notes

1. K. J. Lohmann, *Nature* **464**, 1140 (2010).
2. M. M. Walker, T. E. Dennis, J. L. Kirschvink, *Curr. Opin. Neurobiol.* **12**, 735 (2002).
3. W. Wiltschko, R. Wiltschko, *Science* **176**, 62 (1972).
4. W. Wiltschko, R. Wiltschko, *J. Comp. Physiol.* **191**, 675 (2005).
5. R. Wiltschko, I. Schiffner, P. Fuhrmann, W. Wiltschko, *Curr. Biol.* **20**, 1534 (2010).
6. S. Johnsen, K. J. Lohmann, *Nat. Rev. Neurosci.* **6**, 703 (2005).
7. N. F. Putman, C. S. Endres, C. M. Lohmann, K. J. Lohmann, *Curr. Biol.* **21**, 463 (2011).
8. M. Liedvogel *et al.*, *Eur. J. Neurosci.* **25**, 1166 (2007).
9. D. Heyers, M. Zapka, M. Hoffmeister, J. M. Wild, H. Mouritsen, *Proc. Natl. Acad. Sci. U.S.A.* **107**, 9394 (2010).
10. P. Semm, D. Nohr, C. Demaine, W. Wiltschko, *J. Comp. Physiol.* **155**, 283 (1984).
11. P. Nemec, J. Altmann, S. Marhold, H. Burda, H. H. A. Oelschlager, *Science* **294**, 366 (2001).
12. J. P. Vargas, J. J. Siegel, V. P. Bingman, *Brain Res. Bull.* **70**, 158 (2006).
13. A. Möller, S. Sagasser, W. Wiltschko, B. Schierwater, *Naturwissenschaften* **91**, 585 (2004).
14. T. Ritz *et al.*, *Biophys. J.* **96**, 3451 (2009).
15. H. Cadiou, P. A. McNaughton, *J. R. Soc. Interface* **7** (suppl. 2), S193 (2010).
16. G. Fleissner *et al.*, *J. Comp. Neurol.* **458**, 350 (2003).
17. Y. Harada, M. Taniguchi, H. Namatame, A. Iida, *Acta Otolaryngol.* **121**, 590 (2001).
18. L. Q. Wu, J. D. Dickman, *Curr. Biol.* **21**, 418 (2011).
19. J. D. Dickman, Q. Fang, *J. Comp. Neurol.* **367**, 110 (1996).
20. K. L. McArthur, J. D. Dickman, *J. Neurophysiol.* **105**, 1689 (2011).
21. M. Winklhofer, J. L. Kirschvink, *J. R. Soc. Interface* **7** (suppl. 2), S273 (2010).
22. D. T. Edmonds, *Proc. Biol. Sci.* **249**, 27 (1992).
23. M. M. Walker, *J. Theor. Biol.* **250**, 85 (2008).
24. K. J. Lohmann, C. M. F. Lohmann, N. F. Putman, *J. Exp. Biol.* **210**, 3697 (2007).

Acknowledgments: We thank D. Angelaki for comments and guidance in the analyses; K. Reed and J. Chen for technical assistance; C. Fetsch and B. Lindseth for help in pilot investigations; and S. Aamodt for critical review. Much of the work was conducted at Washington University in St. Louis and was supported by a National Institute for Deafness and Other Communication Disorders grant (DC007618) to J.D.D. Data are made available as part of the supplementary materials.

Supplementary Materials

www.sciencemag.org/cgi/content/full/science.1216567/DC1
Materials and Methods
Fig. S1
References (*25*–*30*)
Movie S1

14 November 2011; accepted 11 April 2012
Published online 26 April 2012;
10.1126/science.1216567

New Products

UVMAN
For info: +44-(0)-8432-894844 | www.uvman.co.uk

RADIOMETER/PHOTOMETER

The AccuMAX Series of digital radiometers/photometers provide accurate readouts for ultraviolet (UV) irradiance, visible illuminance, and luminance light readings. The readout units are specially calibrated for use with a full line of interchangeable sensor detectors. When equipped with a sensor detector, the AccuMAX readout unit can satisfy nearly any laboratory or life science application, including fluorescent inspection and UV dosing. Single-wavelength sensor detectors are available in both standard range and extended range. The standard range provides UV readings from microwatts to milliwatts and the extended range provides measurements from milliwatts to watts. All sensors are ideal for checking the intensities of fluorescent UV tubes and HID UV bulbs. AccuMAX meters are microprocessor-controlled with software-driven functions. The readout unit has user-customized settings to work with a wide variety of interchangeable sensor detectors. Powered by two 9 V alkaline batteries, the readout unit is lightweight and portable with a large, easy-to-read LCD screen.

PLATE MOVER

The new Orbitor BenchTrak is a fully customizable plate mover with quick-connect modules. The Orbitor BenchTrak significantly extends the functionality and versatility of the renowned Orbitor RS plate mover, providing a fully customizable automation solution that fits into existing laboratory space. Multiple Orbitor BenchTraks can connect to form complex system layouts, and a range of "click-in" components, such as instrument loading platforms, mezzanines, guarding, and microplate stores, can be easily incorporated to address almost any workflow requirement. The PC-driven Orbitor BenchTrak features the Momentum 3 software, which enables users to configure it for a wide variety of benchtop workflows including sample preparation, ELISA, nucleic acid and protein purification, cell or biochemical assays, real-time polymerase chain reaction, and next generation sequencing. A new LOCaMotion touch screen teaching wizard guides users through the configuration process. The Orbitor BenchTrak empowers the user to create and customize a benchtop workstation that is ideal for automating their unique workflow applications.

Thermo Fisher Scientific
For info: 905-332-2000 | www.thermoscientific.com/orbitor

BIOCHEMISTRY ANALYZER

With clean lines, a smaller footprint, and a host of new features to benefit the operator, the new YSI 2900 advanced biochemistry analyzer is a perfect combination of YSI's trusted enzyme electrode technology with everything users would expect. Able to handle the widest range of sample containers, up to and including a 96-well plate, the YSI 2900 produces a result in approximately 60 seconds for glucose, lactate, ethanol, and 12 other important bioprocess parameters with accuracy comparable to HPLC. The icon driven user interface and built-in training videos make operation simple, while the up-to-date hardware ensures a rapid, highly accurate result with robust sampling of viscous samples or high cell counts. The system's built-in sample handling capability eliminates the need for a separate autosampler and enhanced connectivity options including USB and Ethernet, ensure fast and straightforward data downloads.

Xylem Analytics
For info: 781-937-4100 | www.xylemanalytics.com

RECEPTOR SIGNALING PATHWAY PANEL

The Milliplex Map EpiQuant Receptor Signaling Pathway panel has been designed for assessing the functional states of cells by profiling a range of receptor signaling pathway proteins. The Luminex-based approach enables the profiling of 26 analytes including total and phosphorylated receptor tyrosine kinases, nonreceptor tyrosine kinases, cellular kinases, and a phosphotase with picomolar sensitivities. Users can easily design customized panels by selecting only the analytes of interest. Site-specific, quantitative measurements with picomolar sensitivity support diverse sample types and many research and drug discovery applications. Compared to traditional detection techniques such as Western blots, mass spectrometry analyses, and radioactive phosphorylation assays, the EpiQuant Receptor Signaling Pathway panel provides faster results, increased assay throughput, and specificity. The new panel provides highly validated and characterized immunoassay antibodies, all necessary reagents, and optimized protocols.

EMD Millipore
For info: 800-645-5476 | www.millipore.com/bmia

POSPIVIROID DETECTION

A new, highly sensitive two-step polymerase chain reaction (PCR) assay can be used to detect several important Pospiviroids known to cause significant damage in ornamental, citrus, and solanaceous crops. Agdia's own conventional two-step reverse transcriptase PCR (RT-PCR) is ideal for testing crops subject to phytosanitary restrictions and requirements. The Agdia designed RT-PCR can detect the presence of these destructive pathogens at levels 10 times lower than possible with commonly used single-step RT-PCR. Fast and highly reliable, the Agdia Pospiviroid PCR will screen for the following viroid infections: Potato spindle tuber viroid (PSTVd), Tomato chlorotic dwarf viroid (TCDVd), Tomato apical stunt viroid (TASVd), Tomato planta macho viroid/Mexican pepita viroid (TPMVd/MPVd), Chrysanthemum stunt viroid (CSVd), and Citrus exocortis viroid (CEVd). Agdia's Pospiviroid primers are not degenerate and allow for highly specific sequencing matches, when needed.

Agdia
For info: 800-622-4342 | www.agdia.com

Electronically submit your new product description or product literature information! Go to **www.sciencemag.org/products/newproducts.dtl** for more information.

Newly offered instrumentation, apparatus, and laboratory materials of interest to researchers in all disciplines in academic, industrial, and governmental organizations are featured in this space. Emphasis is given to purpose, chief characteristics, and availability of products and materials. Endorsement by *Science* or AAAS of any products or materials mentioned is not implied. Additional information may be obtained from the manufacturer or supplier.

Science Careers Advertising

For full advertising details, go to ScienceCareers.org and click For Employers, or call one of our representatives.

Tracy Holmes
Worldwide Associate Director
Science Careers
Phone: +44 (0) 1223 326525

UNITED STATES & CANADA

E-mail: advertise@sciencecareers.org
Fax: 202-289-6742

Tina Burks
Midwest/West Coast/
Canada/South America
Phone: 202-326-6577

Elizabeth Early
East Coast & Corporate
Phone: 202-326-6578

Marci Gallun
Sales Administrator
Phone: 202-326-6582

Online Job Posting Questions
Phone: 202-312-6375

EUROPE & REST OF WORLD

E-mail: ads@science-int.co.uk
Fax: +44 (0) 1223 326532

Simone Jux
Phone: +44 (0)1223 326529

Lucy Nelson
Phone: +44 (0)1223 326527

Kelly Grace
Phone: +44 (0) 1223 326528

JAPAN

Yuri Kobayashi
Phone: +81-6-6627-9250
E-mail: ykobayas@aaas.org

CHINA & TAIWAN

Ruolei Wu
Phone: +86-1367-1015-294
E-mail: rwu@aaas.org

All ads submitted for publication must comply with applicable U.S. and non-U.S. laws. *Science* reserves the right to refuse any advertisement at its sole discretion for any reason, including without limitation for offensive language or inappropriate content, and all advertising is subject to publisher approval. *Science* encourages our readers to alert us to any ads that they feel may be discriminatory or offensive.

Science Careers
From the journal *Science* AAAS

The key to innovation and success in any lab or company is to have a workforce anchored by diversity across all levels—from research to management. Studies repeatedly show that productivity and profitability are enhanced by bringing together people with different perspectives to problem solve.

The key to building this diversity within your organization is to hire the most qualified scientists from a range of backgrounds. Reaching these scientists becomes less challenging when you let *Science* do the work for you.

- Your job ad is seen by 700,000 readers around the globe from varied backgrounds
- Your job ad sits on special bannered pages promoting diversity opportunities
- Bonus distribution to Drug Discovery Week, 6–8 August in San Francisco, CA.

Customized packages to correspond with this special feature are available

Support diversity by advertising in this special feature.

For recruitment in science, there's only one Science ScienceCareers.org

To Book Your Ad, Contact:

Midwest, West Coast US/ Canada/South America:
Tina Burks
Phone: 202-326-6577
E-mail: tburks@aaas.org

In Europe and Rest of World:
E-mail: ads@science-int.co.uk
Lucy Nelson
Telephone: +44 (0)1223 326527

Simone Jux
Telephone: +44 (0) 1223 326529

East Coast US/Corporate:
Elizabeth Early
Phone: 202-326-6578
E-mail: eearly@aaas.org

In Japan: **Yuri Kobayashi**
Telephone: +81-6-6627-9250
E-mail: ykobayas@aaas.org

In China/Korea/Singapore/ Taiwan/Thailand: **Ruolei Wu**
Telephone: +86-1367-1015-294
E-mail: rwu@aaas.org

Produced by the *Science*/AAAS Custom Publishing Office

Get a Career Plan that Works.

An exceptional career requires insightful planning and management. That's where *Science* Careers comes in. From job search to career enhancement, *Science* Careers has the tools and resources to help you achieve your goals. Get yourself on the right track today and get a real career plan that works. Visit **ScienceCareers.org**.

Science Careers
From the journal *Science* AAAS

ScienceCareers.org

The UNIVERSITY of OKLAHOMA
Health Sciences Center

Department of Cell Biology
University of Oklahoma Health Sciences Center,
College of Medicine

The Department of Cell Biology (**http://w3.ouhsc.edu/cell_biology**) at the University of Oklahoma Health Sciences Center (OUHSC) invites applications for a tenure/tenure-track faculty position, with rank commensurate with qualifications. Exceptional candidates at any level are encouraged to apply. The successful applicant will conduct a productive research program in the broad fields of cancer, cell and/or molecular biology, neuroscience, or education. This position will involve teaching Gross Anatomy to professional and graduate students.

Candidates must show evidence of productive research accomplishments. A candidate for Associate or Full Professor must have a currently funded research program. All candidates are expected to develop/maintain a fully independent research program addressing fundamental questions in an area of modern cell biology or education, participate in the teaching missions of the department and form productive interactions with colleagues and other scientists at the OUHSC. Research using model organisms is of particular interest.

The position includes a competitive salary, multi-year start-up package, and ample laboratory space. Additional local funding is available on a competitive basis through the Oklahoma Center for Advancement of Science and Technology, seed grants and NIH-sponsored institutional grants. OUHSC maintains outstanding Core Facilities (**http://www.oumedicine.com/body.cfm?id=6030**) that support flow cytometry, confocal imaging, mass spectrometry, gene chip technology and sequencing technology for expression profiling, genetic analysis and ChIP-seq.

Please submit a PDF file containing a *curriculum vitae*, a description of current and future research plans, copies of representative publications (no more than three), and complete contact information for three references to **Paula Slaughter** at **CBSEARCHCOMM@ouhsc.edu**. Confidential inquiries may also be addressed to **Paula Slaughter** at **CBSEARCHCOMM@ouhsc.edu**. The review process will begin on **June 1, 2012**.

The University of Oklahoma is an Equal Opportunity/Affirmative Action Employer.

DANA-FARBER
CANCER INSTITUTE

Research Fellow
T Cell Receptor Biology

A postdoctoral position is available immediately to participate in an exciting new area of T cell receptor (TCR) biology involving mechanotransduction. The successful candidate must have a PhD or equivalent and be highly motivated. He/she will work with a team of immunologists and structural biologists seeking to explore the details of how mechanical force upon pMHC ligation signals from the TCR ectodomains through their transmembrane and cytoplasmic tails. The ideal candidate should have excellent skills in biochemistry, molecular biology and T cell functional studies including transfection of T cells, cell growth and functional analysis as well as flow cytometry.

Research Fellow
Thymic Development

A postdoctoral position is now available for a highly motivated scientist to study thymic development involving plexin-semaphorin regulated migration of thymocytes. The successful candidate should have a PhD degree and familiarity with basic techniques such as animal handling, multicolor flowcytometry, multicolor confocal microscopy and cell biology. Research experience in immunology and strong background in T cell development/migration are essential, and some expertise in biochemistry/molecular biology is helpful.

If interested, please send your CV, a brief summary of research experience and names of three referees to: Ellis Reinherz, MD, Professor of Medicine, Harvard Medical School and the Department of Medical Oncology, Dana-Farber Cancer Institute, 450 Brookline Ave., Boston, MA 02215; Email: ellis_reinherz@dfci.harvard.edu.

Dana-Farber Cancer Institute is an Affirmative Action/Equal Opportunity Employer.

UNIVERSITY OF CALIFORNIA
UCRIVERSIDE

Health ▪ Sustainability ▪ Policy ▪ Technology

LIVING THE PROMISE

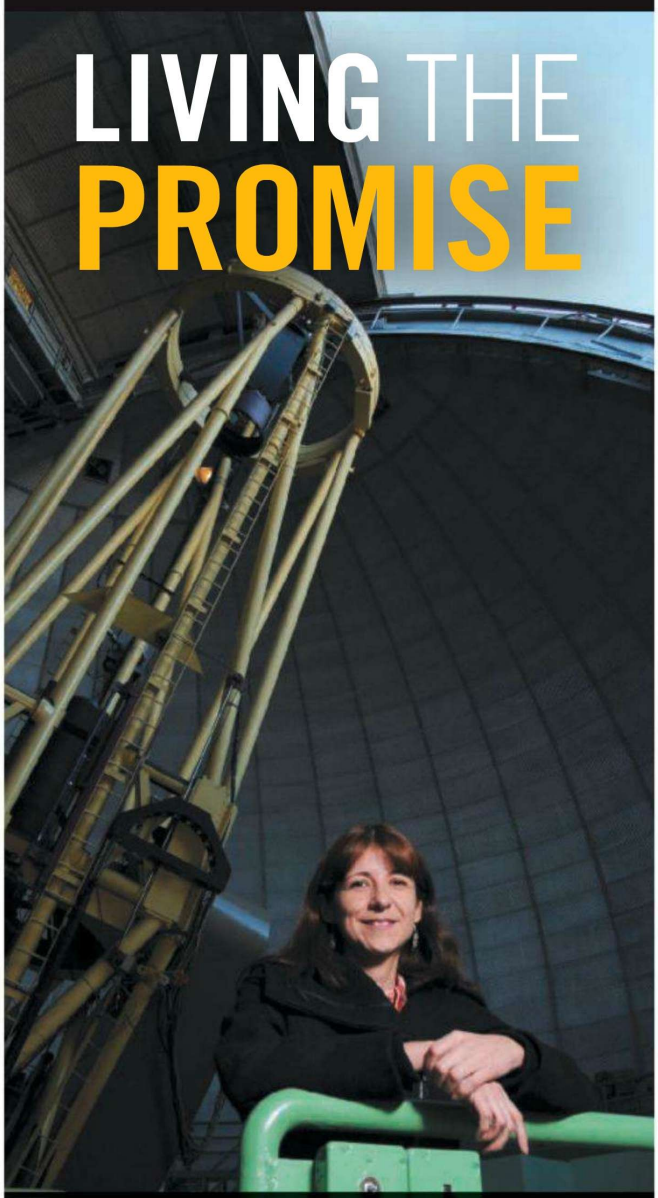

Breakthrough Research

Galaxy quest: UCR astronomers explore the universe and study the role of black holes in galaxy formation.

Explore more technology impacts
promise.ucr.edu

Science Careers online @sciencecareers.org

Learn how current events are impacting your work.

***Science*Insider, the new policy blog from the journal *Science*,** is your source for breaking news and instant analysis from the nexus of politics and science.

Produced by an international team of science journalists, *Science*Insider offers hard-hitting coverage on a range of issues including climate change, bioterrorism, research funding, and more.

Before research happens at the bench, science policy is formulated in the halls of government. Make sure you understand how current events are impacting your work. Read *Science*Insider today.

www.ScienceInsider.org

*Science*Insider
Breaking news and analysis from the world of science policy

Science
AAAS

PRIZES

KUWAIT PRIZE 2012
Invitation for Nominations

The **Kuwait Foundation for the Advancement of Sciences (KFAS)** institutionalized the **KUWAIT Prize** to recognize distinguished accomplishments in the arts, humanities and sciences. The Prizes are awarded annually in the following categories:

A. Basic Sciences
B. Applied Sciences
C. Economics and Social Sciences
D. Arts and Literature
E. Arabic and Islamic Scientific Heritage

The Prizes for **2012** will be awarded in the following fields:

1. Basic Sciences	:	Molecular Biology
2. Applied Sciences	:	Energy
3. Economic and Social Sciences	:	Management Science
4. Arts and Literature	:	Theatre
5. Arabic and Islamic Scientific Heritage	:	Arabic and Islamic Scientific Heritage

Foreground and **Conditions** of the Prize:

1. Two prizes are awarded in each category:
   *A Prize to recognize the distinguished scientific research of a Kuwaiti citizen, and,
   *A Prize to recognize the distinguished scientific research of an Arab citizen.
2. The candidate should not have been awarded a Prize for the submitted work by any other institution.
3. Nominations for these Prizes are accepted from individuals, academic and scientific centers, learned societies, past recipients of the Prize, and peers of the nominees. No nominations are accepted from political entities.
4. The scientific research submitted must have been published during the ***last twenty*** years.
5. Each Prize consists of a cash sum of K.D. 30,000/- (approx. U.S.$100,000/-), a Gold medal, a KFAS Shield and a Certificate of Recognition.
6. Nominators must clearly indicate the distinguished work that qualifies their candidate for consideration.
7. The results of KFAS decision regarding selection of winners are final.
8. The documents submitted for nominations will not be returned regardless of the outcome of the decision.
9. Each winner is expected to deliver a lecture concerning the contribution for which he was awarded the Prize.
10. The nominee must complete the Kuwait Prize CV form.

Inquiries concerning the KUWAIT PRIZE and nominations including complete curriculum vitae and updated lists of publications by the candidate with **four copies** of each of the published papers should be received before **1/12/2012** and addressed to:

The Director General

The Kuwait Foundation for the Advancement of Sciences - P.O. Box: 25263, Safat - 13113, Kuwait. Tel: (+965) 22429780 / Fax: 22403891 / E-Mail: **prize@kfas.org.kw**
You can also visit the foundation's web site **www.kfas.org** to identify foreground and conditions of the prize.

POSITIONS OPEN

THE UNIVERSITY OF ARIZONA
Arizona Health Sciences Center

Tucson & Phoenix, AZ

Director of the University of Arizona Cancer Center

The University of Arizona (UA) invites inquiries, nominations, and applications for the position of Director of its Cancer Center during an exciting period of expansion and change at College of Medicine campuses in both Tucson and Phoenix. The only NCI-designated Comprehensive Cancer Center serving the state of Arizona, the Center has been at the forefront of advances in basic science and translational cancer research, oncology education and clinical patient care for more than 35 years.

The University seeks a dynamic and entrepreneurial Director to lead its matrix structured Center, and to enhance further the UA Cancer Center's (UACC) accomplishments and trajectory of excellence. The UACC Director has responsibility for the overall strategic leadership, vision, direction, and management of the Center for its daily operations, continued expansion and long term growth. Reporting to the Deans of the College of Medicine in Tucson and Phoenix, the Director serves as the official spokesperson and representative of the Center. A complete position description can be viewed at http://www.wittkieffer.com/file/UACCDirector.pdf.

Qualified candidates must hold an MD, PhD, MD/PhD or equivalent terminal degree; possess a distinguished and sustained record of peer reviewed funding, research and scholarship in basic science or clinical research; and meet UA criteria for appointment to a senior level faculty position. Excellent interpersonal skills, demonstrated successful leadership, administrative experience and budgetary management skills are required.

Nominations and applications including a letter of interest and a resume or CV can be sent in confidence via email to Witt/Kieffer, the University's executive search consultants, specifically Karen Otto (630-575-6145) and Brian Bloomfield (949-797-3548), at uacancercenterdir@wittkieffer.com.

The University of Arizona is an EEO/AA Employer M/W/D/V

WITT / KIEFFER

AWARDS

SWEDISH FOUNDATION for STRATEGIC RESEARCH

announces a call for proposals for the 2012

INGVAR CARLSSON AWARD

The aim of the programme is to identify and support young, well-qualified postdocs who intend to start independent, lasting and creative research careers on their return to Sweden.

The Foundation has set aside a maximum amount of SEK 36 million to fund up to twelve (12) three-year grants of SEK 3 million each (including overhead). The grants include a personal scholarship of SEK 50,000 that will be awarded each recipient. A leadership training programme will be arranged for the grantees. Participation in this leadership programme is mandatory. This announcement covers research in the natural sciences, engineering and medicine as well as multidisciplinary research integrating these areas.

The application process takes place in one step; full proposals only are accepted. The proposals must be written in English and submitted via the web portal of the Foundation at **http://apply.stratresearch.se**.
All applications must be submitted by **5 September 2012 at 14:00 (2 pm CET) at the latest.**

Detailed instructions and eligibility criteria will be found at the web portal.

www.stratresearch.se

Science Careers online @sciencecareers.org

FACTS & FICTION

Careers in Industry and Academia

Trying to figure out the next step in your career? Join us for a roundtable discussion that will look at facts and fiction surrounding academic and industry career options for PhD-level scientists. Get some nuts and bolts advice on how to research career options, what questions to ask, and how to best prepare for various careers.

- Do industry and academic careers require different skill sets?
- Do industry jobs have better compensation? Less autonomy?
- Do academic scientists have less work/life balance?

For answers view our roundtable discussion for free at:

ScienceCareers.org/webinar

Science Careers
From the journal *Science* AAAS

Produced by the *Science*/AAAS Business Office.

JOHNS HOPKINS
UNIVERSITY

The **Soft Materials Mechanics Laboratory** and the **Glaucoma Center of Excellence** invite applications for a **postdoctoral position** for a funded project in the area of experimental biomechanics to characterize the mechanical behavior of eye tissues, particularly the sclera and optic nerve head, in mouse models of glaucoma. The candidate is required to have a Ph.D. in Mechanical Engineering, Bioengineering, or a related field; and be experience in developing and conducting mechanical experiments on soft tissues. Experience with digital image correlation is desirable.

To apply, submit a complete curriculum vitae, representative publications, and the names and addresses of two references:

Prof. T. D. (Vicky) Nguyen
Harry A. Quigley, MD
Email: vicky.nguyen@jhu.edu
Email: hquigley@jhmi.edu

Thao (Vicky) Nguyen
Assistant Professor
The Johns Hopkins University
Department of Mechanical Engineering
125 Latrobe Hall
3400 N. Charles Str.
Baltimore, MD 21218
Phone: (410) 516-4538
Fax: (410) 516-7254
vicky.nguyen@jhu.edu
http://me.jhu.edu/tnguy108

CNPEM

Director for the Brazilian Bioethanol Science and Technology Laboratory (CTBE)

The **Brazilian National Center for Research in Energy and Materials (CNPEM)**, in Campinas, Brazil, is seeking candidates for the post of Director of **CTBE**. Applicants should send a letter of intent and a **Curriculum Vitae** to: diretoriageral@abtlus.org.br. CNPEM also houses three other national laboratories: the National Laboratory of Synchrotron Light (LNLS), the National Laboratory of Biosciences (LNBio), and the National Laboratory of Nanotechnology (LNNano). CNPEM is a social organization associated to the Ministry of Science, Technology and Innovation (MCTI).
www.bioethanol.org.br

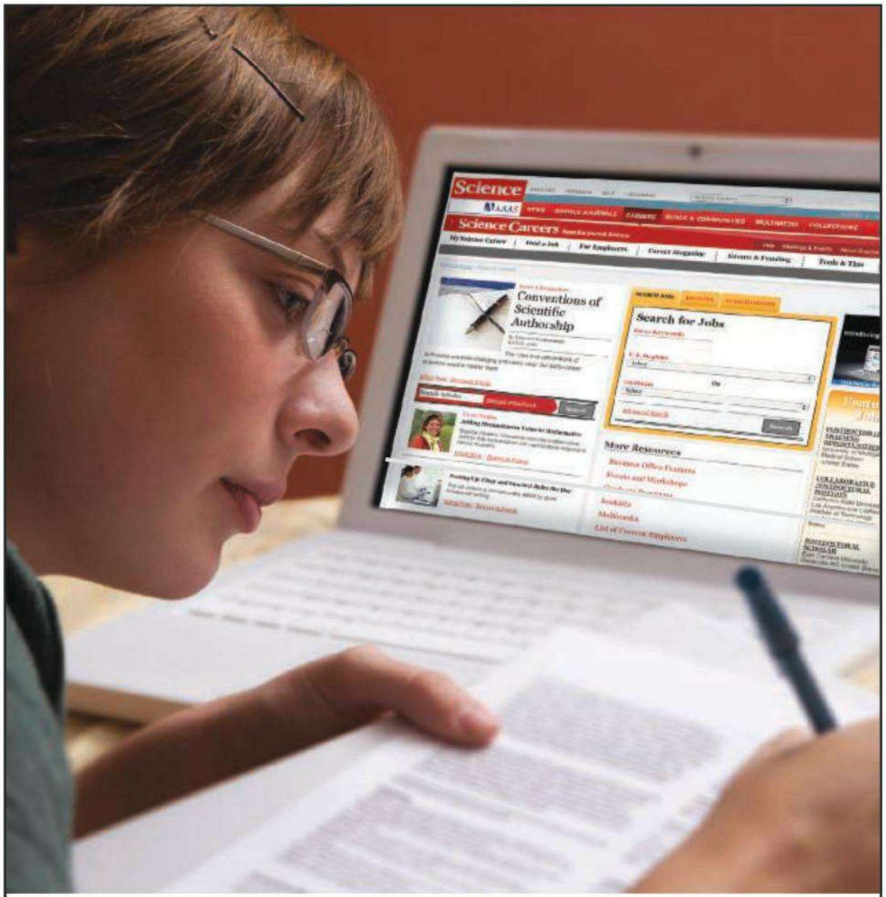

AAAS is here –
helping scientists achieve career success.

Every month, over 400,000 students and scientists visit ScienceCareers.org in search of the information, advice, and opportunities they need to take the next step in their careers.

A complete career resource, free to the public, *Science* Careers offers a suite of tools and services developed specifically for scientists. With hundreds of career development articles, webinars and downloadable booklets filled with practical advice, a community forum providing answers to career questions, and thousands of job listings in academia, government, and industry, *Science* Careers has helped countless individuals prepare themselves for successful careers.

As a AAAS member, your dues help AAAS make this service freely available to the scientific community. If you're not a member, join us. Together we can make a difference.

To learn more, visit
aaas.org/plusyou/sciencecareers

AAAS + U = Δ

POSITIONS OPEN

Tulane University

Outstanding **POSTDOCTORAL FELLOWS** are sought to conduct research into the pathogenesis of AIDS. Using the nonhuman primate model of AIDS we are examining host and viral determinants and mechanisms that underlie host control of and protection from infection.

The successful candidate will have a DVM, M.D., or Ph.D. in the life sciences along with evidence of first author papers published or accepted in peer-reviewed journals. The candidate will also have excellent written and verbal communication skills and analytical capabilities and a solid understanding of immunology and virology and techniques such as polychromatic flow cytometry, immunohistochemistry, and in situ hybridization. Molecular biology skills will also be useful. To apply, send a cover letter and curriculum vitae and the names of three individuals who may be contacted for references to: **Andrew A. Lackner,** DVM, Ph.D.; Professor of Microbiology, Immunology and Pathology; Director, Tulane National Primate Research Center at **e-mail: rita@tulane.edu.**

Tulane University and Louisiana State University are Affirmative Action and Equal Opportunity Educators and Employers. Individuals from under-represented minorities are strongly encouraged to apply.

DEPARTMENT OF CELL AND DEVELOPMENTAL BIOLOGY
University of Michigan Medical School

The University of Michigan Department of Cell and Developmental Biology is soliciting applications from outstanding scholars for a tenure-track or tenured position at the **ASSISTANT** or **ASSOCIATE PROFESSOR** level, as part of a cluster hire in the Reproductive Sciences. Research focusing on the biology of embryonic stem cells (ESC), induced pluripotent stem cells (iPSC), gonadal stem cells, and/or germ cell biology is strongly encouraged. Candidates should have MD, Ph.D., or M.D.-Ph.D. degrees with relevant postdoctoral training and a record of outstanding research with exceptional potential. Applicants should send a curriculum vitae, three reprints, a one- to two-page summary of research plans, and provide the names of three references by August 1, 2012, to:

Ms. Lori Longeway
Cell and Developmental
109 Zina Pitcher Place
3069 BSRB
Ann Arbor, MI 48109

Or submit electronically to **e-mail: longeway@umich.edu.**

POSTDOCTORAL POSITION
Department of Biochemistry
Vanderbilt University

A postdoctoral position funded by the NIH is available immediately to work on the structure and function of P450 enzymes in steroid hormone biosynthesis (*J. Biol. Chem.* **287:**10613–10622, 2012).

Candidates must have a Ph.D., a strong background in chemistry or biochemistry and experience in macromolecular X-ray crystallography. All crystallographic data collections are being conducted remotely or in person at the Advanced Photon Source, Argonne National Laboratory, to which Vanderbilt crystallographers have extensive access via the Life Sciences CAT at sector 21.

Please electronically send your curriculum vitae and the names of at least two references until June 30, 2012 to: **Professor Martin Egli, Department of Biochemistry, Vanderbilt University, School of Medicine, Nashville, TN 37232, USA. E-mail: martin.egli@vanderbilt.edu.**

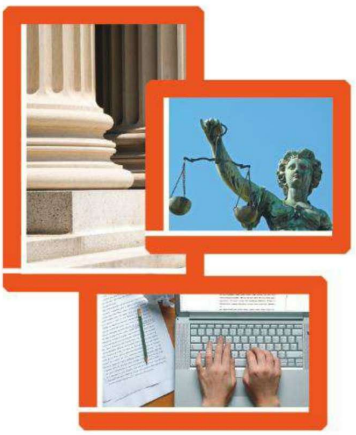

Nontraditional Careers: Opportunities Away From the Bench
Webinar

Want to learn more about exciting and rewarding careers outside of academic/industrial research? View a roundtable discussion that looks at the various career options open to scientists and strategies you can use to pursue a nonresearch career.

Now Available On Demand
www.sciencecareers.org/webinar

Produced by the *Science*/AAAS Business Office.

Science Careers
From the journal *Science* AAAS

Your career is our cause.

Get help from the experts.

www.sciencecareers.org

- Job Postings
- Job Alerts
- Resume/CV Database
- Career Advice
- Career Forum

Science Careers
From the journal *Science* AAAS

Find your future here.

Science Careers
From the journal *Science* AAAS

www.ScienceCareers.org

Widely Recognized Original & Guaranteed
KlenTaq1
8¢/u
Truncated Taq DNA Polymerase Withstand 99°C
US Pat #5,436,149
Call: **Ab Peptides**
Fax: 314•968•8988
e-mail: abpeps@msn.com
1•800•383•3362
www.abpeps.com

44

best practices for overcoming skepticism post-Climategate.

One more data point on why you should spend more time at membercentral.aaas.org. There you can enjoy webinars, videos, blogs, discounts, and downloads geared for people who prefer content based on empirical evidence.

membercentral.aaas.org

AAAS MEMBERCENTRAL

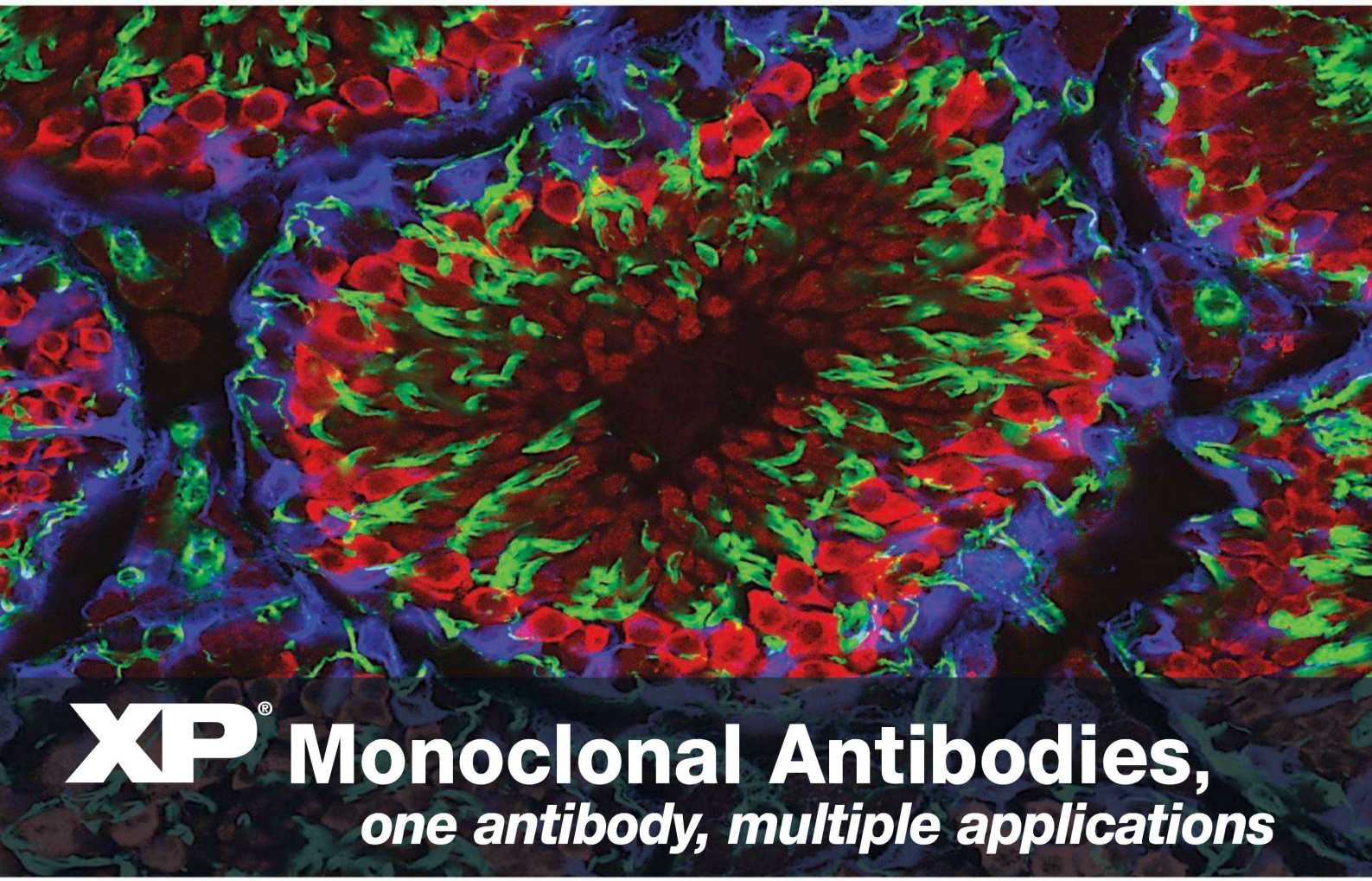

XP® Monoclonal Antibodies,
one antibody, multiple applications

Unparalleled product quality, validation, and technical support.

XP® monoclonal antibodies are a line of high quality rabbit monoclonal antibodies exclusively available from Cell Signaling Technology. Any product labeled with XP has been carefully selected based on superior performance in the most relevant applications.

XP monoclonal antibodies are generated using XMT® technology, a proprietary monoclonal method developed at Cell Signaling Technology. This technology provides access to a broad range of antibody-producing B cells unattainable with traditional monoclonal technologies, allowing more comprehensive screening and the identification of XP monoclonal antibodies.

eXceptional specificity
As with all of our antibodies, the antibody is specific to your target of interest, saving you valuable time and resources.

+ eXceptional sensitivity
The antibody will provide a stronger signal for your target protein in cells and tissues, allowing you to monitor expression of low levels of endogenous proteins, saving you valuable materials.

+ eXceptional stability and reproducibility
XMT technology combined with our stringent quality control ensures maximum lot-to-lot consistency and the most reproducible results.

= eXceptional Performance™
XMT technology coupled with our extensive antibody validation and stringent quality control delivers XP monoclonal antibodies with eXceptional Performance in the widest range of applications.

Above: Confocal IF analysis of rat testis using Miwi (D92B7) XP® Rabbit mAb #6915 (red pseudocolor) and Vimentin (D21H3) XP® Rabbit mAb (Alexa Fluor® 647 Conjugate) #9856 (blue pseudocolor). Actin filaments were labeled with DY-554 phalloidin (green pseudocolor).

For experimental details, additional information, and a complete list of available XP® monoclonal antibodies visit…

www.cellsignal.com

Cell Signaling TECHNOLOGY®

Orders (toll-free) 1-877-616-2355 | **Technical support** (toll-free) 1-877-678-8324 support@cellsignal.com | **Inquiries** info@cellsignal.com | **Environmental Commitment** eco.cellsignal.com

© 2012 Cell Signaling Technology, Inc. XMT®, XP®, eXceptional Performance™, CST™, and Cell Signaling Technology® are trademarks of Cell Signaling Technology, Inc. Alexa Fluor® is a trademark of Molecular Probes, Inc.